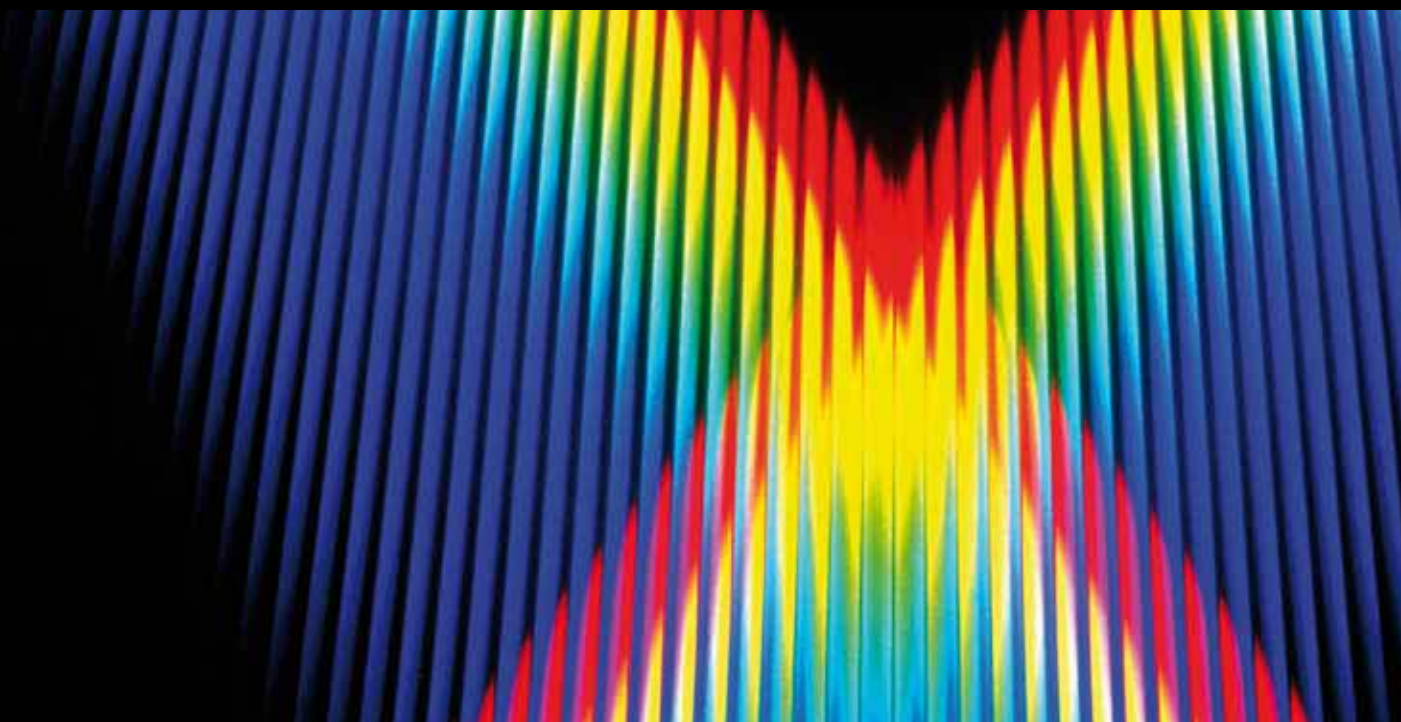


VIBRATIONAL SPECTROSCOPY: STRUCTURAL ANALYSIS FROM MOLECULES TO NANOMATERIALS

GUEST Editors: AHMED AAMOUCHE, SERGIO ARMENTA, AND JEAN-VALÈRE NAUBRON



Vibrational Spectroscopy: Structural Analysis from Molecules to Nanomaterials

International Journal of Spectroscopy

Vibrational Spectroscopy: Structural Analysis from Molecules to Nanomaterials

Guest Editors: Ahmed Aamouche, Sergio Armenta,
and Jean-Valre Naubron



Copyright © 2011 Hindawi Publishing Corporation. All rights reserved.

This is a special issue published in volume 2011 of "International Journal of Spectroscopy." All articles are open access articles distributed under the Creative Commons Attribution License, which permits unrestricted use, distribution, and reproduction in any medium, provided the original work is properly cited.

Editorial Board

| | | |
|--------------------------------|------------------------------|------------------------------|
| Maher S. Amer, USA | Karol Jackowski, Poland | Dhiraj Sardar, USA |
| S. Michael Angel, USA | Jukka Jokisaari, Finland | Stefan Schmatz, Germany |
| Hakan Arslan, Turkey | Jozef Kaiser, Czech Republic | K. W. Michael Siu, Canada |
| Rolf W. Berg, Denmark | Wei Kong, USA | Shigehiko Takegami, Japan |
| A.M. Brouwer, The Netherlands | Jaan Laane, USA | Veronica Vaida, USA |
| Steven G. Buckley, USA | Linda B. McGown, USA | Akihide Wada, Japan |
| Andres D. Campiglia, USA | Jeanne L. McHale, USA | Adam P. Wax, USA |
| Chak Keung Chan, Hong Kong | Giovanni Meloni, USA | Christopher T. Williams, USA |
| Ramachandra R. Dasari, USA | Li June Ming, USA | Kam-Sing Wong, Hong Kong |
| Craig J. Eckhardt, USA | Guillermo Moyna, USA | Jin Zhang, USA |
| Hicham Fenniri, Canada | Eugene Oks, USA | Guang Zhu, Hong Kong |
| M. Ashraf Gondal, Saudi Arabia | David Ramaker, USA | Erik R. Zuiderweg, USA |
| Peter B. Harrington, USA | Hans Riesen, Australia | |

Contents

Vibrational Spectroscopy: Structural Analysis from Molecules to Nanomaterials, Ahmed Aamouche, Sergio Armenta, and Jean-Valère Naubron
Volume 2011, Article ID 795694, 2 pages

On the Pressure and Temperature Dependence of the Absorption Coefficient of NH₃, F. Aousgi, S. Hadded, and H. Aroui
Volume 2011, Article ID 816548, 7 pages

First Observation of Defined Structural Motifs in the Sulfur-Iodine Thermochemical Cycle and Their Role in Hydrogen Production, Víctor H. Ramos-Sánchez, John Tomkinson, Jesús Muñiz-Soria, Edgar Valenzuela, and Robin Devonshire
Volume 2011, Article ID 691217, 14 pages

Molecular Self-Assembling of N-Methylacetamide in Solvents, Hideyuki Minami and Makio Iwahashi
Volume 2011, Article ID 640121, 7 pages

Conformational Analysis in Solution of a Chiral Bisoxazoline Molecule: Vibrational Circular Dichroism Spectroscopy and Density Functional Theory Study, A. Aamouche and P. J. Stephens
Volume 2011, Article ID 905045, 11 pages

Polymer Characterization by Combined Chromatography-Infrared Spectroscopy, James L. Dwyer and Ming Zhou
Volume 2011, Article ID 694645, 13 pages

Distribution of Heat Stabilizers in Plasticized PVC-Based Biomedical Devices: Temperature and Time Effects, Lidia Maria Bodecchi, Caterina Durante, Marcello Malagoli, Matteo Manfredini, Andrea Marchetti, and Simona Sighinolfi
Volume 2011, Article ID 641257, 8 pages

Effect of Artificial Saliva on the Apatite Structure of Eroded Enamel, Xiaojie Wang, Boriana Mihailova, Arndt Klocke, Stefanie Heidrich, and Ulrich Bismayer
Volume 2011, Article ID 236496, 9 pages

In Situ IR Characterization of CO Interacting with Rh Nanoparticles Obtained by Calcination and Reduction of Hydrotalcite-Type Precursors, F. Basile, I. Bersani, P. Del Gallo, S. Fiorilli, G. Fornasari, D. Gary, R. Mortera, B. Onida, and A. Vaccari
Volume 2011, Article ID 458089, 8 pages

Improving SERS Detection of *Bacillus thuringiensis* Using Silver Nanoparticles Reduced with Hydroxylamine and with Citrate Capped Borohydride, Hilsamar Félix-Rivera, Roxannie González, Gabriela Del Mar Rodríguez, Oliva M. Primera-Pedrozo, Carlos Ríos-Velázquez, and Samuel P. Hernández-Rivera
Volume 2011, Article ID 989504, 9 pages

Infrared and Raman Spectroscopic Study of Carbon-Cobalt Composites, André Tembre, Jacques Hénocque, and Martial Clin
Volume 2011, Article ID 186471, 6 pages

Editorial

Vibrational Spectroscopy: Structural Analysis from Molecules to Nanomaterials

Ahmed Aamouche,¹ Sergio Armenta,² and Jean-Valère Naubron³

¹ Département des Sciences de la Matière, Faculté Polydisciplinaire de Safi, Cadi Ayyad University, 46000 Safi, Morocco

² Department of Chemistry, Faculty of Sciences, Universitat Autònoma de Barcelona, Bellaterra, 08193 Barcelona, Spain

³ Spectropole, FR1739, Campus Saint Jérôme, Aix-Marseille Université, 13397 Marseille, France

Correspondence should be addressed to Ahmed Aamouche, a.aamouche@ucam.ac.ma

Received 8 September 2011; Accepted 8 September 2011

Copyright © 2011 Ahmed Aamouche et al. This is an open access article distributed under the Creative Commons Attribution License, which permits unrestricted use, distribution, and reproduction in any medium, provided the original work is properly cited.

Vibrational spectroscopy has become one of the key techniques for the structural recognition of molecular systems and measuring their interactions. Its spectral range, corresponding to vibrational transitions, leads to knowledge of the functional groups of the analyzed systems. Since the discovery of infrared radiation, two centuries ago, then Raman scattering a century later, these techniques have undergone extraordinary breakthrough to a variety of applications on small molecules and on macromolecules alike. Due to recent wide applications, we have encouraged our peers to contribute either original research or review articles that will recapitulate the continuing advancement to interpret molecular and even material structure using vibrational spectroscopy mainly infrared absorption.

In this work, we were particularly interested in articles tackling the junction of the three domains: physics, chemistry, and biology. Obviously, the selected topics do not represent all the advances in this field. Nevertheless, they will provide an assorted knowledge to the readers. We should not forget to thank the authors for their worthy contributions and also to recognize the reviewers' assistance. This special issue encloses ten papers, eight of them exploit the infrared absorption, three relayed the Raman scattering, and one paper utilizes the inelastic neutron scattering. In various circumstances, other experimental techniques, as electronic microscopy or liquid chromatography, were combined to the vibrational spectroscopy. A half of these papers illustrate a molecular system, whereas the other half considers a material nanostructure. Finally, two of the papers use the theoretical methods to simulate vibrational spectra. The order of

appearance of these papers was according to the atomic size of the studied system.

In the first paper entitled "On the pressure and temperature dependence of the absorption coefficient of NH₃," F. Aousgi et al. have used Fourier transform infrared spectroscopy (FTIR) and the multispectrum fitting technique in order to determine the absorption coefficients at the center and in the wings of 60 lines pertaining to the PP branch of the ν4 band of NH₃ as a function of NH₃ and N₂ pressures for different temperatures. In agreement with previous works, they showed that the variations of the self-absorption coefficient at the center and in the wings of a given line are not the same and are functions of the pressure. In addition, they established that the temperature dependence of the absorption coefficient of NH₃-N₂ mixture fit closely an exponential law.

In the second paper, "First observation of defined structural motifs in the Sulfur-Iodine Thermochemical Cycle, and their role in hydrogen production," V. H. Ramos-Sánchez et al. investigates the ionic species coexisting in the HI_x feed of the Sulfur-Iodine thermochemical cycle. They revealed for the first time, evidence for the presence of discrete water structural motifs under specific conditions. This kind of study has attracted the most attention worldwide for the carbon-free energy source and the valuable reagent gas production.

In the third paper, "Molecular Self-Assembling of N-Methylacetamide in Solvents," H. Minami et al. studied by near-infrared (NIR) spectroscopy the self-association of

N-methylacetamide in different solvents at various temperatures and concentrations. The different dielectric properties of the solvents and, of course, the temperature and concentration drastically affect the aggregation number of N-methylacetamide, being obtained the higher association degree with tetrachloroethylene.

In the fourth paper, the research of A. Aamouche et al. “Conformational analysis in solution of a chiral bis-oxazoline molecule: vibrational circular dichroism spectroscopy and density functional theory study” is focused on the evaluation of FTIR and vibrational circular dichroism (VCD) spectroscopies as unavoidable tools for the conformational analysis and the elucidation of the absolute configuration of large chiral molecules like the bis-oxazoline named IndaBOX. In the introduction, the authors remind use of the fundamental aspects of the VCD theory. Then follows a careful description of the conformations of IndaBOX and their calculated IR and VCD spectra. Finally, the contributions of the spectra of each conformation to the measured spectra are evaluated showing the possibilities of VCD spectroscopy for conformational analysis and determination of the absolute configuration of chiral molecules. This paper is a festschrift in honor of Pr. Philip J. Stephens 70th Birthday.

In the fifth paper, entitled “Polymer characterization by combined chromatography-infrared spectroscopy,” J. L. Dwyer et al. describe a trademark instrumentation that provides the benefit or resolving polymer populations into discrete identifiable entities, by combining chromatographic separation with continuous infrared spectra acquisition. The given examples include additives analysis, resolution of polymer blends, composition characterization of copolymers, analysis of degradation byproducts, and techniques of analysis of reactive polymer systems.

In the sixth paper entitled “Distribution of heat stabilizers in plasticized PVC-based biomedical devices: temperature and time effects,” L. M. Bodecchi et al. constitutes an attempt to the description of the possible behavior of medical grade Poly Vinyl Chloride heat stabilizers (calcium and zinc carboxylates), as regard temperature and time. Thanks to the attenuated total reflectance (ATR), it was possible to hypothesize that reaction and redistribution phenomena probably concur together to determine the additives allocation in the biomaterial as a function of temperature and time.

In the seventh paper, “Effect of artificial saliva on the apatite structure of eroded enamel,” X. Wang et al. identify the citric acid-induced changes in the structure of the mineral component of enamel stored in artificial saliva by ATR-FTIR spectroscopy. The process of loosening and breaking of [P–O–Ca] atomic linkages in enamel after citric acid treatment was studied, and additional treatments with basic fluoride-containing solutions were also evaluated.

In the eighth paper entitled “In-situ IR characterization of CO interacting with Rh nanoparticles obtained by calcination and reduction of hydrotalcite-type precursors,” F. Basile et al. characterized by FTIR spectroscopy of adsorbed CO and transmission electron microscopy (TEM), the Rh nanoparticles obtained after reduction in hydrogen of severely calcined Rh/Mg/Al hydrotalcite-type phases. The effect of reducing calcination temperature on the obtained

Rh crystal size has been investigated through the CO adsorption on the Rh nanoparticles. The role of interlayer anions in the precursors affects the properties of the final materials and different materials prepared from silicate, instead of carbonate, containing precursors were investigated.

In the ninth paper entitled “Improving SERS Detection of *Bacillus thuringiensis* using Silver Nanoparticles reduced with Hydroxylamine and with Citrate Capped Borohydride,” Félix-Rivera et al. identify biochemical components of the cell wall and endospores of *Bacillus thuringiensis* by surface-enhanced Raman scattering spectroscopy using silver nanoparticles. Activation, aggregation, and surface charge modification was studied and optimized in order to obtain high spectral quality. This kind of signal enhancements has a useful biodiagnosis applications.

In the final article entitled “Infrared and Raman spectroscopic study of carbon-cobalt composites,” A. Tembre et al. analyze carbon-cobalt thin films. The combination of FTIR and Raman spectroscopies together with high-resolution TEM suggests the presence of either amorphous or crystallized phases in correlation with cobalt composition. It has been reported that the incorporation in the carbon network of various metallic atoms, like Co, is a good alternative to improve the tribological, electric, and magnetic properties of carbon films for high-density storage applications.

Ahmed Aamouche
Sergio Armenta
Jean-Valère Naubron

Research Article

On the Pressure and Temperature Dependence of the Absorption Coefficient of NH₃

F. Aousgi, S. Hadded, and H. Aroui

Laboratoire de Physique Moléculaire, Ecole Supérieure des Sciences et Techniques de Tunis, 5 Avenue Taha Hussein, Tunis 1008, Tunisia

Correspondence should be addressed to F. Aousgi, aousgiefethi@yahoo.fr and H. Aroui, haroui@yahoo.fr

Received 27 June 2011; Accepted 24 August 2011

Academic Editor: Jean-Valère Naubron

Copyright © 2011 F. Aousgi et al. This is an open access article distributed under the Creative Commons Attribution License, which permits unrestricted use, distribution, and reproduction in any medium, provided the original work is properly cited.

The effects of pressure and temperature on the absorption coefficient of ammonia (NH₃) gas self-perturbed and perturbed by nitrogen (N₂) gas have been measured. We varied the gas pressure from 10 to 160 Torr and the temperature from 235 to 296 K in order to study the absorption coefficient at the center and the wings of lines in the ν_4 band of NH₃. These measurements were made using a high resolution (0.0038 cm⁻¹) Bruker Fourier-transform spectrometer. These spectra have been analyzed using the method of multipressure technique permitting to succeed to an evolution of the absorption coefficient with the pressure and the quantum numbers J and K of the NH₃ molecule. The results show that the absorption coefficient varies as a quadratic function of the pressure at the center of a given line. However, it has a linear evolution in the wings of the line. Moreover, the absorption coefficients are inversely proportional to temperature in the wings when NH₃ lines are broadened by N₂. The retrieved values of these coefficients were used to derive the temperature dependence of N₂ broadening NH₃ lines. The absorption coefficients were shown to fit closely the well-known exponential law.

1. Introduction

The infrared spectroscopic investigations of the atmospheres of stars, planets, and their satellites, using infrared spectroscopy, not only provide valuable information about the chemical elements that they consist of, but also about the horizontal and the vertical distribution of their minor constituents. Due to the complexity of the line profiles used to model the spectral shapes (absorption, broadening, intensity), it is necessary to determine experimentally the line parameters of the spectra in order to test the models being used.

Several studies in the literature have investigated the spectral properties of NH₃ in several infrared bands. Aroui et al. [1] have studied the self-broadening and line intensities, Nouri et al. [2] have studied the temperature dependence of pressure broadening, and other authors [3, 4] were interested in the absorption coefficient at the line centers of NH₃. Experimentally absorption coefficients for broadband ArF excimer radiation laser were determined for NH₃ at temperatures up to 3500 K [5]. Measurements of the NH₃

absorption coefficients at CO₂ laser wavelengths have been done by Zelinger et al. [5] using photoacoustic spectroscopy. NH₃ absorption coefficients were also measured by Allario and Seals [6] using several transitions of a CO₂ laser for small concentrations of NH₃ perturbed by N₂. The influence of CO₂ Laser line width on the measured absorption coefficients of atmospheric ammonia has been studied by Voitsekhovskaya et al. [7].

The focus of the present study is to present absorption line profile measurements of NH₃ in the 6 μm region (^PP branch of the ν_4 band). In this range, we resolved the spectra for different J and K quantum numbers. We have determined the absorption coefficients in the centers and in the wings of NH₃ lines self-perturbed and perturbed by N₂ at various pressures (10–160 Torr). The measurements were made for different gas temperatures 235, 245, 268, and 296 K. The analysis was made as a function of J and K quantum numbers, and the results were compared to the previous investigations.

TABLE 1: Experimental parameters.

| Studied gas | Temperature (K) | Pressure of the perturbed gas (mbar) | Cell length (cm) |
|----------------------------------|--------------------|--------------------------------------|------------------|
| NH ₃ -NH ₃ | 296 | 10~141 | 2.5 |
| NH ₃ -N ₂ | 235, 245, 268, 296 | 10~141 | 15 |

2. Experimental

The measurements were made using a high-resolution Bruker Fourier transform spectrometer (Bruker IFS 120 HR) [8, 9]. This spectrometer is equipped with different components: a Globar source, a KBr beam splitter, a filter eliminating infrared radiation above 2500 cm⁻¹, and a photovoltaic HgCdTe detector cooled at 77 K by liquid nitrogen.

The spectral resolution was about 0.0038 cm⁻¹ after apodization with a triangular function. This value is equal to the half-width at half maximum of the apparatus function approximated in the calculations by a Gaussian shape. This approximation has a negligible contribution to systematic errors since the pressure-broadened lines were much larger [2, 10]. Ammonia gas in natural abundances was provided by Air Liquid France with stated purity of 98.5%. The spectra were measured at different pressures covering the lines of the ^PP branch of the ν₄ band of ammonia. NH₃ and N₂ gases were contained in a metallic cell with a 2.5 cm path length for NH₃ self-perturbed, and in a Pyrex glass cell with a 15 cm path length for NH₃ perturbed by N₂. Both of the absorption cells are sealed by CaF₂ windows.

The pressures of the gases were measured accurately using three calibrated capacitive MKS Baratron transducers with full-scale readings of 10, 100, and 1000 mbar. The accuracy of these manometers is 0.5% of the readout. Ammonia sample pressures were allowed to stabilize for sufficient time before the spectrum of the sample was finally recorded.

For NH₃ self-perturbed, the pressure was varied from 5 to 120 mbar, whereas for NH₃ perturbed by N₂ we varied the gas pressure from 10 to 160 Torr. For the present experiments, the temperatures varies from 235 to 296 K. Each temperature was monitored by three calibrated thermocouples (Pt-100).

The measured intensity of the incident light (I_0) and the transmitted light (I) at wave-number σ were converted to transmission spectra $\tau(\sigma, T)$ using Lambert-Beer's law

$$\tau(\sigma, T) = \frac{I(\sigma, T)}{I_0(\sigma, T)}. \quad (1)$$

Table 1 summarizes the experimental parameters. The spectral region for this study is between 1470 and 1600 cm⁻¹. Figure 1 shows short transmittance spectra of NH₃ around 1550 cm⁻¹ exhibiting some prominent lines of the ^PP branch. These spectra were recorded at $T = 296$ K. At low pressure, the lines are separated, but when the pressure increases the lines widen and begin to overlap.

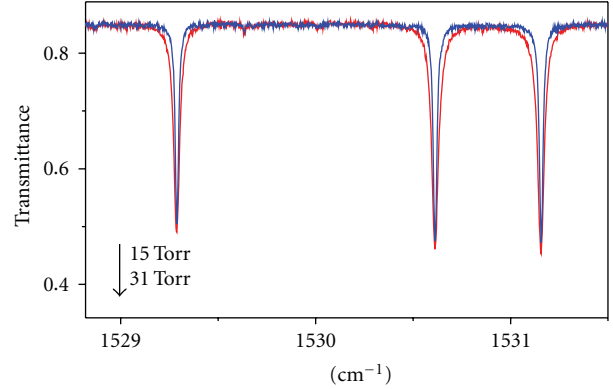


FIGURE 1: Transmittance spectrum of NH₃ around 1550 cm⁻¹ showing some lines of the ^PP branch of the ν₄ band. The pressures of NH₃ are 15 and 31 mb.

3. Fitting Procedures

The absorption coefficient of an isolated line of the ν₄ band is obtained by comparing the recorded line with a synthetic line. The adjustment is performed using the Rosenkranz profile given [11, 12] by

$$\alpha(\sigma) = \frac{P_{\text{NH}_3}}{\pi} \sum_{\text{line } k} S_k \frac{PY_k(\sigma - \sigma_k) + P\gamma_k}{(\sigma - \sigma_k)^2 + (P\gamma_k)^2}, \quad (2)$$

where P_{NH_3} is the NH₃ pressure, P is the partial pressure of the perturbing gas, k represents the line $\nu_i J_i \rightarrow \nu_f J_f$, S_k its intensity, σ_k its wave number including the collisional shift δ ($\delta = \sigma_k - \sigma_0$, σ_0 the unperturbed or zero pressure wave number), γ_k its broadening coefficient, and Y_k its mixing parameter.

The modelled transmission $\tau(\sigma)$ is the result of a convolution of $\alpha(\sigma)$ with a Doppler profile (α_{Dop}) and the apparatus function of the spectrometer (F_{App}) [10].

$$\tau(\sigma)$$

$$= \int_{-\infty}^{+\infty} F_{\text{App}}(\sigma - \sigma') \exp \left[-l \int_{-\infty}^{+\infty} \alpha_{\text{Dop}}(\sigma' - \sigma'') \alpha(\sigma'') d\sigma'' \right] d\sigma', \quad (3)$$

where l represents the length of the absorption cell.

The differences between the experimental and calculated spectra were minimized by adjusting the parameters PS_k , σ_k , $P\gamma_k$, and PY_k using a nonlinear least-squares multipressure fitting technique where all spectra at various pressures are successively adjusted using (3). An example of multipressure fit in the case of ^PP(7, 3)_s line for four NH₃ pressures (30, 60, 91, and 120 mbar) is shown in Figure 2. Residual (measured minus calculated) spectra are shown in the lower part of graphs.

As illustrated by this figure, the theoretical model given by (3) proves sufficiently accurate to fit very well the observed spectral lines without accounting for Dicke narrowing and/or speed dependence and demonstrates at the same time that the line coupling cannot be neglected.

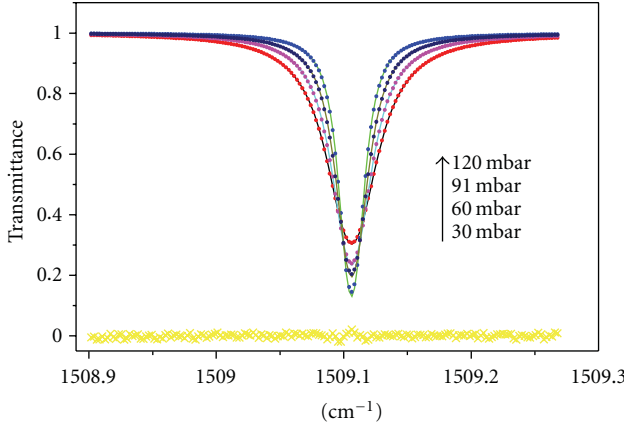


FIGURE 2: Results of multipressure fits for the $^P P(7, 3)_s$ line in the ν_4 band of NH_3 self-perturbed at 296 K. (—) and (●) are the measured and calculated values, respectively. Residual (measured minus calculated) spectra are shown in the lower part of the graphs.

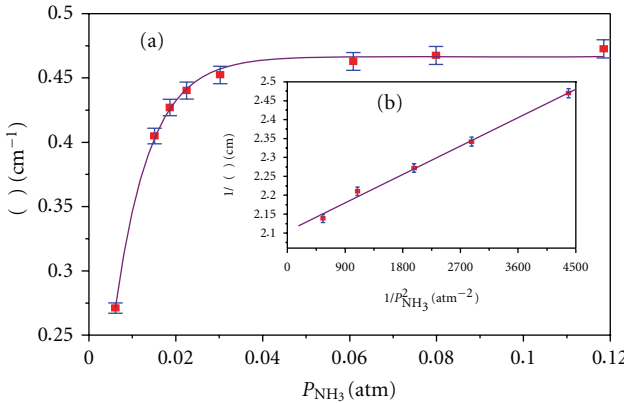


FIGURE 3: Variation of the absorption coefficient and its inverse in the center of the $^P P(8, 3)_s$ line versus P_{NH_3} and $1/P_{\text{NH}_3}^2$, respectively, at $T = 296$ K.

4. Results Analysis

4.1. Line Center Absorption Coefficients. We have made measurements of the absorption coefficients for 60 isolated lines of NH_3 in the spectral region between 1470 and 1600 cm^{-1} . For illustration, the evolution of the absorption coefficient at $T = 296$ K for the $^P P(8, 3)_s$ line at various pressures of NH_3 is shown in Figure 3(a).

In the low-pressure regime, we notice that the absorption coefficient of a given line varies as a quadratic function of pressure as given by the following equation:

$$\alpha = C^{\text{te}} P_{\text{NH}_3}^2, \quad (4)$$

where C^{te} is a constant value depending on the individual line.

This figure shows that at high-pressure region, the absorption coefficient tends towards a constant value and hence becomes independent of pressure.

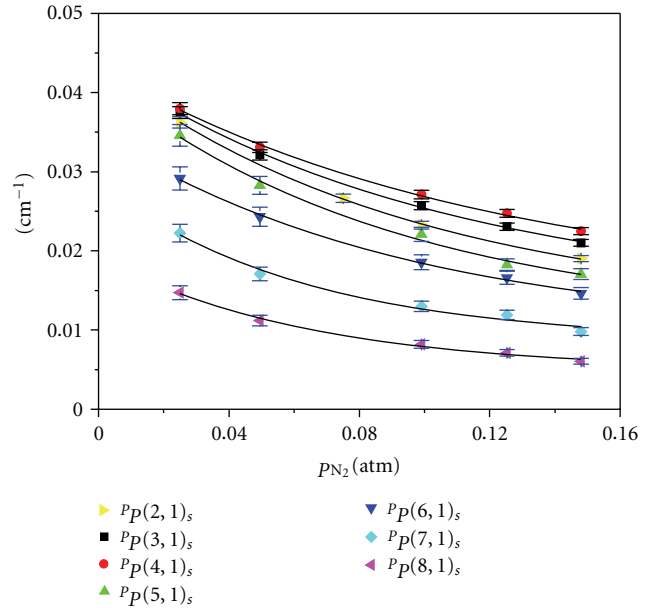


FIGURE 4: Variation of the absorption coefficient in the line center versus the N_2 pressure (P_{N_2}) for the $^P P(J, 1)_s$ lines.

These results are in agreement with those published in [4], where the author studied some lines of the ν_2 band of NH_3 .

The inverse of the absorption coefficient ($1/\alpha$) as a function of the square of the NH_3 pressure is plotted in Figure 3(b) for the $^P P(8, 3)_s$ line. Indeed, one can see that these two parameters vary linearly. The slope of the obtained straight line is related to the line intensity and self-broadening coefficient of the considered line [4].

Results obtained for NH_3 perturbed by N_2 , show that the peak absorption coefficient, for the 60 lines studied in this work, is decreasing with the N_2 pressure. Figure 4 illustrates the variation of the line center absorption coefficients versus the N_2 pressure for the $^P P(J, 1)_s$ lines at $T = 296$ K. This figure also shows that the absorption coefficient α decreases with the pressure of the perturbing gas. Moreover, it illustrates that α decreases with quantum number J for a given K . For example, the α of $^P P(2, 1)_s$ line is greater than that of $^P P(8, 1)_s$ line.

Figure 5 represents the evolution of the absorption coefficient α with the quantum number J in the case of NH_3-NH_3 gas mixture at $T = 296$ K and $P = 32$ Torr. The coefficient α has a maximum at $J = 4$ for the $^P P(J, 1)$ lines and decreases monotonically for $K \geq 2$ with increasing J .

According to the literature [10, 13], the line intensity S_0 depends on the statistical weight factor g_s , which is related to the quantum numbers J and K . The intensities of the transition having a statistical weight $g_s = 2$ (i.e., for $K = 3n$, $n = 1, 2, 3, \dots$) are generally higher than of those lines having a statistical weight $g_s = 1$ for $K \neq 3n$. As illustrated by Table 4, one can conclude that the absorption coefficients and the line intensities vary in the same way as a function of the quantum numbers.

TABLE 2: Self-absorption coefficient of the two wings of ${}^P P(5, 2)_s$ and ${}^P P(7, 4)_s$ lines as a function of the square of NH₃ pressure ($P_{\text{NH}_3}^2$) at $T = 296$ K.

| $P_{\text{NH}_3}^2 \times 10^4$ (atm ²) | ${}^P P(5, 2)_s$ left | ${}^P P(5, 2)_s$ right | ${}^P P(7, 4)_s$ left | ${}^P P(7, 4)_s$ right |
|---|-----------------------|------------------------|-----------------------|------------------------|
| 2.28 | 14.9 | 14.4 | — | 1.64 |
| 18 | 61 | — | 48.5 | — |
| 37 | 123.8 | 125.9 | 80.5 | 81.5 |
| 63 | 191.5 | 191.5 | 122.1 | 121.5 |
| 140 | 384.4 | 382.3 | 256.5 | 256.3 |

TABLE 3: Absorption coefficient of two wings of the ${}^P P(7, 2)_a$ for NH₃-N₂ mixtures as a function of N₂ pressure (P_{N_2}) at $T = 268$ K.

| $P_{\text{N}_2} \times 10^3$ (atm) | $\alpha/P_{\text{NH}_3} \times 10^2$ (cm ⁻¹ atm ⁻¹) | ${}^P P(7, 2)_a$ right | ${}^P P(7, 2)_a$ left |
|------------------------------------|--|------------------------|-----------------------|
| 29.6 | 15.1 | 13.8 | |
| 59.2 | 19.4 | 18.4 | |
| 89.6 | 24.1 | 23.9 | |
| 121.9 | 27.7 | 26.7 | |
| 138.9 | 30.8 | 30.1 | |

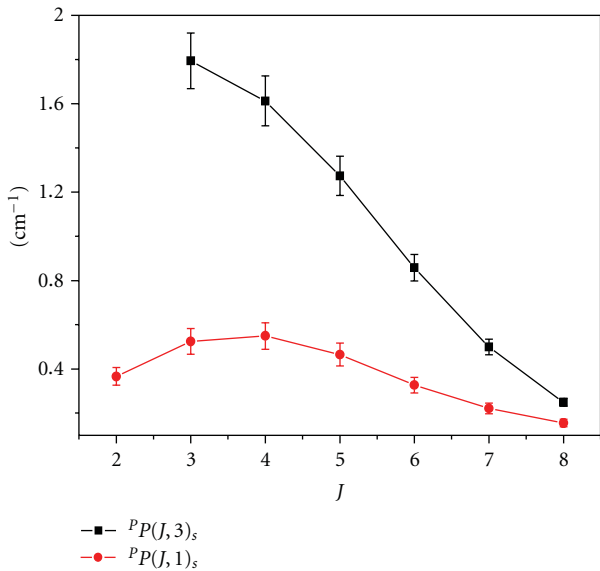


FIGURE 5: Variation of the absorption coefficient of ${}^P P(J, 3)_s$ and ${}^P P(J, 1)_s$ lines with the quantum numbers J and K . Case of NH₃-NH₃ gas mixture at $P = 32$ Torr for $T = 295$ K.

4.2. Line Wing Absorption Coefficients. According to our analysis, we observe a quadratic dependence of the absorption coefficient as a function of pressure of the NH₃ gas that can be modeled as follows [14]:

$$\alpha = A_0(\sigma, T)P_{\text{NH}_3}^2, \quad (5)$$

$A_0(\sigma, T)$ is the normalized absorption coefficient depending on the temperature and the wave number σ of the line; P_{NH_3} is the NH₃ pressure. Table 2 gives the self-absorption coefficient of the two wings of ${}^P P(5, 2)_s$ and ${}^P P(7, 4)_s$ lines

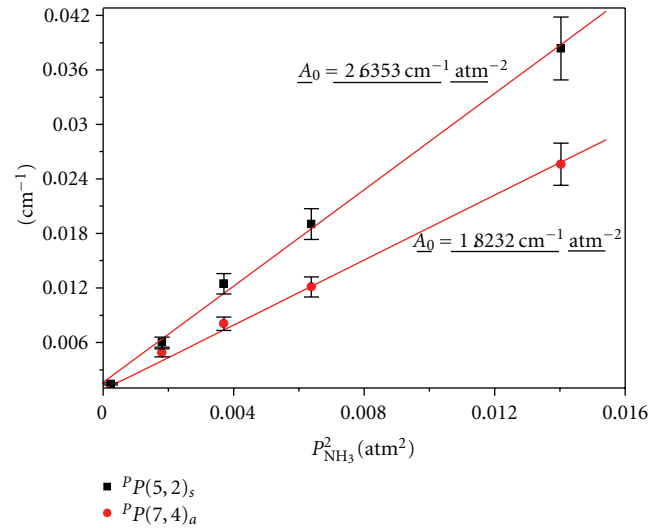


FIGURE 6: Variation of self-absorption coefficient in the right wings of ${}^P P(5, 2)_s$ and ${}^P P(7, 4)_s$ lines as a function of the square of NH₃ pressure ($P_{\text{NH}_3}^2$): Case of NH₃-NH₃ gas mixture at $T = 296$ K.

as a function of the square of NH₃ pressure ($P_{\text{NH}_3}^2$) at $T = 296$ K. Figure 6 shows the variation of self-absorption coefficient of the right wings of ${}^P P(5, 2)_s$ and ${}^P P(7, 4)_s$ lines as a function of the square of NH₃ pressure ($P_{\text{NH}_3}^2$). One can see that the wing absorption coefficients increase linearly with pressure.

All the self-absorption coefficients measured for the pressure and temperature ranges considered in this study validate the above quadratic pressure dependence given by (5).

For NH₃-N₂ gas mixtures, a sample of the absorption coefficient α for the two wings of the ${}^P P(7, 2)_a$ line as a function of N₂ pressure (P_{N_2}) at $T = 268$ K is given by Table 3. This table reveals an increasing of α with P_{N_2} . So the coefficient α can be described by the following equation [15]:

$$\alpha = A_0(\sigma, T)P_{\text{NH}_3}^2 + B_0(\sigma, T)P_{\text{NH}_3}P_{\text{N}_2}, \quad (6)$$

where $B_0(\sigma, T)$ is the normalized absorption coefficient.

The $A_0(\sigma, T)$ and $B_0(\sigma, T)$ parameters were determined using (6) and the absorption coefficient values for the right and left wings of the each line considered in this work. The results at $T = 296$ K are given in Table 4 for 32 ro-vibrational antisymmetric lines in the ${}^P P$ branch of the ν_4 band along with the estimated errors given in parentheses.

TABLE 4: Values of the normalized absorption coefficients A_0 and B_0 for NH_3 broadened by N_2 at $T = 296 \text{ K}$.

| Transition | $\sigma (\text{cm}^{-1})$ | NH ₃ -NH ₃ | | NH ₃ -N ₂ | |
|-----------------------------------|---------------------------|--|---|--|---|
| | | $A_0 (\text{cm}^{-1} \text{ atm}^{-2}) (\sigma_{\text{left}})$ | $A_0 (\text{cm}^{-1} \text{ atm}^{-2}) (\sigma_{\text{right}})$ | $B_0 (\text{cm}^{-1} \text{ atm}^{-2}) (\sigma_{\text{left}})$ | $B_0 (\text{cm}^{-1} \text{ atm}^{-2}) (\sigma_{\text{right}})$ |
| ^P P(2, 1) _a | 1591.1050 | 1.467 (0.098) | 1.493 (0.063) | 2.731 (0.437) | 2.448 (0.245) |
| ^P P(2, 2) _a | 1595.0801 | 6.759 (0.348) | 1.045 (0.069) | 3.228 (0.233) | 2.799 (0.303) |
| ^P P(3, 1) _a | 1572.4882 | 3.282 (0.139) | 3.435 (0.065) | 2.807 (0.100) | 2.956 (0.542) |
| ^P P(3, 3) _a | 1579.6363 | 16.39 (0.431) | 2.216 (0.047) | 3.859 (0.274) | 4.176 (0.183) |
| ^P P(4, 1) _a | 1554.7340 | 2.065 (0.047) | 2.009 (0.050) | 3.490 (0.329) | 3.006 (0.207) |
| ^P P(4, 2) _a | 1558.2494 | 1.344 (0.046) | 1.370 (0.011) | 2.815 (0.269) | 2.923 (0.218) |
| ^P P(4, 3) _a | 1561.3835 | 4.217 (0.086) | 4.1741 (0.150) | 9.782 (0.707) | 9.632 (0.462) |
| ^P P(4, 4) _a | 1564.0825 | 10.40 (0.186) | 0.566 (0.042) | 2.338 (0.203) | 5.111 (0.511) |
| ^P P(5, 1) _a | 1538.0102 | 0.860 (0.083) | 0.838 (0.058) | 3.693 (0.372) | 3.343 (0.171) |
| ^P P(5, 2) _a | 1541.0041 | 2.520 (0.075) | 2.272 (0.021) | 2.883 (0.540) | 2.893 (0.534) |
| ^P P(5, 3) _a | 1543.8550 | 2.468 (0.07) | 2.990 (0.029) | 5.638 (0.248) | 5.391 (0.583) |
| ^P P(5, 4) _a | 1546.3315 | 5.805 (0.194) | 4.610 (0.270) | 4.829 (0.028) | 4.013 (0.539) |
| ^P P(5, 5) _a | 1548.4290 | 13.527 (0.381) | 2.471 (0.142) | 2.920 (0.220) | 3.510 (0.208) |
| ^P P(6, 1) _a | 1522.3847 | 1.370 (0.033) | 1.518 (0.024) | 2.020 (0.384) | 1.021 (0.134) |
| ^P P(6, 2) _a | 1522.7763 | — | — | 2.006 (0.399) | 1.894 (0.064) |
| ^P P(6, 3) _a | 1527.0615 | 2.822 (0.093) | 2.583 (0.053) | 4.232 (0.364) | 4.313 (0.372) |
| ^P P(6, 4) _a | 1529.2897 | 1.524 (0.015) | 1.553 (0.058) | 2.424 (0.146) | 2.172 (0.221) |
| ^P P(6, 5) _a | 1531.1590 | 1.571 (0.07) | 1.4164 (0.056) | 3.784 (0.522) | 3.003 (0.625) |
| ^P P(6, 6) _a | 1532.6831 | 20.697 (0.570) | 2.250 (0.118) | 4.430 (0.076) | 9.116 (0.919) |
| ^P P(7, 2) _a | 1509.4479 | 1.818 (0.053) | 1.863 (0.108) | 1.415 (0.044) | 1.445 (0.055) |
| ^P P(7, 3) _a | 1511.3125 | 1.169 (0.064) | 1.510 (0.047) | 1.183 (0.195) | 1.312 (0.247) |
| ^P P(7, 4) _a | 1513.0439 | 1.823 (0.094) | 1.888 (0.074) | 1.657 (0.131) | 1.431 (0.442) |
| ^P P(7, 5) _a | 1514.6055 | 2.319 (0.176) | 2.145 (0.141) | 1.810 (0.157) | 1.500 (0.104) |
| ^P P(7, 6) _a | 1515.8819 | 3.013 (0.035) | 3.074 (0.162) | 2.200 (0.179) | 1.946 (0.226) |
| ^P P(7, 7) _a | 1516.8521 | 8.994 (0.217) | 1.248 (0.070) | 2.080 (0.120) | 2.632 (0.091) |
| ^P P(8, 1) _a | 1494.2421 | 0.375 (0.038) | 0.334 (0.009) | 1.116 (0.113) | 1.180 (0.101) |
| ^P P(8, 2) _a | 1493.5269 | — | — | 1.145 (0.142) | 1.328 (0.215) |
| ^P P(8, 3) _a | 1496.1740 | 0.546 (0.105) | 0.597 (0.072) | 2.357 (0.153) | 2.785 (0.261) |
| ^P P(8, 4) _a | 1497.6750 | 1.982 (0.104) | 2.123 (0.071) | 4.054 (0.261) | 4.521 (0.276) |
| ^P P(8, 6) _a | 1499.8028 | 2.199 (0.022) | 2.877 (0.264) | 2.710 (0.236) | 2.499 (0.917) |
| ^P P(8, 7) _a | 1500.5103 | 11.869 (1.307) | 10.742 (1.414) | — | — |
| ^P P(8, 8) _a | 1500.9439 | 7.227 (0.231) | 2.221 (0.335) | 1.423 (0.349) | 1.799 (0.368) |

These errors correspond to the statistical errors expressed as one-time standard deviation for all spectroscopic parameters determined in this work. As expected, the errors vary widely with the lines. The stronger and less blended ones are better determined. For the lines which are too weak or too strongly blended, no reliable fit could be obtained. For this reason, some lines have been disregarded. The assignments of the lines considered in this table are taken from [16]. Within the experimental errors, as seen by Table 4, the values of $A_0(\sigma, T)$ and $B_0(\sigma, T)$ are practically identical for the two wings.

Figure 7 shows the variation of the absorption coefficient with the N_2 pressure for the two wings of the ^PP(7, 2)_a line for NH₃-N₂ mixtures at $T = 268 \text{ K}$. As shown by this figure, the variation of the absorption coefficient divided by the NH₃ pressure (α/P_{NH_3}) with the N₂ pressure is linear. Also, we observe that the values of α/P_{NH_3} and $A_0(\sigma, T)$ parameters

are practically the same for the left and right wings of the lines.

4.3. Temperature Dependence. Spectra of the ν_4 band of NH₃ perturbed by N₂ were recorded at four temperatures 235, 245, 268, and 296 K for different pressures of nitrogen (P_{N_2}). For these spectra, the pressure of NH₃ was fixed. Variation of the absorption coefficient α at the line center as a function of P_{N_2} for the ^PP(5, 2)_s line for $T = 235$ and 265 K is shown by Figure 8 which illustrates a decreasing of the absorption coefficient with temperature.

According to Shi and Zhang and Bauer et al. [17, 18], the temperature dependence of absorption coefficient $\alpha(T)$ could be presented by the simple power law:

$$\alpha = \alpha(T_0) \left(\frac{T}{T_0} \right)^A, \quad (7)$$

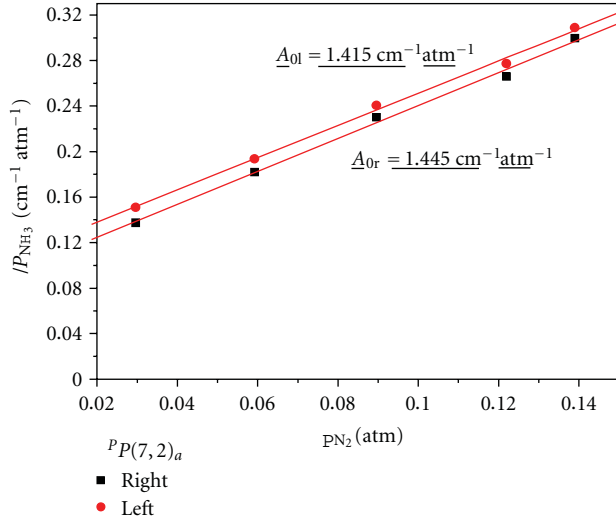


FIGURE 7: Variation of α/P_{NH_3} versus the N_2 pressure (P_{N_2}) for the two wings of the ${}^P\text{P}(7,2)_a$ line perturbed by N_2 at $T = 268 \text{ K}$.

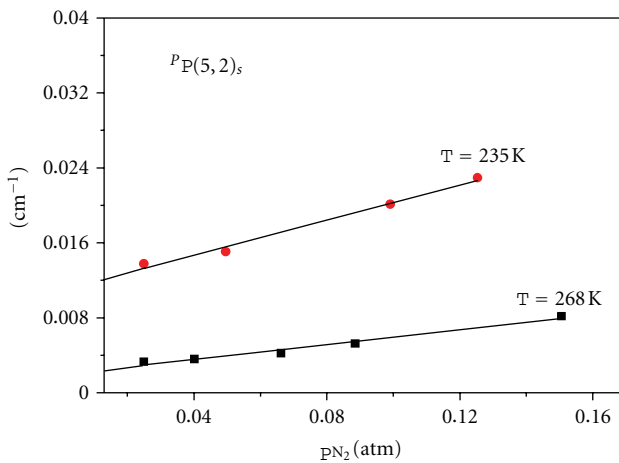


FIGURE 8: Variation of the absorption coefficient as a function of the N_2 pressure (P_{N_2}) for the ${}^P\text{P}(5,2)_s$ line for the temperatures $T = 235 \text{ K}$ and 268 K .

where A is the temperature exponent and T_0 is the reference temperature. In our case $T_0 = 235 \text{ K}$.

From the measured values of the absorption coefficients for the considered temperatures, one can determine the values of the exponent A as the slope of least square fits from the graphs of $\ln(T/\alpha(T_0))$ as a function of $\ln(T/T_0)$. The straight lines obtained for all the transitions considered in this work validate (7) within the indicated temperature range. Figure 9 illustrates the variation of $\ln[\alpha(T)/\alpha(235)]$ as a function of $\ln(T/235)$ for the ${}^P\text{P}(5,2)_a$ line. The variation is linear; the slope of the line obtained from a linear regression gives a temperature exponent $A = -0.619 \pm 0.016$.

This dependence is in agreement with the work performed by Bauer et al. [18] in their study of the temperature dependence of the absorption coefficient of H_2O transitions.

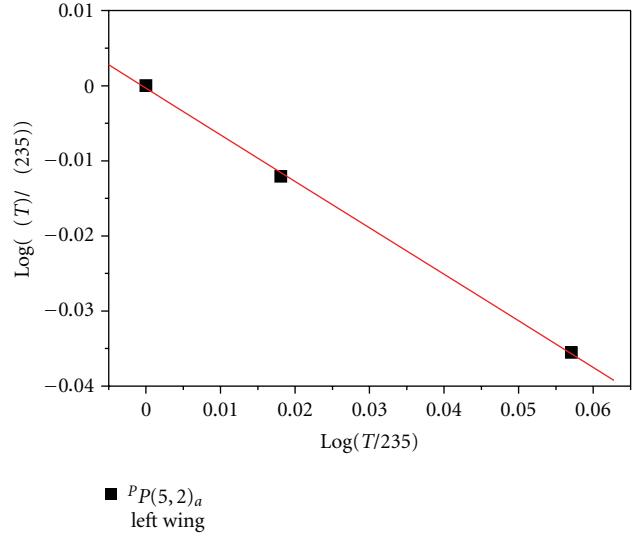


FIGURE 9: Variation of $\ln[\alpha(T)/\alpha(235)]$ as a function of $\ln(T/235)$ for the left wing of ${}^P\text{P}(5,2)_a$ line. The slope of the line obtained from a linear regression represents the temperature exponent $A = -0.619 \pm 0.016$.

5. Conclusion

Using spectra recorded using a Fourier transform spectrometer and a multispectrum fitting technique, we have determined the absorption coefficients at the center and in the wings of 60 lines pertaining to the ${}^P\text{P}$ branch of the ν_4 band of NH_3 as a function of NH_3 and N_2 pressures for different temperatures. The present results are in agreement with other recent measurements. In the low-pressure region, the self-absorption coefficient at the center of a given line varies with pressure as a quadratic function. At higher pressures, this coefficient tends to become constant. For $\text{NH}_3\text{-N}_2$ mixture, the values of the absorption coefficients exhibit a decreasing with N_2 pressure.

In the wings of the lines, these coefficients show an increasing with the square of NH_3 pressure, while for $\text{NH}_3\text{-N}_2$ gas mixtures they increase with N_2 pressure.

For this gas mixture, we have studied the temperature dependence of absorption coefficient which fits closely an exponential law. The temperature exponents of this law were derived for the ${}^P\text{P}(5,2)_a$ line.

References

- [1] H. Aroui, S. Nouri, and J. P. Bouanich, “ NH_3 self-broadening coefficients in the ν_2 and ν_4 bands and line intensities in the ν_2 band,” *Journal of Molecular Spectroscopy*, vol. 220, no. 2, pp. 248–258, 2003.
- [2] S. Nouri, J. Orphal, H. Aroui, and J. M. Hartmann, “Temperature dependence of pressure broadening of NH_3 perturbed by H_2 and N_2 ,” *Journal of Molecular Spectroscopy*, vol. 227, no. 1, pp. 60–66, 2004.
- [3] D. F. Davidson, A. Y. Chang, K. Kohse-Höinghaus, and R. K. Hanson, “High temperature absorption coefficients of O_2 , NH_3 , and H_2O for broadband ArF excimer laser radiation,”

- Journal of Quantitative Spectroscopy and Radiative Transfer*, vol. 42, no. 4, pp. 267–278, 1989.
- [4] K. Benzerhouni, *Absorption spectroscopy of ammonia and study of the laser ($^{15}\text{NH}_3 + \text{N}_2$) for population inversion*, Ph.D. thesis, Orsay, France, 1988.
 - [5] Z. Zelinger, I. Jancik, and P. Engst, “Measurement of the NH_3 , CCl_2F_2 , CHClF_2 , CFCl_3 , and CClF_3 absorption coefficients at isotopic $^{13}\text{C}^{16}\text{O}_2$ laser wavelengths by photoacoustic spectroscopy,” *Applied Optics*, vol. 31, no. 33, pp. 6974–6975, 1992.
 - [6] F. Allario and R. K. Seals, “Measurements of NH_3 absorption coefficients with a $\text{C}^{13}\text{O}^{16}$ laser,” *Applied Optics*, vol. 14, no. 9, pp. 2229–2233, 1975.
 - [7] O. K. Voitsekhovskaya, E. N. Aksenova, and F. G. Shatrov, “Influence of CO_2 -laser linewidth on the measured absorption coefficients of atmospheric water vapor and ammonia,” *Applied Optics*, vol. 38, no. 12, pp. 2337–2341, 1999.
 - [8] P. Jacquinot, “The luminosity of spectrometers with prisms, gratings, or Fabry Perot etalons,” *The Journal of the Optical Society of America*, vol. 44, pp. 761–765, 1954.
 - [9] A. Predoi-Cross, G. C. Mellau, R. M. Lees, and B. P. Winnissner, “Fourier transform infrared spectroscopy of the first CO-stretch overtone band of $^{13}\text{CH}_3\text{OH}$,” *Journal of Molecular Spectroscopy*, vol. 189, no. 2, pp. 144–152, 1998.
 - [10] S. Hadded, H. Aroui, J. Orphal, J. P. Bouanich, and J. M. Hartmann, “Line broadening and mixing in NH_3 inversion doublets perturbed by NH_3 , He, Ar, and H_2 ,” *Journal of Molecular Spectroscopy*, vol. 210, no. 2, pp. 275–283, 2001.
 - [11] P. W. Rosenkranz, “Shape of the 5 mm oxygen band in the atmosphere,” *IEEE Transactions on Antennas and Propagation*, vol. 23, no. 4, pp. 498–506, 1975.
 - [12] A. Lévy, N. Lacome, and C. Chackerian Jr., *Spectroscopy of the Earth’s Atmosphere and Interstellar Medium*, Academic Press, New York, NY, USA, 1992.
 - [13] H. Aroui, S. Nouri, and J. P. Bouanich, “ NH_3 self-broadening coefficients in the v_2 and v_4 bands and line intensities in the v_2 band,” *Journal of Molecular Spectroscopy*, vol. 220, no. 2, pp. 248–258, 2003.
 - [14] R. Le Doucen, C. Cousin, C. Boulet, and A. Henry, “Temperature dependence of the absorption in the region beyond the $4.3-\text{m}$ band head of CO_2 . 1: pure CO_2 case,” *Applied Optics*, vol. 24, no. 6, pp. 897–906, 1985.
 - [15] C. Cousin, R. Le Doucen, C. Boulet, and A. Henry, “Temperature dependence of the absorption in the region beyond the $4.3-\text{m}$ band head of CO_2 . 2: N_2 and O_2 broadening,” *Applied Optics*, vol. 24, no. 22, pp. 3899–3907, 1985.
 - [16] H. Sasada, Y. Endo, E. Hirota, R. L. Poynter, and J. S. Margolis, “Microwave and Fourier-transform infrared spectroscopy of the $v_4 = 1$ and $v_2 = 2$ s states of NH_3 ,” *Journal of Molecular Spectroscopy*, vol. 151, no. 1, pp. 33–53, 1992.
 - [17] G. Shi and H. Zhang, “The relationship between absorption coefficient and temperature and their effect on the atmospheric cooling rate,” *Journal of Quantitative Spectroscopy and Radiative Transfer*, vol. 105, no. 3, pp. 459–466, 2007.
 - [18] A. Bauer, M. Godon, J. Carlier, Q. Ma, and R. H. Tipping, “Absorption by H_2O and $\text{H}_2\text{O}-\text{N}_2$ mixtures at 153 GHz,” *Journal of Quantitative Spectroscopy and Radiative Transfer*, vol. 50, no. 5, pp. 463–475, 1993.

Research Article

First Observation of Defined Structural Motifs in the Sulfur-Iodine Thermochemical Cycle and Their Role in Hydrogen Production

Víctor H. Ramos-Sánchez,^{1,2} John Tomkinson,³ Jesús Muñiz-Soria,²
Edgar Valenzuela,² and Robin Devonshire¹

¹High Temperature Science Laboratories, Department of Chemistry, The University of Sheffield, Sheffield S3 7HF, UK

²Programa Académico de Ingeniería en Energía, Universidad Politécnica de Chiapas, Calle Eduardo J. Selvas S/N, Col. Magisterial, 29010 Tuxtla Gutiérrez, Chis, Mexico

³ISIS Pulsed Neutron and Muon Source, Science and Technology Facilities Council, Rutherford Appleton Laboratory, Didcot OX11 0QX, UK

Correspondence should be addressed to Víctor H. Ramos-Sánchez, vhramos@upchiapas.edu.mx

Received 14 February 2011; Accepted 27 March 2011

Academic Editor: Ahmed Aamouche

Copyright © 2011 Víctor H. Ramos-Sánchez et al. This is an open access article distributed under the Creative Commons Attribution License, which permits unrestricted use, distribution, and reproduction in any medium, provided the original work is properly cited.

The present paper investigates the ionic species coexisting in the HI_x feed of the sulfur-iodine thermochemical cycle. For this purpose, Raman and inelastic neutron scattering as well as molecular modelling were applied to the study of the binary $\text{HI}-\text{H}_2\text{O}$ system and the ternary $\text{HI}-\text{I}_2-\text{H}_2\text{O}$ and $\text{KI}-\text{I}_2-\text{H}_2\text{O}$ systems. Raman spectra, obtained at 298 K, strongly suggest the coexistence of I_3^- , $\text{I}^-(\text{I}_2)$, and $\text{I}^-(\text{I}_2)_2$ species. Whereas on the other hand, inelastic neutron scattering spectra (20 K) revealed, for the first time, evidence for the presence of discrete water structural motifs under specific conditions. Molecular modelling of two idealized structures has allowed us to establish a reasonable interpretation of the important structural motifs in these systems, in terms of the azeotrope of the $\text{HI}-\text{H}_2\text{O}$ system and the pseudoazeotrope of the $\text{HI}-\text{I}_2-\text{H}_2\text{O}$ system.

1. Introduction

Thermochemical cycles (TC), which decompose feedwater to generate hydrogen and oxygen, are a promising route to the large-scale hydrogen production. The primary product of these closed-cycle chemical reactions, hydrogen, is both a carbon-free energy source and a valuable reagent gas (*N.B. the current industry annual demand for hydrogen is of about 0.1 Gton, of which only 2% is produced from renewable sources*) [1–3].

The TC that has attracted the most attention worldwide is the sulfur-iodine cycle (SI-TC), the first stage of which is the exothermic Bunsen reaction:



This is followed by two endothermic reactions, one for each of the two reaction products, H_2SO_4 and HI . The decomposition reaction for H_2SO_4



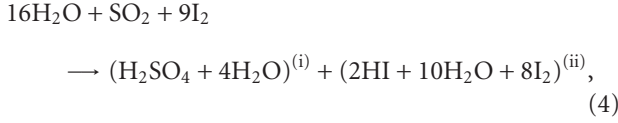
requires high temperatures whilst the decomposition reaction for HI



requires only modest temperatures. Overall, this three-step scheme is seen to regenerate the reagents, SO_2 and I_2 , whilst splitting water into H_2 and O_2 gases.

It was discovered by General Atomics in the late 1970s that when the Bunsen reaction was operated with excess H_2O and I_2 , a spontaneous separation into two aqueous acid

phases occurred. The lighter phase contained predominantly H_2SO_4 , and the heavier phase containing most of the HI [4, 5]. This gravity-driven phase separation makes an important contribution to the overall efficiency of the SI-TC. Under these reaction conditions it is more realistic to represent the Bunsen separation, Reaction (1), as follows:



where (i) represents the lighter H_2SO_4 -rich phase, and (ii) represents the heavier HI-rich phase, referred to here as the HI_x phase, or simply HI_x [4, 6]. The two phases (i) and (ii) are the respective feeds to the separate H_2SO_4 and HI decomposition stages of the SI-TC. The conditions of temperature and composition necessary for the $\text{H}_2\text{O}-\text{I}_2-\text{HI}-\text{H}_2\text{SO}_4$ system to produce the phase separation, and the compositions of the separate phases, have been investigated [7, 8].

1.1. General Description of the System. The phase diagram of the $\text{HI}-\text{I}_2-\text{H}_2\text{O}$ ternary system at room temperature is given in Figure 1 and shows four distinct phases. Under typical reaction conditions, and except for traces of the sulfur-containing species, the HI_x phase of the SI-TC has the following mole fraction composition [9]: $x_{\text{HI}} = 0.10$; $x_{\text{I}_2} = 0.40$; $x_{\text{H}_2\text{O}} = 0.50$, and is seen in Figure 1 to lie in the liquid-solid region of the room temperature system. Phase diagrams for the $\text{HI}-\text{I}_2-\text{H}_2\text{O}$ system at higher temperatures have been estimated [5]. These support observations that at temperatures typical for the Bunsen reaction, 120°C, the HI_x composition lies in the homogenous liquid phase, a phase which becomes lower in $x_{\text{H}_2\text{O}}$, and higher in x_{I_2} , with increasing temperature [5].

To produce H_2 gas from the HI_x feed of the Bunsen reaction *via* Reaction (3) it is necessary to reduce both the I_2 and H_2O mole fractions. Although the spontaneous phase separation in the GA SI-TC is potentially highly advantageous for the overall cycle efficiency, a problem arises from the high, *ca.* 5.0, $x_{\text{H}_2\text{O}}/x_{\text{HI}}$ mole ratio in HI_x . This is close to the $x_{\text{H}_2\text{O}}/x_{\text{HI}}$ mole ratio in the $\text{HI}-\text{H}_2\text{O}$ azeotrope, 5.8 at 25°C [10]. As a consequence, it is not possible to concentrate the HI by straightforward distillation, and other means are being explored, for example, using phosphoric acid [4] and membrane separation [11].

1.2. Species Present in the $\text{HI}-\text{I}_2-\text{H}_2\text{O}$ System. The species present in the $\text{HI}-\text{H}_2\text{O}$ [8, 12] and $\text{HI}-\text{I}_2-\text{H}_2\text{O}$ [13] systems have been investigated previously using Infrared and Raman spectroscopy but molar compositions close to that of the HI_x phase of the SI-TC were not considered.

A recent spontaneous raman scattering (SRS) study has specifically addressed the issue of which I_2 -containing species are present in the HI_x region of the $\text{HI}-\text{I}_2-\text{H}_2\text{O}$ phase diagram. The homogeneous liquid phase compositions that exist within the scope of the partial phase diagram, shown

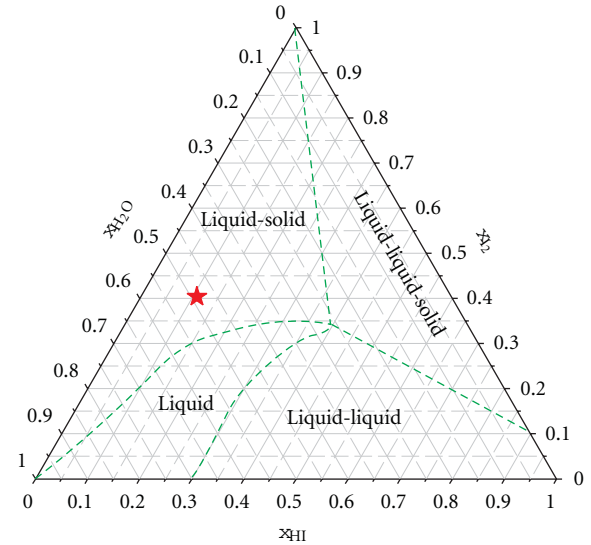


FIGURE 1: Ternary phase diagram of the $\text{HI}-\text{I}_2-\text{H}_2\text{O}$ system showing the four phases occurring at 297 K [5]. The composition of the HI_x phase in the GA SI-TC is allocated with a star.

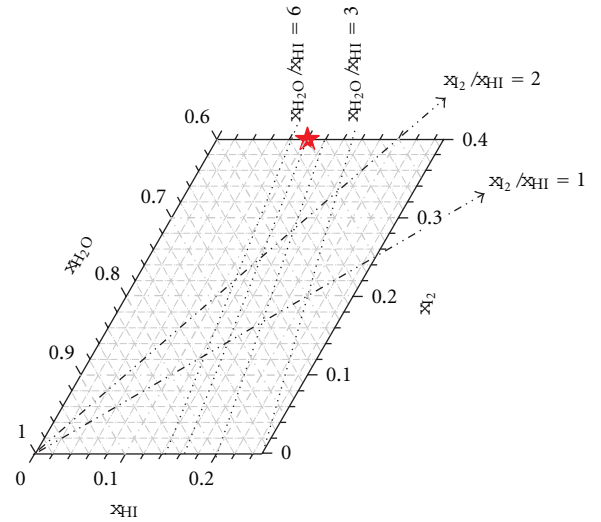


FIGURE 2: A truncated ternary phase diagram of the $\text{HI}-\text{I}_2-\text{H}_2\text{O}$ system superimposed with lines of different constant $x_{\text{I}_2}/x_{\text{HI}}$ and $x_{\text{H}_2\text{O}}/x_{\text{HI}}$ mole ratios. This diagram delimits the region of interest of the present study.

in Figure 2, were investigated over a range of different temperatures [14].

The Raman activity of the I_2 -containing species present in the system made it possible to rationalise the observations in terms of the following hydrated species: I^- ; *symmetric* I_3^- ; *unsymmetric* I_3^- ($\text{I}^-(\text{I}_2)$); I_5^- ($\text{I}^-(\text{I}_2)_2$). The relative dominance of the various polyiodide species was found to depend on the mole ratio $x_{\text{I}_2}/x_{\text{HI}}$. When $x_{\text{I}_2}/x_{\text{HI}} \leq 1$, the $\text{I}^-(\text{I}_2)$ predominates; when $x_{\text{I}_2}/x_{\text{HI}}$ is between 1 and 2 the species $\text{I}^-(\text{I}_2)$ and $\text{I}^-(\text{I}_2)_2$ are both important; when $x_{\text{I}_2}/x_{\text{HI}} \geq 2$ the $\text{I}^-(\text{I}_2)_2$ species predominates. Lines of constant $x_{\text{I}_2}/x_{\text{HI}}$ are straight lines emanating from the corner of the phase diagram where $x_{\text{H}_2\text{O}} = 1.0$. In Figure 2, lines for the fixed $x_{\text{I}_2}/x_{\text{HI}}$ mole ratios, 1 and 2, are drawn.

A further influence on local structures present in the homogenous fluid phase of the HI-I₂-H₂O system, the region of our interest to the SI-TC, is the mole ratio $x_{\text{H}_2\text{O}}/x_{\text{HI}}$. Previous *ab initio* calculations have identified stable aquo-complexes of isolated, neutral HI, and the ion pair H⁺I⁻. These complexes were found to be most stable for $x_{\text{H}_2\text{O}}/x_{\text{HI}}$ mole ratios of 3 and 4, respectively [15]. Lines of constant $x_{\text{H}_2\text{O}}/x_{\text{HI}}$ mole ratio for integer values 3, 4, 5, and 6 are shown in Figure 2 (these lines encompass the HI-H₂O azeotrope, *see above*). It is clear that the relative amount of water available to interact with I₂-containing species of any kind is important in interpreting the solvation structures present in the homogeneous fluid region and it is anticipated that a hexa-aquo complex will be important in diluted systems.

In the case of the present paper we shall use molecular models of the HI-H₂O and HI-I₂-H₂O systems to explore their dynamics. Also, in order to assist in such molecular insights we shall consider the KI-I₂-H₂O system, which by comparison to the HI-I₂-H₂O system will ease the discrimination of the spectral contribution from the counterion H⁺; as well as the evaluation of concentration regimes with $x_{\text{H}_2\text{O}}/x_{\text{I}^-}$ mole ratios below 3.5, which due to commercial availability of hydriodic acid are not achievable for the ternary system HI-I₂-H₂O.

1.3. Vibrational Spectroscopy. Bulk liquid water and aqueous solutions have been thoroughly investigated using vibrational spectroscopy. Infrared spectroscopy and SRS have both been used to determine hydrogen bond distances [16], with SRS being especially useful to study local structures, for example, water clusters or hydrated ions, within bulk liquid water due to its sensitivity to short-range interactions [17]. SRS has been widely exploited in structural investigations of water and aqueous solutions containing a wide variety of electrolytes [17].

Inelastic neutron scattering (INS), on the other hand, provides an alternative view of the vibrational spectra of ionic aqueous solutions. INS is free of resonance effects, has high sensitivity to hydrogen atom vibrations, and has a very wide spectral range from 16 to 4000 cm⁻¹. Its freedom from optical selection rules enables it to observe vibrational modes that are inactive in optical spectra. Recent developments in INS instrumentation have improved access to the intermolecular motions of the water ice phases [18]. *Measured INS spectral intensities are directly comparable with those calculated from the output of modern ab initio programs and this explains the common practice of using these programs to understand INS results* [19].

The objective of the present paper is to exploit the benefits of INS to study the HI_x phase of the SI-TC in combination with optical techniques. Data from both the liquid and the glassy states of samples of the HI-H₂O, HI-I₂-H₂O and KI-I₂-H₂O systems are presented, and qualitative interpretation is given in terms of the dynamics of the molecules involved. Our final objective will be to attain an initial insight into the chemical structures involved in the occurrence of the azeotropes in the HI-H₂O and the HI-I₂-H₂O systems.

2. Experimental

Measured amounts of potassium iodide, iodine, and HI₅₇ (hydriodic acid 57 wt%), or HI₆₇ (hydriodic acid 67 wt%) were added to volumetric flasks and made up with deionised water. All reagents were high purity, 99.99% or better, from Sigma Aldrich, except for HI₆₇ which was obtained from Fluka. Immediately after being made up the solutions were homogenised by agitating for five minutes.

We estimate that the compositions of the mixtures were fixed to better than 0.01 wt% by this process. However, uncertainties in HI and I₂ concentrations are larger than 0.01 wt% as a consequence of the uncertainty in the wt% of HI present in the HI₅₇ and HI₆₇ stock solutions and the action of unspecified oxidation processes which slowly releases I₂ in these solutions. To avoid using chemically stabilised HI stock solutions the I₂ and HI wt% in HI₅₇ and HI₆₇ were determined immediately prior to use by titration against sodium thiosulfate and sodium hydroxide, respectively. The uncertainties in the HI and I₂ compositions of prepared samples are effectively proportional to x_{HI} , and have a maximum of 0.5 wt% in HI₆₇.

The stoichiometric HI mole fractions (x_{HI}) in HI₅₇ and HI₆₇ are 0.157 and 0.222, respectively, and a wide range of HI-I₂-H₂O samples could be prepared conveniently by simply adding I₂ and H₂O to one or other of these HI solutions. The range of x_{HI} accessible by dilution in this way is to the low x_{HI} side of the boundary line given by the relation: $x_{\text{H}_2\text{O}} = 0.78(1 - x_{\text{I}_2})$. The ternary solutions with KI could be prepared with x_{KI} values larger than the limiting values possible for x_{HI} .

The homogenised systems were sealed within customized quartz cells, described elsewhere [20].

The quartz cells were used both in the SRS measurements performed at room temperature, 298 K, and the INS measurements performed at 20 K.

2.1. Sample Composition. The compositions of the samples investigated in this study, together with details of the respective measurement conditions, are given in Table 1 and represented graphically on the suitably truncated room temperature HI-I₂-H₂O ternary phase diagram shown in Figure 3 (N.B. the KI contents of samples S10 and S11 are shown using the HI scale). The compositions of the samples were distributed throughout the region of interest in the phase diagram (see Section 1) with the additional constraint that all compositions of the HI-I₂-H₂O system were within the region that is liquid at room temperature, that is, to the right of the phase boundary (shown as green dashed line in Figure 1), whereas the samples of the KI-I₂-H₂O system lie on the edge of the liquid phase boundaries described elsewhere [21].

2.2. Spontaneous Raman Scattering (SRS) Measurements. Dispersive Raman measurements were made using a Renishaw RM1000 Raman microscope and a Renishaw Ramascope System 2000 spectrometer equipped, respectively, with 514.5 and 785 nm excitation lasers. Raman spectra in the

TABLE 1: The compositions of samples used in this study together with details of the excitation wavelength used.

| Sample | x_{HI} | x_{KI} | x_{I_2} | $x_{\text{H}_2\text{O}}$ | Excitation λ/nm |
|--------|-----------------|-----------------|------------------|--------------------------|--------------------------------|
| S1 | 0.157 | — | 0.000 | 0.843 | 514.5; 785 |
| S2 | 0.222 | — | 0.000 | 0.778 | 514.5; 785 |
| S3 | 0.170 | — | 0.079 | 0.751 | 514.5 |
| S4 | 0.196 | — | 0.100 | 0.704 | 514.5 |
| S5 | 0.118 | — | 0.076 | 0.806 | 514.5 |
| S6 | 0.187 | — | 0.159 | 0.654 | 514.5 |
| S7 | 0.115 | — | 0.180 | 0.705 | 514.5 |
| S8 | 0.154 | — | 0.307 | 0.539 | 514.5 |
| S9 | 0.118 | — | 0.249 | 0.633 | 514.5 |
| S10 | — | 0.199 | 0.200 | 0.601 | 514.5 |
| S11 | — | 0.153 | 0.276 | 0.571 | 514.5 |

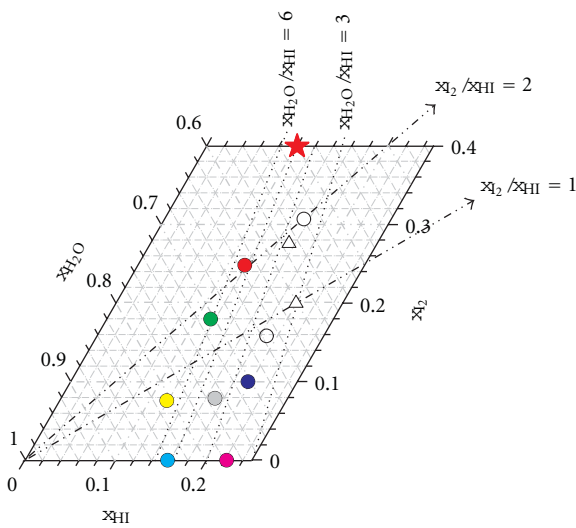


FIGURE 3: Sample compositions at 298 K placed on diagram shown in Figure 2. Circles represent samples of the $\text{HI}-\text{I}_2-\text{H}_2\text{O}$ system; whereas triangles correspond to samples of the $\text{KI}-\text{I}_2-\text{H}_2\text{O}$ system.

region from 20 to 400 cm^{-1} , important in measurements of condensed phase I_2 -containing species, were obtained using a near excitation tunable (NExT) filter accessory for the RM1000 instrument, use of which precludes measurement of the depolarization ratios of Raman active bands. Raman spectra in the region from 200 to 4000 cm^{-1} were obtained using the two spectrometers with their respective notch holographic filters. On both instruments, Raman spectra were measured in the backscattering configuration using incident laser powers of a few 10 s mW . For NExT measurements the RM1000 instrument was used in static scan mode, with a slit width of $5 \mu\text{m}$ and a $20\times$ objective lens. Typical exposure times were 60 s , with 60 accumulations being made per sample. For notch mode measurements the instruments were used in extended scan mode, with a slit width of $15 \mu\text{m}$ and a $20\times$ objective lens. Typical exposure times were 10 s for the RM1000 and 0.1 s for the Ramascope 2000, with between 10 and 30 accumulations being made per sample depending on the scattering strength of the sample.

Raman shift calibrations were performed at both the beginning and end of each measurement session using the 520.0 cm^{-1} resonance from a silicon wafer sample.

A Raman microscope accessory made it possible to perform excitation and scattered light collection normal to the flat face of a vertically oriented cell. The temperature of the samples during the measurements using 514.5 nm excitation was close to 298 K ; the temperature of the two samples measured using 785 nm excitation was not as closely monitored but was similar.

2.3. Inelastic Neutron Scattering (INS) Measurements. The INS measurements were performed on samples maintained at 20 K after they had been initially quenched in a cryostat operating at about 50 K . The dosed cells were mounted in the neutron beam of the TOSCA spectrometer [22, 23], at the ISIS Facility, at Rutherford Appleton Laboratory. TOSCA is a pulsed neutron, indirect geometry, low band-pass spectrometer with good spectral resolution ($\Delta E_t/E_t \approx 2\%$) [22, 23]. Spectral data were collected for approximately six hours and transformed into conventional scattering law versus energy transfer E_t/cm^{-1} , using standard programs. The resulting INS spectra appear noisy in comparison to the Raman spectra obtained from the same samples (see below) because typical neutron fluxes are about ten orders of magnitude less than photon flux from lasers.

2.4. Description of the Working Model Systems. In order to gain some insight into the interpretation of the INS spectra, four working models, $4w_1$ (based on a geometry proposed elsewhere [24]), $3w_1$, $2w_1$, and $1w_1$, were evaluated, two of which were assumed to explain the molecular dynamics of the $\text{HI}-\text{H}_2\text{O}$ and the $\text{HI}-\text{I}_2-\text{H}_2\text{O}$ systems. Both models are idealised conceptions, since all interactions with their surroundings are neglected (isolated model), and the complicating influence of the abovementioned I_2 -containing species was reduced by considering only one iodine atom within the negatively charged aquo-complexes.

The first model, $4w_1$, is a water tetramer coupled to an iodide ion, see Figure 4, classified within the C_4 point group. It shows 33 fundamental modes, which are distributed as follows: $\Gamma_{\text{vib}} = 8A + 9B + 16E$. The other model, $3w_1$, is a water trimer with an associated central iodide ion, see Figure 4, with C_3 symmetry, and 24 fundamental modes: $\Gamma_{\text{vib}} = 8A + 16E$. Particular labelling for each water molecule, as well as description of the vibrational modes has been partially based on work reported elsewhere [25].

2.5. Computational Chemistry Calculations. The optimized geometries as well as vibrational frequencies of the putative structure of the aquo-complexes were calculated in GAUSSIAN 03 [26], using the second-order Moller-Plesset Perturbation Theory, MP2 computational method [27], which explicitly accounts for dispersion effects, important in the description of hydrogen bonding. The Stuttgart small core pseudorelativistic effective core potential [28] with 25 valence electrons was employed for iodine. The ECP was used with the valence triple- f plus one polarization type

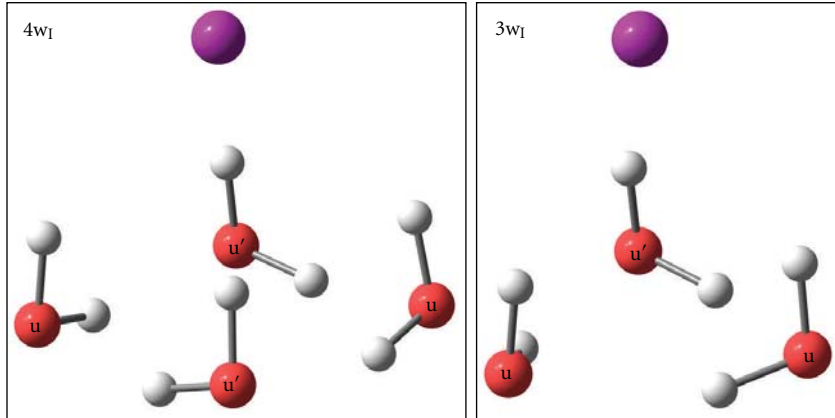


FIGURE 4: Optimized geometries of the working models $4w_1$ and $3w_1$. Water molecules within the complexes are labelled to ease description of the vibrational modes.

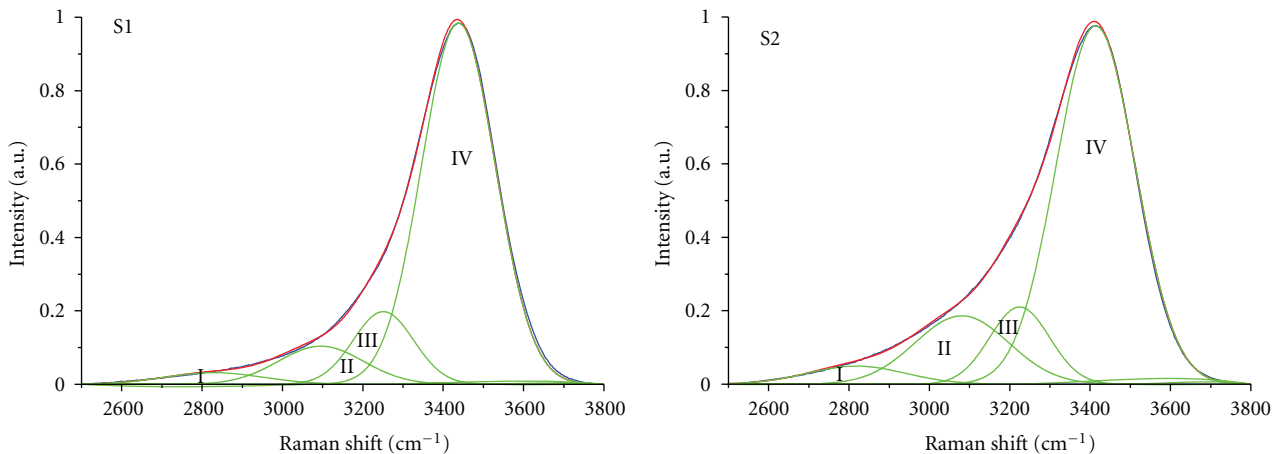


FIGURE 5: Raman spectra, within the region from 2500 cm^{-1} to 3800 cm^{-1} , of samples S1 and S2 taken using 514.5 nm excitation at 298 K and shown on a common intensity scale normalised to the most intense feature in each spectrum.

(TZVP), which is an optimized contracted Gaussian basis set for iodine, calculated by Schäfer et al. [29]. In the case of hydrogen and oxygen, the TZVP basis set was used [29, 30]. The final output files from the calculations, which contain the eigenvalues and eigenvectors, were processed in ACLIMAX [31] to generate calculated INS spectra for comparison with observed spectra from TOSCA.

3. Results and Discussion

3.1. The Binary System: HI-H₂O

3.1.1. 2,800–3,800 cm⁻¹ Region. SRS is known to provide useful information in this region in contrast to TOSCA where its high momentum transfer results in the suppression of intensities and only indistinct spectra are observed.

The two samples of the HI-H₂O binary system, S1 ($x_{\text{H}_2\text{O}}/x_{\text{HI}} = 5.4$) and S2 ($x_{\text{H}_2\text{O}}/x_{\text{HI}} = 3.5$) showed strong features in their 514.5 nm excitation SRS spectra in the OH stretch region from $2,800$ to $3,800\text{ cm}^{-1}$. The compositions of these two samples are chosen specially: S1 is quite close to

the actual azeotrope of the HI-H₂O system; S2 has the lowest $x_{\text{H}_2\text{O}}/x_{\text{HI}}$ mole ratio feasible. This latter ratio is of particular interest since it has been observed that in other halide acids (i.e., HCl, HBr) a minimum of four water molecules is needed to stabilize ionic structures [32, 33].

The respective SRS spectra of each sample comprise a single, strong, asymmetric band with a maximum near $3,400\text{ cm}^{-1}$. The good quality of the spectra made it possible to fit four Gaussians to the observed profile leaving low fitting residuals. The fitting process was guided by former band analysis studies carried out on hydriodic acid solutions [12]. Thus in accordance with this study, four bands were fitted in each spectrum, as illustrated in Figure 5. The centre of gravity as well as relative intensity and full width at half maximum (FWHM) of each Gaussian component are given in Table 2.

Component Raman bands in this region have normally been associated with the dynamics of the local hydrogen bonding network, including hydroxonium interactions. Thus, in this work, band I and band II have been assigned to antisymmetric, ν_3 , and symmetric, ν_1 , stretching of the

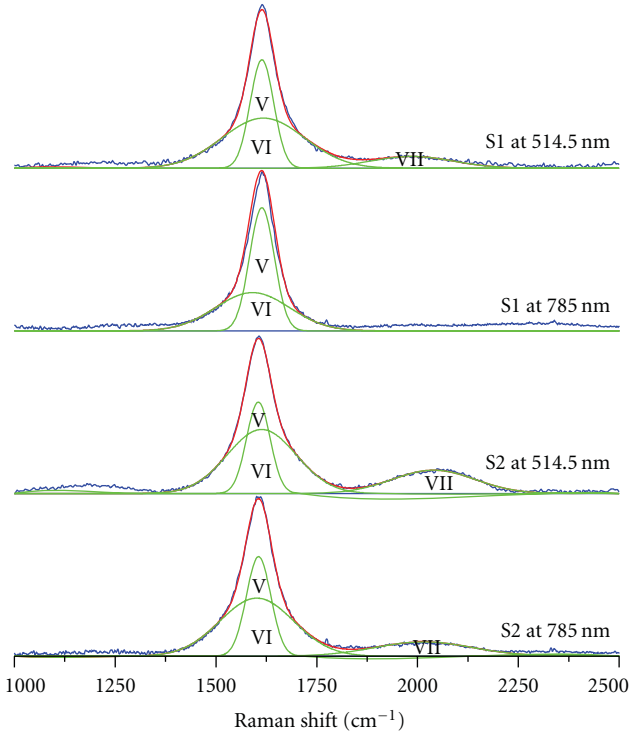


FIGURE 6: Raman spectra, within the region from 1000 cm^{-1} to 2500 cm^{-1} , of samples S1 and S2 taken at 298 K using excitation sources of 514.5 nm and 785 nm.

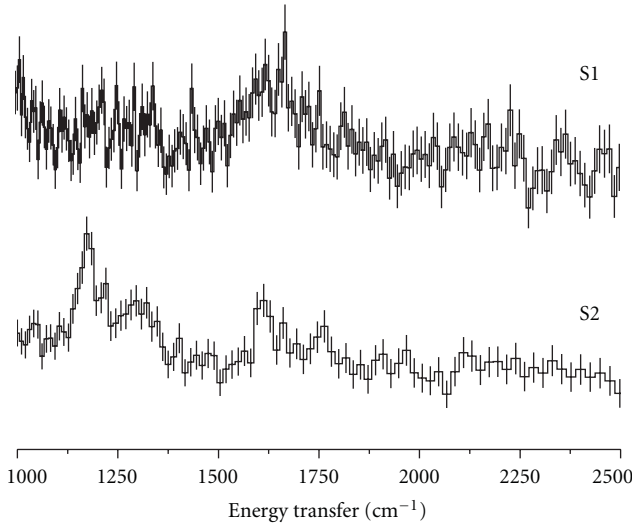


FIGURE 7: INS spectra, within the region from 1000 cm^{-1} to 2500 cm^{-1} , of samples S1 and S2 taken at 20 K. Vertical lines along the INS spectra represent error bars.

hydroxonium ions (H_3O^+), in agreement with previous studies [8, 34]. Both bands showed an enhancement in S2, revealing a higher hydroxonium concentration in this system. Typically, hydroxonium ions are not observed in the bulk of dilute solutions of hydriodic acid. The hydroxonium ions are a defect within the hydrogen bonding network, and are usually forced to the surface, where they have been detected

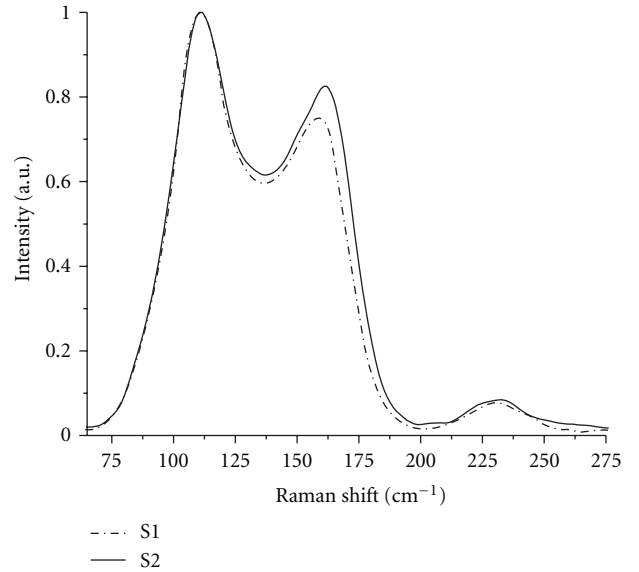


FIGURE 8: Raman spectra, within the region from 50 cm^{-1} to 275 cm^{-1} , of samples S1 and S2 taken using 514.5 nm excitation at 298 K and shown on a common intensity scale normalised to the most intense feature in each spectrum.

[35]. Here, however, probably in the case of S1, but almost certainly in the case of S2, the limited number of water molecules produces hydroxonium ions within the bulk of the local hydrogen bonding network, where they are detected. Support for the occurrence of hydroxonium ions in the bulk can be found in recent simulations, which revealed the existence of these bulk ions in 1 M hydriodic acid solutions [36].

On the other hand, bands III and IV are more closely related to the water's hydrogen bonding network. Thus, band III has been attributed to bulk amorphous water [37], more specifically to ν_1 of water molecules exhibiting a tetrahedral configuration [12, 38]. Band IV has been assigned to ν_3 of those water molecules associated with the iodide hydration shell [12, 38]. This band displays an important intensity enhancement in S2, (this is not obvious from Figure 5 due to spectral normalization). Such intensity increase is clearly due to the increased polarizability of those water molecules forming the iodide solvation sphere. In the S2 sample, with its relatively smaller number of water molecules, most of them will be in hydration spheres [38]. Band IV is assigned according to the "Rull" model [17] and is dominated by contributions from the linear H-bond of the $\text{OH}\cdots\text{I}$ solvation complex rather than the bifurcated or interstitial H-bond.

3.1.2. $1,000\text{--}2,500\text{ cm}^{-1}$ Region

SRS Spectra. The SRS spectra of this region, collected with two different excitation sources, have been analysed. The resultant component bands are shown in Figure 6, and their details are summarised in Table 3.

TABLE 2: Bands recovered by deconvolution of the Raman spectra obtained from samples of the HI-H₂O binary system (S1, S2) at 298 K and 514.5 nm in the spectral region 2800–3800 cm⁻¹. The entries for each band in this and subsequent tables, (from left to right) comprise band position; (within brackets) relative intensity normalized to the most intense band in each spectrum; (within brackets in italics) and bandwidth. Additionally the final column shows the $x_{\text{H}_2\text{O}}/x_{\text{HI}}$ mole ratio.

| Sample | Band I/cm ⁻¹ | Band II/cm ⁻¹ | Band III/cm ⁻¹ | Band IV/cm ⁻¹ | $x_{\text{H}_2\text{O}}/x_{\text{HI}}$ |
|--------|-------------------------|--------------------------|---------------------------|--------------------------|--|
| S1 | 2829 (0.04; 289.2) | 3096 (0.12; 248.8) | 3251 (0.16; 177.3) | 3438 (1.00; 216.1) | 5.4 |
| S2 | 2818 (0.06; 286.4) | 3081 (0.22; 274.1) | 3225 (0.16; 175.4) | 3414 (1.00; 232.9) | 3.5 |

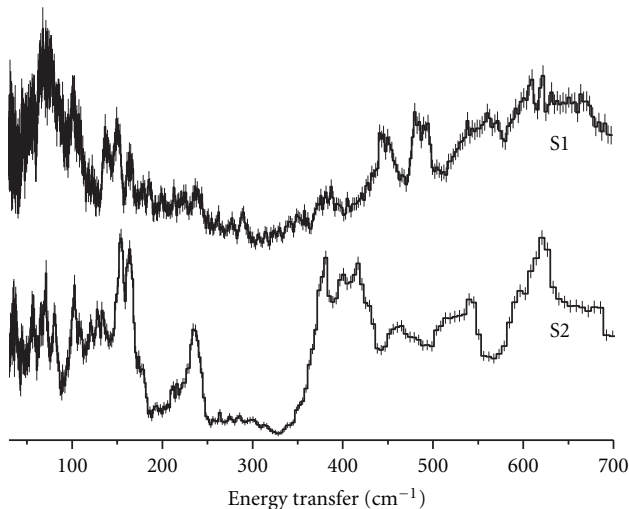


FIGURE 9: INS spectra, within the region from 30 cm⁻¹ to 700 cm⁻¹, of samples S1 and S2 taken at 20 K.

The strong, asymmetric feature at *ca.* 1600 cm⁻¹ is usually associated with the water bending mode, ν_2 , and has been decomposed into two component bands [39, 40], one sharp, the other broad. In agreement with this early work, band V is attributed to the ν_2 of water molecules exhibiting tetrahedral configuration and band VI has been assigned to ν_2 of water molecules linked to iodide ion solvation shells. Support for these assignments is the noticeable shift of band VI to higher wavenumbers, as the excitation wavelength approaches the absorption of the complex ion OH· · · I. Band V has a constant centre of gravity irrespective of the excitation wavelength.

The SRS spectra in Figure 6 also show the presence of a seventh broad band at *ca.* 2000 cm⁻¹, band VII. This band demonstrates a resonance enhancement (it is strong in S2, with 514.5 nm, but is inactive in S1, with 785 nm) and a clear dependence on HI concentration. Rather than assigning band VII to a water combination band (e.g., $\nu_2 + \nu_L$), it is more reasonable to assign it to H₂O· · · HI complexes. Earlier Raman studies on supersaturated solutions of other hydrogen halides [41] suggest that a Raman feature near 2040 cm⁻¹ would be present in highly concentrated hydriodic acid.

INS Spectra. INS spectra of the same spectral region, see Figure 7, also show bands V and VI at *ca.* 1600 cm⁻¹ in both S1 and S2, although broader in S1. Exclusively observed in the INS spectrum of S2, is a band at *ca.* 1170 cm⁻¹.

Hydroxonium ions may account for this band; since their detection is clearly eased by the low temperature, 20 K, at which measurements were carried out that greatly suppresses proton diffusion [42]. Moreover, the concentration of S2, 10.27 M, is above the concentration threshold, >7 M, established for the observation of the ion's symmetric bending mode, ν_2 , in hydrogen halide solutions [8].

Given this assignment, it is possible that the band at *ca.* 1600 cm⁻¹ in S2 might have a different origin from that presented above. Under this interpretation, with the extinction of band V, the two well-defined peaks at *ca.* 1613 and 1750 cm⁻¹ would then be assigned to band VI and the antisymmetric bending mode, ν_4 , of the hydroxonium ion.

3.1.3. 30–700 cm⁻¹ Region

SRS Spectra. The SRS spectra obtained using the notch filter show only two weak, semiobscured, bands at *ca.* 330 cm⁻¹ and 480 cm⁻¹ under 514.5 nm excitation. These are overtone progressions and combinations resulting from a resonance enhancement, discussed below.

More useful SRS spectra were acquired using the NExT Filter at 514.5 nm and these are shown in Figure 8. An SRS study of these systems in this region has recently been reported and discussed in detail by our research group and they are only briefly summarised here [14].

One very weak Raman band *ca.* 85 cm⁻¹ and another five bands are located at *ca.* 111, 137, 160, 230, and 337 cm⁻¹ and can all be attributed to I₂-containing species.

Specifically, all bands except for the band *ca.* 160 cm⁻¹ somehow derive from an I₃⁻ species with equidistant bonds whereas the band at *ca.* 160 cm⁻¹ represents only an I₂ grouping within an *unsymmetric* I₃⁻. The structure of the I₃⁻ ion responsible for this band can be represented as I⁻(I₂).

The bands overall located *ca.* 111, 230, and 337 cm⁻¹ are assigned to the symmetric stretch, the fundamental at *ca.* 111 cm⁻¹, and its first and second overtones at *ca.* 230 and 337 cm⁻¹, respectively. The bands at *ca.* 85 and 137 cm⁻¹ are the bending and antisymmetric stretching modes of *symmetric* I₃⁻. At first glance the assignment of the overtone series might seem dubious, since it does not seem to fit with the anharmonic oscillator model. However, we have recently demonstrated the attenuation of these two overtones changing the excitation frequency off resonance to 1064 nm [14]. Furthermore, Kiefer and Bernstein [43] also reported similar band positions for CsI₃ in aqueous solution, which are in close agreement with our assignment.

TABLE 3: The Raman bands recovered by deconvolution of the spectra obtained from samples of the HI-H₂O binary system (S1, S2) at 298 K in the spectral region 1000–2500 cm⁻¹. Results in bold were obtained at 514.5 nm, whereas the rest were acquired at 785 nm.

| Sample | Band V/cm ⁻¹ | Band VI/cm ⁻¹ | Band VII/cm ⁻¹ | x _{H₂O} /x _{HI} |
|--------|--------------------------|---------------------------|---------------------------|--|
| S1 | 1614 (0.62; 68.9) | 1617 (1.00; 240.8) | 1986 (0.24; 242.7) | 5.4 |
| | 1614 (1.00; 72.3) | 1591 (0.93; 216.6) | — | |
| S2 | 1605 (0.49; 68.6) | 1613 (1.00; 201.1) | 2040 (0.44; 241.4) | 3.5 |
| | 1606 (0.57; 71.4.) | 1601 (1.00; 215.3) | 2015 (0.33; 285.0) | |

TABLE 4: Calculated vibrational modes of 4w_I together with their individual descriptions. Mode description: H_b and H_f refer to hydrogen atoms within the water molecules that are hydrogen bonded or free, respectively; superscripts n and nc stand for concerted and nonconcerted motion respectively; ν₃ for antisymmetric stretch; ν₁ for symmetric stretch; ν₂ for bending mode; ω for wag; ρ for rock; τ for twist; / used to separate concerted motions from nonconcerted motions. Modes descriptions in bold font highlight the normal modes of water. Compression, distortion, and twist modes refer to the tetramer ring, except for those in italics which refer to motions of the whole complex.

| 4w _I (C ₄) | $\Gamma_{\text{vib}} = 8A + 9B + 16E$ | | | | | | | |
|-----------------------------------|--|---|-------|--|---|-------|--|---|
| ν | Calculated A (cm ⁻¹) | Description | ν | Calculated B (cm ⁻¹) | Description | ν | Calculated E (cm ⁻¹) | Description |
| 1 | 3796 | ν₃^c (uu'uu') | 9 | 3760 | ν₃^{nc} (uu/u'u') | 18 | 3771 | ν₃^{nc} (u'u'u'u) |
| 2 | 3627 | ν₁^c (uu'uu') | 10 | 3704 | ν₁^{nc} (u'uu'u) | 19 | | ν₃^{nc} (uu'/uu') |
| 3 | 1712 | ν₂^c (uu'uu') | 11 | 1718 | ν₂^{nc} (u'u'u'u) | 20 | 3674 | ν₁^{nc} (u'u'u'u) |
| 4 | 925 | ω^c (H _b uu'uu') | 12 | 586 | ω^{nc} (H _b uu/u'u') | 21 | | ν₁^{nc} (uu'/uu') |
| 5 | 625 | ρ^c (uu'uu') | 13 | 465 | τ^{nc} (uu/u'u') | 22 | 1707 | ν₂^{nc} (uu'/uu') |
| 6 | 379 | τ^c (H _f uu'uu') | 14 | 377 | ρ^{nc} (uu/u'u') | 23 | | ν₂^{nc} (u'u'u'u) |
| 7 | 169 | <i>Compression</i> | 15 | 201 | Distortion | 24 | 723 | ω^{nc} (H _b u'u/u'u) |
| 8 | 91 | <i>Compression</i> | 16 | 89 | Twist | 25 | | ω^{nc} (H _b uu'/uu') |
| | | | 17 | 59 | Distortion | 26 | 559 | τ^{nc} (H _b u'u/u'u) |
| | | | | | | 27 | | τ^{nc} (H _b uu'/uu') |
| | | | | | | 28 | 362 | ρ^{nc} (H _f u'u/u'u) |
| | | | | | | 29 | | ρ^{nc} (H _f uu'/uu') |
| | | | | | | 30 | 189 | Distortion |
| | | | | | | 31 | | Distortion |
| | | | | | | 32 | 88 | <i>Rocking</i> |
| | | | | | | 33 | | <i>Rocking</i> |

INS Spectra. In contrast to SRS spectra the INS spectra in this region are very rich in features, see Figure 9. This apparent contradiction is easily resolved when it is realized that SRS spectra give information on the I₂-containing species present and INS gives information on the hydrogenous species present. INS provides information about the water surrounding the iodide complex ions in this system.

It is also worth underlining that samples studied on TOSCA reach 273 K within 5 s and once frozen no significant structural differences are expected. Glass formation can be inferred in samples of the binary system, given that HCl and HBr form glasses at concentrations higher than 20 wt% and 30 wt% respectively [42].

We shall assume that there are two contributors to the observed INS spectral profile, first, free water molecules in a tetrahedral hydrogen bonding network (as found in pure water), and, second, water molecules taking part in the ionic solvation shells. The INS spectrum of S1 is then seen to be due to the presence of both species and that of S2 is dominated by the water envelope of the iodide ions.

This is approximately in line with simple expectations based on the mole ratio of water to HI. We recall that previous studies suggested that at least 4 water molecules are needed to stabilize iodide ions [15, 35]. Then, in S1 there is an excess of water molecules ($x_{H_2O}/x_{HI} = 5.4$) but in S2 a deficit ($x_{H_2O}/x_{HI} = 3.5$). The INS of S2 is sharply featured and convincingly fits expectations from a locally structured system like a hydration shell. The INS spectrum of S1 is more diffuse and best compared to that of water in its more “open” ice structures [18]. Here we note that our systems, although locally ordered, show no long-range order, as demonstrated by the lack of Bragg features in the diffraction bank of TOSCA.

Here, we recall that our interpretation of the INS spectra will be through the two model systems, 4w_I and 3w_I, discussed above. In this respect, Tables 4 and 5 show the unscaled calculated frequencies obtained for the working models 4w_I and 3w_I.

We have proposed the above working models based on the fact that there is insufficient water ($x_{H_2O}/x_{HI} = 3.5$) to

TABLE 5: Calculated vibrational modes of $3w_1$ together with their individual descriptions. Compression, distortion, and twist modes refer to the trimer ring, except for those in italics which refer to motions of the whole complex.

| $3w_1$ (C_3) | $\Gamma_{\text{vib}} = 8A + 16E$ | | | | |
|------------------|----------------------------------|--|-------|----------------------|---|
| ν | Calculated A | Description | ν | Calculated E | Description |
| | (cm^{-1}) | | | (cm^{-1}) | |
| 1 | 3711 | $\nu_3^c (\mathbf{uu}'\mathbf{u})$ | 9 | 3789 | $\nu_3^{nc} (\mathbf{u}'\mathbf{u}/\mathbf{u})$ |
| 2 | 3705 | $\nu_1^c (\mathbf{uu}'\mathbf{u})$ | 10 | | $\nu_3^{nc} (\mathbf{uu}'/\mathbf{u})$ |
| 3 | 1712 | $\nu_2^c (\mathbf{uu}'\mathbf{u})$ | 11 | 3710 | $\nu_1^{nc} (\mathbf{u}'\mathbf{u}/\mathbf{u})$ |
| 4 | 832 | $\omega^c (\mathbf{H}_b \mathbf{uu}'\mathbf{u})$ | 12 | | $\nu_1^{nc} (\mathbf{uu}'/\mathbf{u})$ |
| 5 | 597 | $\tau^c (\mathbf{H}_f \mathbf{uu}'\mathbf{u})$ | 13 | 1687 | $\nu_2^{nc} (\mathbf{uu}'/\mathbf{u})$ |
| 6 | 390 | $\rho^c (\mathbf{uu}'\mathbf{u})$ | 14 | | $\nu_2^{nc} (\mathbf{u}'\mathbf{u}/\mathbf{u})$ |
| 7 | 172 | <i>Compression</i> | 15 | 607 | $\omega^{nc} (\mathbf{H}_b \mathbf{u}'\mathbf{u}/\mathbf{u})$ |
| 8 | 101 | <i>Compression</i> | 16 | | $\omega^{nc} (\mathbf{H}_b \mathbf{uu}'/\mathbf{u})$ |
| | | | 17 | 462 | $\tau^{nc} (\mathbf{H}_b \mathbf{u}'/\mathbf{u}/\mathbf{u})$ |
| | | | 18 | | $\tau^{nc} (\mathbf{H}_b \mathbf{uu}'/\mathbf{u})$ |
| | | | 19 | 343 | $\rho^{nc} (\mathbf{H}_f \mathbf{u}'/\mathbf{u}/\mathbf{u})$ |
| | | | 20 | | $\rho^{nc} (\mathbf{H}_f \mathbf{uu}'/\mathbf{u})$ |
| | | | 21 | 150 | <i>Distortion</i> |
| | | | 22 | | <i>Distortion</i> |
| | | | 23 | 91 | <i>Rocking</i> |
| | | | 24 | | <i>Rocking</i> |

TABLE 6: Relevant mole ratios of the samples representative of the $\text{HI-I}_2\text{-H}_2\text{O}$ and $\text{KI-I}_2\text{-H}_2\text{O}$ ternary systems; which were used in this study.

| Sample | $x_{\text{I}_2}/x_{\text{HI}}$ | $x_{\text{I}_2}/x_{\text{KI}}$ | $x_{\text{H}_2\text{O}}/x_{\text{HI}}$ | $x_{\text{H}_2\text{O}}/x_{\text{KI}}$ |
|--------|--------------------------------|--------------------------------|--|--|
| S3 | 0.46 | — | 4.4 | — |
| S4 | 0.51 | — | 3.6 | — |
| S5 | 0.64 | — | 6.8 | — |
| S6 | 0.85 | — | 3.5 | — |
| S7 | 1.57 | — | 6.2 | — |
| S8 | 2.00 | — | 3.5 | — |
| S9 | 2.10 | — | 5.4 | — |
| S10 | — | 1.00 | — | 3.0 |
| S11 | — | 1.81 | — | 3.7 |

stabilize all the iodide ions directly. In terms of our model systems, this mole ratio is obtained when there is one $4w_1$ unit to every $3w_1$ unit. Thus we anticipate that in the case of S2 the hydrated iodide ion is present in both forms.

Figure 10 shows the calculated INS spectra, obtained from ACLIMAX, of both $4w_1$ and $3w_1$. When the calculated spectrum of the $3w_1$ unit is added to a calculated spectrum of the $4w_1$ unit the comparison between the calculated and observed spectra is convincing, as it can be observed in Figure 11. It is, thus, reasonable to accept that the INS spectrum of S2 results from equal contributions from similar structures to those already described above. Here, we do not mean to be understood as suggesting that the calculated spectrum is a “fit” to the observed data, as can often be the case with INS spectra [19]. Rather, that the vibrations of $4w_1$ and $3w_1$ provide an adequate representation of the

observed spectrum and, by extension, the structural model encapsulates the essence of the local water structure in the sample.

It is noteworthy that although four working models, $4w_1$, $3w_1$, $2w_1$, and $1w_1$ were evaluated at first; only three of them resulted in stable geometries: $4w_1$, $3w_1$, and $1w_1$. In accordance with Odde et al., [15] it was found that $4w_1$ and $3w_1$ stabilized in ionic structures whereas $1w_1$ behaved as an undissociated HI-water cluster: $\text{HI}(\text{H}_2\text{O})$. Even though both $4w_1$ and $3w_1$ are stable moieties, it is well known that the former is more stable than the latter [15]. Thus, bearing all the above in mind, it is feasible to consider $1w_1$ as responsible of some of the spectral features within the INS spectrum of S2. Indeed, Figure 12 juxtaposes the calculated INS spectrum of $1w_1$ with the experimental data obtained at TOSCA. Such comparison, however, does not exhibit an agreement as significant as the one observed in Figure 11, particularly in the middle section, which in the actual spectrum is somehow flat.

The doublet at *ca.* 158 cm^{-1} remains unassigned in this scheme and may be related to the Raman band at *ca.* 160 cm^{-1} observed in an earlier study of glassy hydrogen halide aqueous solutions. This band was assigned to the stretching vibrations of the $\text{OH}\cdots\text{I}$ hydrogen bond [8]. In the same way the asymmetric band at *ca.* 235 cm^{-1} has to be attributed to an optical mode [44] caused by specific positions and orientations of the hydrogen bonds within the local structures of S2; suggesting, perhaps, that our working model $4w_1$ should adopt an S4 point group symmetry to better fit the experimental observations.

Coupled with the above, the calculated vibrational frequencies, listed in Tables 4 and 5, also help to rationalize the offset and broadening observed between the Raman spectra of S1 and S2 in the OH stretch region from 2800 to 3800 cm^{-1} . According to these results, the spectral contour in this region is expected to be broadened and blue-shifted as the aquo-complexes squeeze in more water molecules. In particular the offset in band IV reflects an enhanced hydrogen bonding in the iodide hydration shells present in S2.

3.2. Ternary Systems: $\text{HI-I}_2\text{-H}_2\text{O}$, $\text{KI-I}_2\text{-H}_2\text{O}$. The mole ratios $x_{\text{I}_2}/x_{\text{HI}}$ and $x_{\text{H}_2\text{O}}/x_{\text{HI}}$ will be of particular significance in explaining the SRS and INS spectra, respectively, and therefore their values, for the ternary systems are given in Table 6, as an aid in the discussion of results of this section.

3.2.1. $30\text{--}700\text{ cm}^{-1}$ Region

We note that none of the ternary systems showed discernible Raman bands above 700 cm^{-1} , mainly due to a strong fluorescence background at both 514.5 nm and 785 nm . In the case of INS spectra, the overall picture is very similar, with the majority of spectral features appearing below 700 cm^{-1} , with the exception of the water bending mode *ca.* 1600 cm^{-1} .

TABLE 7: Comparison of the INS and unscaled calculated frequencies, cm^{-1} . Note: le—left edge; vw—very weak; sp—strong peak; bp—broad peak; re—right edge; h—hump; sh—shoulder; d—doublet; m—medium; w—weak.

| Calculated | | | | Observed INS at 20 K | | | | | Additional interpretations |
|------------|--------------------------|------------|-------------------------------------|---|--|--|-------------------|-------------------|--|
| $3w_I$ | Π | $4w_I$ | Π | S2 | S6 | S8 | S10 | S11 | |
| 462 | ν_{17} ν_{18} | 625 559 | ν_5 ν_{26} ν_{27} | 620 ^{bp} 542 ^{re} 503 ^{le} | | | | 540 ^{le} | |
| | | | | 456 ^h 429 ^{sh} | 420 ^{re} | 420 ^{vw} | 450 ^{re} | 450 ^{bp} | |
| | ν_6 | 379 377 | ν_6 ν_{14} | 408 ^{bp} | 389 ^{le} | 388 ^{le} | 370 ^{le} | 373 ^{bp} | |
| 343 | ν_{19} ν_{20} | 362 | ν_{28} ν_{29} | 380 ^{sp} | | 341 ^m | | 325 ^m | |
| | | | | | 300 ^{sp} | 309 ^{sp} | 290 ^{sp} | 300 ^{sp} | Optical modes due to specific positions and orientations of the H-bond |
| | | 201 | ν_{15} | 235 ^{sp} 211 ^{vw} | 195 ^m | 192 ^m | | 188 ^m | |
| 150 | ν_{21} ν_{22} | | | | 177 ^m | 178 ^m | | 175 ^m | |
| | | | | | 163 ^m | | 159 ^m | 160 ^m | H_3O^+ vibrations |
| | ν_8 | | | 163 ^d 154 ^d | | | | | |
| 101 | | 88 | ν_{32} ν_{33} | 102 ^{sp} | 126 ^{sp} 100 ^d 92 ^d | 130 ^{sp} 100 ^d 91 ^d | 118 ^{sp} | 117 ^{sp} | H_3O^+ vibrations |
| | | | | | 80 ^{sp} | 83 ^{sp} | 81 ^m | | |
| | | 59 | ν_{17} | 65 ^{sp} 50 ^{sp} | 65 ^{sp} 50 ^{sp} | 62 ^m 50 ^m | | | Not assigned |

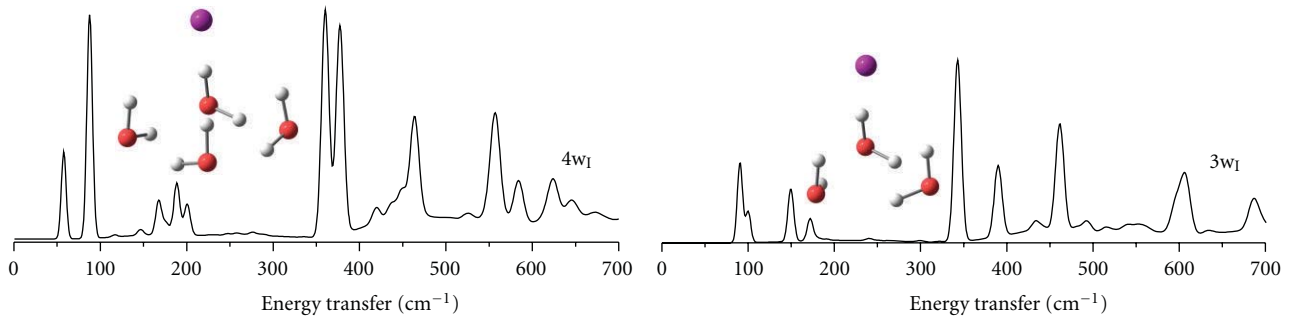
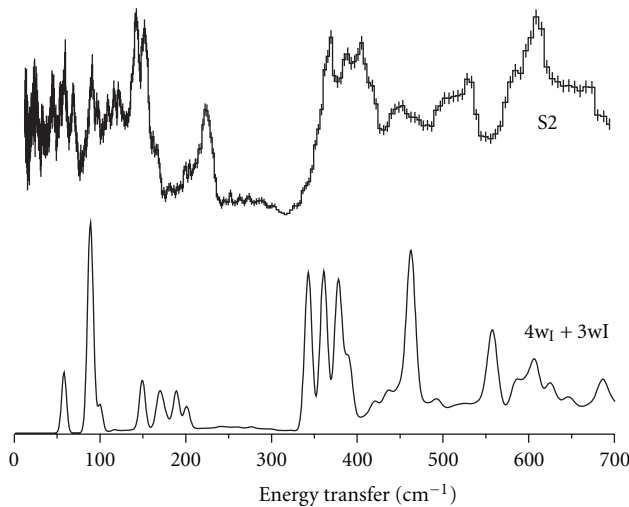
SRS Spectra. As for the binary system (see SRS Spectra Section 3.1.3) the HI-I₂-H₂O system also exhibits a consistent set of 6 component bands [14]. These bands were located approximately *ca* 85 cm^{-1} (very weak, broad and not always discernible), 112, 141, 166, 225 and 337 cm^{-1} . Bands at *ca* 85, 112, 141, 225, and 337 cm^{-1} correspond to the *symmetric* I₃⁻ ion, again present in this system. However, the most remarkable aspect of this system is the displacement of the band at *ca* 166 cm^{-1} , this varies from 161 to 170 cm^{-1} , depending on the sample's composition. This is clearly shown in Figure 13(a), the band is related to the I⁻(I₂)_n species earlier discussed in Section 1.2 (a fuller discussion of this band and its displacement can be found elsewhere [14]).

In the KI-I₂-H₂O system 6 bands were identified, a very weak band *ca* 85 cm^{-1} and another five bands located *ca* 110, 140, 166, 224, and 337 cm^{-1} . The most notable aspect of this system is the change in relative intensities of bands at 110 and 166 cm^{-1} when compared to samples of similar composition but prepared with HI instead of KI. This might suggest that

the nature of the metal cation and or the pH of the media have an effect in favouring, in the present case, the I₃⁻ species with equidistant I—I bonding.

Figure 13(b) shows the SRS spectra of both samples of the KI-I₂-H₂O system. As was implied above, *symmetric* I₃⁻ and I⁻(I₂) and I⁻(I₂)₂ solvated species are present within the system; although it is apparent from the SRS spectrum of S10 that I⁻(I₂) is greatly suppressed, confirming the predominance of *symmetric* I₃⁻ as previously observed [45].

INS Spectra. It has been already mentioned that the mole ratio $x_{\text{H}_2\text{O}}/x_{\text{HI}}$ is another influence on local structures present in the homogenous fluid phase of the HI-I₂-H₂O system, above all in the region of interest to the S-I cycle. Such influence was made evident by previous *ab initio* calculations, which identified stable aquo-complexes of isolated, neutral HI, and the ion pair H⁺I⁻. These complexes were found to be most stable for $x_{\text{H}_2\text{O}}/x_{\text{HI}}$ mole ratios of 3 and 4, respectively [15]. Lines of constant $x_{\text{H}_2\text{O}}/x_{\text{HI}}$ mole ratio for integer values 3, 4, 5 and 6 are shown in Figure 3. It is clear that the relative

FIGURE 10: Calculated INS spectra of the two idealized models $4w_I$ and $3w_I$.FIGURE 11: Theoretical INS spectrum, resulting from the sum of the calculated INS spectra of $4w_I$ and $3w_I$, compared against the experimental INS spectrum obtained from S2.

amount of water available to interact with I_2 -containing species of any kind is important in interpreting the solvation structures present in the homogeneous fluid region, and it is anticipated that a hexa-aquo complex will be important in diluted systems. We shall use molecular models of the HI-H₂O and HI-I₂-H₂O systems to explore their dynamics.

Despite the explicit presence of iodine within the HI-I₂-H₂O ternary system, spectra similar to those obtained from the HI-H₂O binary system were observed. The mole ratio x_{H_2O}/x_{HI} has clearly the same influence in producing local structures within the ternary system, as it did in the HI-H₂O binary system. Here, however, an extra parameter must be considered, the x_{I_2}/x_{HI} mole ratio, which determines the capability of the iodide ion to coordinate an iodine molecule. Thus, if the x_{I_2}/x_{HI} mole ratio is very close to the integers one (or two), there is a very good chance that the iodide ion couples to one (or two) iodine molecules, as discussed above.

These entities act as a core upon which water molecules grow into local structures, in the same way that the iodide ion acts for the binary system. However, for noninteger x_{I_2}/x_{HI} mole ratios, there is competition between these two local structures.

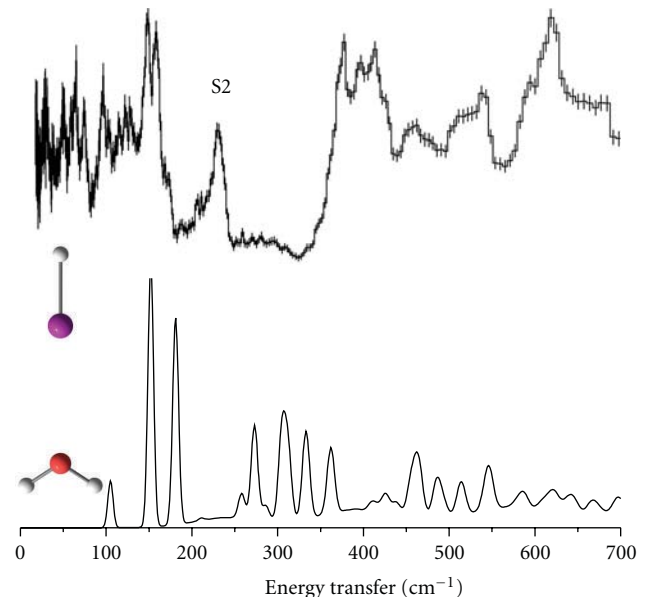
FIGURE 12: Comparison between the calculated INS spectra of the undissociated HI-water cluster: HI(H₂O), aka $1w_I$, and the experimental INS spectrum of S2.

Figure 14 compares two samples of the HI-I₂-H₂O system, which presented evidence of local structure, against two samples of equivalent composition of the KI-I₂-H₂O system. These results are remarkable, and show that the samples corresponding to the HI-I₂-H₂O system presented a similar picture to the one exhibited by the INS spectrum of S2. Furthermore, the lack of features in both INS spectra of the KI-I₂-H₂O samples support the idea that the K^+ ion does not have a strong enough field to withdraw water molecules from the solvent structure [46]. In this case, the I_2 -containing anions (I^- , I_3^- , $I^-(I_2)$, $I^-(I_2)_2$) are those responsible for disrupting the solvent structure.

It is unlikely that either the $4w_I$ or $3w_I$ models could account for the INS spectra of both ternary systems, given its intrinsically higher concentration of the I_2 -containing species. However, it is possible to interpret some of these experimental observations in terms of the INS spectrum of S2.

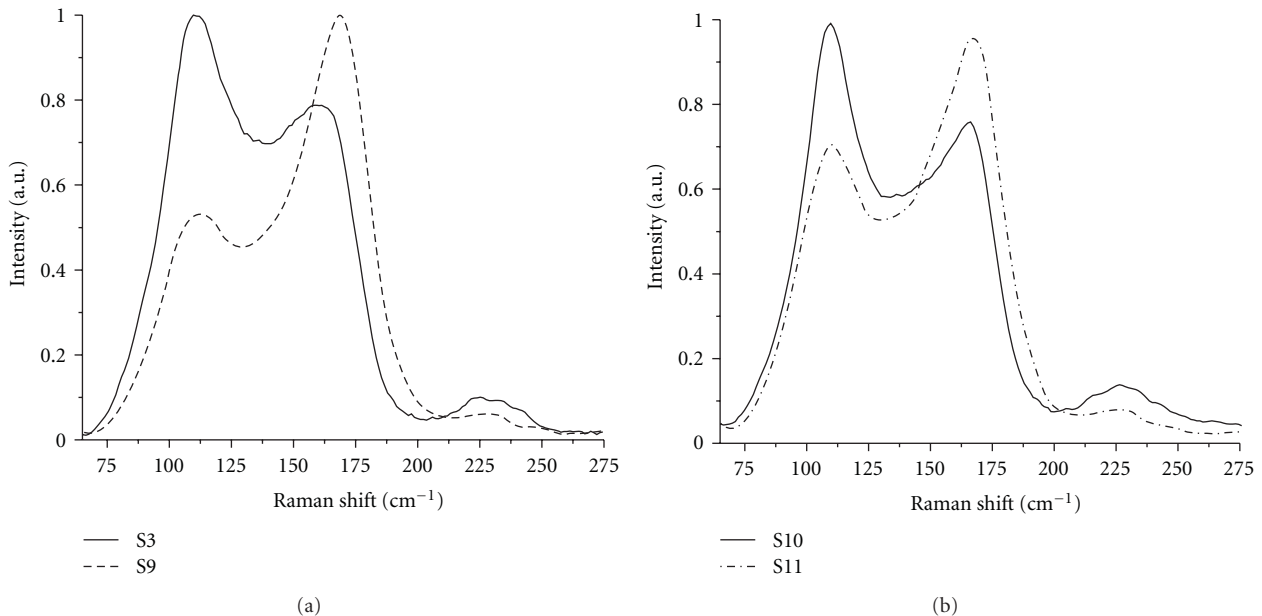


FIGURE 13: Raman spectra obtained at 298 K from samples of the (a) HI-I₂-H₂O and (b) KI-I₂-H₂O systems, within the region from 50 cm⁻¹ to 275 cm⁻¹, using 514.5 nm excitation source.

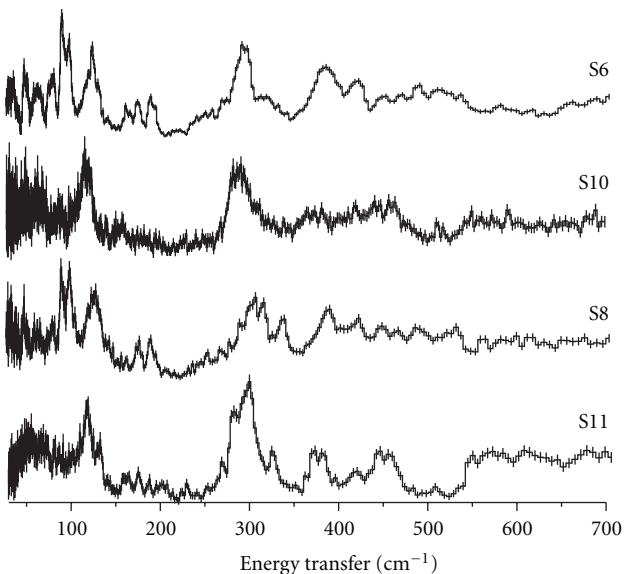


FIGURE 14: INS spectra, within the region from 30 cm^{-1} to 700 cm^{-1} , of representative samples of the HI-I₂-H₂O (S6, S8) and KI-I₂-H₂O (S10, S11) ternary systems at 20 K.

Also present in both spectra is a doublet at *ca.* 96 cm⁻¹ with a strong resemblance to the 158 cm⁻¹ doublet in S2, which was assigned, above, to deformations of the local structures, rather than stretching vibrations of the OH···I as formerly invoked. Conversely, an alternative assignment for both doublets might link them with vibrations of the hydroxonium ion, explaining thus the remarkable frequency shift by force constant changes; this shift might also be

expected in other hydroxonium bands. The occurrence of H⁺ as a counterion in samples where this doublet was observed reinforces such hypothesis.

Additional support to this new assignment scheme has been found through the abovementioned spectral simulation. Such results revealed that the stretching mode of the OH \cdots I moiety within the complex ions: 4w_I and 3w_I occur at 91 and 101 cm $^{-1}$, which could be attributed to bands at ca. 128 and 117 cm $^{-1}$ for the HI-I₂-H₂O and KI-I₂-H₂O systems, respectively. This mode was also apparent in S2 and S1, although at a lower frequency, ca. 100 cm $^{-1}$, in a much better agreement with the idealised models. As in the case of hydroxonium ions band, this mode is also susceptible frequency shift by force constant changes.

Other three bands at *ca.* 163, 177, and 192 cm⁻¹ were identified in the INS spectrum of S6 ($x_{I_2}/x_{HI} = 0.85$), they seem to relate to a triad observed in 4w_I, which have been assigned to compression and distortions of the aquo-complex as a whole. Evidence of such vibrational modes is also found in the spectrum of sample S8. With respect to the KI-I₂-H₂O system, such bands are very weak and hardly discerned in samples S10 and S11.

A very broad and prominent band located at 300 cm^{-1} for the $\text{HI-I}_2\text{-H}_2\text{O}$ system (and *ca.* 290 cm^{-1} for the $\text{KI-I}_2\text{-H}_2\text{O}$) has been attributed to an optical mode caused by specific positions and orientations of the hydrogen bonds within the local structures of the ternary systems [44]. This is a different mode to that described for S2 above, and the presence of either should be taken as evidence of particular hydrogen bonded structures occurring within a given system.

A summary of all the working assignments given for INS spectra of the binary and ternary systems, in the range 30–700 cm⁻¹, is shown in Table 7.

3.3. The Azeotrope Scenario. The azeotrope of the HI-H₂O [10] system and the pseudoazeotrope of HI-I₂-H₂O [7] are both considered detrimental to the process efficiency of the sulfur-iodine thermochemical cycle.

The INS spectra of samples lying either above or below azeotropic or pseudo-azeotropic compositions were rationalized in terms of their respective $x_{\text{H}_2\text{O}}/x_{\text{HI}}$ mole ratios. Spectral evidence of molecular arrangements similar to those of the model complexes was found to predominate in samples whose content of hydrogen iodide (HI) is higher than that of its corresponding azeotrope or pseudoazeotrope. Our working models, 4w_I and 3w_I, although stables depend strongly on relative weak interactions, that is, hydrogen bonding, which somehow explain the particular behaviour of HI_x in one of the engineering approaches to the final stage of the SI-TC, the hydrogen production through direct decomposition of HI_x. Thus when HI_x is deficient in water ($x_{\text{H}_2\text{O}}/x_{\text{HI}} < 4$), as it occurs above the pseudoazeotrope composition where not enough water molecules are longer available to stabilize the ionically dissociated HI_x, the iodide anion (I⁻) recombines with one of the protons (H⁺), and volatile hydrogen iodide, gets evaporated from the surface, which is ultimately decomposed into iodine (I₂) and hydrogen (H₂). Such molecular regime agrees with the observation that in systems exhibiting higher HI mole fractions (x_{HI}) than in the pseudoazeotrope, the SI-TC yields higher hydrogen pressures at the output [7], and it is further supported by similar chemical behaviour reported for other hydrogen halides [47].

4. Conclusions

In the present paper, the capabilities of both SRS and INS have been exploited to generate a more detailed and complete model of the HI_x phase of the GA SI-TC. For this purpose, a set of representative samples of the aqueous HI-H₂O binary system, and both aqueous HI-I₂-H₂O and KI-I₂-H₂O ternary systems were examined. Whereas SRS revealed features corresponding to hydroxonium ions and hydration shells and ultimately confirmed the coexistence of solvated I₂-containing species such as I₃⁻, I⁻(I₂), and I⁻(I₂)₂; INS, on the other hand, exposed the occurrence of local structures at HI concentrations higher than those observed in both HI-H₂O and HI-I₂-H₂O azeotropes. These local structures were then interpreted in terms of a rather simplified and empirical approach, in which two idealized models (4w_I, 3w_I) were used to explain the INS spectra. It is also noteworthy that these models not just satisfied the interpretation of the INS spectra, but also accounted for the azeotropic behaviour of the HI-H₂O and HI-I₂-H₂O systems. This work will set the basis for a more profound chemical understanding of HI_x, which is only possible with definite structural information currently lacking, but that can be acquired through the exploitation of small angle neutron diffraction with isotopic substitution.

Acknowledgments

The authors would like to thank Chris Sammons from the MERI at Sheffield Hallam University for giving access to their Raman facilities, also gratitude to Stewart Parker and "Timmy" Ramirez-Cuesta for the support provided during the operation of TOSCA at ISIS facilities. V. H. Ramos-Sánchez wishes to thank his sponsor CONACYT (Mexican Government) for the award of a full scholarship. This research was funded by the European Community Sixth Framework Program Priority through the HYTHEC Project under contract number 502704.

References

- [1] C. E. Bamberger, "Hydrogen production from water by thermochemical cycles; a 1977 update," *Cryogenics*, vol. 18, no. 3, pp. 170–183, 1978.
- [2] C. E. Bamberger, J. Braunstein, and D. M. Richardson, "Thermochemical production of hydrogen from water," *Journal of Chemical Education*, vol. 55, no. 9, pp. 561–564, 1978.
- [3] G. Marbán and T. Valdés-Solís, "Towards the hydrogen economy?" *International Journal of Hydrogen Energy*, vol. 32, no. 12, pp. 1625–1637, 2007.
- [4] D. O'Keefe, C. Allen, G. Besenbruch et al., "Preliminary results from bench-scale testing of a sulfur-iodine thermochemical water-splitting cycle," *International Journal of Hydrogen Energy*, vol. 7, no. 5, pp. 381–392, 1982.
- [5] J. H. Norman, G. E. Basenbruch, L. C. Brown, D. R. O'Keefe, and C. L. Allen, "Thermochemical water-splitting cycle, bench-scale investigations, and process engineering," Tech. Rep. GA-A16713, General Atomics Co., San Diego, Calif, USA, 1982.
- [6] K. F. Knoche, H. Engels, and J. Thoennissen, "Direct dissociation of hydrogeniodide into hydrogen and iodine from HI,H₂O,I₂-solution," *Advanced Hydrogen and Energy*, vol. 4, pp. 449–455.
- [7] H. Engels and K. F. Knoche, "Vapor pressures of the system HI/HO/I and H," *International Journal of Hydrogen Energy*, vol. 11, no. 11, pp. 703–707, 1986.
- [8] H. Kanno, "Raman study of aqueous HX solutions (X = F, Cl, Br and I) in both liquid and glassy states," *Journal of Raman Spectroscopy*, vol. 24, pp. 689–693, 1993.
- [9] A. Giacconi, G. Caputo, A. Ceroli et al., "Experimental study of two phase separation in the Bunsen section of the sulfur-iodine thermochemical cycle," *International Journal of Hydrogen Energy*, vol. 32, no. 5, pp. 531–536, 2007.
- [10] J. Haase, H. Naas, and H. Thumm, "Experimental investigation on the thermodynamic behavior of concentrated halogen hydrogen acids," *Zeitschrift für Physikalische Chemie*, vol. 37, pp. 210–229, 1963.
- [11] R. H. Elder, G. H. Priestman, B. C. Ewan, and R. W. K. Allen, "The separation of HI in the sulphur-iodine thermochemical cycle for sustainable hydrogen production," *Process Safety and Environmental Protection*, vol. 83, no. 4 B, pp. 343–350, 2005.
- [12] L. M. Levering, M. Roxana Sierra-Hernández, and H. C. Allen, "Observation of hydronium ions at the air-aqueous acid interface: vibrational spectroscopic studies of aqueous HCl, HBr, and HI," *Journal of Physical Chemistry C*, vol. 111, no. 25, pp. 8814–8826, 2007.

- [13] J. Milne, "A Raman spectroscopic study of the effect of ion-pairing on the structure of the triiodide and tribromide ions," *Spectrochimica Acta Part A*, vol. 48, no. 4, pp. 533–542, 1992.
- [14] V. H. Ramos-Sánchez, R. J. Jeans, and R. Devonshire, "Raman scattering studies of the condensed phase of the HI_x feed of the sulfur-iodine thermochemical cycle," *International Journal of Energy Research*, vol. 35, no. 3, pp. 189–208, 2011.
- [15] S. Odde, B. J. Mhin, S. Lee, H. M. Lee, and K. S. Kim, "Dissociation chemistry of hydrogen halides in water," *Journal of Chemical Physics*, vol. 120, no. 20, pp. 9524–9535, 2004.
- [16] R. L. Frost, K. L. Erickson, and M. L. Weier, "Hydrogen bonding in selected vanadates: a Raman and infrared spectroscopy study," *Spectrochimica Acta—Part A*, vol. 60, no. 10, pp. 2419–2423, 2004.
- [17] F. Rull, "Structural investigation of water and aqueous solutions by Raman spectroscopy," *Pure and Applied Chemistry*, vol. 74, no. 10, pp. 1859–1870, 2002.
- [18] J. Li and A. I. Kolesnikov, "Neutron spectroscopic investigation of dynamics of water ice," *Journal of Molecular Liquids*, vol. 100, no. 1, pp. 1–39, 2002.
- [19] P. C. H. Mitchell, S. F. Parker, A. J. Ramirez-Cuesta, and J. Tomkinson, in *Vibrational Spectroscopy with Neutrons*, p. 642, World Scientific Publishing, River Edge, NJ, USA, 1st edition, 2005.
- [20] J. Tomkinson and T. C. Waddington, "Inelastic neutron scattering from zirconium borohydride," *Journal of the Chemical Society, Faraday Transactions 2*, vol. 72, pp. 1245–1250, 1976.
- [21] N. S. Grace, "The Existence of Solid Polyiodides of Potassium at 25°C," *Journal of the Chemical Society*, pp. 594–609, 1931.
- [22] TOSCA, "A World Class Inelastic Neutron Spectrometer," <http://www.isis.stfc.ac.uk/instruments/tosca/publications/tosca-paper6538.pdf>.
- [23] D. Colognesi, M. Celli, F. Cillico et al., "TOSCA neutron spectrometer: the final configuration," *Applied Physics A: Materials Science and Processing*, vol. 74, no. 1, pp. S64–S66, 2002.
- [24] F. D. Vila and K. D. Jordan, "Theoretical study of the dipole-bound excited states of $\text{I}(\text{H}_2\text{O})$," *Journal of Physical Chemistry A*, vol. 106, no. 7, pp. 1391–1397, 2002.
- [25] M. E. Dunn, T. M. Evans, K. N. Kirschner, and G. C. Shields, "Prediction of accurate anharmonic experimental vibrational frequencies for water clusters, $(\text{H}_2\text{O})_n$ ($n = 2–5$)," *Journal of Physical Chemistry A*, vol. 110, no. 1, pp. 303–309, 2006.
- [26] M. J. Frisch, G. W. Trucks, H. B. Schlegel et al., *Gaussian 03, Revision C.02*, Gaussian, Wallingford, Conn, USA, 2004.
- [27] C. Moller and M. S. Plesset, "Note on an approximation treatment for many-electron systems," *Physical Review*, vol. 46, pp. 618–622, 1934.
- [28] D. Andrae, U. Häußermann, M. Dolg, H. Stoll, and H. Preuß, "Energy-adjusted ab initio pseudopotentials for the second and third row transition elements," *Theoretica Chimica Acta*, vol. 77, no. 2, pp. 123–141, 1990.
- [29] A. Schäfer, C. Huber, and R. Ahlrichs, "Fully optimized contracted Gaussian basis sets of triple zeta valence quality for atoms Li to Kr," *The Journal of Chemical Physics*, vol. 100, no. 8, pp. 5829–5835, 1994.
- [30] A. Schäfer, H. Horn, and R. Ahlrichs, "Fully optimized contracted Gaussian basis sets for atoms Li to Kr," *The Journal of Chemical Physics*, vol. 97, no. 4, pp. 2571–2577, 1992.
- [31] A. J. Ramirez-Cuesta, "aCLIMAX 4.0.1, the new version of the software for analyzing and interpreting INS spectra," *Computer Physics Communications*, vol. 157, no. 3, pp. 226–238, 2004.
- [32] A. Milet, C. Struniewicz, R. Moszynski, and P. E. S. Wormer, "Theoretical study of the protolytic dissociation of HCl in water clusters," *Journal of Chemical Physics*, vol. 115, no. 1, pp. 349–356, 2001.
- [33] G. M. Chaban, R. B. Gerber, and K. C. Janda, "Transition from hydrogen bonding to ionization in $(\text{HCl})_n(\text{NH}_3)_n$ and $(\text{HCl})_n(\text{H}_2\text{O})_n$ clusters: consequences for anharmonic vibrational spectroscopy," *Journal of Physical Chemistry A*, vol. 105, no. 36, pp. 8323–8332, 2001.
- [34] R. Chenevert, M. Chamberland, M. Simard, and F. Brisse, "Complexes of 18-crown-6 with oxonium ions derived from transition metal chlorides and hydrochloric acid: 18-crown-6· H_3O^+ · FeCl_4^- , 18-crown-6· H_3O^+ · InCl_4^- , (18-crown-6· H_3O^+)₂· Pd_2Cl_6^- ," *Canadian Journal of Chemistry*, vol. 67, pp. 32–36, 1989.
- [35] V. Buch, J. Sadlej, N. Aytemiz-Uras, and J. P. Devlin, "Solvation and ionization stages of HCl on ice nanocrystals," *Journal of Physical Chemistry A*, vol. 106, no. 41, pp. 9374–9389, 2002.
- [36] M. Mucha, T. Frigato, L. M. Levering et al., "Unified molecular picture of the surfaces of aqueous acid, base, and salt solutions," *Journal of Physical Chemistry B*, vol. 109, no. 16, pp. 7617–7623, 2005.
- [37] P. Andersson, C. Steinbach, and U. Buck, "Vibrational spectroscopy of large water clusters of known size," *European Physical Journal D*, vol. 24, no. 1–3, pp. 53–56, 2003.
- [38] D. Liu, G. Ma, L. M. Levering, and H. C. Allen, "Vibrational spectroscopy of aqueous sodium halide solutions and air-liquid interfaces: observation of increased interfacial depth," *Journal of Physical Chemistry B*, vol. 108, no. 7, pp. 2252–2260, 2004.
- [39] G. E. Walrafen, M. S. Hokmabadi, and W. H. Yang, "Raman investigation of the temperature dependence of the bending V and combination V + V bands from liquid water," *Journal of Physical Chemistry*, vol. 92, no. 9, pp. 2433–2438, 1988.
- [40] M. Freda, A. Piluso, A. Santucci, and P. Sassi, "Transmittance Fourier transform infrared spectra of liquid water in the whole mid-infrared region: temperature dependence and structural analysis," *Applied Spectroscopy*, vol. 59, no. 9, pp. 1155–1159, 2005.
- [41] P. A. Giguère, C. Martel, and S. Turrell, "Hydrogen halide-water complexes in aqueous acids," *Chemical Physics Letters*, vol. 56, no. 2, pp. 231–234, 1978.
- [42] H. Kanno and J. Hiraishi, "Existence of HO ions in glassy aqueous HX solutions (X = Cl and Br)," *Chemical Physics Letters*, vol. 107, no. 4–5, pp. 438–441, 1984.
- [43] W. Kiefer and H. J. Bernstein, "The UV-laser excited resonance raman spectrum of the I ion," *Chemical Physics Letters*, vol. 16, no. 1, pp. 5–9, 1972.
- [44] J. Li, "Inelastic neutron scattering studies of hydrogen bonding in ices," *Journal of Chemical Physics*, vol. 105, no. 16, pp. 6733–6755, 1996.
- [45] R. Thomas and F. H. Moore, "Neutron Diffraction Studies of Polyiodides. I. Potassium Triiodide Monohydrate," *Acta Crystallographica Section B*, vol. B36, pp. 2869–2873, 1980.
- [46] P. S. Leung and G. J. Safford, "A neutron inelastic scattering investigation of the concentration and anion dependence of low frequency motions of HO molecules in ionic solutions," *Journal of Physical Chemistry*, vol. 74, no. 21, pp. 3696–3709, 1970.
- [47] V. E. Bondybey and M. K. Beyer, "How many molecules make a solution?" *International Reviews in Physical Chemistry*, vol. 21, no. 2, pp. 277–306, 2002.

Research Article

Molecular Self-Assembling of *N*-Methylacetamide in Solvents

Hideyuki Minami and Makio Iwahashi

Department of Chemistry, School of Science, Kitasato University, 1-15-1 Kitasato, Minami-ku, Sagamihara 252-0373, Japan

Correspondence should be addressed to Hideyuki Minami, minami@sci.kitasato-u.ac.jp

Received 28 April 2011; Accepted 27 June 2011

Academic Editor: Sergio Armenta Estrela

Copyright © 2011 H. Minami and M. Iwahashi. This is an open access article distributed under the Creative Commons Attribution License, which permits unrestricted use, distribution, and reproduction in any medium, provided the original work is properly cited.

The self-association of *N*-methylacetamide (NMA), which is one of the most simple compound having a peptide bond, in various solvents such as carbon tetrachloride (CCl_4), chloroform, dichloromethane, and acetonitrile was studied through the near-infrared (NIR) spectroscopic observation at various temperatures and concentrations. An analysis assuming a successive association processes for the NMA molecules was applied to the sharp 1470-nm band (the first-overtone band of NH stretching vibration mode attributed to free NH group of NMA monomer and partly to the free, terminal NH group of NMA aggregate); the mean association number for NMA in CCl_4 increases with increasing concentration and decreases with increasing temperature. Comparisons of the association number of NMA in various solvents indicate that the degree of association is in the following order: $\text{CCl}_4 \gg \text{chloroform} = \text{dichloromethane} > \text{acetonitrile}$. Interestingly, the association number of NMA in CCl_4 is thought to be larger than that in its pure liquid.

1. Introduction

Near-infrared (NIR) spectroscopy is a useful analytical method for practical materials [1] and has been applied to various industrial and agricultural problems [2, 3]. The applications, however, have been mostly based on mathematical treatments of the NIR spectra but not on analytical knowledge which the NIR spectra should give. Its applicants to basic chemical problems are still very limited probably because detailed spectral analyses of standard compounds have not been well carried out. On the other hand, NIR spectroscopy has such important technical merits that a liquid quartz cell with the path length of 10 mm or more can be used, remote spectroscopy is applicable, and so on. The use of the long-path-length cell makes us able to obtain the more reliable results especially in concentration. To make full use of the advantages, it is absolutely important to utilize the analytical information which NIR absorptions possess.

By the way, hydrogen-bonding interactions are now known to be important in determining the structural properties of proteins. In particular, hydrogen bonding between the carboxyl oxygen and amide hydrogen atoms in the protein backbone help to stabilize the β -sheet and other motifs [4]. Among the forces that contribute to the stabilization of configuration of protein molecules in solution, intramolecular

hydrogen bonds have often been assigned a key role. Furthermore, hydrogen bonding between peptide groups has indeed been definitely demonstrated in proteins and polypeptides, as well as in model amino acids and small peptides, in the solid state. Hydrogen-bonding interactions play an essential role in protein-ligand interactions and in the mechanism of peptide- and protein-mediated reactions [5–7].

One of the simple protein model peptide system is *N*-methylacetamide (NMA). Therefore, NMA has been extensively studied by a variety of experimental and theoretical methods [8–19]. However, uncertainties still exist concerning the effect of hydrogen bonding on its structure and conformation. In the present study, we measured the NIR spectroscopy of NMA in various solvents such as CCl_4 , CHCl_3 , CH_2Cl_2 , and CH_3CN and calculated the aggregation number by assuming a successive association processes for NMA molecules.

2. Experimental

2.1. Materials. The sample of *N*-methylacetamide (NMA, its purity greater than 99.8%, Tokyo Kasei Kougyou Co. Ltd.) was used after distillation. Sample of NMA- d_1 was synthesized by using the deuterium-proton exchange reaction, by stirring the NMA sample in a large excess amount

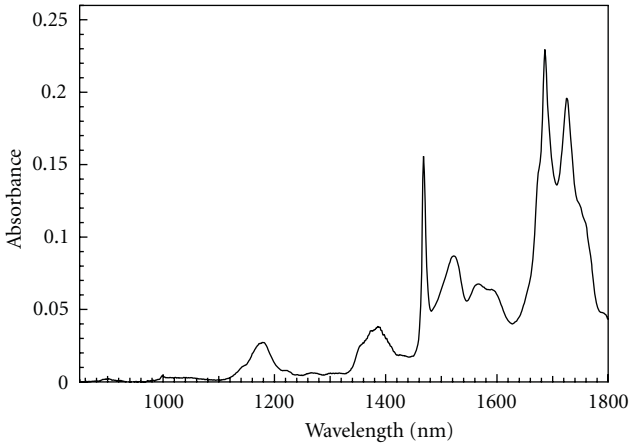


FIGURE 1: NIR spectrum of NMA in CCl_4 (0.8 mol dm^{-3}) at 30°C .

of CH_3OD (ten times amount to the NMA sample) at 40°C , and then by the distillation of the alcohol. This deuterium-proton exchange process was repeated 7 times. Its deuterium content was determined to be 98% by NIR spectroscopic observation. Carbon-disulfide-free sample of carbon tetrachloride (CCl_4 , its purity greater than 99.5%, Nakaraites Co. Ltd.) was dried by 7 hrs refluxing over P_2O_5 and distilled under an atmosphere of dried nitrogen. The samples of dichloromethane and chloroform (CH_2Cl_2 and CHCl_3 , their purities greater than 99%, Wako Junyaku Kogyo Co. Ltd.) were used after distillation also under nitrogen gas atmosphere. The sample of acetonitrile (CH_3CN , its purity greater than 99.9%, Wako Junyaku Kogyo Co. Ltd.) was used without further purification.

2.2. Near-Infrared Spectroscopic Measurement. The NIR spectra were measured at a resolution of 1.0 nm on a Hitachi-3500 spectrophotometer. A quartz cell having 5.0 or 10 mm path length was used. A Hitachi temperature-regulated cell holder (No. 131-0040) was used to maintain the temperature of the sample within $\pm 0.05^\circ\text{C}$. Temperature control of the thermostat water was carried out with a temperature controller (Yamato-Komatsu colonics circulator model CTE 32).

2.3. Density Measurement. The densities for the samples of pure liquid and the CCl_4 solution of NMA were measured on a vibration-type densimeter (Anton Paar Model DMA 58) over temperature range of 10.0 – $65.0 \pm 0.05^\circ\text{C}$. Degassed pure water was used for calibrating the densimeter. The absorbances were corrected for variation in the number of molecules in the light path due to the density change with temperature.

3. Results and Discussion

NIR spectra of the NMA in its pure liquid and in its CCl_4 solutions were measured in the 800 – 1800 nm region over a temperature range of 10 – 60°C .

As an example, Figure 1 shows the NIR spectrum of NMA in CCl_4 (0.8 mol dm^{-3}) at 30°C . According to [20, 21],

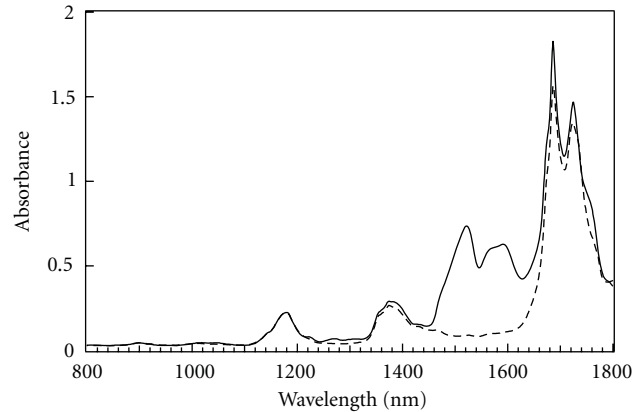


FIGURE 2: NIR spectra of samples of pure NMA (solid line) and NMA- d_1 (dashed line) at 30°C . Comparison of the two spectra indicates that the bands of the pure sample of NMA in the 1460 – 1620-nm region are only due to the vibration of NH group of NMA molecule.

the 1180-nm band is assigned to the second overtone of symmetric C-H stretch vibration; the 1380-nm band, to the combination bands of CH vibration; the strong bands near 1680 and 1720 nm , to the first overtone of asymmetric and symmetric C-H stretch vibrations. On the other hand, the sharp 1470-nm band is thought to be attributable to the free NH vibration of monomer NMA; the large and broadband around 1520 nm , to the vibration of the free, terminal NH moiety of hydrogen-bonded NMA aggregate [21]; and the broad 1560 and 1600-nm bands, to the hydrogen-bonded NMA aggregates [21]. Liu et al. [22] studied precisely the dissociation of hydrogen-bonded NMA in the pure liquid state by two-dimensional Fourier-transform NIR correlation spectroscopy. They reported that the 1473-nm (6790 cm^{-1}) band is assigned to the free NH group of monomer NMA; the 1504-nm (6650 cm^{-1}) band, to the terminal-free (free-end) NH groups of the dimer; the 1536-nm (6510 cm^{-1}) band, to the free-end NH group of oligomer; the 1553-nm (6440 cm^{-1}), to the hydrogen-bonded NH groups of dimer or small oligomers; the 1600-nm (6250 cm^{-1}) band, to the hydrogen-bonded NH groups of oligomers. In order to confirm additionally the validity of this NH band assignments in the 1460 – 1620 nm region, we measured the NIR spectrum of NMA- d_1 sample at 30°C .

Figure 2 shows the NIR spectra of pure liquid NMA (solid line) and NMA- d_1 (dotted line) samples at 30°C . The bands existing around 1460 – 1620 nm in the spectrum of the pure liquid sample of NMA apparently disappear in the spectrum of NMA- d_1 . The bands due to CH vibrations are not observed in this region of the spectrum of NMA- d_1 . This means that the bands of NMA in its pure liquid in the 1460 – 1620 nm region are attributable almost to the several vibrations of NH groups. Furthermore, in the spectrum of the pure liquid sample of NMA, the 1470-nm band due to the free NH moiety of NMA monomer is almost negligible; the two large bands are attributable to the free-end NH moiety of the hydrogen-bonded NMA aggregates and to the hydrogen-bonded NH of aggregates, respectively.

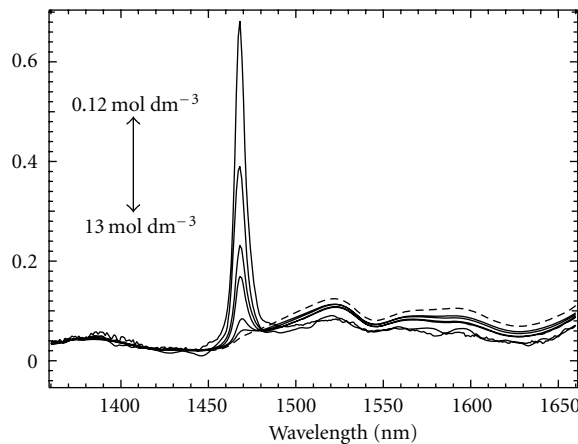


FIGURE 3: Concentration dependence of the apparent molar absorptivity ϵ of NMA in CCl_4 ($0.12, 0.25, 0.6, 1.0, 4.0$, and 8.0 mol dm^{-3}) and in pure liquid (13.0 mol dm^{-3} ; dashed line) at 30°C . The ϵ value was obtained by dividing the observed absorbance by the light-path length of the cell and the NMA concentration. The 1470-nm band due to the free NH moiety of monomer steeply increases with decreasing concentration of NMA, while the 1520 and 1600-nm bands due to the hydrogen-bonded NMA aggregates slightly decrease. The dashed line denotes the pure liquid sample of NMA. The ϵ of pure liquid at 1470 nm is very small compared with those at low concentrations.

Figure 3 represents the concentration dependence of the spectra in the $1460\text{--}1620 \text{ nm}$ region of NH vibration of NMA in CCl_4 solutions and in pure liquid state (dashed line) at 30°C . In this figure, the intensity of the absorption bands for NMA is presented in terms of the apparent molar absorptivity ϵ which was obtained by dividing the observed absorbance by the light path length of the cell and the NMA concentration. Concentrations, C , of NMA solutions were $0.12, 0.25, 0.6, 1.0, 4.0, 8.0$, and 13.0 mol dm^{-3} (pure liquid sample), respectively.

The apparent ϵ of 1470-nm band due to the NH vibration of NMA monomer steeply increases with a decrease in the NMA concentration; the relatively broad 1520-nm band due to the free, terminal NH moiety of the hydrogen-bonded NMA aggregate slightly decreases; the broad 1550–1600 nm band due to the NH groups in the NMA aggregates also slightly decreases.

As denoted by the dashed line in Figure 3, the apparent molar absorptivity value, ϵ_p , for the terminal NH group of the hydrogen-bonded NMA for the pure liquid was $0.0206 \text{ cm}^{-1} \text{ mol}^{-1} \text{ dm}^3$ at 1470 nm.

Apparently, at low concentration, the contribution of the tail part of the terminal NH band of NMA aggregate to the free monomer NH band at 1470 nm is extremely small. Thus, the contribution of the tail part of the free, terminal NH moiety of the hydrogen-bonded NMA aggregates is almost negligible at low concentrations.

From the spectra of the pure liquid NMA and NMA- d_1 samples, we have estimated that the bands due to the CH vibrations would not exist in the $1460\text{--}1620\text{-nm}$ region. However, there remains a possibility that the deuterium-

hydrogen exchange of NMA is not complete. Consequently, the slight contribution of CH vibration may still remain in the $1460\text{--}1620 \text{ nm}$ region.

Therefore, to eliminate completely the bands due to the CH vibrations from the 1470-nm band due to the NH vibration of NMA monomer, we adopted the spectrum of the pure-liquid NMR sample as a reference at 30°C . One reason is that, as the melting point of NMA crystal is $26\text{--}28^\circ\text{C}$, the pure liquid sample of NMA would not have its monomers at this temperature. In fact, as shown in Figures 2 and 3, pure-liquid NMA sample does not show the 1470-nm monomer band at 30°C . Namely, to obtain the spectra, the spectrum of NMA in pure liquid measured at 30°C was subtracted from all the raw spectra after concentration and density corrections.

In the previous paper [23], to calculate the aggregation numbers of butanol in CCl_4 , we utilized the intensity of the free OH band of monomer butanol.

In the case of NMA, we used also the intensity of the free NH band of NMA monomer at 1470 nm for the calculation of the aggregation number of the NMA in CCl_4 .

Figures 4(a) and 4(b), for examples, show the temperature dependence of the difference spectra of the 0.12 and 0.25 mol dm^{-3} samples of NMA in CCl_4 . At each constant concentration, the 1470-nm band due to the free NH monomer steeply increases with increasing temperature while the broad 1600-nm band due to the hydrogen-bonded NMA aggregate slightly decreases.

Judging from the profiles of Figures 4(a) and 4(b), in the low concentration regions, the subtraction using the spectrum of NMA in pure liquid state seems to be acceptable. However, in the high concentration regions ($0.8, 2.5$, and 8 mol dm^{-3}) as shown in Figures 4(c)–4(e), the contribution of the tail part of the band due to the free-end NH moiety of the hydrogen-bonded NMA aggregates to the 1470-nm monomer band becomes too large; we probably do the oversubtraction of the contribution of the tail part at high concentrations above 0.8 mol dm^{-3} . Thus, we evaluated the mean aggregation number of NMA in CCl_4 only below 0.25 mol dm^{-3} .

In the evaluation of the mean aggregation number of NMA, it is essential to know the monomer concentration of NMA; the monomer concentration was calculated by using the apparent molar absorptivity, ϵ , and the molar absorptivity, ϵ_m , for the 1470-nm band due to the free NH group of NMA monomer.

The ϵ_m was obtained from the concentration (C_t) dependence of the absorbance, A , at the peak position of the free NH band of monomer in a low-concentration region, where the NMA molecules exist predominantly as monomers.

NMA gave good straight line in the $A\text{-}C_t$ relationships under the condition of $C_t < 0.008 \text{ mol dm}^{-3}$ at various temperatures. From the slopes of the lines, we evaluated $2.08 \pm 0.13 \text{ cm}^{-1} \text{ mol}^{-1} \text{ dm}^3$ as ϵ_m of free NH vibration of monomer NMA. The obtained ϵ_m value is almost independent of temperature. This value is good agreement with the reported data by Klotz and Franzen [24] ($2.0 \text{ mol}^{-1} \text{ cm}^{-1} \text{ dm}^3$) and by Liu et al. [21] ($1.97 \text{ mol}^{-1} \text{ cm}^{-1} \text{ dm}^3$) and is somewhat larger than that by Krikorian [25] ($1.63 \text{ mol}^{-1} \text{ cm}^{-1} \text{ dm}^3$).

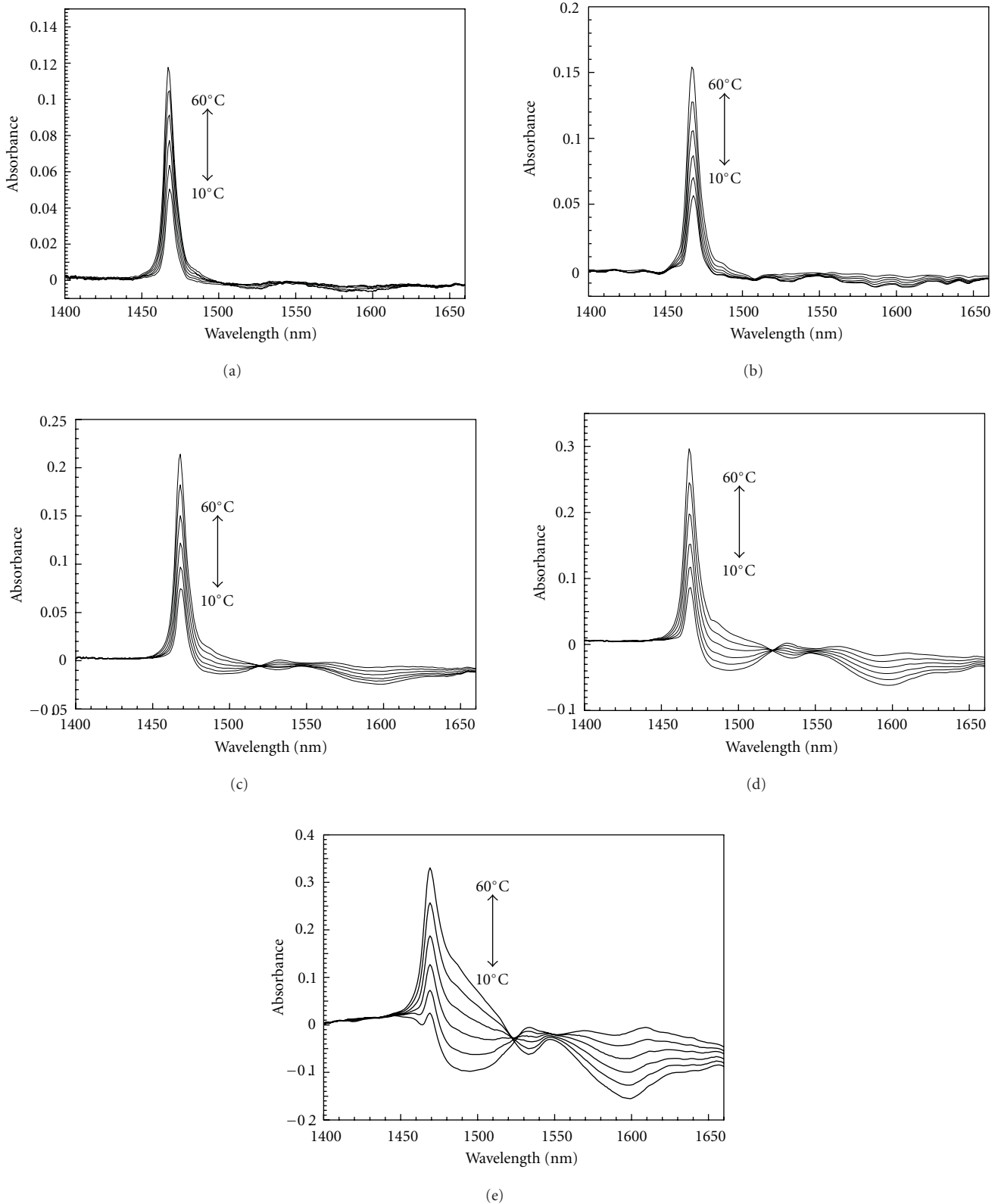
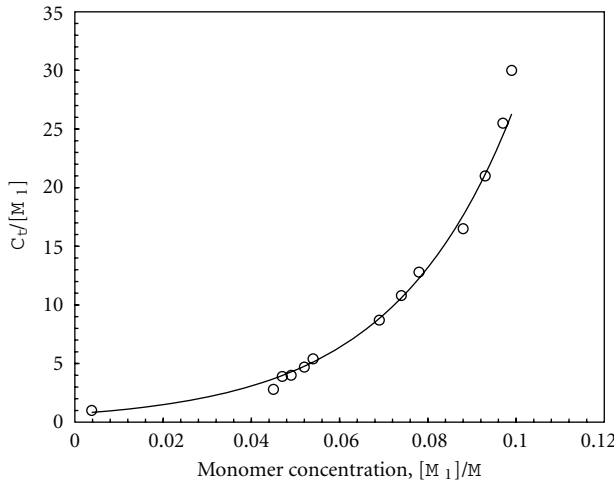


FIGURE 4: Temperature dependence ($10\text{--}60^\circ\text{C}$) of difference spectra of NMA in CCl_4 ((a) 0.12 mol dm^{-3} ; (b) 0.25 mol dm^{-3} ; (c) 0.80 mol dm^{-3} ; (d) 2.5 mol dm^{-3} ; (e) 8.0 mol dm^{-3}). The spectrum of pure liquid sample of NMA at 30°C was taken as a reference. The subtraction was carried out after the concentration and density corrections of the pure NMA and CCl_4 solution samples. The 1470-nm band due to the free NH of monomer increases with increasing temperature and the 1520-nm band due to the free, terminal NH moiety of hydrogen-bonded NMA aggregates decreases with increasing temperature. The free, terminal NH moiety of the hydrogen-bonded NMA aggregates seems to be oversubtracted below 30°C as shown in Figures 4(c), 4(d), and 4(e).

FIGURE 5: $C_t/[M_1]$ versus $[M_1]$ relationship for NMA at 20°C.

3.1. Evaluation of the Mean Association Number. Trabelsi et al. [26] reported that the NMA molecules exist somewhat as the ring cis trimer as well as the linear trans trimer at liquid state. However, in the relatively dilute CCl_4 solution, the NMA molecules would associate into large aggregates through the following successive process:

$$\begin{aligned} M_1 + M_1 &= M_2; \quad \beta_2 = \frac{[M_2]}{[M_1]^2}, \quad \therefore [M_2] = \beta_2[M_1]^2, \\ M_2 + M_1 &= M_3; \quad \beta'_3 = \frac{[M_2]}{[M_2][M_1]}, \quad \therefore [M_3] = \beta'_3[M_1]^3. \\ &\vdots \quad \vdots \quad \vdots \end{aligned} \quad (1)$$

For i -mer, in general,

$$M_{i-1} + M_1 = M_i; \quad \beta'_i = \frac{[M_i]}{[M_{i-1}][M_1]}, \quad \therefore [M_i] = \beta'_i[M_1]^i, \quad (2)$$

where $\beta_i = \beta_2\beta'_3, \dots, \beta'_{i-1}; \beta'_3, \beta'_4, \dots$, and β'_i are the association constants for each process, and β_2, β_3, \dots , and β_i , the overall association constants for the formation of dimer, trimer, and i -mer, respectively. $[M_1], [M_2], [M_3], \dots$ and $[M_i]$ denote the concentrations of monomer, dimer, trimer, and i -mer, respectively. In the equations, both types of aggregates, that is, linear and cyclic ones, are possible for the i -mers. In practice, however, cyclic aggregates would not be coexistent with open-linear species. This is because most NMA molecules exist in flat, transform structure; the formation of cyclic aggregates is thought to be very difficult. In addition, cyclic structures exhibit more order (less freedom), and, therefore, their formation involves greater entropy loss than for the formation of the equivalent open structures. Consequently, the main oligomer species would be linear types of species. Thus, as a first approximation we applied the simple successive aggregation process for the formation of the linear-type oligomer species.

The total concentration, C_t , can be expressed in terms of the monomer concentration, $[M_1]$.

$$\begin{aligned} C_t &= [M_1] + 2[M_2] + 3[M_3] + \dots + i[M_i] + \dots \\ &= \sum i[M_i] = \sum i\beta_i[M_1]^i. \end{aligned} \quad (3)$$

On the other hand, if we regard the oligomers (dimer, trimer, tetramer, and so on) as a sort of particle, the total concentration of the particles, C_m , would be represented by(4)

$$\begin{aligned} C_m &= [M_1] + [M_2] + [M_3] + \dots + [M_i] + \dots \\ &= \sum [M_i] = \sum \beta_i[M_1]^i. \end{aligned} \quad (4)$$

Differentiation of (4) with respect to $[M_1]$ and combination with (3) leads to(5)

$$\frac{dC_m}{d[M_1]} = \sum i\beta_i[M_1]^{i-1} = \frac{\sum i\beta_i[M_1]^i}{[M_1]} = \frac{C_t}{[M_1]}. \quad (5)$$

Thus, the C_m is represented by the integral of (5)

$$C_m = \int_{\sim 0}^{[M_1]} \frac{C_t}{[M_1]} d[M_1]. \quad (6)$$

In practice, the C_m can be evaluated graphically through the successive area integral of the $C_t/[M_1]$ versus $[M_1]$ relationship, with the use of $[M_1]$ at an arbitrary C_t .

Then, the mean association number, \bar{N} , which includes monomer species, is expressed as follows:

$$\bar{N} = \frac{C_t}{C_m}. \quad (7)$$

The value of $[M_1]$ necessary for evaluating the C_m and finally \bar{N} values can be estimated from the apparent molar absorptivity, ϵ , and the molar absorptivity ϵ_m for the free NH band (at 1470 nm) of monomer.

As a typical example, the $C_t/[M_1]$ versus $[M_1]$ relationship for NMA at 30°C is shown in Figure 5. $C_t/[M_1]$ increases gradually and steeply with an increase in $[M_1]$. The graphical successive area integral of the relationship gave the C_m at an arbitrary $[M_1]$ or C_t . Then, the \bar{N} at the arbitrary C_t was evaluated with (7) by using the obtained C_m value.

The \bar{N} versus C_t relationships at various constant temperatures for NMA in CCl_4 are shown in Figure 6. At a constant temperature, the \bar{N} value increases with an increase in concentration. At constant concentration, the \bar{N} value decreases with increasing temperature.

Similar observations were carried out for the NMA samples in CH_2Cl_2 , CHCl_3 , and CH_3CN solutions. In these cases, the absorptions due to the solvents themselves are included in the observed spectra. Therefore, the removal of the spectra due to the solvents from the observed spectra was carried out after the background and density corrections. After these calculating procedures, similar calculation as same as the case of CCl_4 solution was carried out.

As an example the obtained results for the mean aggregation number \bar{N} of NMA in these solvents at 20°C are

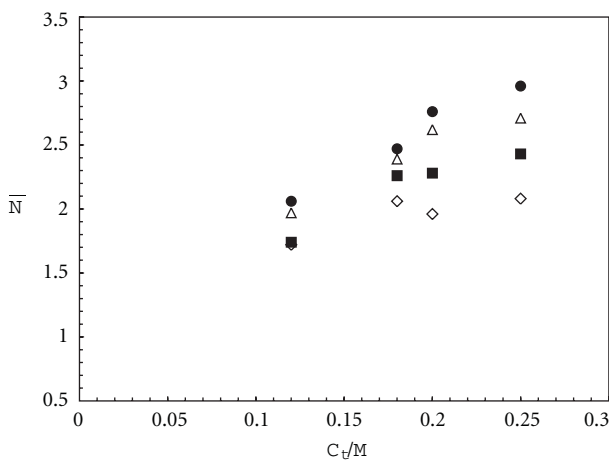


FIGURE 6: Mean aggregation number, \bar{N} , versus total concentration, C_t , of NMA at various temperatures: • denotes 10°C ; Δ , 20°C ; ■, 30°C ; \Diamond , 40°C .

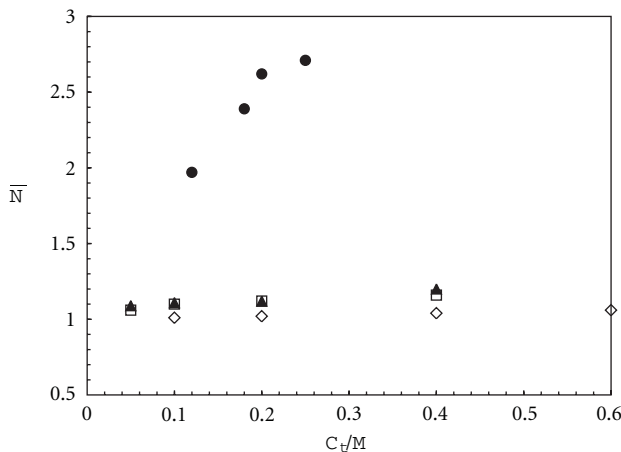


FIGURE 7: Mean aggregation number, \bar{N} , versus total concentration, C_t , of NMA in various solvents at 20°C . • denotes CCl_4 ; ▲, CH_2Cl_2 ; □, CHCl_3 ; \Diamond , CH_3CN .

plotted in Figure 7. In the case of the solvents such as CH_2Cl_2 , CHCl_3 , and CH_3CN , the contributions of the free, terminal NH groups of the NMA aggregates to the monomer band were very small, and then the concentration regions for the calculation of aggregation number are wide, compared with the case in CCl_4 . The \bar{N} value of NMA in CH_3CN is almost 1 and very slightly increases with increasing concentration of NMA. In addition, the \bar{N} values of NMA in CH_2Cl_2 and CHCl_3 also slightly increase with increasing concentration of NMA but slightly larger than that in CH_3CN . Namely, the NMA molecules aggregate most greatly in CCl_4 . The dielectric constants of CH_3CN , CH_2Cl_2 , CHCl_3 , and CCl_4 have been reported as 37.5, 9.1, 4.9, and 2.205 at 20°C [27], respectively. The dielectric constant of the solvents is thought to contribute the degree of association of NMA molecule.

In the low dielectric solvent such as CCl_4 , the NMA aggregation progresses steeply with increasing the concentration of NMA molecule.

By the way, is there a difference in the profile of the aggregates of NMA in nonpolar solvent such as CCl_4 and in pure liquid? Then, we investigated effect of CCl_4 on the aggregation profile of NMA.

3.2. Effect of Nonpolar Solvent on the Aggregation Profile of NMA Molecules. Figures 4(c) and 4(e) exhibit the temperature dependence of the difference spectra for NMA in CCl_4 solution at high concentrations: 0.8, 2.5, and 8.0 mol dm^{-3} . The difference spectra were obtained by subtracting the spectrum of pure NMA sample at 30°C as a reference from other spectra measured at various temperatures after density correction.

Interestingly, the difference spectra below 30°C has a large minimum at 1510 nm which is very close to the band of the free, terminal NH of aggregate of NMA, while the 1600 nm band due to the hydrogen-bonded aggregates of NMA does not so decrease. This suggests that the number of terminal NH group decreases in CCl_4 and that the aggregates become more large-sized clusters in CCl_4 . Namely, nonpolar solvent such as CCl_4 may promote the formation of larger aggregate of NMA molecules. The solvent having low dielectric constant dislike the NMA molecules and may promote the formation of large clusters. With increasing temperature, the large cluster would dissociate more easily and then monomer band increases in its intensity. In addition, the number of the free, terminal NH groups of the oligomers would increase with increasing temperature. The aggregate structures in CCl_4 and in liquid, however, should be clarified by more additional experiments.

4. Conclusions

Aggregation numbers of NMA in various solvents, such as CCl_4 , CHCl_3 , CH_2Cl_2 , and CH_3CN , were obtained by using NIR spectroscopic observation. The order of the degree of association is $\text{CCl}_4 \gg \text{CHCl}_3 \approx \text{CH}_2\text{Cl}_2 > \text{CH}_3\text{CN}$. The cluster size increases with increasing NMA concentration and decreases with increasing temperature. In the solvent having a high dielectric constant, the aggregation number of NMA is very small, while in the solvent having a low dielectric constant that of NMA is very large. In addition, the nonpolar solvent such as CCl_4 promotes the cluster size of NMA.

Acknowledgment

The authors are grateful to Mr. Ryo Wakasugi, Miss. Yuka Mochizuki, and Masatoshi Yokomizo for their assistances with the NIR observation.

References

- [1] F. McClure, *Analytical Chemistry*, vol. 43A, p. 66, 1994.
- [2] P. Williams and K. Norris, Eds., *Near-Infrared Technology in the Agricultural and Food Industries*, AACC Press, 2nd edition, 2001.
- [3] Y. Ozaki, W. F. McClure, and A. A. Christy, Eds., *Near-Infrared Spectroscopy in Food Science and Technology*, John Wiley & Sons, 2006.

- [4] G. E. Schulz and R. G. Schirmer, *Principles of Protein Structure*, Springer, New York, NY, USA, 1998.
- [5] I. D. Kuntz and W. Kauzmann, "Hydration of proteins and polypeptides," *Advances in Protein Chemistry*, vol. 28, pp. 239–345, 1974.
- [6] L. Packer, *Methods in Enzymology*, vol. 127, pp. 1–416, 1986.
- [7] M. Kitano, T. Fukuyama, and K. Kuchitsu, *Bulletin of the Chemical Society of Japan*, vol. 46, p. 384, 1973.
- [8] R. J. Albers, A. B. Swanson, and G. C. Kresheck, "An equilibrium centrifugation study of the self-association of N-methylacetamide in carbon tetrachloride solutions at 25°," *Journal of the American Chemical Society*, vol. 93, no. 25, pp. 7075–7078, 1971.
- [9] H. Guo and M. Karplus, "Ab initio studies of hydrogen bonding of N-methylacetamide: structure, cooperativity, and internal rotational barriers," *Journal of Physical Chemistry*, vol. 96, no. 18, pp. 7273–7287, 1992.
- [10] R. Ludwig, O. Reis, R. Winter, F. Weinhold, and T. C. Farrar, "Quantum cluster equilibrium theory of liquids: temperature dependence of hydrogen bonding in liquid N-methylacetamide studied by IR spectra," *Journal of Physical Chemistry B*, vol. 102, no. 46, pp. 9312–9318, 1998.
- [11] D. G. Regan, B. E. Chapman, and P. W. Kuchel, "PGSE NMR diffusion study of the self-association of N-methylacetamide in carbon tetrachloride," *Magnetic Resonance in Chemistry*, vol. 40, pp. S115–S121, 2002.
- [12] S. Trabelsi and S. Nasr, "Intermolecular association in liquid N-methylacetamide as studied by x-ray scattering," *Journal of Chemical Physics*, vol. 121, no. 13, pp. 6380–6385, 2004.
- [13] M. A. Czarnecki and K. Z. Haufa, "Effect of temperature and concentration on the structure of N-methylacetamide-water complexes: near-infrared spectroscopic study," *Journal of Physical Chemistry A*, vol. 109, no. 6, pp. 1015–1021, 2005.
- [14] K. Kwac and M. Cho, "Hydrogen bonding dynamics and two-dimensional vibrational spectroscopy: N-methylacetamide in liquid methanol," *Journal of Raman Spectroscopy*, vol. 36, no. 4, pp. 326–336, 2005.
- [15] S. Trabelsi, M. Bahri, and S. Nasr, "X-ray scattering and density-functional theory calculations to study the presence of hydrogen-bonded clusters in liquid N-methylacetamide," *Journal of Chemical Physics*, vol. 122, no. 2, Article ID 024502, pp. 1–8, 2005.
- [16] T. W. Whitfield, G. J. Martyna, S. Allison, S. P. Bates, H. Vass, and J. Crain, "Structure and hydrogen bonding in neat N-methylacetamide: classical molecular dynamics and raman spectroscopy studies of a liquid of peptidic fragments," *Journal of Physical Chemistry B*, vol. 110, no. 8, pp. 3624–3637, 2006.
- [17] S. Trabelsi, S. Nasr, M. Bahri, and M. C. Bellissent-Funel, "Molecular association in deuterated liquid N-methylacetamide-water complex: neutron diffraction and density functional theory study," *Journal of Molecular Structure*, vol. 842, no. 1–3, pp. 93–99, 2007.
- [18] L. Piatkowski and H. J. Bakker, "Vibrational relaxation pathways of AI and AII modes in N-methylacetamide clusters," *Journal of Physical Chemistry A*, vol. 114, no. 43, pp. 11462–11470, 2010.
- [19] S. K. Pattanayak, N. Prashar, and S. Chowdhuri, "Effect of temperature and pressure on the structure, dynamics, and hydrogen bond properties of liquid N-methylacetamide: a molecular dynamics study," *Journal of Chemical Physics*, vol. 134, no. 15, article 54506, 2011.
- [20] S. E. Krikorian and M. Mahpour, "The identification and origin of N-H overtone and combination bands in the near-infrared spectra of simple primary and secondary amides," *Spectrochimica Acta Part A*, vol. 29, no. 7, pp. 1233–1246, 1973.
- [21] Y. Liu, N. A. Czarnecki, and Y. Ozaki, *Applied Spectroscopy*, vol. 48, p. 1095, 1994.
- [22] Y. Liu, Y. Ozaki, and I. Noda, "Two-dimensional Fourier-transform near-infrared correlation spectroscopy study of dissociation of hydrogen-bonded N-methylacetamide in the pure liquid state," *Journal of Physical Chemistry*, vol. 100, no. 18, pp. 7326–7332, 1996.
- [23] M. Iwahashi, M. Suzuki, N. Katayama et al., "Molecular self-assembling of butan-1-ol, butan-2-ol, and 2-methylpropan-2-ol in carbon tetrachloride solutions as observed by near-infrared spectroscopic measurements," *Applied Spectroscopy*, vol. 54, no. 2, pp. 268–276, 2000.
- [24] I. M. Klotz and J. S. Franzen, "Hydrogen bonds between model peptide groups in solution," *Journal of the American Chemical Society*, vol. 84, no. 18, pp. 3461–3466, 1962.
- [25] S. E. Krikorian, "Determination of dimerization constants of cis- and trans-configured secondary amides using near-infrared spectrometry," *Journal of Physical Chemistry*, vol. 86, no. 10, pp. 1875–1881, 1982.
- [26] S. Trabelsi, S. Nasr, M. Bahri, and M. C. Bellissent-Funel, "Local order in fully deuterated liquid N-methylacetamide (C₃D₇NO) as studied by neutron diffraction and density-functional theory calculations," *Journal of Physical Chemistry B*, vol. 110, no. 49, pp. 25021–25025, 2006.
- [27] J. A. Riddick and W. B. Bunger, *Organic Solvents*, John Wiley & Sons, 1970.

Research Article

Conformational Analysis in Solution of a Chiral Bisoxazoline Molecule: Vibrational Circular Dichroism Spectroscopy and Density Functional Theory Study

A. Aamouche¹ and P. J. Stephens²

¹Faculté Polydisciplinaire de Safi, Université Cadi Ayyad, 46000 Safi, Morocco

²Department of Chemistry, University of Southern California, Los Angeles, CA 90089-0482, USA

Correspondence should be addressed to A. Aamouche, a.aamouche@ucam.ac.ma

Received 26 July 2011; Accepted 30 August 2011

Academic Editor: Jean-Valère Naubron

Copyright © 2011 A. Aamouche and P. J. Stephens. This is an open access article distributed under the Creative Commons Attribution License, which permits unrestricted use, distribution, and reproduction in any medium, provided the original work is properly cited.

The conformations of the chiral bisoxazoline: 2,2'-methylenebis[3a,8a-dihydro-8H-indeno[1,2-d]oxazole] (also named *IndaBOX*), have been studied. Density functional theory (DFT) calculations identify four inequivalent stable conformations. Two, I and II have, C_2 symmetry; two, III and IV, have C_1 symmetry. The electronic energies of I–IV are ordered: I < II < III < IV. The span in energy is <1.0 kcal/mole. Vibrational unpolarised absorption and circular dichroism spectra have been predicted for the four conformations using DFT. Comparison of population-weighted spectra to experimental spectra of CHCl_3 and CDCl_3 solutions in mid-IR region strongly supports the DFT predictions of the number, structures, and relative energies of the conformations of *IndaBOX*. This shows that DFT predicts spectra with a high degree of reliability. We will undoubtedly illustrate the advantage added by vibrational circular dichroism spectroscopy in conformational analysis and in the absolute configuration determination.

1. Introduction

We report a study of the conformations of a chiral bisoxazoline: 2,2'-methylenebis[3a,8a-dihydro-8H-indeno[1,2-d]oxazole], **1**, in solution using ab initio vibrational spectroscopy. The molecular structure of **1** is represented on Scheme 1.

In combination with metal salts, chiral bisoxazolines catalyse a wide variety of asymmetric transformations, in many cases with high enantioselectivity [1–5]. To date, although the X-ray structures of several metal complexes of chiral bisoxazolines have been reported [6–10], there appear to have been no structural studies of chiral bisoxazolines alone. Here, we report a study of the bisoxazoline, **1**, using ab initio density functional theory (DFT) [11, 12], in combination with vibrational unpolarised absorption (IR) and vibrational circular dichroism (VCD) [13–16] spectroscopies. **1** is a flexible molecule; internal rotation can occur about the CC1 and CC2 bonds. We seek to establish the structures and relative energies of the stable conformations of **1**.

DFT has had a major impact on molecular structure calculations. For many years, wavefunction functional theory (WFT; i.e., HF/SCF and MP_ns) has been the method of choice. The DFT approach expresses ground-state properties, such as total energies, equilibrium positions dipole, and magnetic moments, in terms of electronic density and spin density. The need to include the electron correlation in calculations and the discovery of accurate approximations to exchange-correlation energy density functional raise the DFT popularity. The computational advantage of DFT originates from the fact that the electron density has three spatial coordinates, regardless of the number of electrons in the system. Thus, DFT allows the calculation of properties for systems with almost hundred atoms, a feat not generally possible with high-level WFT methods.

For simplicity, in earliest quantum mechanics treatment, nuclear and electronic motions were separated by using Born-Oppenheimer approximation and by assuming harmonic vibrational motion. To calculate vibrational spectra of a system in a fluid phase, harmonic frequencies and relative

intensities of each transition are predicted. The IR absorption intensities derive from the dependence of molar extinction coefficient ε on frequencies ν . However, VCD intensities originate from the variation of the difference $\Delta\varepsilon(\nu) = \varepsilon_L - \varepsilon_R$ resulting from the response to the left (ε_L) and right (ε_R) polarization. The theory of electromagnetic wave-molecule interactions, throughout a $g \rightarrow k$ vibrational transition, leads to (1) [16]:

$$\varepsilon(\nu) = \frac{8\pi^3 N\nu}{(2.303) 3000 hc} \sum_{g,k} \alpha_g D_{gk} L_{gk}, \quad (1)$$

$$\Delta\varepsilon(\nu) = \frac{32\pi^3 N\nu}{(2.303) 3000 hc} \sum_{g,k} \alpha_g D_{gk} L_{gk},$$

where N , h , and c are the usual constants; α_g is the number of molecules in g state; L_{gk} is the normalized Lorentzian function variable on ν and molecular excitation frequency ν_{gk} (2) [17]:

$$L_{gk}(\nu) = \frac{1}{\pi} \frac{\gamma_{gk}^2}{(\nu - \nu_{gk})^2 + \gamma_{gk}^2}, \quad (2)$$

where γ_{gk} is the half-width at half-height of the transition line. Dipole strengths D_{gk} and rotatory strengths R_{gk} are linked, respectively, to the electric μ_{el} and magnetic μ_{mag} operators by means of transition moments (3) [18]:

$$D_{gk} = |\langle g | \vec{\mu}_{el} | k \rangle|^2, \quad (3)$$

$$R_{gk} = \text{Im} \{ \langle g | \vec{\mu}_{el} | k \rangle \cdot \langle k | \vec{\mu}_{mag} | g \rangle \}.$$

Considering only the vibrational ground state $g = 0$ and fundamental transitions involving one mode alone to the states $k = 1$, the fundamental transition moments in mode i are (4):

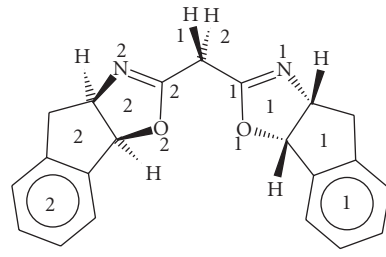
$$\langle 0 | (\mu_{el})_\beta | 1 \rangle_i = \left(\frac{\hbar}{4\pi\omega_i} \right)^{1/2} \sum_{\lambda\alpha} S_{\lambda\alpha,i} P_{\alpha\beta}^\lambda, \quad (4)$$

$$\langle 0 | (\mu_{mag})_\beta | 1 \rangle_i = -(4\pi\hbar^3)^{1/2} \sum_{\lambda\alpha} S_{\lambda\alpha,i} M_{\alpha\beta}^\lambda,$$

where $P_{\alpha\beta}^\lambda$ are the atomic polar tensors (APTs) and $M_{\alpha\beta}^\lambda$ are the atomic axial tensors (AATs) for the nucleus λ along the directions $\alpha, \beta = x, y$, or z . $S_{\lambda\alpha,i}$ are the transformation matrix elements between nuclear Cartesian coordinates X and nuclear normal coordinates Q (5) [19]:

$$X_{\lambda\alpha} = \sum_i S_{\lambda\alpha,i} Q_i. \quad (5)$$

Basically to get all possible conformations for any molecule, the potential energy surface (PES) needs first to be scanned. After the resolution of all optimal molecular geometries, the harmonic force field (HFF), the energies, and the electronic population are obtained. The diagonalization of the Hessian matrix (HFF with respect to nuclear Cartesian coordinates X) produces normal modes frequencies, the



(+) -1

SCHEME 1

vibronic wavefunctions, and the transformation matrix S . In sum, the prediction of the IR and VCD spectra requires the calculation of three major parameters: (i) the fundamental frequencies ν_i ; (ii) the dipole strengths D_i (via harmonic APTs elements) for the IR lines; (iii) the rotatory strengths R_i (via APTs and AATs elements) for the VCD peaks.

In practice, the AATs elements cannot be determined within Born-Oppenheimer approximation. This occurs from the vanishing of the electronic contribution to the magnetic moment μ_{mag} associated with the vibrational transition in the ground electronic state [20, 21]. So the exact formulations of VCD intensities has been resolved by taking into account high-order corrections in vibronic wavefunctions. The admixture of electronic excited state and ground states wavefunctions was accomplished by using nuclear kinetic energy or magnetic field perturbation theories [21, 22].

Over the last decades, DFT has increasingly become the method of choice in predicting molecular properties. The variety of properties which can be calculated using DFT has increased dramatically. Subsequently, the functionals sophistication and accuracy has increased; particularly important has been the development of hybrid density functionals. Becke had constructed new functionals (B3) taking into consideration the exchange and the correlation aspects. Additional suggestions gives birth to the most popular functionals B3LYP (Lee, Yang, and Parr) and B3PW91 (Perdew and Wang) [23–25]. These functionals describe correctly the electronic proprieties of numerous molecular and materials compounds.

Elsewhere to describe molecular orbitals, many basis sets are applied. They are a linear combination of a series of atomic orbital exponentials, usually Gaussian functions [26]. In our calculation the choice of the basis set 6-31G* and of the functional (B3PW91) has enabled an optimal exploitation of the computational resources via Gaussian program and deliver remarkably precise results for various systems [27]. Of particular interest here is the development of analytical derivative methods for calculating harmonic force fields (HFFs) and atomic polar tensors (APTs), which together permit the prediction of vibrational unpolarised absorption spectra, and for calculating atomic axial tensors (AATs), which together with HFFs and APTs permit the prediction of VCD spectra for chiral molecules [16]. As a result of the use of Gauge-invariant atomic orbitals (GIAOs), AATs are calculated at the same level of accuracy as APTs.

Absorption and VCD spectra were synthesized from the calculated frequencies, the dipole strengths, and the rotatory strengths, assuming constant Lorentzian bandshapes ($\gamma = 4 \text{ cm}^{-1}$). Intrinsically, the VCD sign and magnitude are expressed by the anisotropy ratio g . This ratio is defined experimentally as the VCD extinction coefficient $\Delta\epsilon$ to the IR extinction coefficient ϵ ; $g = \Delta\epsilon/\epsilon$. Theoretically, g is linked to the quotient of the rotatory strength R and the dipole strength D ; $g = 4R/D$. This leads to VCD signals normally four to six orders of magnitude smaller than the IR signals.

Studies of a number of rigid chiral molecules have shown that DFT, implemented using hybrid functionals and sufficiently large basis sets, can predict absorption and VCD spectra with a high degree of reliability [28–35]. As a result, DFT, in combination with absorption and VCD spectroscopies, provides a reliable basis for analyzing the conformational structures of flexible chiral molecules. A number of such molecules have already been studied [36–45]. Here, we extend these studies to the chiral bisoxazoline, **1** (known as *IndaBOX*). The involvement of this compound in many asymmetric synthesis, catalysis, and surface grafting imposes the structural characterization including its chirality. DFT calculation on this type of ligands was first performed for isobutyleneBox [46]. This structurally simple C_2 symmetry case was compared with NMR spectroscopic parameters to probe the behavior as chelate complex with Cu(I). The configuration of **1** analogs was extensively investigated in many references [47–53]. The present VCD study is original on such chiral molecules. We will report here the structural parameters of **1** determined by DFT calculation along with the corresponding IR and VCD spectra compared to the measurements.

2. Methods

Experimental unpolarised vibrational absorption spectra of **1** were obtained in solution in CHCl_3 , CDCl_3 , and CH_2Cl_2 using a Nicolet MX1 spectrometer at a resolution of 1 cm^{-1} . Experimental VCD spectra were obtained using a Bomem/BioTools ChiralIR spectrometer at a resolution of 4 cm^{-1} . VCD spectra of (+)- and (-)-**1** were obtained using scan times of 1 hour. The VCD spectrum of (\pm) -**1** constituted the baseline. The "half-difference" spectrum, $[\Delta\epsilon(-) - \Delta\epsilon(+)]/2$, and the "half-sum" spectrum, $[\Delta\epsilon(-) + \Delta\epsilon(+)]/2$, were obtained thence. The former provides the final VCD spectrum. The latter defines the reliability of the VCD spectrum; deviations from zero are due to noise and to polarization artifacts which are not identical in the (+), (-), and (\pm) spectra. All experiments used a variable-path cell (*Specac*) with KBr windows.

(+)- and (-)-**1** were obtained from Aldrich. Specified chemical purities were 98% for both (+)- and (-)-**1**. Specified specific rotations $[\alpha]_D^{22}$ were $+353$ and -353° ($c = 3.7$, CHCl_3), respectively. Solutions of (\pm) -**1** were obtained by mixing solutions of (+)- and (-)-**1**.

Hartree-Fock (HF) and DFT calculations of (+)-**1** were carried out using Gaussian [27]. The functionals used in DFT calculations were B3PW91 and B3LYP. The $6-31G^*$

and STO-3G basis sets were used. Unpolarised absorption and VCD spectra were synthesized from frequencies, dipole strengths, and rotational strengths, assuming Lorentzian band shapes.

Studies on rigid molecules had proven their exactness mostly for the absolute configuration determination as the conformation of such molecules is unique and stable. However, flexible molecules require conformations search for instance by scanning freely the torsional bonds. Therefore, the torsions multiplicity complicates definitely the potential energy surface (PES), exploration. Once the structure and relative energy of each stable conformation is established, the subsequent vibrational spectra are calculated. Assuming a Boltzmann distribution, the composite theoretical spectra are summed, weighting each by the fractional population, giving conformationally averaged spectra. Vibrational spectra are an exquisitely sensitive function of molecular structure. In particular, in the case of flexible molecules, vibrational spectra depend sensitively on conformation and provide a basis for conformational analysis. In the case of chiral molecules, VCD spectra are generally more sensitive to conformation than absorption spectra. As a result, in the conformational analysis of chiral molecules the combined use of absorption and VCD spectra is substantially more powerful than the use of absorption spectra alone. The association of both IR and VCD (predicted and experimental) spectra yields more credible assignment as the bands are now either positive or negative.

3. Results

Internal rotation in **1** can occur about the C–C1 and C–C2 bonds. We have searched for stable conformations as follows. First, an initial exploration at the HF/STO-3G level located a stable conformation possessing C_2 symmetry: structure I. This structure was reoptimized at the B3PW91/6-31G* level. Next, a scan of the PES, varying the two dihedral angles $\phi_1 = \text{H}1\text{CC}1\text{O}1$ and $\phi_2 = \text{H}1\text{CC}2\text{O}2$ independently, was carried out over the ranges $\phi_1, \phi_2 = -180^\circ - +180^\circ$, in steps of 10° . All other internal coordinates were fixed at the values of the B3PW91/6-31G* optimized structure. The scan was carried out at the HF/STO-3G level. The results obtained are shown in Figure 1. The PES exhibits six minima. One corresponds to structure I. The five additional minima are labelled II, IIIa, IIIb, IVa, and IVb. Structures II, IIIa, IIIb, IVa, and IVb were then optimised at the B3PW91/6-31G* level. Structure II possesses C_2 symmetry. Structures IIIa, IIIb, IVa, and IVb possess C_1 symmetry. IIIa and IIIb are equivalent, as are IVa and IVb. IIIa and IIIb are interconverted by rotation of the molecule by 180° ; IVa and IVb are interconverted in the same way.

The four inequivalent B3PW91/6-31G* structure are shown in Figure 2. The main structural parameters of the $(\text{O}1\text{C}1\text{N}1)\text{CH}1\text{H}2(\text{O}2\text{C}2\text{N}2)$ moieties are given in Table 1. The obtained electronic energies of I–IV are given in Table 2. The span is $< 1 \text{ kcal/mole}$, and the order is I $<$ II $<$ III $<$ IV. Populations predicted from the B3PW91 and B3LYP energies are also given in Table 2. Structures I–IV have also

TABLE 1: Nonbonded distances (Å) in the (O1C1N1)CH1H2(O2C2N2) moieties for the four conformations of (+)-1.

| | I B3PW91 | I B3LYP | II B3PW91 | II B3LYP | III B3PW91 | III B3LYP | IV B3PW91 | IV B3LYP |
|-------|-------------|------------|--------------|-------------|---------------|--------------|--------------|-------------|
| H1–N1 | 2.570 | 2.575 | 3.155 | 3.166 | 2.584 | 2.593 | 3.192 | 3.206 |
| H1–O1 | 3.306 | 3.315 | 2.711 | 2.723 | 3.306 | 3.314 | 2.651 | 2.650 |
| H1–N2 | 3.119 | 3.123 | 2.636 | 2.585 | 3.329 | 3.252 | 3.115 | 3.201 |
| H1–O2 | 2.747 | 2.758 | 3.391 | 3.314 | 2.934 | 2.643 | 2.748 | 2.622 |
| H2–N1 | 3.119 | 3.122 | 2.634 | 2.585 | 3.418 | 2.621 | 3.202 | 2.595 |
| H2–O1 | 2.747 | 2.758 | 3.385 | 3.314 | 2.824 | 3.353 | 2.640 | 3.317 |
| H2–N2 | 2.569 | 2.575 | 3.156 | 3.166 | 3.221 | 3.229 | 3.137 | 3.152 |
| H2–O2 | 3.307 | 3.315 | 2.709 | 2.723 | 2.571 | 2.574 | 2.699 | 2.693 |
| N1–N2 | 4.732 | 4.744 | 4.682 | 4.684 | 3.692 | 3.696 | 3.715 | 3.711 |
| O1–O2 | 3.322 | 3.325 | 3.430 | 3.386 | 4.230 | 4.239 | 4.253 | 4.279 |

TABLE 2: Electronic energies E and populations P of conformations I, II, III, and IV of **1**^a.

| | B3PW91/6-31G* | | B3LYP/6-31G* | |
|-----|---------------|------|--------------|------|
| | E | P | E | P |
| I | 0.00 | 49.2 | 0.00 | 48.0 |
| II | 0.41 | 24.8 | 0.33 | 27.5 |
| III | 0.71 | 15.0 | 0.77 | 13.1 |
| IV | 0.89 | 11.0 | 0.85 | 11.4 |

^aE in kcal/mol, P in % (calculated assuming a Boltzmann distribution and T = 293° K).

been optimized at the B3LYP/6-31G* level. Qualitatively, the structures are identical to the B3PW91/6-31G* structures. Quantitative differences in bond lengths, bond angles, and dihedral angles are small. B3LYP/6-31G* and B3PW91/6-31G* energies differ by <0.1 kcal/mole. Once we take into account the free thermal energy, the B3PW91/6-31G* energy differences decreases. The free energies of I–IV are differently ordered: I < III < IV < II. More spectacularly, the span in free energies is smaller <0.3 kcal/mole (III versus I drop to 0.05 kcal/mol, IV versus I becomes 0.19 kcal/mol, whereas II versus I is 0.26 kcal/mol). The validity of stability lowering for the conformation II should be estimated with a tightest spectral analysis.

In order to assess the reliability of these predictions we have compared the vibrational absorption and circular dichroism spectra predicted for structures I, II, III, and IV, and for mixtures of these structures, to the experimental spectra. See Table 3, placed in a supplementary information section available online at doi:10.1155/2011/905045, that shows the whole 123 B3PW91/6-31G* vibrational modes listing.

4. Discussion

Our DFT calculations show that (1) several stable conformations of **1** exist, differing very little (<1 kcal/mole) in energy; (2) in each conformation, the CNO plane of each oxazole ring is oriented in one of three orientations, interrelated by ~120° rotations about the CC1 or CC2 bonds; (3) of the possible combinations of C1N1O1 and C2N2O2 orientations, four correspond to inequivalent stable

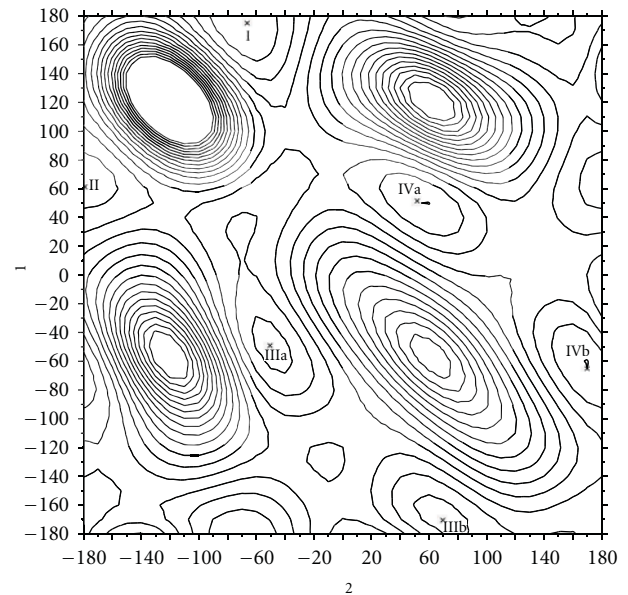


FIGURE 1: HF/STO-3G PES of **1**. $\phi_1 = \text{H}1\text{CC}1\text{O}1$ and $\phi_2 = \text{H}1\text{CC}2\text{O}2$. All other internal coordinates are fixed at the B3PW91/6-31G* optimized values of structure I. Contour spacing is 0.5 kcal/mole. The values of ϕ_1, ϕ_2 for structures I, II, IIIa, IIIb, IVa, and IVb after optimization at the B3PW91/6-31G* level are indicated (x).

conformations; (4) the two lowest energy conformations, I and II, possess C_2 symmetry; the two of highest energy, III and IV, possess C_1 symmetry.

To shed light on the results obtained for **1**, we have studied the molecule methyl oxazole, **2**. Its molecular structure is represented on Scheme 2.

Specifically, we have calculated the PES of **2** with respect to rotation of the methyl group at the B3PW91/6-31G* level. Minima are found at 120° intervals. In each stable conformation, one C–H bond of the methyl group is coplanar with the NCO moiety of the oxazole ring; the C–H H is “cis” with respect to the NCO N and “trans” with respect to the NCO O. The barrier to internal rotation is 1.3 kcal/mole; at the top of the barrier, one C–H bond is coplanar with the NCO group, its H being “cis” to O and

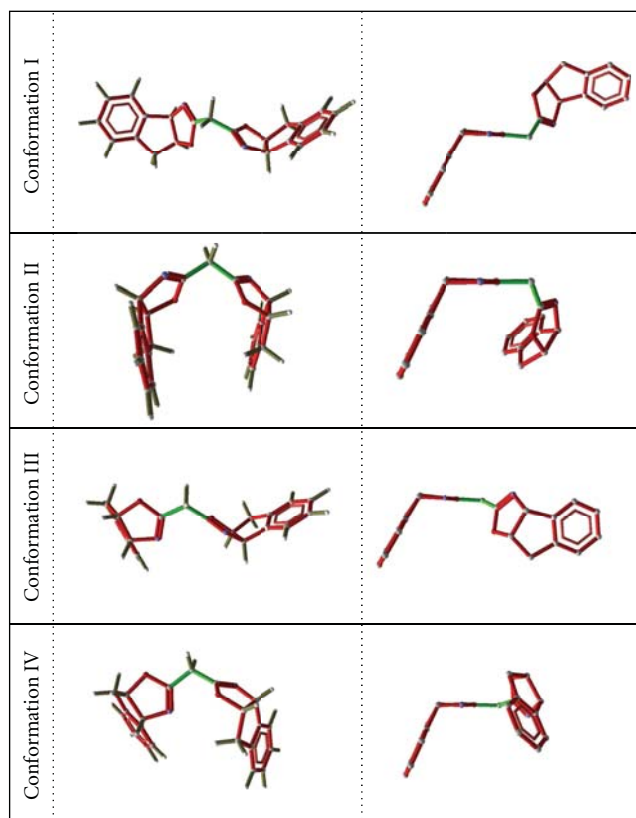
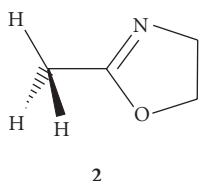


FIGURE 2: The B3PW91/6-31G* structure of **1**. Each one of the four conformations is visualized from two orientations. On the left side is an optimal view (including hydrogens), whereas the right side view gives one moiety versus the plan of the other.



SCHEME 2

“trans” to N. Thus, the alignment of the NCO groups in the most stable conformation I is reasonable.

In structure I, the N1C1O1 and N2C2O2 planes are very nearly coplanar with the CH1 and CH2 bonds, respectively. N1 and N2 and O1 and O2 are symmetrically located with respect to the C1CC2 plane. In structure II, the N1C1O1 and N2C2O2 planes are very nearly coplanar with the CH2 and CH1 bonds, respectively. Again, N1 and N2 and O1 and O2 are symmetrically located with respect to the C1CC2 plane. Thus, structure II is obtained from structure I by a rotation of each NCO group by $\sim 120^\circ$. Qualitatively, the (N1C1O1)CH1H2(N2C2O2) moiety of structure II is obtained by reflection of that of structure I in the C1CC2 plane. In structures III and IV, the orientations of the O1C1N1 and CH1H2 groups are qualitatively the same as in structures I and II, respectively. The O2C2N2 groups, on

the other hand, are oriented differently. In both structures III and IV, the O2C2N2 plane nearly bisects the CH1H2 angle, with N2 nearly eclipsing C1.

The structures of the three rings of the oxazolidine moieties of **1** vary very little with conformation. All are close to planar. The maximum dihedral angle for the five atoms of the oxazole ring is 7.0° in I, 6.6° in II, $8.8^\circ/6.9^\circ$ in III, and $9.3^\circ/8.0^\circ$ in IV (where the rings are inequivalent, the two angles are for rings 1/2). The maximum dihedral angle for the five atoms of the cyclopentane ring is 7.3° in I, 7.3° in II, $9.1^\circ/7.3^\circ$ in III, and $10.0^\circ/8.6^\circ$ in IV. The maximum dihedral angle of the six atoms of the benzene ring is 0.3° in I, 0.3° in II, $0.3^\circ/0.3^\circ$ in III, and $0.6^\circ/0.5^\circ$ in IV.

We have evaluated the structures and relative energies of the conformations of **1** predicted by DFT using vibrational spectroscopy. Calculated vibrational unpolarised absorption and VCD spectra of conformations I, II, III, and IV differ significantly, the variation being dramatically greater for the VCD spectra. As a result, the predicted spectra of **1** are sensitive to the conformational composition. Using populations calculated assuming that the conformational free energy differences are equal to the DFT energy differences, we have synthesized composite spectra for **1** and compared them to the experimental spectra in the mid-IR spectral region. Allowing for the limitations of B3PW91 and B3LYP harmonic calculations at the 6-31G* basis set level, the results are in convincing agreement with experiment.

Experimental mid-IR absorption and VCD spectra of **1**, measured in CHCl_3 and CDCl_3 , are shown in Figure 3. Mid-IR absorption and VCD spectra predicted for I–IV at the B3PW91/6-31G* level are shown in Figures 4, 5, 6, 7, 8, and 9, together with the composite spectra obtained by summing the population-weighted contributions of I–IV and the experimental spectra. Examination of Figures 4–9 leads to the following broad conclusions:

- (1) the predicted spectra of I, II, III, and IV differ; the VCD spectra vary much more dramatically than the absorption spectra;
- (2) the contributions of I to the predicted composite absorption and VCD spectra predominate, due to its greater population;
- (3) the contributions of II, III, and IV are quantitatively significant in certain spectral regions; as a result, the predicted composite spectra differ significantly from the spectra of I alone. The difference is greater for the VCD spectra than for the absorption spectra;
- (4) several modes of II, III, and/or IV are predicted to give rise to absorption and/or VCD resolved from the modes of I;
- (5) the composite absorption and VCD spectra are in good overall agreement with the experimental spectra; the contributions of II, III, and IV are clearly discernible.

In order to compare the predicted and experimental spectra in close detail, we have divided the whole spectrum into many regions. Here, we choose to point the most significant features and changes.

The first noteworthy section is located in Figures 4 and 5 (between 800 cm^{-1} and 1150 cm^{-1}). The absorption “A,” containing several, partially resolved bands, can be assigned predominantly to modes 40–45 of I, modes 40–45 of II, and modes 44 and 45 of III and IV. The agreement of predicted and experimental spectra is poor, and detailed assignment is not straightforward. The VCD “A” is oscillatory, with two + features corresponding to the two absorption maxima and two features in between and to higher frequency of these features, respectively. The predicted VCD exhibits the same qualitative behavior. The lower frequency +, – features originate predominantly in modes 40/41 and 42 of I, respectively. The higher frequency +, – features are dominated by modes 44 and 45 of II respectively. (Note that modes 44 and 45 of I are predicted to give - and + VCD, respectively, opposite in sign to the observed signs of the two higher frequency features.) The absorption “B” can be assigned predominantly to modes 46 of I and 47 of II and III. The VCD “B” is +, in contrast to the predicted VCD, predominantly due to modes 46/47 of I and 47 of II, which are -. The absorption “C” is composite, with a clearly resolved shoulder to lower frequency of the peak. The two features are assigned predominantly to modes 49 and 50 of I. The VCD “C” is +; a shoulder to lower frequency of the peak is barely visible. The predicted VCD is +, originating predominantly in modes 50 of I and II, with a weak + feature at lower frequency originating predominantly in modes 49 of II and III. (Note that both modes 48 and 49 of I are predicted to give weak VCD.) The absorption “D” can be assigned predominantly to modes 51/52 of I and II. The VCD of “D” is -, in agreement with the predicted VCD, which originates predominantly in modes 52 of I and II. The absorption “E” can be assigned to modes 54 of I and II. The VCD “E” is large and +, as is the predicted VCD, which originates predominantly in mode 54 of I. The absorption “F” consists of a very strong central feature, with a shoulder clearly resolved to lower frequency and several shoulders visible to higher frequency. The predicted absorption consists of a strong central feature, attributable predominantly to modes 58–60 of I, mode 58 of II, modes 57/58 of III, and mode 58 of IV; a strong shoulder to lower frequency, originating in modes 57 of I, II, and IV; a weak shoulder to higher frequency originating in modes 63 of I and II. We assign the latter to the highest frequency shoulder observed experimentally. The observed VCD “F” is large and bisignate, as in the predicted VCD, which originates predominantly in modes 58–60 of I for the – band and in mode 63 of I and II for the + band (note that the later mode changes the sign between the two conformation). The absorption “G” can be assigned to modes 64 of I, II, and IV. The VCD “G” is – and very weak. The predicted VCD is also very weak, but +, originating predominantly in mode 64 of II. The absorption “H” is assignable to modes 65/66 of I, II, III, and IV. The VCD “H” is +, consistent with the predicted VCD, which originates predominantly in modes 65 of I, 66 of II, 66 of III, and 65/66 of IV.

The second notable section is located in Figures 6 and 7 (between 1100 cm^{-1} and 1550 cm^{-1}). The absorption

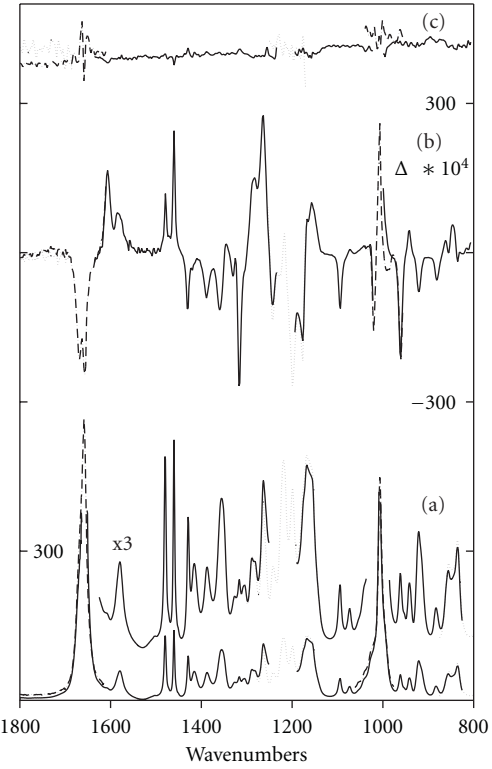


FIGURE 3: Mid-IR ($800\text{--}1800\text{ cm}^{-1}$) absorption and VCD spectra of 1. —: IR: (825–1005, 1008–1190, 1250–1652, 1663–1800 cm^{-1}), VCD: (806–1000, 1022–1194, 1234–1636 cm^{-1}), 0.50M in CHCl_3 ; dots line: IR: (800–875, 1131–1300 cm^{-1}), VCD: 1171–1254 cm^{-1} , 0.40M in CDCl_3 ; dashed line: IR: (976–1061, 1615–1800 cm^{-1}), VCD: (957–1040, 1610–1800 cm^{-1}), 0.20M in CH_2Cl_2 . (a) Absorption spectrum, (b) VCD “half-difference” spectrum of (+)-1, (c) VCD “half-sum” spectrum.

“J” contains several partially resolved bands. The predicted absorption is also complex, originating in modes 67–73 of I and II and 67–74 of III and IV. The VCD “J” is bisignate. The VCD can be assigned predominantly to modes 67–71 of I; the + VCD originates principally in modes 73 of I, modes 72/73 of II, and modes 73 of III and IV. The absorption “K” originates predominantly in modes 74/75 of I and II. The VCD “K” is large and +. The predicted VCD is +, originating predominantly in modes 74/75 of I and 74 of II, but relatively weak. The absorption “L” can be assigned predominantly to modes 78 of I and II. The VCD “L” is -, consistent with the predicted VCD, which originates predominantly in modes 78 of I and II. (Note that the VCD of II is opposite in sign to that of I and the predicted VCD involves a large cancellation of oppositely signed contributions.) The weak absorption “M” is attributed predominantly to mode 79 of I. The VCD “M” is strong and +, consistent with the predicted VCD which originates predominantly in mode 79 of I. The absorption “N” consists of a peak together with a shoulder to lower frequency. The former can be assigned to mode 80 of I; the latter can be assigned to modes 80 of II, III, and IV. The VCD “N” is – and strong; VCD corresponding to the low frequency shoulder is not clearly observed. The predicted VCD of modes 80 of I–IV is uniformly –, that of I

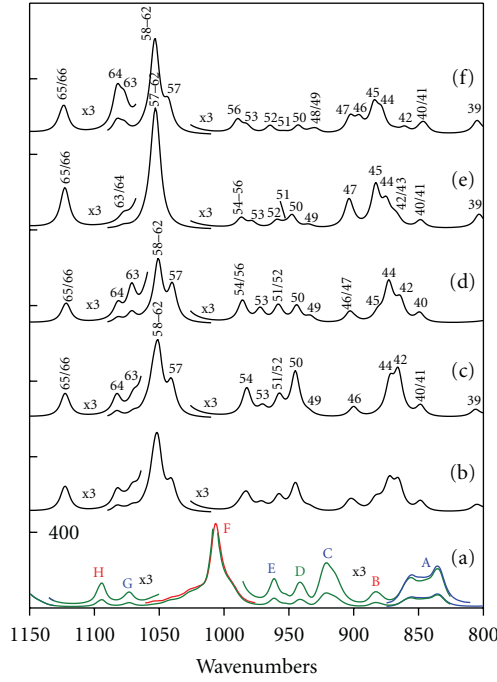


FIGURE 4: Mid-IR ($800\text{--}1150\text{ cm}^{-1}$) absorption spectrum of 1. (a) Experimental spectrum (from Figure 3); (b) composite calculated spectrum; (c) B3PW91/6-31G* spectrum of I; (d) B3PW91/6-31G* spectrum of II; (e) B3PW91/6-31G* spectrum of III; (f) B3PW91/6-31G* spectrum of IV. The composite spectrum is obtained using the percentage populations of I–IV in Table 2. Fundamentals are numbered. Band shapes are Lorentzian ($\gamma = 4.0\text{ cm}^{-1}$).

being strong, in agreement with experiment. The absorption “P” comprises two, partially resolved bands. The lower frequency component is assignable predominantly to mode 83 of II, while the higher frequency component is assignable predominantly to modes 85 of I and II. The VCD “P” is unresolved and $-$. The absorption “Q” comprises a triplet of bands, assignable predominantly to mode 86 of I, modes 87/88 of I and II, and modes 88 of III and IV, respectively. The VCD “Q” is strong and $+$ in the central feature and weaker and $+$ in the two outer features. The strong VCD originates predominantly in mode 87 of I. The lower frequency feature is assignable to mode 86 of I and mode 87 of IV. The higher frequency feature is assignable to mode 88 of II. The absorption “R” is broad and attributable to modes 89–92 of I and II, together with mode 90 of IV. The predicted VCD is bisignate: the lower frequency component originates predominantly in modes 89 of I and 90 of II; the higher frequency $+$ component originates predominantly in modes 91/92 of I and II (note that the contributions of I and II are of opposite sign). The predicted VCD is in qualitative agreement with the bisignate VCD observed experimentally. The absorption “S” originates exclusively in modes 92 of III and IV; no absorption of I or II is predicted in this region. The VCD of both modes are predicted to be $+$, in agreement with the observed VCD. The absorption “T” is assignable to modes 93 of I, II, III, and IV. The VCD “T” is weak and $+$. The predicted VCD is also $+$ and weak,

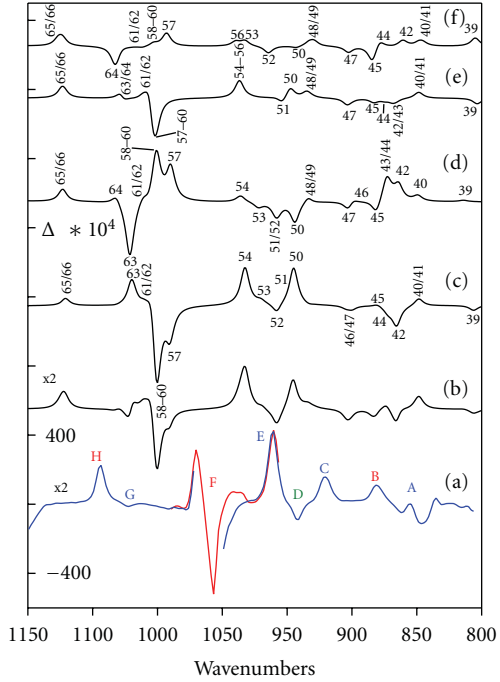


FIGURE 5: Mid-IR ($800\text{--}1150\text{ cm}^{-1}$) VCD spectrum of 1. (a) Experimental spectrum (from Figure 3); (b) composite calculated spectrum; (c) B3PW91/6-31G* spectrum of I; (d) B3PW91/6-31G* spectrum of II; (e) B3PW91/6-31G* spectrum of III; (f) B3PW91/6-31G* spectrum of IV. The composite spectrum is obtained using the percentage populations of I–IV in Table 2. Fundamentals are numbered. Band shapes are Lorentzian ($\gamma = 4.0\text{ cm}^{-1}$).

originating predominantly in I, II, and III. The absorption “X” is assignable to modes 94/95 of I, II, III, and IV. The VCD “X” is $+$. The predicted VCD is also $+$, originating in all four conformations. The absorption “Y” is assignable to modes 96/97 of I, II, III and IV. The VCD “Y” is $-$. The predicted VCD is also $-$, originating in all four conformations. The absorption “Z” is assignable to modes 98/99 of I, II, III and IV. The VCD “Z” is $-$. The predicted VCD is also $-$, originating in all four conformations.

Above 1500 cm^{-1} (Figures 8 and 9), three absorption features are observed: “ α ”, “ β ”, and “ γ ”, the latter being very intense. The absorptions “ α ” and “ β ” are assignable predominantly to modes 100/101 and 102/103 of I, respectively. The absorption “ γ ” exhibits a shoulder to higher frequency of the peak. The peak absorption is assigned to modes 104 of I and II. The shoulder is assigned to modes 104/105 of III and IV. The VCD “ α ” and “ β ” are $-$ in agreement with the predicted VCD which is attributable to modes 100/101 and 102/103 of I, II, III, and IV, respectively. The VCD “ γ ” comprises two $+$ features. The lower frequency component is assignable to modes 104 of I and II; the higher frequency component is attributable predominantly to mode 105 of I.

Ultimately, the calculated composite absorption and VCD spectra thus yield a satisfactory assignment of the experimental absorption and VCD spectra. Unambiguous evidence of significant populations of II, III, and IV is provided by the detailed comparison of predicted and

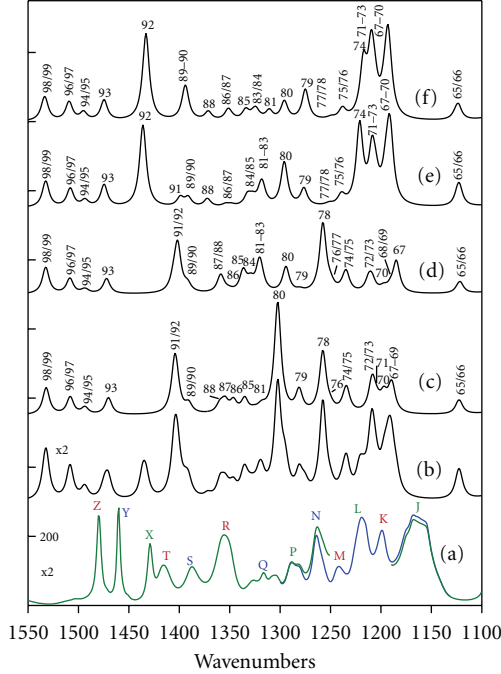


FIGURE 6: Mid-IR ($1100\text{--}1550\text{ cm}^{-1}$) absorption spectrum of **1**. (a) Experimental spectrum (from Figure 3); (b) composite calculated spectrum; (c) B3PW91/6-31G* spectrum of I; (d) B3PW91/6-31G* spectrum of II; (e) B3PW91/6-31G* spectrum of III; (f) B3PW91/6-31G* spectrum of IV. The composite spectrum is obtained using the percentage populations of I–IV in Table 2. Fundamentals are numbered. Band shapes are Lorentzian ($\gamma = 4.0\text{ cm}^{-1}$).

experimental spectra. In particular, the agreement is better than when the experimental spectra are compared to the calculated spectra for conformation I alone. That is, without including the contributions of conformations II, III, and IV, the experimental spectra are much less satisfactorily assigned. On one hand, more than one region clearly demand the presence of II, III, and IV to be convincingly assigned, in particular, the absorption and VCD of the former originate in III, and IV, whose modes 92 lie within broad windows in the spectra of I and II. The absorption and VCD of the latter are not fully resolved. However, in absorption the contributions of III and IV are clearly evident in the high frequency shoulder to the main absorption. In VCD the relative intensities of the two features require the contribution of II. On the other hand, in order to evaluate the alteration in conformational contributions between the two classifications (electronic energies and the free energies cases), an accurate spectral analysis is necessary. We should then deconvolute the experimental spectra taking into account all the predicted bands with an accurate weight. This is the only way how to deduce the true population ratios of the four conformations. However, according to the present analysis, the conformation II contribution appears to be more significant than that of conformation IV.

The analysis of the mid-IR absorption and VCD spectra thus strongly supports the reliability of the predictions of our DFT/6-31G* calculations. In particular, predicted

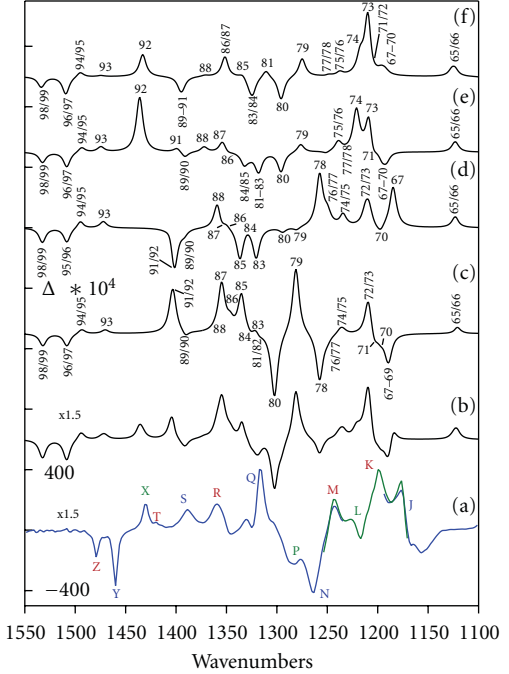


FIGURE 7: Mid-IR ($1100\text{--}1550\text{ cm}^{-1}$) VCD spectrum of **1**. (a) Experimental spectrum (from Figure 3); (b) composite calculated spectrum; (c) B3PW91/6-31G* spectrum of I; (d) B3PW91/6-31G* spectrum of II; (e) B3PW91/6-31G* spectrum of III; (f) B3PW91/6-31G* spectrum of IV. The composite spectrum is obtained using the percentage populations of I–IV in Table 2. Fundamentals are numbered. Band shapes are Lorentzian ($\gamma = 4.0\text{ cm}^{-1}$).

energy ordering and differences of conformations I–IV are clearly qualitatively correct. Our analysis does not lead to quantitative values for the free energy differences of the four conformations. We have shown previously (in the case of 3-methylcyclohexanone [37]) that quantitative deconvolution of the experimental spectra into the component contributions of individual conformations provides free energy differences. However, the greater complexity of a similar analysis of the spectra of **1**, possessing more conformations and a greater vibrational density of states, has led us to defer such analysis to a future date.

5. Conclusion

DFT structures and relative energies of all possible conformations using vibrational spectroscopy of **1** (IndaBOX) have been evaluated. Vibrational spectra provide a basis for the conformational analysis. For chiral molecules both IR and VCD spectra can be measured. Calculated IR and VCD spectra of stable conformations are found significantly different. The variation is noticeably greater in the VCD spectra. The limitations to the B3PW91 harmonic calculations at the 6-31G* basis set level provide a result in credible agreement with the experiment. In particular, without including the contributions of at least first less stable conformations, experimental spectra are much less satisfactorily assigned. As a result, the collective use of IR and VCD spectra is

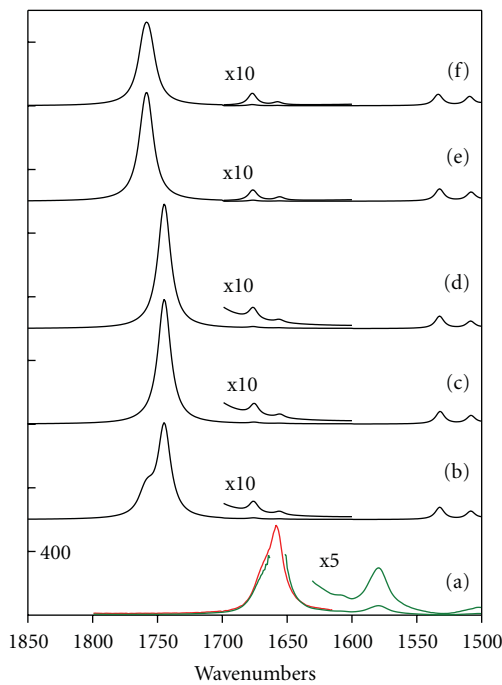


FIGURE 8: Mid-IR ($1500\text{--}1850\text{ cm}^{-1}$) absorption spectrum of **1**. (a) Experimental spectrum (from Figure 3); (b) composite calculated spectrum; (c) B3PW91/6-31G* spectrum of I; (d) B3PW91/6-31G* spectrum of II; (e) B3PW91/6-31G* spectrum of III; (f) B3PW91/6-31G* spectrum of IV. The composite spectrum is obtained using the percentage populations of I–IV in Table 2. Fundamentals are numbered. Band shapes are Lorentzian ($\gamma = 4.0\text{ cm}^{-1}$).

substantially more powerful than the use of IR spectra alone. Elsewhere the inclusion of other theoretical treatments such as anharmonicity or solvent effect seems unnecessary for the present investigation.

This kind of methodology provides a practical demonstration of VCD profit for full structural analysis. The gain of this direct and rapid tool resides in not requiring chiral reference molecules, single crystal growing approaches, or heavy atom association involved in other techniques. Recently similar studies are in agreement with this conclusion [54–57]. The growing use of this technique is also perceived elementary in case of the biological building blocks in order to elucidate proteins conformations and chirality [58]. At the present time, the expanding implementation in other program packages (CADPAC, DALTON, etc.) and the technical transformation of many spectrometers (JASCO, BRUKER, etc.) will certainly empower the VCD utilization.

The development of this strategy relies on the evolution of three related domain. First, the instrumental aspect requires the use of sophisticated materials and electronics to eliminate any external artifact particularly when using a single enantiomer in small quantities. Second, to circumvent the limitations of molecular size, the theoretical methods need the implementation of more procedures. Third, the computational technology should optimize more efficiently the use of hardware resources. These hints will provide an attractive alternative to other techniques for both absolute

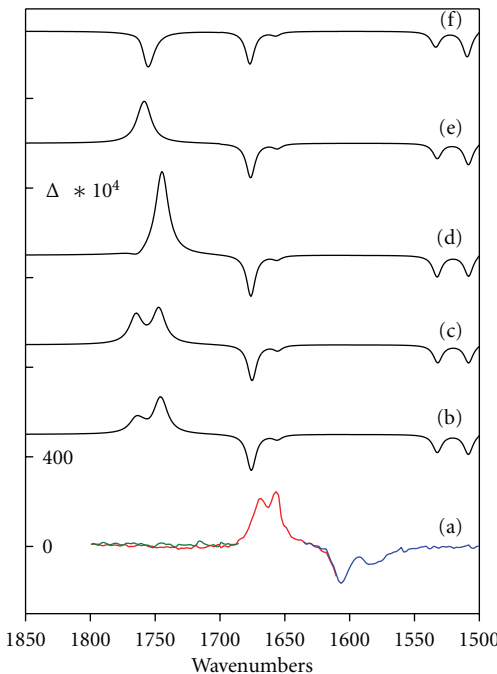


FIGURE 9: Mid-IR ($1500\text{--}1850\text{ cm}^{-1}$) VCD spectrum of **1**. (a) Experimental spectrum (from Figure 3); (b) composite calculated spectrum; (c) B3PW91/6-31G* spectrum of I; (d) B3PW91/6-31G* spectrum of II; (e) B3PW91/6-31G* spectrum of III; (f) B3PW91/6-31G* spectrum of IV. The composite spectrum is obtained using the percentage populations of I–IV in Table 2. Fundamentals are numbered. Band shapes are Lorentzian ($\gamma = 4.0\text{ cm}^{-1}$).

configuration determination and conformational analysis. Perhaps this will persuade more companies, notably pharmaceutical, to take advantage from this promising tool.

Acknowledgments

The authors are grateful to F. J. Devlin (Department of Chemistry, University of Southern California, Los Angeles) for discussions and assistance endowed to this work. This paper is dedicated to 70th anniversary of Professor Philip J. Stephens (specially for his contribution to the VCD spectroscopy).

References

- [1] J. W. Faller and A. Lavoie, "Highly enantioselective Diels-Alder catalysis with a chiral ruthenium bisoxazoline complex," *Journal of Organometallic Chemistry*, vol. 630, no. 1, pp. 17–22, 2001.
- [2] D. Rechavi, B. Albela, L. Bonneviot, and M. Lemaire, "Understanding the enantioselectivity of a heterogeneous catalyst: the influence of ligand loading and of silica passivation," *Tetrahedron*, vol. 61, no. 29, pp. 6976–6981, 2005.
- [3] S. Tanaka, M. Tada, and Y. Iwasawa, "Enantioselectivity promotion by achiral surface functionalization on SiO₂-supported Cu-bis(oxazoline) catalysts for asymmetric Diels-Alder reactions," *Journal of Catalysis*, vol. 245, no. 1, pp. 173–183, 2007.

- [4] J.-M. Lee, J. Kim, Y. Shin et al., "Heterogeneous asymmetric Henry reaction using a chiral bis(oxazoline)-copper complex immobilized on magnetically separable mesocellular mesoporous silica support," *Tetrahedron Asymmetry*, vol. 21, no. 3, pp. 285–291, 2010.
- [5] E. Framery, B. Andrioletti, and M. Lemaire, "Recent progress in homogeneous supported asymmetric catalysis: example of the BINAP and the BOX ligands," *Tetrahedron Asymmetry*, vol. 21, no. 9-10, pp. 1110–1124, 2010.
- [6] A. S. Abu-Surrah, M. Kettunen, K. Lappalainen, U. Piironen, M. Klinga, and M. Leskelä, "Synthesis of new chiral diimine palladium(II) and nickel(II) complexes bearing oxazoline- and myrtanyl-based nitrogen ligands. Crystal structure of the C₂-symmetric complex [(1R,2S)-inda-boxPdCl₂]," *Polyhedron*, vol. 21, no. 1, pp. 27–31, 2002.
- [7] K. Matsumoto, K. Jitsukawa, and H. Masuda, "Preparation of new bis(oxazoline) ligand bearing non-covalent interaction sites and an application in the highly asymmetric Diels-Alder reaction," *Tetrahedron Letters*, vol. 46, no. 34, pp. 5687–5690, 2005.
- [8] D. Frain, F. Kirby, P. McArdle, and P. O'Leary, "Preparation, structure and catalytic activity of copper(II) complexes of novel 4,4'-BOX ligands," *Tetrahedron Letters*, vol. 51, no. 31, pp. 4103–4106, 2010.
- [9] S. Telalović and U. Hanefeld, "Noncovalent immobilization of chiral cyclopropanation catalysts on mesoporous TUD-1: comparison of liquid-phase and gas-phase ion-exchange," *Applied Catalysis A*, vol. 372, no. 2, pp. 217–223, 2010.
- [10] N. Merle, K. W. Törnroos, V. R. Jensen, and E. Le Roux, "Influence of multidentate N-donor ligands on highly electrophilic zinc initiator for the ring-opening polymerization of epoxides," *Journal of Organometallic Chemistry*, vol. 696, no. 8, pp. 1691–1697, 2011.
- [11] P. Fulde, in *Electron Correlations in Molecules and Solids*, p. 39, Springer, Berlin, Germany, 1995.
- [12] R. M. Dreizler and E. K. U. Gross, *Density Functional Theory*, Springer, Berlin, Germany, 1990.
- [13] E. Charney, *The Molecular Basis of Optical Activity: Optical Rotatory Dispersion and Circular Dichroism*, Wiley, New York, NY, USA, 1979.
- [14] L. D. Barron, *Molecular Light Scattering and Optical Activity*, Cambridge University Press, Cambridge, UK, 1982.
- [15] T. M. Lwory, *Optical Rotatory Power*, Longmans, Green and Co, London, UK, 1935.
- [16] P. J. Stephens, "The theory of vibrational circular dichroism," in *Encyclopedia of Spectroscopy and Spectrometry*, p. 2415, Academic Press, London, UK, 1999.
- [17] R. W. Kawiecki, F. Devlin, P. J. Stephens, R. D. Amos, and N. C. Handy, "Vibrational circular dichroism of propylene oxide," *Chemical Physics Letters*, vol. 145, no. 5, pp. 411–417, 1988.
- [18] L. Rosenfeld, "Quantenmechanische theorie der natürlichen optischen aktivität von flüssigkeiten und gasen," *Zeitschrift für Physik*, vol. 52, no. 3-4, pp. 161–174, 1929.
- [19] P. J. Stephens, "Gauge dependence of vibrational magnetic dipole transition moments and rotational strengths," *Journal of Physical Chemistry*, vol. 91, no. 7, pp. 1712–1715, 1987.
- [20] M. A. Lowe, G. A. Segal, and P. J. Stephens, "The theory of vibrational circular dichroism: trans-1,2-dideuteriocyclopropane," *Journal of the American Chemical Society*, vol. 108, no. 2, pp. 248–256, 1986.
- [21] P. J. Stephens, "Theory of vibrational circular dichroism," *Journal of Physical Chemistry*, vol. 89, no. 5, pp. 748–752, 1985.
- [22] L. A. Nafie and T. B. Freedman, "Vibronic coupling theory of infrared vibrational transitions," *The Journal of Chemical Physics*, vol. 78, no. 12, pp. 7108–7116, 1982.
- [23] R. G. Parr and W. Yang, *Density-Functional Theory of Atoms and Molecules*, Oxford University Press, New York, NY, USA, 1989.
- [24] A. D. Becke, "Density-functional thermochemistry. III. The role of exact exchange," *The Journal of Chemical Physics*, vol. 98, no. 7, pp. 5648–5652, 1993.
- [25] J. P. Perdew and W. Yue, "Accurate and simple density functional for the electronic exchange energy: generalized gradient approximation," *Physical Review B*, vol. 33, no. 12, pp. 8800–8802, 1986.
- [26] W. J. Hehre, L. Radom, P. V. R. Schleyer, and J. A. Pople, *Ab Initio Molecular Orbital Theory*, John Wiley & Sons, New York, NY, USA, 1986.
- [27] GAUSSIAN, M. J. Frisch, Gaussian, Inc., Pittsburgh, Pa, USA, 1998.
- [28] F. J. Devlin, P. J. Stephens, J. R. Cheeseman, and M. J. Frisch, "Prediction of vibrational circular dichroism spectra using density functional theory: camphor and fenchone," *Journal of the American Chemical Society*, vol. 118, no. 26, pp. 6327–6328, 1996.
- [29] F. J. Devlin, P. J. Stephens, J. R. Cheeseman, and M. J. Frisch, "Ab initio prediction of vibrational absorption and circular dichroism spectra of chiral natural products using density functional theory: camphor and fenchone," *Journal of Physical Chemistry A*, vol. 101, no. 35, pp. 6322–6333, 1997.
- [30] F. J. Devlin, P. J. Stephens, J. R. Cheeseman, and M. J. Frisch, "Ab initio prediction of vibrational absorption and circular dichroism spectra of chiral natural products using density functional theory: α-Pinene," *Journal of Physical Chemistry A*, vol. 101, no. 51, pp. 9912–9924, 1997.
- [31] C. S. Ashvar, P. J. Stephens, T. Eggimann, and H. Wieser, "Vibrational circular dichroism spectroscopy of chiral pheromones: frontal (1,5-dimethyl-6,8-dioxabicyclo[3.2.1]octane)," *Tetrahedron Asymmetry*, vol. 9, no. 7, pp. 1107–1110, 1998.
- [32] C. S. Ashvar, F. J. Devlin, P. J. Stephens, K. L. Bak, T. Eggimann, and H. Wieser, "Vibrational absorption and circular dichroism of mono- and dimethyl derivatives of 6,8-dioxabicyclo[3.2.1]octane," *Journal of Physical Chemistry A*, vol. 102, no. 34, pp. 6842–6857, 1998.
- [33] C. S. Ashvar, F. J. Devlin, and P. J. Stephens, "Molecular structure in solution: an ab initio vibrational spectroscopy study of phenyloxirane," *Journal of the American Chemical Society*, vol. 121, no. 12, pp. 2836–2849, 1999.
- [34] A. Aamouche, F. J. Devlin, and P. J. Stephens, "Determination of absolute configuration using circular dichroism: troger's Base revisited using vibrational circular dichroism," *Chemical Communications*, no. 4, pp. 361–362, 1999.
- [35] A. Aamouche, F. J. Devlin, and P. J. Stephens, "Structure, vibrational absorption and circular dichroism spectra, and absolute configuration of Tröger's base," *Journal of the American Chemical Society*, vol. 122, no. 10, pp. 2346–2354, 2000.
- [36] F. J. Devlin and P. J. Stephens, "Ab initio density functional theory study of the structure and vibrational spectra of cyclohexanone and its isotopomers," *Journal of Physical Chemistry A*, vol. 103, no. 4, pp. 527–538, 1999.
- [37] F. J. Devlin and P. J. Stephens, "Conformational analysis using ab initio vibrational spectroscopy: 3- Methylcyclohexanone," *Journal of the American Chemical Society*, vol. 121, no. 32, pp. 7413–7414, 1999.

- [38] P. J. Stephens and F. J. Devlin, "Determination of the structure of chiral molecules using ab initio vibrational circular dichroism spectroscopy," *Chirality*, vol. 12, no. 4, pp. 172–179, 2000.
- [39] A. Aamouche, F. J. Devlin, and P. J. Stephens, "Conformations of chiral molecules in solution: ab initio vibrational absorption and circular dichroism studies of 4,4a,5,6,7,8-hexahydro-4a-methyl-2(3H)-naphthalenone and 3,4,8,8a-tetrahydro-8a-methyl-1,6(2H,7H)-naphthalenedione," *Journal of the American Chemical Society*, vol. 122, no. 30, pp. 7358–7367, 2000.
- [40] A. Aamouche, F. J. Devlin, P. J. Stephens, J. Drabowicz, B. Bujnicki, and M. Mikołajczyk, "Vibrational circular dichroism and absolute configuration of chiral sulfoxides: tert-butyl methyl sulfoxide," *Chemistry European Journal*, vol. 6, no. 24, pp. 4479–4486, 2000.
- [41] P. J. Stephens, A. Aamouche, F. J. Devlin, S. Superchi, M. I. Donnoli, and C. Rosini, "Determination of absolute configuration using vibrational circular dichroism spectroscopy: the chiral sulfoxide 1-(2-methylnaphthyl) methyl sulfoxide," *Journal of Organic Chemistry*, vol. 66, no. 11, pp. 3671–3677, 2001.
- [42] F. J. Devlin, P. J. Stephens, P. Scafato, S. Superchi, and C. Rosini, "Determination of absolute configuration using vibrational circular dichroism spectroscopy: the chiral sulfoxide 1-thiocroman S-oxide," *Tetrahedron Asymmetry*, vol. 12, no. 11, pp. 1551–1558, 2001.
- [43] P. J. Stephens, F. J. Devlin, and A. Aamouche, "Determination of the structures of chiral molecules using Vibrational Circular Dichroism spectroscopy," in *Chirality: Physical Chemistry*, J. M. Hicks, Ed., vol. 810 of *ACS Symposium Series*, chapter 2, pp. 18–33, 2002.
- [44] P. J. Stephens, F. J. Devlin, and J.-J. Pan, "The determination of the absolute configurations of chiral molecules using Vibrational Circular Dichroism (VCD) spectroscopy," *Chirality*, vol. 20, no. 5, pp. 643–663, 2008.
- [45] Company internal report, Sanofi-Aventis, Toulouse, France, 1999.
- [46] E. Da Plama Carreiro, S. Chercheja, A. J. Burke, J. P.P. Ramalho, and A. I. Rodrigues, "Isbut-box: a new chiral C2 symmetric bis-oxazoline for catalytic enantioselective synthesis," *Journal of Molecular Catalysis A*, vol. 236, no. 1-2, pp. 38–45, 2005.
- [47] R. P. Singh, "Spectroscopic studies on complexes of magnesium (II) with C2-chiral bis-oxazolines," *Spectrochimica Acta Part A*, vol. 53, no. 11, pp. 1713–1717, 1997.
- [48] M. P. Sibi, G. Petrovic, and J. Zimmerman, "Enantioselective radical addition/trapping reactions with α,β -disubstituted unsaturated imides. Synthesis of anti-propionate aldols," *Journal of the American Chemical Society*, vol. 127, no. 8, pp. 2390–2391, 2005.
- [49] G. Desimoni, G. Faita, and K. A. Jørgensen, "C2-symmetric chiral bis(oxazoline) ligands in asymmetric catalysis," *Chemical Reviews*, vol. 106, no. 9, pp. 3561–3651, 2006.
- [50] I. Gallou and C. H. Senanayake, "cis-1-amino-2-indanol in drug design and applications to asymmetric processes," *Chemical Reviews*, vol. 106, no. 7, pp. 2843–2874, 2006.
- [51] T. Tsubogo, S. Saito, K. Seki, Y. Yamashita, and S. Kobayashi, "Development of catalytic asymmetric 1,4-addition and [3 + 2] cycloaddition reactions using chiral calcium complexes," *Journal of the American Chemical Society*, vol. 130, no. 40, pp. 13321–13332, 2008.
- [52] K. Lang, J. Park, and S. Hong, "Development of bifunctional aza-bis(oxazoline) copper catalysts for enantioselective Henry reaction," *Journal of Organic Chemistry*, vol. 75, no. 19, pp. 6424–6435, 2010.
- [53] A. K. Ghosh, "Capturing the essence of organic synthesis: from bioactive natural products to designed molecules in today's medicine," *Journal of Organic Chemistry*, vol. 75, no. 23, pp. 7967–7989, 2010.
- [54] T. Bürgi, A. Vargas, and A. Baiker, "VCD spectroscopy of chiral cinchona modifiers used in heterogeneous enantioselective hydrogenation: conformation and binding of non-chiral acids," *Journal of the Chemical Society, Perkin Transactions*, vol. 2, no. 9, pp. 1596–1601, 2002.
- [55] J. Vachon, S. Harthong, B. Dubessy et al., "The absolute configuration of an inherently chiral phosphonatocavand and its use toward the enantioselective recognition of L-adrenaline," *Tetrahedron Asymmetry*, vol. 21, no. 11-12, pp. 1534–1541, 2010.
- [56] H. Izumi, S. Futamura, L. A. Nafie, and R. K. Dukor, "Determination of molecular stereochemistry using vibrational circular dichroism spectroscopy: Absolute configuration and solution conformation of 5-formyl-cis,cis-1,3,5-trimethyl-3-hydroxymethylcyclohexane-1-carboxylic acid lactone," *Chemical Record*, vol. 3, no. 2, pp. 112–119, 2003.
- [57] F. J. Devlin, P. J. Stephens, and P. Besse, "Are the absolute configurations of 2-(1-hydroxyethyl)-chromen-4-one and its 6-bromo derivative determined by X-ray crystallography correct? A vibrational circular dichroism study of their acetate derivatives," *Tetrahedron Asymmetry*, vol. 16, no. 8, pp. 1557–1566, 2005.
- [58] T. A. Keiderling, "Protein and peptide secondary structure and conformational determination with vibrational circular dichroism," *Current Opinion in Chemical Biology*, vol. 6, no. 5, pp. 682–688, 2002.

Research Article

Polymer Characterization by Combined Chromatography-Infrared Spectroscopy

James L. Dwyer and Ming Zhou

Spectra Analysis Instruments, Inc., 257 Simarano Drive, Marlborough, MA 01752-3070, USA

Correspondence should be addressed to James L. Dwyer, dwyerpadre@gmail.com

Received 3 May 2011; Revised 25 July 2011; Accepted 21 August 2011

Academic Editor: Ahmed Aamouche

Copyright © 2011 J. L. Dwyer and M. Zhou. This is an open access article distributed under the Creative Commons Attribution License, which permits unrestricted use, distribution, and reproduction in any medium, provided the original work is properly cited.

Infrared spectroscopy is widely used in the analysis and characterization of polymers. Polymer products are not a singular species, but rather, they are a population of polymer molecules varying in composition and configuration plus other added components. This paper describes instrumentation that provides the benefit or resolving polymer populations into discrete identifiable entities, by combining chromatographic separation with continuous spectra acquisition. The technology also provides a way to determine the mass distribution of discrete components across the chromatographic distribution of a sample. Various examples of application of this technology to polymer products are described. Examples include additives analysis, resolution of polymer blends, composition characterization of copolymers, analysis of degradation byproducts, and techniques of analysis of reactive polymer systems.

1. Introduction

“The primary motivation for determining the structure of a polymer chain is to relate the structure to the performance properties of the polymer in end use. If a polymer chain is completely characterized and the structural basis of its properties is known, the polymerization can be optimized and controlled to produce the best possible properties from the chemical system” [1].

This paper addresses hyphenated chromatography-IR spectrometry instrumentation and the data processing and presentation techniques that can reveal the compositional and molecular structural properties of polymer materials.

In analysis of polymers, no single technique can provide as much information as can Fourier transform infrared spectrometry (FTIR). Many commercial polymer products are not simply a single homopolymer, but rather are multicomponent systems. To obtain maximum information regarding the product, one must utilize some fractionation process prior to spectroscopy.

Polymer products are quite complex. They may consist of mixtures of discrete components. The polymerization process typically yields variations in structure and composition as polymerization proceeds. These variations dictate the physical properties (strength, flexibility, melting point, and glass transition temperatures, to name a few) in the resulting product. In some cases, it is desirable to have invariant structure and composition throughout the population of polymer chains, while in other cases, such variations are specifically generated by the manipulation of the polymerization process. Characterization of distributed composition and structural properties, therefore, is essential to physical properties optimization and control. This paper offers a number of examples demonstrating the utility of this technology.

2. Hyphenated Chromatography-FTIR Spectrometry: Technology and Instrumentation Description

Note. The use of the word “peak” refers to a chromatogram. “Band” is used in describing infrared spectral bands.

A limitation of classical infrared spectroscopy is the inability to characterize or identify components in a mixture. Chromatography is a powerful tool for resolving/separating solutes, but provides no molecular identification of solute components. Liquid Chromatography-FTIR (LC-FTIR) addresses this limitation by chromatographic separation of mixed solutes coupled to a spectrometer which processes the eluting resolved constituents and acquires their discrete spectra. This publication illustrates the use of hyphenated LC-FTIR to provide graphical and numeric information regarding multicomponent samples.

A hot-melt adhesive was analyzed by gel permeation chromatography-FTIR (GPC-FTIR). A sample was injected onto a suitable chromatographic column, and the column eluant passed to a continuous sample collecting module containing an FTIR spectrophotometer. The sample chromatogram is effectively “painted” onto an IR transparent medium as a continuous stripe of solutes eluate. Sequential spectra collected along this stripe are the basis of a time-arrayed data set of sample composition as a function of elution time.

Figure 1 shows chromatographic and spectral data obtained from a data set. The uppermost graphic is an infrared chromatogram of the deposited sample C-H stretch bands of the sample. Below that are specific elution time spectra of the discrete components. By choosing spectral bands that are unique to each solute, one can see and measure the distribution of the individual solute components across the elution profile, even when those components may not be chromatographically resolved. In one integrated procedure, GPC-FTIR can provide molecular/structural characterization of complex multicomponent samples. This paper presents a number of examples of polymer characterizations, focusing on the data processing techniques to show composition and distribution of various multicomponent polymeric samples.

There have been numerous developments of instrumentation that could provide LC-FTIR capability. Two fundamental approaches have emerged: (1) flow cells and (f2) solvent elimination systems. The flow-cell approach, analogous to ubiquitous LC-UV (liquid flow cell detectors operating in the ultraviolet range) systems, has limited utility when applied to LC-IR. The latter has poor detection limits, due to limited optical path length and to interfering IR bands generated by the LC mobile phase. There is several thousand times as much mobile phase, as there is solute in the flow cell during the elution, and any absorbance by the mobile phase will swamp the sample in spectral regions, where the mobile phase has any IR absorbance. As a result, flow cells can be utilized only for the spectral regions in which the mobile phase exhibits no absorbance. LC-IR flow cell methods have been used for polymers that possess structure that manifests itself in such solvent spectral window regions, but they typically require complex chemometric statistical methods to determine composition based on the severely limited spectral regions available. Short-chain branching in polyolefins is measured via LC-FTIR using flow cell methods. Recently, the structural characterization of polycarbonates was reported, utilizing 2-dimensional chromatography, flow

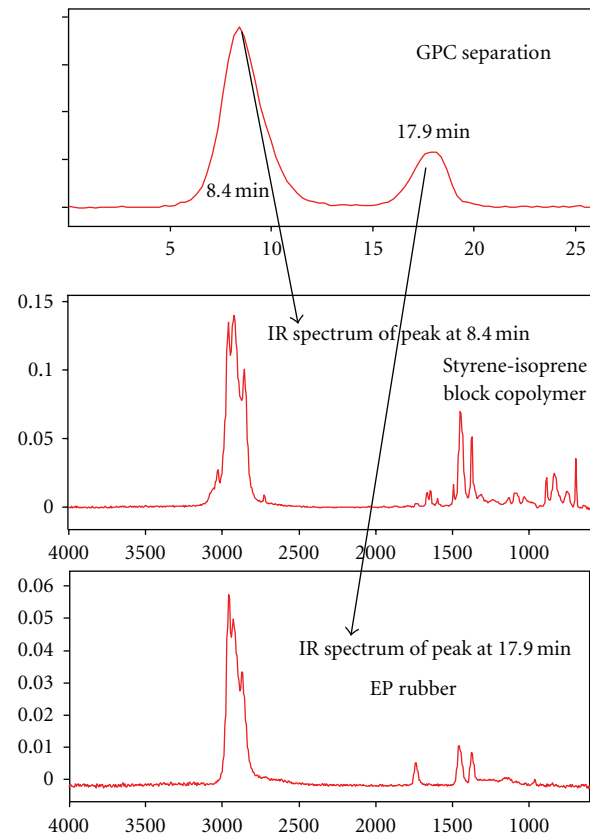


FIGURE 1: Hot-melt adhesive components identification.

cells, and multivariate statistical analysis of the raw data mass [2] (an extremely time-consuming, complex methodology).

Most of the instrumentation development has centered on solvent elimination processes. Some solvent elimination devices made use of microbore chromatography columns which would deposit eluant droplets into wells on a moving plate, which could, after evaporation, yield reflectance or transmission spectra. It was apparent that the use of nozzle systems could be used for evaporative removal of eluant, depositing the solutes as dry solids. Bieman and Gagel developed an instrument that directed column eluant through a pneumatic nebulizer, depositing the nonvolatile solutes onto the surface of a slowly revolving germanium disk as regular track [3, 4]. Griffiths et al. [5] achieved subnanogram sensitivity by use of microbore columns and a glass capillary nebulizer operating in an evacuated chamber. Dekmesian [6] extended applications of solute deposition to mobile-phase solvents of very high boiling point, such as trichloro benzene, a mobile phase regularly used in chromatography of polyolefins. He achieved adequate evaporative capacity by using a combination of ultrasonic nebulization, high vacuum, and high temperatures within the solute deposition chamber.

3. Equipment

Figure 2 shows the principal components of the system (The DiscovIR, Spectra Analysis Instruments, Inc.). At the right is

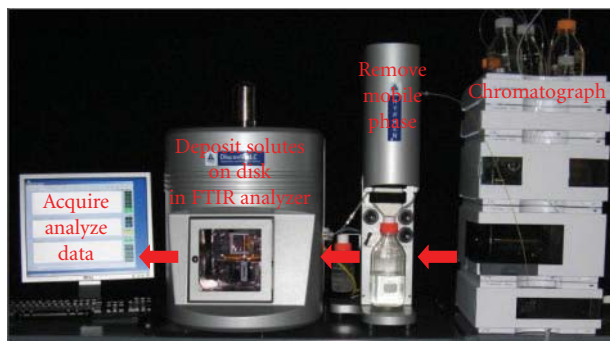


FIGURE 2: DiscovIR HPLC-IR analyzer.

an unmodified HPLC system. Column eluant flows to a unit that nebulizes the solutes and evaporates the liquid mobile phase from the eluate. The nebulized solute particles and solvent vapor then pass to a cooling section that condenses solvent vapor and drains it to a waste bottle. Solutes are propelled by a combination of carrier gas and residual solvent vapor to a nozzle located above the surface of the IR transparent Zn Se disk. A small proportion of the solvent remains with the nebulized solute particles, thereby providing some cohesion to the deposit track. In the high vacuum environment of the deposition chamber, residual solvent flashes off the deposited solute prior to the deposit passing through the FTIR energy beam. The nebulization apparatus is autoregulating and readily accommodates solvent gradient LC protocols. Carrier gas, disk temperature, and chamber vacuum controls serve to optimize the nozzle deposition process, and solvent elimination.

In polymer work gel permeation chromatography (GPC) is most commonly employed, but other chromatography modes, such as reverse-phase, work quite satisfactorily. Unlike HPLC-IR flow cells, this type of interface eliminates all chromatography mobile phase and has none of the spectral interference limitations encountered in use of chromatography-IR flow cells.

With the exception of the IR chromatograms shown in Figure 15, all GPC chromatograms are shown simply as elution time. When a molecular weight (MW) axis is desired, one can apply a scale transform to the data set, or the time axis of the chromatogram. Calibration is done with conventional GPC methods, employing appropriate calibration standards.

An overall schematic is shown in Figure 3. The source infrared energy is focused on the solute track, and the transmitted IR beam passes to the detector of a Fourier transform interferometer. The interferometer generates a spectrum every 0.5 seconds and stores acquired IR spectra as a time-ordered data set. Spectral resolution is a selectable parameter. For the cited examples, a spectral resolution of 8 cm^{-1} was employed. To improve signal/noise ratio and short range smoothing of the solid-phase solute deposit of the single scan spectra, a triangular weighted moving average is optionally used, typically with thirty scans/averaged for each data point.

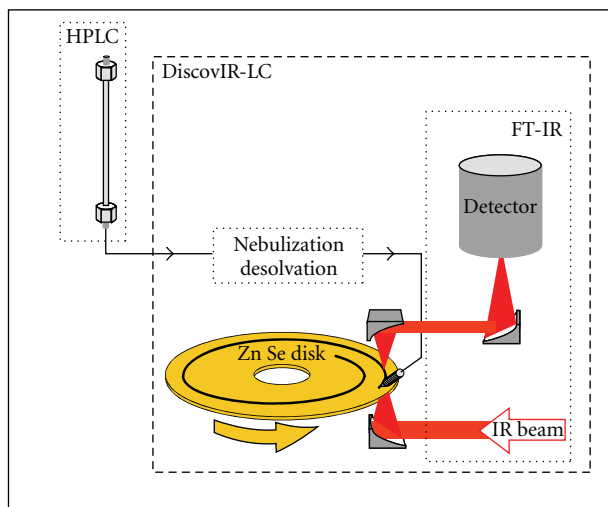


FIGURE 3: Instrument schematic representation.

Instrument automated operation and data analysis is provided by software resident on a dedicated computer. The system has all the functionality associated with FT-IR bench instruments, and including spectral library capabilities.

Equipment utilized for LC-FTIR polymer analysis is shown in Figure 2. A single computer using a Windows operating system and customized Galactic/Grams software serves for both control of sample runs and data analysis. The software encompasses a powerful array of data processing algorithms and display modes for single spectra and multiple file data sets. Most applications utilize molecular weight separation as the chromatography step, but other chromatography modes, such as reverse-phase chromatography and critical condition solvent chromatography, can be readily applied.

4. Application Examples

This presentation focuses on the techniques of utility in extracting compositional information from LC-IR of various polymeric materials. For experimental parameters used in these analyses, please refer to the Section 5 near the end of the presentation. Applications of the following types are illustrated throughout the content of this publication. A useful way to categorize type of applications is shown in Table 1.

The “hyphenation” of liquid chromatography with Infrared spectroscopy provides the opportunity to resolve multicomponent samples and contain spectral information about the individual components. In the case of polymers, one can reveal changing composition/configuration of polymer molecules across the molecular weight distribution. Applications described include polymer characterizations based on composition, configuration, and conformation of polymer molecules.

- (i) “The *composition* of a molecule defines the nature of the atoms and their type of bonding irrespective of their spatial arrangement.

TABLE 1: Polymer industry GPC-FTIR application types.

| | |
|---------------------------------|---|
| (i) Components identification | (i) Copolymers: comonomer distribution |
| (ii) Deformulation | (ii) Aging/environmental changes |
| (iii) Reactive systems analysis | (iii) Lot-to-lot characterization “good versus bad” |

- (ii) The *configuration* of chemical groups characterizes a chemical state of a molecule. Different configurations constitute different chemical individuals and cannot be converted into one another without rupture of chemical bonds.
- (iii) The *conformation* of chemical groups characterizes the geometrical state of a molecule. Different conformations of a molecule can be produced by rotation about single bonds without rupture of chemical bonds. Changes in conformation arise from physical considerations such as temperature, pressure, or stress and strain” [7].

4.1. Deformulation: Analysis of Lubricant Polymeric Additives. The following example is a characterization of polymeric additives present in a heavy duty diesel engine lubricant. Petroleum-based motor oils are manufactured with a complex “additives package” that provide for optimal performance in the harsh operating environment of internal combustion engines. A significant fraction of motor oils consists of synthetic polymers. Functions of these polymers include viscosity-temperature modulation and the dispersion of sludge generated in the environment of an operating engine.

A sample of (unused) motor oil was injected onto a gel permeation chromatography (GPC) column which was coupled to a DiscovIR FTIR system. Figure 4 depicts the data collected from the higher molecular weight components of the oil sample. The X-axis is spectral frequency (wave number). The Y-axis is elution time, and the Z-axis is spectral absorbance. These early eluting components are high molecular weight and are solid-phase when deposited on the zinc selenide (Zn-Se) collection disk. The lubricant itself is liquid hydrocarbon oil, and at 12.2-minute elution time, a valve was actuated to divert column eluate from deposition on the collection disk.

Casual inspection of the deposit spectra indicate that the polymer material is made up of at least two components. The first elution material has an intensity maximum at 9.2 minutes, corresponding to a MW of 600 k Daltons Figure 5.

4.1.1. Identification of the First Elution Peak. Inspection of the spectrum yielded the following observations:

- (i) typical aromatic C–H stretches (3082 cm^{-1} , 3061 cm^{-1} , 3027 cm^{-1}),
- (ii) ring breathing modes (1601 cm^{-1} , 1493 cm^{-1}),
- (iii) aromatic ring out of plane bends (698 cm^{-1} , 756 cm^{-1}),
- (iv) 1735 cm^{-1} carbonyl,

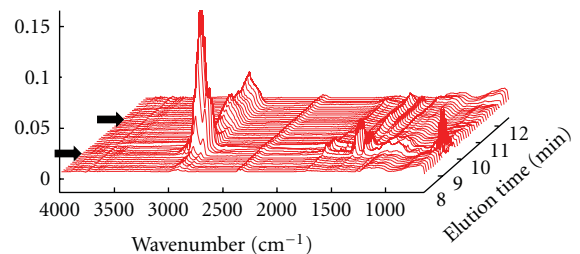


FIGURE 4: Time-ordered spectra from the GPCFTIR analysis of diesel motor oil.

- (v) C–O stretches in the 1200 – 1000 cm^{-1} region,
- (vi) bands associated with conjugated dienes are absent.

4.1.2. Identification of the Second Elution Peak. The spectra of this elution region are those of a styrene-acrylate copolymer. This is consistent with the viscosity index improvers used in engine lubricants.

The broad eluant profile in the 10–12 minute elution timeframe provided the spectrum in Figure 6. Spectra present the same bands across this region; indicating a homogenous chemistry, with a broad variation of molecular weight (30,000–8000 mw). This spectrum is characteristic of the dispersant polyisobutylene succinimide (PIBS). The broad elution profile of this material suggests a heterogeneity of molecular weight in this fraction, but no clear evidence of compositional drift in the comonomers. The ratio of bands {dimethyl (1367 cm^{-1})/imide (1700 cm^{-1})} decreases by only about 10% across the elution time of 10.5–12.2 min.

Note in the above spectra that a 700 cm^{-1} band is present only in the first solute peak. Similarly, a 1220 cm^{-1} band is present only in the second solute peak. The data analysis software that is incorporated with the instrument provides for the generation of infrared chromatograms of selected spectral bands. This powerful feature enables the analyst to generate a chromatogram that shows the distribution of a particular polymeric component even when the polymer components are not completely resolved chromatographically.

Figure 7, thus, reveals the molecular weight distribution chromatograms of both components. In large industrial applications, such as diesel powered railroad locomotives the level of these additives is monitored, and replenished as necessary to maintain performance of the lubricant.

4.2. Deformulation: Polymer Band Chromatograms. Polymer composition or configuration chromatograms can aid in the deformulation of complex systems. Figure 8 is an analysis of an automotive tire rubber formulation. In a similar manner,

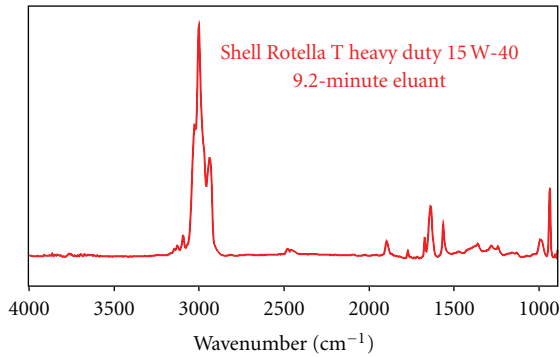


FIGURE 5: First elution peak spectrum.

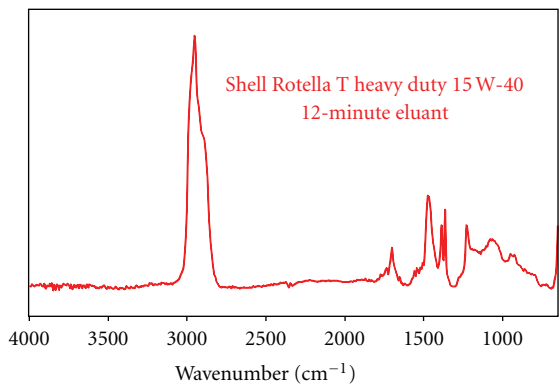


FIGURE 6: Second elution peak spectrum.

this sample was run on a GPC column, with tetrahydrofuran (THF) as the mobile phase. The sample is styrene-butadiene rubber (SBR) used in automotive tire manufacture, of which 150 μL was injected at a concentration of 0.15% (wt./vol.).

Initial inspection of the data suggested a polymer or polymers containing (trans) butadiene and styrene. These styrene (700 cm^{-1}) and diene (967 cm^{-1}) chromatograms virtually overlap in shape and elution times. This indicates a styrene butadiene rubber (SBR) copolymer in which the ratio of the comonomers is invariant across the molecular weight distribution of the copolymer.

The third (maximum band intensity) chromatogram is generated from the CH stretch bands and closely corresponds to the total mass of solutes. Notice that there is a sharp rise in this IR chromatogram at 31 minutes, and that this elution profile extends to lower molecular weights than do the comonomers. Examination of a spectrum at 31 minutes elution time indicates a different composition than the copolymer.

The chromatogram of the 1707 cm^{-1} band has a completely different distribution from the SBR polymer. It elutes at the tail of the SBR profile and has a different spectrum. The 1700 cm^{-1} band is generated by a carbonyl of lower molecular weight additive, included with the polymer to promote cross-linking with other components that will be added to the final formulation. This illustrates the ability to deformulae or identify the discrete components that

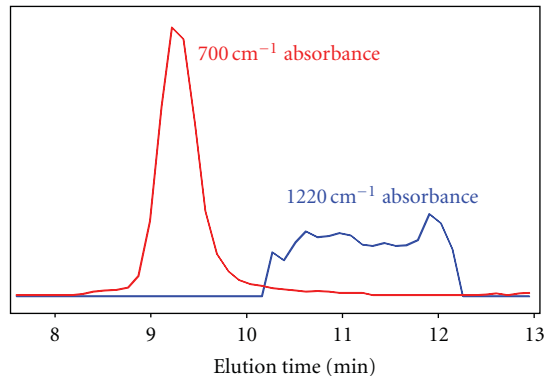


FIGURE 7: Infrared band chromatograms of the deposited sample.

comprise this sample. The technique can be applied to more complex samples by selecting spectral bands unique to each component.

4.3. Overlapping IR Chromatograms of Polymer Blends. In many, if not most, polymer blend samples, there is significant molecular weight overlap of the different polymer components. This example illustrates the data processing techniques used to characterize such solute overlaps.

This blend sample shows two polymers that have at least one pair of mutually exclusive bands. The uppermost in Figure 9 is the GPC-FTIR chromatogram of the sample. Two spectra are displayed, taken at the points indicated by the red and blue bars on the chromatogram. They show the differing spectra of the two components. A spectrum taken in the middle of this chromatogram would show the spectral patterns of both solutes. Below are the infrared chromatograms at 1705 cm^{-1} and 1734 cm^{-1} bands Figure 10.

The discrete mw weight distributions of each blend component are readily apparent. If one selects two spectra from the tails of the overall distribution, as in Figure 9, spectra of each component sufficient for identification can be obtained. Weighted spectral subtractions of one from the other will improve the spectral identification of each component. This is useful when spectral libraries are being used to aid identification.

4.4. Copolymers: Composition Drift. Copolymers are complex. During polymer synthesis the molecular population varies simultaneously in molecules size, concentration, and composition.

The reaction rates of the comonomers are seldom exactly equal. As a consequence the comonomer proportions will often change as polymerization proceeds. This is called "composition drift". Generally, composition drift will alter the finish physical properties of a copolymer. In some instance, the polymer chemist desires a minimum of composition drift, whilst in others a particular drift profile is deliberately sought [8–10]. Drift, therefore, must be determined and polymerization process controls (such as programmed stepwise addition of the monomers) [11] must be instituted to control composition drift, so as to achieve desired final properties of the copolymer product.

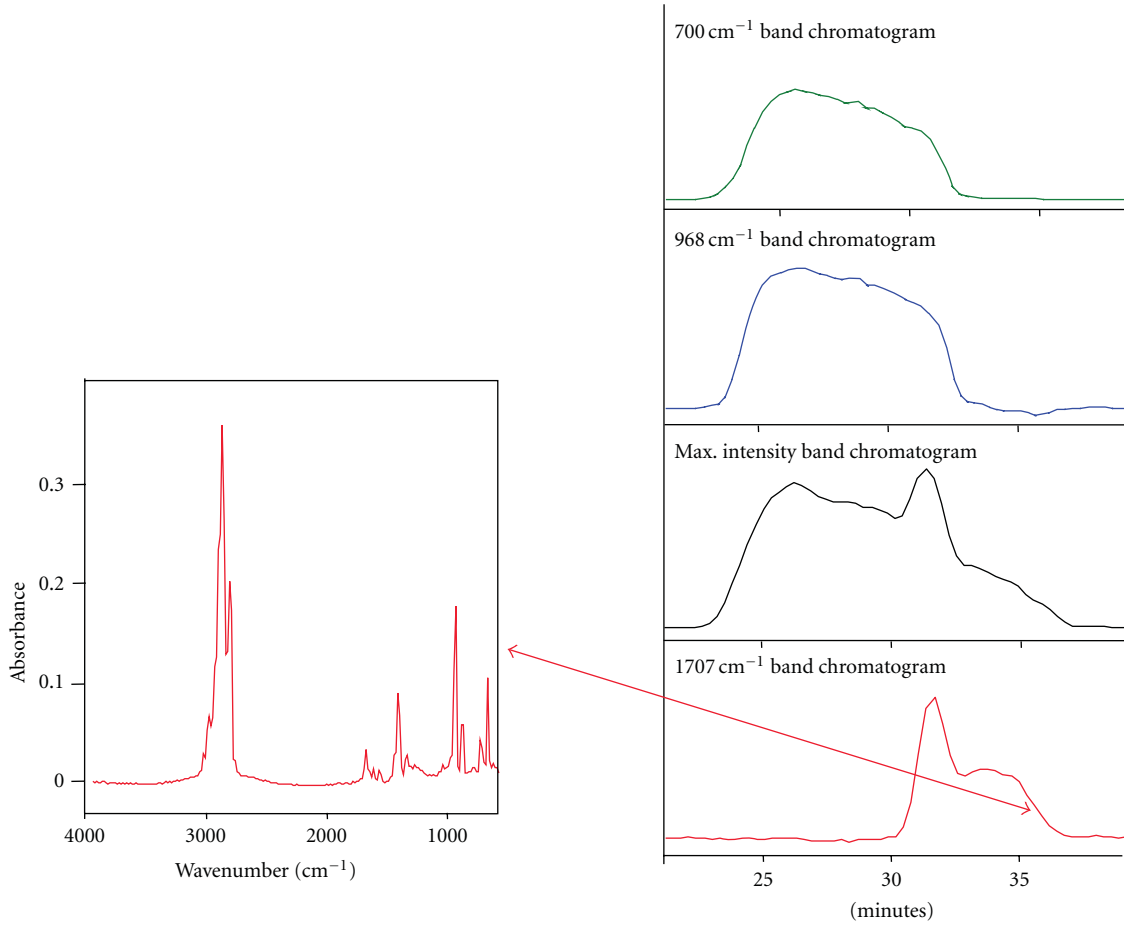


FIGURE 8: Tire polymer sample.

Typically, the total mass chromatogram of the polymer chains resembles a probability distribution plot—at a maximum in the region of the average molecular weight, and tapering off to nothing at the high and low molecular weight extremes of the distribution. Both the total mass and comonomer concentration are varying across the GPC elution profile. At any point in the chromatographic elution, a comonomer spectral band intensity is a product of the instantaneous elution mass and the per cent concentration of the comonomer.

Figure 11 illustrates conceptually the simultaneous variation in molecular weight and comonomer composition. Hyphenated GPC-FTIR analysis provides a very useful technique to measure composition drift in copolymer synthesis. The following example is an analysis of composition drift in a copolymer of styrene and (trans)butadiene.

This is the bulk spectrum of the copolymer. Useful IR bands for determination of composition are color highlighted. The (trans)butadiene is the green band, and the three styrene bands are highlighted in red Figure 12.

Figure 13 shows the time-ordered spectra of the fingerprint region of the copolymer spectra. The strongest absorption bands of the comonomers are indicated.

Assuming that the deposited chromatogram conforms to the Lambert-Beer law of band absorbances, the absorbance

of a spectral band at any place along the elution curve is equal to the product of the band extinction coefficient the solute deposit thickness, and the concentration of the comonomer in the copolymer

$$A_{\nu i} = \varepsilon_{\nu i} b C_i, \quad (1)$$

where $A_{\nu i}$ is the absorbance of component i at wavenumber ν , $\varepsilon_{\nu i}$ is the molar absorptivity of component i , b is the film thickness, C_i is the fraction of component i in the FTIR sample beam, and ratio chromatogram is $A_{\nu 1}/A_{\nu 2}$

$$\text{Bands Ratio} = \frac{A_{\nu 1}}{A_{\nu 2}} = \frac{\varepsilon_{\nu 1} \cdot C_1}{\varepsilon_{\nu 2} \cdot C_2} = k \frac{C_1}{C_2}. \quad (2)$$

Equation (2) has the effect of cancelling out the varying deposited mass “ b ” across the elution profile. The value of the absorbance ratio at all points is dictated simply by the comonomers extinction coefficients and their respective concentrations. It can be seen that there is a considerable composition variation with high concentrations of styrene comonomer in the high and low molecular weight tails and relatively less in the midst of the chromatogram. This is a simple and very effective method for measuring the composition drift of copolymer materials Figure 14.

This example shows composition drift measurements of a styrene-butadiene copolymer. A peak ratio chromatogram

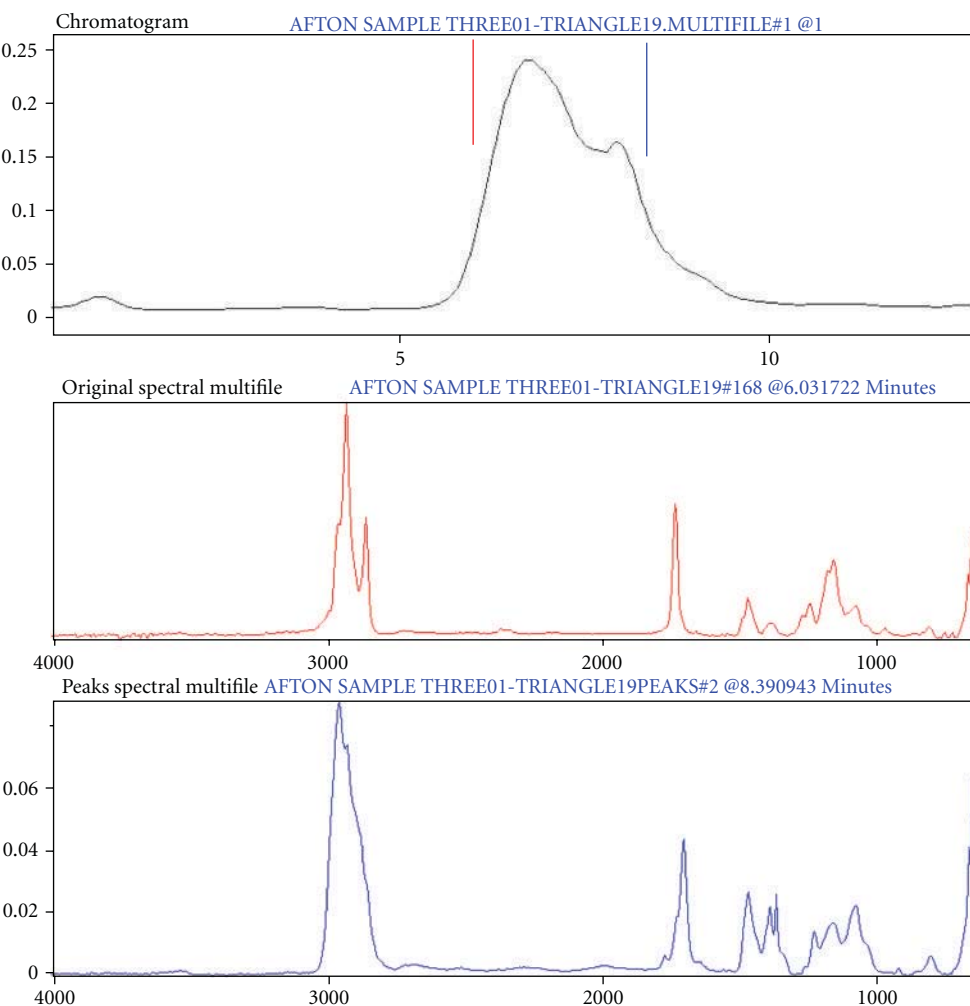


FIGURE 9: Two component polymer blend: overlapping MW distributions.

of the styrene/diene absorbance ratio was generated. The ratio chromatogram was algebraically transformed to a plot of polymer styrene content as a function of molecular weight. The 968 cm^{-1} (diene) and 1495 cm^{-1} (styrene) absorbance intensities were used for the absorbance ratio. A bulk spectrum of a known overall composition copolymer will provide the value (k , (2)) of extinction coefficient ratio.

4.5. Lot-to-Lot Characterization: Composition Drift in Copolymer Pharmaceutical Excipients. Polymer excipients are increasingly used to enhance and control the delivery of active pharmaceutical ingredients (APIs). They play an especially crucial role in delivery of poorly soluble drugs [12, 13]. An oral drug must:

- (i) withstand the rigors of the compounding and fabrication processes,
- (ii) retain efficacy during shelf life,
- (iii) make the passage through the stomach without undue decomposition,

(iv) be released in the GI tract with adequate bioavailability and with a desired release kinetic profile.

Performance is achieved by control of both the chemical and physical properties of the excipient package. Both polymer blends and copolymers are used in this field.

Figure 15 demonstrates compositional drift of samples of Copovidone, a widely used pharmaceutical tablet excipient. It is a vinyl-pyrrolidone/vinyl acetate copolymer. The analytical method was similar to that used in the styrene/butadiene example. Infrared chromatograms were generated for of the total eluting polymer mass (maximum intensity infrared bands), and for infrared bands centered at 1740 cm^{-1} (acetate) and 1680 cm^{-1} (pyrrolidone). The dotted line curves are the GPC chromatograms of the total polymer mass, and the solid lines the vinyl acetate comonomer distribution. As is apparent, both the average molecular weights and compositional drift varied in the three samples, with resulting differences in performance. With the aid of calibration standards, one can transform the band ratio chromatograms to quantitative determinations of comonomer distribution (shown on the right vertical axis).

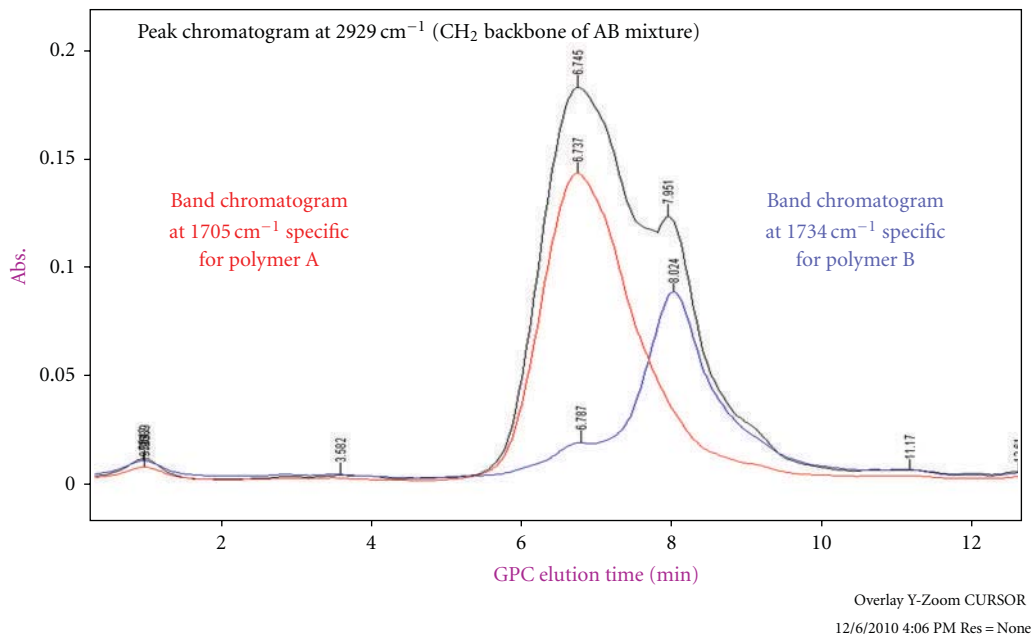


FIGURE 10: Band chromatograms showing distribution of two components.

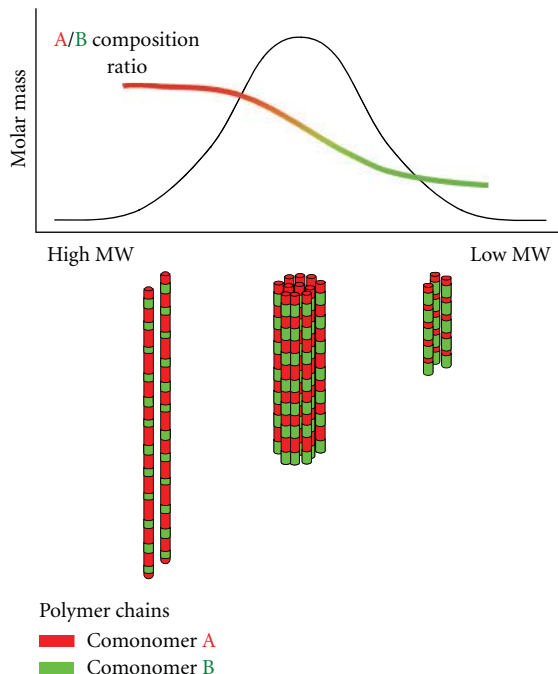


FIGURE 11: GPC mass distribution and varying concentration of comonomers.

The polymer sample with the most variable comonomer distribution showed problems in end-use performance.

4.6. Utilization of Configuration/Conformation Artifacts.

Infrared spectrometry not only reveals the *composition* functional groups (esters, ethers, nitriles, amides, and silicones), present in a

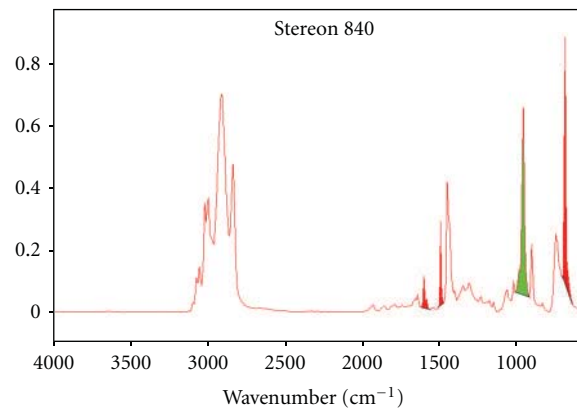


FIGURE 12: Bulk spectrum of a styrene/butadiene copolymer.

polymer, but also *configuration* and *conformation* properties such as stereoisomers, cis-trans configurations, crystallinity, and stereoregularity.

The following analysis of polyolefins shows how conformational spectral bands can aid in the deformulation of olefin polymers.

There are many commercially available polyolefin polymers, and they have a broad range of physical performance attributes. Polyolefins can be synthesized as high modulus structural materials, soft rubbers, and most everything in between. They are made chiefly from the monomers ethylene and propylene and possess only carbon and hydrogen atoms.

Polyolefins are, by definition, constituted of only carbon and hydrogen. Principal bands are limited. At first glance, vibrational spectroscopy might seem to be of scant utility,

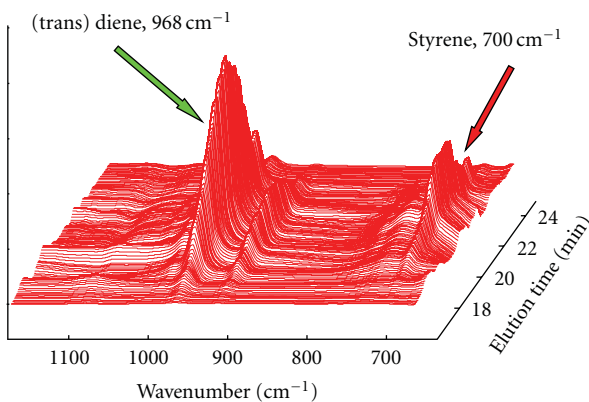


FIGURE 13: GPC-IR data map of SBR copolymer.

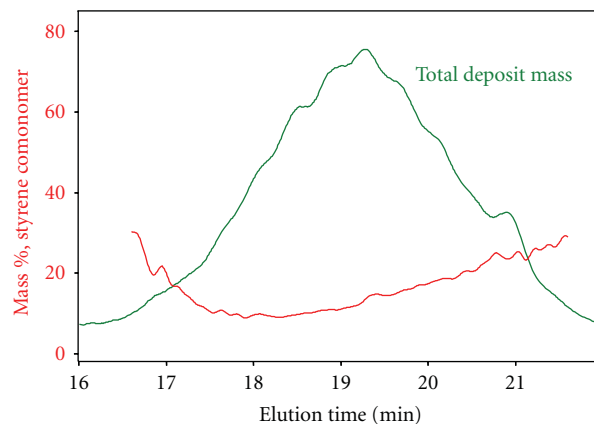


FIGURE 14: Band chromatograms of the comonomers butadiene and styrene.

but the configuration/conformation properties of olefin polymers make infrared spectroscopy possibly the most useful tool available for characterization. It is also the configuration/conformation properties that determine many of the physical properties of a polyolefin.

Three samples of olefin polymers were analyzed by GPC-FTIR. Referring to Figure 16, we see the following.

Sample 1 is polypropylene homopolymer.

Sample 2 is an ethylene propylene copolymer.

Sample 3 is determined to be a blend of polypropylene homopolymer, ethylene/propylene copolymer, and ethylene/butene copolymer.

The sample was analyzed for molecular and composition drift as in the previous examples. For brevity, the molecular weight distributions of composition and composition drift are not repeated here. This example points out the composition and configuration aspects used to characterize Sample 3.

- The 720 cm^{-1} evidences some splitting, suggesting crystallinity in long sequences of ethylene comonomer.
- The 1155 cm^{-1} band is a methyl branch band of polypropylene and is common to all samples.

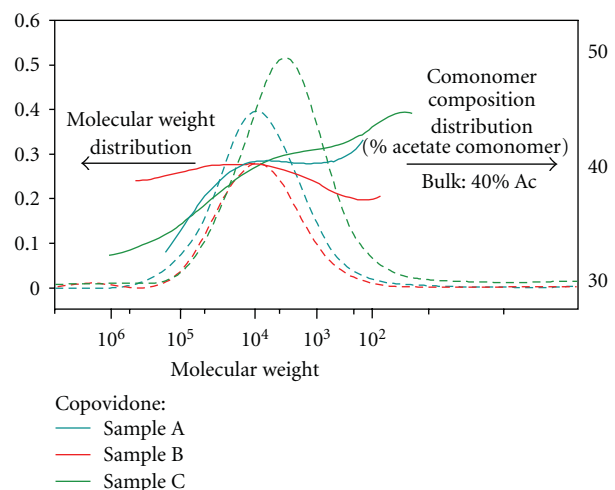


FIGURE 15: Compositional drift variations in a pharmaceutical excipient.

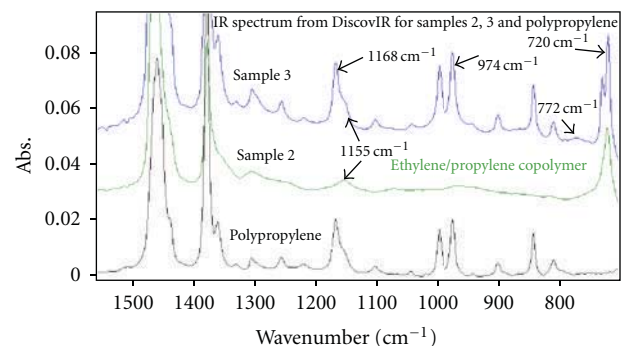
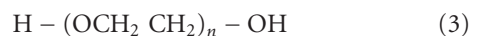


FIGURE 16: IR spectra of three polyolefin products.

- The presence of the 772 cm^{-1} indicates the butene comonomer in Sample 3. This is supported by similar elution chromatograms (not shown) of the 720 cm^{-1} and 772 cm^{-1} bands.
- The ethylene/propylene, by contrast, shows no such peak splitting. This infers that the peak splitting arises from long ethylene sequences of ethylene comonomer in the ethylene/butene copolymer.
- Sample 1 is an isotactic polypropylene, as evidenced by the 1168 cm^{-1} band. Sample 2 is atactic. The presence of the isotactic PP band in sample 3 arises from the blend of sample 2 and sample 1.

4.7. Aging/Environmental Changes: Polymer Synthesis and Degradation Problems. Polyethylene glycol (PEG) is a polyether terminated with hydroxyl groups. It is a low molecular weight polymer with the depicted structure



Polyethylene glycol is widely used in both consumer products and medicinal formulations. In medical applications, PEG is used as a protective molecule for active ingredients. “PEGylation” of proteins (bonding of active ingredient

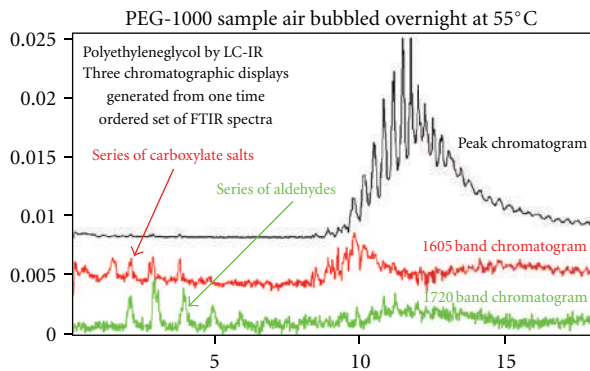


FIGURE 17: Oxidative changes of Polyethylene glycol.

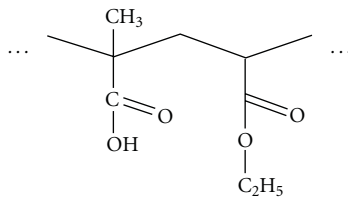


FIGURE 18: Eudragit backbone molecular structure.

proteins to PEG) is used to modify the biological uptake of the protein. In formulations, PEG is also used to modify the absorption of ingested medications (Figure 17).

In such applications, degradation of the PEG can have an adverse effect on the shelf life or potency of the medication.

After the oxidation process, the bulk material showed weak IR bands at 1720 cm⁻¹ and 1640 cm⁻¹, which were absent from the original PEG 1000. Examination by LC-FTIR revealed two series of oxidative cleavage products: one series containing aldehyde functionality and the other a series of carboxylic acid salts, which account for the extra IR bands. This information gives insight towards preservation strategies for extending the shelf life of formulations containing PEG. RP-LC/FTIR results are shown.

Functional group chromatograms revealed a series of aldehyde and carboxylated salt oligomers produced by the oxidation process. Air oxidation of PEG generates unstable peroxides, typical of the autoxidation of ethers. The peroxides then react further, leading to cleavage of the PEG chain between oxygen and carbon atoms.

The resulting aldehydes and carboxylate salts are PEG oligomers with oxidized end groups. Both of these more polar series elute early in the reverse-phase chromatogram. The bulk material shows the carboxylate IR band at 1640, consistent with a tightly bound cation such as a transition metal. This suggests a cleanup technique for preservation of the bulk material to improve the shelf life of products containing PEG.

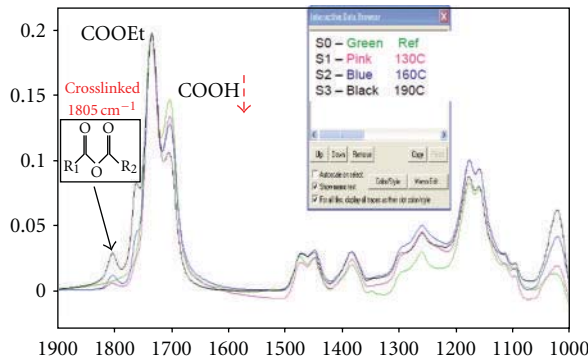


FIGURE 19: Undesired cross-linking of a pharmaceutical polymeric excipient.

In a similar vein, Figure 19 shows the thermally induced crosslinking of a pharmaceutical excipient which is co-extruded with an active pharmaceutical ingredient.

4.8. Thermally Induced Crosslinking of Pharmaceutical Excipient.

Eudragit L100-55 excipient is a copolymer with the polymer backbone structure as shown in Figure 18.

Extrusion is performed at an elevated temperature. A GPC-FTIR analysis of product under various extrusion conditions revealed that a side group was cleaved from the polymer backbone, with resultant formation of anhydride cross-links. This has a deleterious effect on release characteristics of the active ingredient.

4.9. Reactive Systems Analysis: Paints and Coatings.

Many coatings are based on chemical reaction for their “drying” or “curing”. Epoxy and urethane systems are examples of liquid polymer materials that treat to form hard films or objects.

Oil-based paints are the most ubiquitous of reactive coatings. Paints consist of polymers dissolved in oils such as linseed oil, soya oil, and various vegetable oils. These oils are unsaturated fatty acids, and they have the ability to form adducts with the polymer component under appropriate reaction conditions.

During the coating synthesis, some portions of the vegetable oil will become adducted to the polymer mass. Upon exposure to oxygen, these unsaturates will cross-link to form a solid film (drying).

Figure 20 shows the use of GPC-FTIR to determine the degree of adduction of a paint oil vehicle into the polymer component of the paint. The blue chromatogram is generated by the ester carbonyl of the vehicle. The monomeric oil shows an elution peak centered at 32 minutes. The early eluting portion of carbonyl functionality (20–31 min) is bound to the polymer mass, and this adduct has a higher molecular weight (and earlier elution time) than the monomer.

To make a quantitative assessment of monomer-polymer partitioning of the oil, the area under the carbonyl IR chromatogram was integrated, and a judgment was made as to the polymer/monomer partition (ca. 31 minutes).

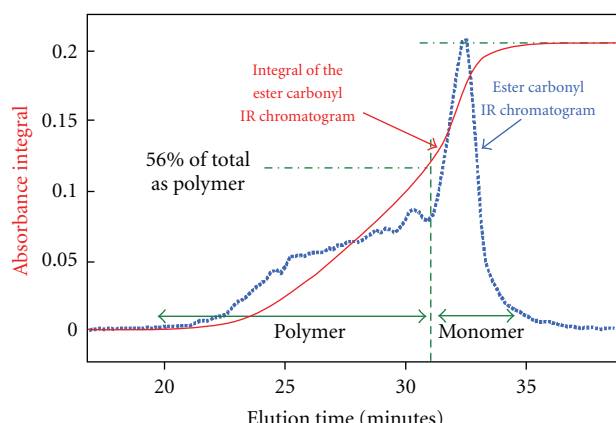


FIGURE 20: Paint: partitioning of oil into the polymer fraction.

Scalar values of the integral function were taken at this time and at the maximum of the integral curve, resulting in a determination of 56% inclusion of the oil into the polymer mass.

This is a postreaction end state analysis of the sample. The technique can be extended to monitoring real-time reaction kinetics of processes whose total reaction times are greater than one hour. The limiting factor is the cycle time of the chromatography column.

5. Experimental Conditions for Described Applications

(4.1) Deformulation: Analysis of Lubricant Polymeric Additives.

| | |
|------------------------------------|---|
| <i>Sample</i> | Shell rotella T SAE 15 W-40 diesel engine oil |
| <i>Chromatography</i> | |
| <i>Column</i> | GPC: Jordi mixed bed: 25 × 1 cm |
| <i>Mobile phase</i> | Tetrahydrofuran (THF) |
| <i>Flow rate</i> | 1 mL/min |
| <i>Injection volume</i> | 50 µL |
| <i>Sample concentration</i> | 90 mg/mL |
| <i>Deposition and spectrometry</i> | |
| Cyclone temperature | 260°C |
| Pressure, Cyclone | 400 torr |
| Pressure, sample deposit chamber | 6.4 torr |
| Carrier gas flow | 380 cc/min |
| Condenser temp | 5°C |
| Zn Se disk translation rate | 3 mm/min |
| Disk temp | 20°C |
| Nebulizer power | 6 Watts |

(4.3) Overlapping IR Chromatograms of Polymer Blends.

| | |
|------------------------------------|---------------------------|
| <i>Sample</i> | Polymer blend |
| <i>Chromatography</i> | |
| <i>Column</i> | GPC: waters styragel HR 4 |
| <i>Mobile phase</i> | Tetrahydrofuran (THF) |
| <i>Flow rate</i> | 1 mL/min |
| <i>Injection volume</i> | 100 µL |
| <i>Sample concentration</i> | 3 mg/mL |
| <i>Deposition and spectrometry</i> | |
| Cyclone temperature | 150°C |
| Pressure, cyclone | 369 torr |
| Pressure, sample deposit chamber | 4.7 torr |
| Carrier gas flow | 380 cc/min |
| Condenser temp | 15°C |
| Zn Se disk translation rate | 3 mm/min |
| Disk temp | 0°C |
| Nebulizer power | 5 Watts |

(4.4) Copolymers: Composition Drift.

| | |
|------------------------------------|---|
| <i>Sample</i> | Firestone 721AC styrene/butadiene copolymer |
| <i>Chromatography</i> | |
| <i>Column</i> | GPC: Jordi 50 × 1 cm mixed bed: linear DVB |
| <i>Mobile phase</i> | Tetrahydrofuran (THF) |
| <i>Flow rate</i> | 1 mL/min |
| <i>Injection volume</i> | 5 µL |
| <i>Sample concentration</i> | 12 mg/mL |
| <i>Deposition and spectrometry</i> | |
| Cyclone temperature | 248°C |
| Pressure, cyclone | 400 torr |
| Pressure, sample deposit chamber | 5.8 torr |
| Carrier gas flow | 321 cc/min |
| Condenser temp | -10°C |
| Zn Se disk translation rate | 3 mm/min |
| Disk temp | 90°C |
| Nebulizer power | 1 Watt |

(4.5) Lot to Lot Characterization: Composition Drift in Copolymer Pharmaceutical Excipients. The chromatograph used in this application was a Waters 150°C chromatograph, operating at 145°C.

| | | |
|---|---|---|
| <i>Sample</i> | Copovidone (BASF Kollidon VA64) | (4.7) <i>Aging/Environmental Changes: Polymer Synthesis and Degradation Problems.</i> |
| <i>Chromatography</i> | | |
| Column | Shodex OHpak SB-806 M HQ | <i>Sample</i> |
| Mobile phase | MeOH/H ₂ O, 0.05 M acetic acid | Polyethylene glycol (PEG 1000), partially air oxidized in 15% acetonitrile/water |
| Flow rate | 1 mL/min | <i>Chromatography</i> |
| Injection volume | 150 μL | Column |
| Sample concentration | 0.35% | Reverse-phase eclipse C-18, 4.6 × 50 mm |
| <i>Deposition and spectrometry</i> | | 10–90% acetonitrile gradient, 30 min |
| Cyclone temperature | 21°C | Flow rate |
| Pressure, cyclone | 750 torr | 1 mL/min |
| Pressure, sample deposit chamber | 2.6 torr | Injection volume |
| Carrier gas flow | 0 cc/min | Sample concentration |
| Condenser temp | 20°C | <i>Deposition and spectrometry</i> |
| Zn Se disk translation rate | 3 mm/min | Cyclone temperature |
| Disk temp | 25°C | Pressure, cyclone |
| Nebulizer power | 0 Watts | Pressure, sample deposit chamber |
| | | Carrier gas flow |
| | | 370 cc/min |
| | | Condenser temp |
| | | 5°C |
| | | Zn Se disk translation rate |
| | | 3 mm/min |
| | | Disk temp |
| | | −20°C |
| | | Nebulizer Power |
| | | 13.5 Watts |
| (4.6) Utilization of Configuration/Conformation Artifacts. A sample of PEG 1000 (polyethylene glycol of average molecular weight 1000) was subjected to vigorous air oxidation and then analyzed it by reverse-phase LC-IR to learn about the identity and distribution of the oxidation products within the bulk polymer. | | |
| <i>Sample</i> | Blend of polyolefins | <i>Sample</i> |
| <i>Chromatography</i> | | Eudragit L100–55 |
| Column | GPC: Jordi DVB mix bed 25 cm × 1 cm, 5 μm | <i>Chromatography</i> |
| Mobile phase | 1,2,4 trichlorobenzene (TCB) | Column |
| Flow rate | 1 mL/min | Jordi gel DVB mixed bed-250 × 10 mm |
| Injection volume | 100 μL | Mobile phase |
| Sample concentration | 25 mg/mL | THF |
| <i>Deposition and spectrometry</i> | | Flow rate |
| Cyclone temperature | 375°C | 1 mL/min |
| Pressure, cyclone | 109 torr | Injection volume |
| Pressure, sample deposit chamber | 1 torr | 100 μL |
| Carrier gas flow | 57 cc/min | Sample concentration |
| Condenser temp | 20°C | 5 mg/mL |
| Zn Se disk translation rate | 3 mm/min | <i>Deposition and spectrometry</i> |
| Disk temp | 90°C | Cyclone temperature |
| Nebulizer power | 10 Watts | 150°C |
| | | Pressure, cyclone |
| | | 460 torr |
| | | Pressure, sample deposit chamber |
| | | 5.2 torr |
| | | Zn Se disk translation rate |
| | | 3 mm/min |
| | | Disk temp |
| | | −15 to ~ −20°C |
| 6. Summary | | |
| The multidistributed attributes of polymer systems present a huge challenge to the analyst. Infrared spectrometry has proved to be a superior tool in polymer analysis, but is | | |

severely limited by the multicomponent nature of polymer samples. Traditional sample fractionation followed by FTIR analysis can yield results but is extremely costly on terms of time and effort.

The advent on practical LC-FTIR technology addresses this need. It is suited to multiple applications for the analysis and characterization of polymer materials. Several examples of utility are presented in this paper. The combination of LC-FTIR instrumentation coupled with the interpretative capabilities of infrared software greatly assists in the interpretive aspects of infrared spectra and renders hyphenate LC-FTIR a practical working technique for polymer scientists and synthesis chemists.

References

- [1] J. L. Koenig, *Spectroscopy of Polymers*, American Chemical Society, Washington, DC, USA, 1991.
- [2] L. Coulier, E. Kaal, and T. Hankemeier, "Hyphenation of infrared spectroscopy to liquid chromatography for qualitative and quantitative polymer analysis: degradation of poly(bisphenol A)carbonate," *Journal of Chromatography A*, vol. 1130, no. 1, pp. 34–42, 2006.
- [3] J. J. Gagel and K. Biemann, "The continuous infrared spectroscopic analysis of reversed phase liquid chromatography separations," *Microchimica Acta*, vol. 95, no. 1–6, pp. 185–187, 1988.
- [4] K. Biemann and J. J. Gagel, "Method and apparatus for continuous collection of chromatographic effluent US Patent 4,843,243," 1989.
- [5] P. R. Griffiths, K. L. Norton, and J. Andrew, "A unified approach to the chromatography-FTIR interface: GC-FTIR, SFC-FTIR, and HPLC-FTIR with subnanogram detection limits," *Lange Microchemical Journal*, vol. 46, no. 3, pp. 261–270, 1992.
- [6] A. Dekmesian, "Method and apparatus for collecting samples for analysis of chemical composition US Patent 5039614," 1991.
- [7] Ibid. 1, p2.
- [8] J. Schiers and D. Priddy, *Modern Styrenic Polymers: Polystyrenes and Styrenic Copolymers*, Wiley Series in Polymer Science, 2003.
- [9] J. M. Asua, Ed., *Polymer Reaction Engineering*, Wiley-Blackwell, New York, NY, USA, 2007.
- [10] J. Benkoski, G. Fredrickson, and E. Kramer, "The effects of composition drift on random copolymer reinforcement of polymer-polymer interfaces," in *Proceedings of the Annual March Meeting*, Washington State Convention Center Seattle, Seattle, Wash, USA, March 2001, Washington Meeting ID: MAR01, abstract #C19.004.
- [11] R. D. Mathis, *Modern Plastics Encyclopedia*, McGraw-Hill, New York, NY, USA, 1988.
- [12] *Drug Delivery Technology*, vol. 8, 2008.
- [13] H. Foltzman and A. Quadir, "Copovidone—a copolymer with unique formulation properties," *Drug Delivery Technology*, vol. 8, no. 8, pp. 22–27, 2008.

Research Article

Distribution of Heat Stabilizers in Plasticized PVC-Based Biomedical Devices: Temperature and Time Effects

Lidia Maria Bodecchi,¹ Caterina Durante,^{2,3} Marcello Malagoli,¹ Matteo Manfredini,¹ Andrea Marchetti,^{2,3} and Simona Sighinolfi^{2,3}

¹ Gambio Dasco S.p.A, Via Modenese 30, 41036 Modena, Italy

² Department of Chemistry, University of Modena and Reggio Emilia, Via G. Campi 183, 41125 Modena, Italy

³ INSTM, UdR of Modena, 41125 Modena, Italy

Correspondence should be addressed to
Andrea Marchetti, andrea.marchetti@unimore.it

Received 20 April 2011; Revised 13 June 2011; Accepted 14 June 2011

Academic Editor: Ahmed Aamouche

Copyright © 2011 Lidia Maria Bodecchi et al. This is an open access article distributed under the Creative Commons Attribution License, which permits unrestricted use, distribution, and reproduction in any medium, provided the original work is properly cited.

Thermoplastic polymers can be viewed as a dynamic framework in which additives allocation is strongly dependent on the system's chemistry. Considering the complexity of the distribution phenomena that may occur in plastics obtained by blending polymeric resins with different additives, this work constitutes an attempt to the description of the behavior of PVC heat stabilizers (calcium and zinc carboxylates), as regard temperature and time. Thanks to the Fourier Transform Infrared Spectroscopy, it is possible to observe a first decreasing trend of the additives related IR-bands as a function of the increasing temperature and the higher the temperature the faster the decrease of the heat stabilizers intensities bands is, with respect to time. Additives distribution in not sterilized, sterilized, aged not sterilized and aged sterilized materials have been investigated to determine their behavior with respect to temperature, from 30 to 120°C, and time. A simulated supplementary aging process equivalent to 9 months aging was carried out on aged not sterilized and aged sterilized materials to gain more data on the transport/reaction phenomena these additives in the plastic material. Experimental evidences allow hypothesizing that reaction and redistribution phenomena probably concur to determine the additives allocation in PVC as a function of temperature and time.

1. Introduction

Poly(vinyl chloride) (PVC) is one of the most important plastic material available today in terms of global market figures and production volumes, with widespread applications in different areas. The reasons for its worldwide importance, among physical-chemical characteristics, are, on one side, its compatibility with a large number of other products (e.g., plasticizers, heat stabilizers, and lubricants) that are able to modify PVC's chemical and physical properties to obtain from rigid to flexible end products even with complex shapes and, on the other side, the low production costs [1].

The study of different PVC plasticizers has always been a big concern [2–6] for the great amounts of such additives and the potential toxic effects [7–10] which some of them have been charged of in the last decades. On the contrary, less attention has been paid to the investigation of the intrinsic

stability of mixture, including PVC resins, plasticizers, and thermal stabilizers, along with their dispersion in the blends, and of all those events which may alter such distribution, that is, additives migration, segregation, or degradation phenomena [11–14]. Among PVC additives, particular attention can be focused to heat or thermal stabilizers. As a matter of fact, it is known that low stability is an inherent property of the polymer that undergoes severe degradation even at relatively low temperatures [15]. In order to prevent the polymer degradation and increase the PVC thermal stability, the use of heat stabilizers is required [1]. The choice of the proper heat stabilizers depends, on one hand, on plasticization, lubrication, and cost parameters and, on the other hand, on the use and applications of the PVC end product [1, 16, 17]. In particular, for flexible (plasticized) biomedical PVC-based disposables, calcium and zinc carboxylates are the only heat stabilizers permitted by the most important national

and international ruling bodies, such as the European Pharmacopoeia [18].

Far away from being a steady state or showing a fixed structure, thermoplastic polymers can be viewed as a dynamic framework with the long polymeric chains swelled by a system of smaller molecules (those of the plasticizers), wherein other additives, whenever present, are dispersed. The distribution of the additives is strongly dependent on the chemistry of the various components and, as a first approximation, on their relative affinity in terms of apolar-polar or steric hindrance [19]. The bulk-to-surface allocation is also governed by thermodynamics, and it will be expected that a proper amount of energy (thermal, radiative, etc.) could alter or modify such distribution, affecting the final functional properties of the end product. Previous studies [2, 16] highlighted the distribution of additives, such as calcium and zinc carboxylates, as a function of the simulant that comes in contact with different PVC-based blends, from rigid to plasticized ones. At the same time, the photo-oxidation of PVC films, stabilized by calcium and zinc stearates, was studied using gravimetry, IR, and UV-visible spectrometry [20–22]. Moreover, when dealing with zinc and calcium stabilizers, a different and opposite behavior of the additives can be stressed out during the extrusion process; in particular, zinc stearate tends to move, “segregate”, towards the metal surface of the die faster than calcium stearate does [23, 24].

Thus, heat stabilizers molecules can move within the plasticized resin upon various solicitations coming from the outside environments also at ambient temperature. Therefore, surface properties of materials, and thus the intrinsic distribution of the various additives of the blends, become of utmost relevance when medical devices are concerned [3, 4, 12, 25], and, in particular, when blood contacting items, like blood storage bags, catheters for vascular access, tubing, and so forth, are dealt with. In this case, bearing in mind the large number of processes that a plasticized PVC-based blend has to undergo before a finished medical device is manufactured, a possible segregation or a different distribution of additives from the surface to the bulk of the material or device was supposed, as reported in previous studies [11, 12].

In particular, results obtained from different authors [2, 11, 12, 16, 23, 24] highlighted that the radiation sterilization step seems to induce a different allocation of the metal soaps from the surface to the bulk of the examined tubing components, protecting the PVC resin itself from thermal and ionizing degradation phenomena resulting from the sterilization process. On the other hand, accelerated aging test seems to cause a further thermodynamic-supported segregation of additives from the bulk to the surface of the material on the basis of the different “affinity” of the resin and the heat stabilizers [25]. In fact, surface morphology and additives nature, concentration, and distribution, as well as PVC itself, influence the blood compatibility of the polymer, namely, the haemocompatibility of the blood contact surface/device. Adverse reactions can be triggered by nonhaemocompatible materials when they come in contact with blood such as trombi formation, emboli, and, in general, all the characteristic processes included under the

wide field of haemostasis [3, 4, 12, 26]. Among the different causes that lie behind the trombogenic characteristics of polymer surfaces, several activation factors and cofactors can be mentioned and in particular the action of many metal ions, such as calcium, zinc, and iron play a fundamental role in blood clotting [27, 28]. Therefore, the presence of metal soaps additives on the inner surface of tubes in contact with blood is a typical case study, where the monitoring of the processing steps has to account for structural phenomena of the modification and migration of chemical species within a plasticized PVC-blend, whose long-terms effects have not been totally disclosed yet.

The present work constitutes a preliminary attempt and experimental approaches to the description of the possible behavior of heat stabilizers in PVC-based tubing components used for extracorporeal medical disposable devices. In particular, this work is focused on the study of the supposed migration of calcium and zinc soaps in extruded tubes as a function of temperature and time. The analytical technique chosen for this purpose is the Fourier transform infrared spectroscopy (FT-IR) combined with a single reflection accessory for attenuated total reflectance (ATR) golden gate equipped with a heated-diamond top plate. In this configuration, surface-sensitive information may be gained thanks to the combination of the FT-IR with the ATR accessory resulting in a final sampling depth of some micrometers [29, 30]. Moreover, the heated-diamond top-plate, allowed us to study the kinetic distribution of additives as regard to the temperature change. In the actual work, different typologies of products, namely, sterilized, nonsterilized, and aged samples were characterized by FT-IR/ATR measurements.

2. Experimental Section

2.1. Materials. The medical device, which the whole study dealt with, is a circuitry for extracorporeal haemodialysis. This disposable allows extracorporeal blood circulation from and to the patient through an artificial kidney *via* a peristaltic pump during a haemodialysis treatment. Such circuitry is a complex assembly of different components, either molded or extruded.

Samples selected for the present experiments belong to one of the extruded components, that is, the tubing, whose surface exposed to the blood during a dialysis treatment is characterized by one of the largest area among those of the components constituting the assembly. All the selected samples were characterized by the same starting developing formulation and were produced by pilot laboratory equipment. Formulation includes plasticizer (di-(2-ethylhexyladipate), DEHA), thermal stabilizers, such as calcium and zinc carboxylate which present a good miscibility with the used plasticizer, and lubricants and other additives in a very limited amount, below 0.5% w/w. The percentage of thermal stabilizers, used for the production of tubing components, is always less than 0.9% [12]. For the present study, two different typologies of tubing, nonsterilized and sterilized, were selected. Sterilization was performed by means of electron beam irradiation (β irradiation) with a typical exposure dose of 25 kGy. From 1 m tubing sample, sterilized and

nonsterilized, a tube fragment, 10 cm long, was dissected, and then two subsections, 1 cm long, were obtained. Finally, the 1 cm tube sample was further longitudinally cut into two fragments subjected to FT-IR/ATR analysis. In particular, only the inner surface of each fragment was analyzed, since this is the tubing part that comes in contact with blood during the haemodialysis treatment.

Samples collection and analysis were performed as follows:

- (a) within 1 month from tubing production (sterilized and nonsterilized),
- (b) after 1 year from tubing production (aged sterilized and aged nonsterilized).

Moreover, one-year aged sterilized and one-year nonsterilized samples, after IR-ATR analysis, were subjected to a simplified protocol for accelerated aging, SPAAs, in order to test their behavior with respect to time and temperature. IR spectra were collected by applying the same measuring protocol.

2.2. Simplified Protocol for Accelerated Aging, SPAAs. A simplified protocol for accelerated aging (known as “10-degree rule”), based on the Arrhenius’ collision theory, has been used as additional aging test [25]. With this method a device or material is subjected, for a short time, to stresses that are more severe than normal environmental or operational conditions in order to determine the response of the system under normal-usage conditions over a relatively long time.

The relationship between oven test time, Time_{T_1} days, and shelf-life time, Time_{RT} days, is as follows:

$$\text{Time}_{T_1} = \frac{\text{Time}_{RT}}{Q_{10} \exp(T_1 - T_{RT})/10}, \quad (1)$$

where T_1 represents the oven aging temperature, °C, T_{RT} represents the room temperature, ambient or use/storage conditions, °C, and Q_{10} is the reaction rate coefficient which is equal to 2 for medical polymers [31, 32].

For the present study, one-year-old samples were stored for 9 days in oven at a temperature of 70°C corresponding to an equivalent time of 36 weeks (9 months) at normal condition, that is 20°C–22°C (ambient temperature). Therefore, after this treatment samples should simulate a 21-month-old tubing.

2.3. Spectroscopic Techniques. Infrared spectra were collected by means of a Bruker VERTEX 70 FT-IR spectrometer equipped with a Mercury Cadmium Telluride, MCT, detector. The instrument was combined with a single reflection ATR accessory (Golden Gate) constituted of a heated-diamond top plate supplied by Specac Ltd. (UK). All the spectra were acquired over 32 scans at a resolution of 1 cm⁻¹ between 4000 and 600 cm⁻¹ and, for each 1 cm long sampled section; three different measurements were obtained on the inner surface at random locations. Considering the refractive indices of the internal diamond and of a polymer, such as plasticized PVC, to be 2.4 and 1.5 respectively,

roughly 2 μm depth from the material surface were sampled with an incidence radiation angle of 45° [29]. Intimate contact between the diamond internal reflectance element and the sample was achieved using a preset torque lock device. FT-IR measurements were carried out at 30°C, 50°C, 70°C, 90°C, and 120°C, respectively, in presence of dry air (dew point –70°C). Different backgrounds were taken for each temperature, and 3-minute delay time was always held before starting each measurement. To check the reproducibility of the overall experiments, measurements were always replicated in different days.

3. Data Analysis

The spectra collected with the ATR golden gate accessory were normalized by means of a standard normal variate, SNV, procedure, in order to reduce the variability contributions due to the differences in the absolute values of the spectra baselines. The mathematical analyses were performed using Matlab R2006B release, implemented with PLS toolbox 4 [33].

4. Results and Discussion

4.1. Temperature Effects. Figure 1 shows the averaged normalized spectra for sterilized (top) and nonsterilized (bottom) samples subjected to FT-IR/ATR measurements carried out at different temperatures, that is, 30°C, 50°C, 70°C, 90°C, and 120°C. Focusing on the two different bands related to calcium and zinc carboxylates, 1576 cm⁻¹ and 1540 cm⁻¹, respectively [16], as shown in Figure 2, it is evident that while nonsterilized samples are characterized by the presence of heat stabilizers on the inner surface of the tube at 30°C, sterilized samples are not. The absence of the bands in the sterilized samples seems to be related to the sterilization process imparted to the tubing component [25]. In fact, high-energy radiation produces scission and crosslinking of the polymer chains, formation of small molecular products, and modification of the chemical structure of the polymer resulting in changes in the materials properties [11, 12, 32]. In the same way, heat stabilizers are able to prevent the dehydrochlorination reaction of PVC acting as primary and secondary stabilizers [1]. Therefore, the experimental evidence for the sterilized samples seems to confirm the high impact of the β sterilization process on the polymer that leads to the heat stabilizers to react its degradation products, such as HCl, at a surface level or by means of their redistribution towards the material in order to prevent the PVC degradation cascade to start or continue.

Figure 2 reports an extended view of the spectral region of interest and shows the effects induced by temperature on the heat stabilizers behavior for nonsterilized samples. In particular, the 1576 cm⁻¹ and 1540 cm⁻¹ bands are present at 30°C, 50°C, and 70°C with a decreasing trend, while at 90°C and 120°C, they disappear. The presence of the calcium/zinc metal soaps on the polymer surface could be mainly due to a kind of chemical incompatibility between the polar PVC backbone and the nonpolar hydrocarbon chain of the stabilizer [25]. As far as the temperature effect

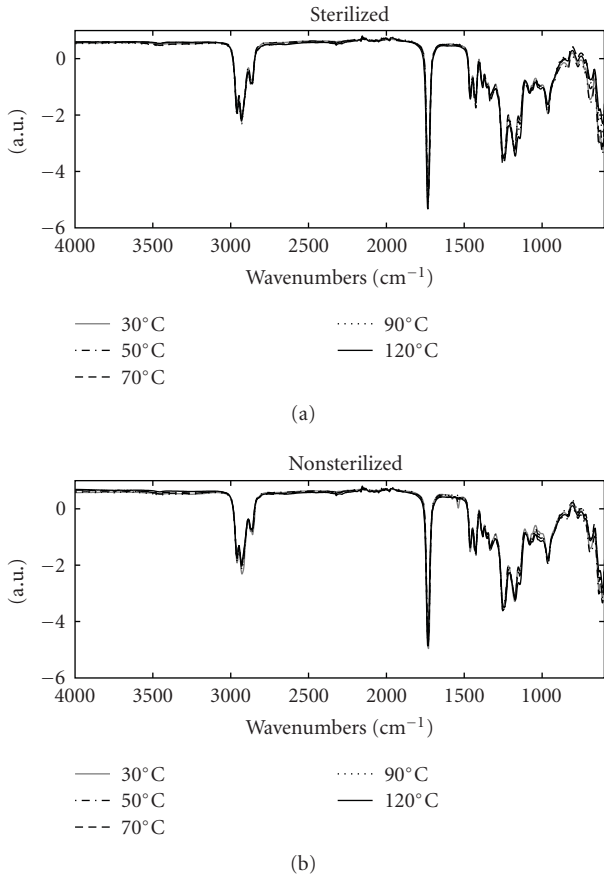


FIGURE 1: Plot of normalized FT-IR/ATR average spectra, wavelengths (cm^{-1}) versus Arbitrary Units (a.u.), (full wave numbers range) of sterilized (a) and nonsterilized samples (b) at 30, 50, 70, 90 and 120°C, respectively.

is concerned, the decrease of the calcium/zinc carboxylates bands on the inner surface of the tube, both for sterilized and nonsterilized samples, as a function of temperature (Figure 2), could be ascribed to a migration phenomena of the heat stabilizers in the plastic polymer material from the surface to the bulk of the tubes or, otherwise, to reaction mechanisms of the additives themselves as a consequence of the heat treatments. Nevertheless, the latter explanation does not completely justify the experimental evidences obtained for nonsterilized samples at temperatures up to 70°C, where the HCl formation should be negligible [34].

4.2. Temperature Effects: Aged Sterilized and Aged Nonsterilized Samples. The above cited behavior was also observed for nonsterilized samples measured after one year from the tubing production process, aged nonsterilized, as depicted in Figure 3. On the other hand, the appearance of the calcium and zinc soaps related bands on the surface of the aged sterilized tubes at 30°C seems to confirm a possible migration phenomena of these species in the plastic polymer probably due to the metal soaps—PVC chemical incompatibility, during the aging process [25].

Figures 4(a) and 4(b) report the comparison of peak areas evaluated for the calcium and zinc stabilizers IR bands

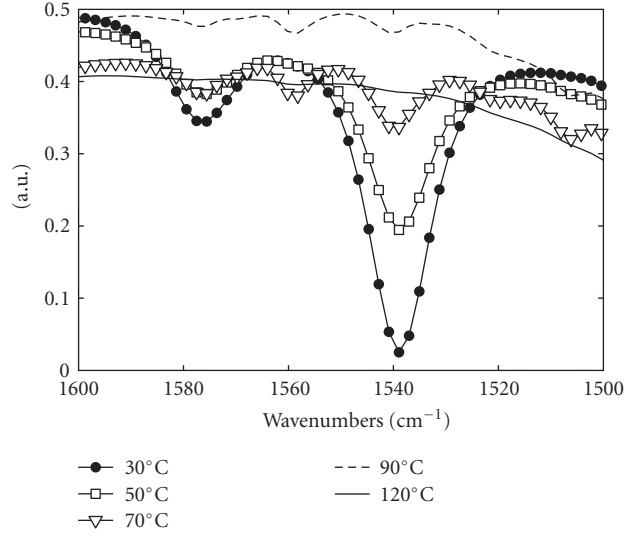


FIGURE 2: Extended view of the normalized FT-IR/ATR average spectra, wavelengths (cm^{-1}) versus Arbitrary Units (a.u.), for nonsterilized samples at 30 (●), 50 (□), 70 (▽), 90 (- -), and 120 (—) °C, respectively.

for nonsterilized, aged nonsterilized, and aged sterilized samples. Nonsterilized samples present a more intense 1540 cm^{-1} band, related to the zinc soaps, with respect to 1576 cm^{-1} band associated to calcium carboxylates. Moreover, calcium soap relative area is larger for aged sterilized samples than for aged nonsterilized ones, while zinc carboxylates relative area is greater for aged nonsterilized samples than for aged sterilized ones. Probably, the different ratio of these additives between aged sterilized and aged nonsterilized samples might be ascribed to the β sterilization imparted to the tubing samples. In fact, during the degradation process of PVC, calcium carboxylates, which have little Lewis acidity property, mostly exhibit HCl scavenger behavior, while zinc soap, which is stronger Lewis acid, not only scavenges HCl, but also substitutes carboxylates for the allylic chlorine atoms [1]. Then, the exchange reaction between zinc chloride and calcium carboxylates regenerates the active zinc additive also avoiding the catalytic effect of zinc chlorides towards PVC degradation [1]. Thus, the reduction of the Zn soaps on the surface of aged sterilized samples might be correlated to the protection mechanism itself of the heat stabilizers and, consequently, to its initial consumption during the sterilization process. Moreover, when stabilizers are almost totally consumed, polyenes begin to appear, and mass loss takes place [20–22].

In PVC processing equipments, operating at high pressure and temperature, an efficient mixing of all ingredients at molecular level should occur in order to make PVC stable to heat during its processing for short period. Nevertheless, the formation of a thin layer of stabilizers at the surface of the PVC material, that constitutes an interface between the metal surface of the die and the polymer, seems to confirm the migration theory of additives as regard temperature [23, 24]. Thus, migration and thermal stability processes probably concur together to the heat stabilizers distribution in the plastic material as a function of temperature and time.

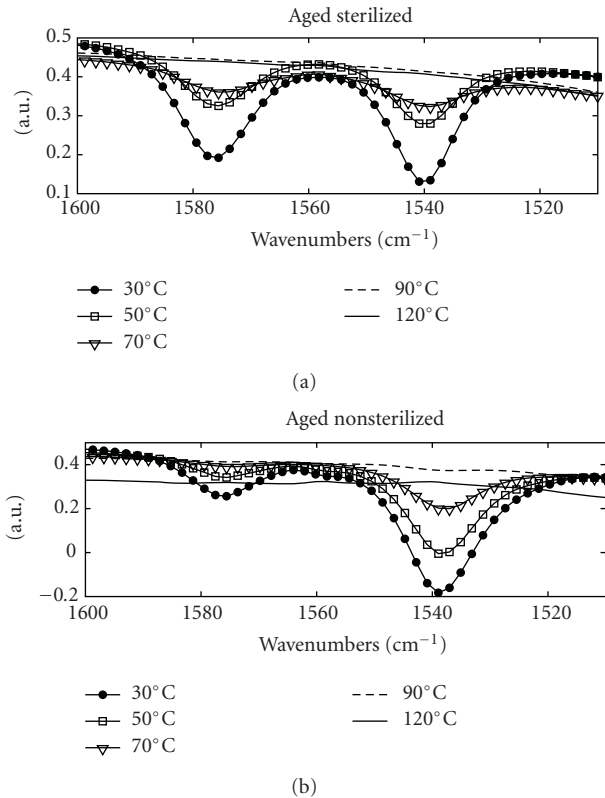


FIGURE 3: Extended view of the normalized FT-IR/ATR average spectra, wavelengths (cm^{-1}) versus Arbitrary Units (a.u.), for one year aged sterilized (a) and one year aged nonsterilized samples (b) at 30°C (●), 50°C (□), 70°C (▽), 90°C (- -), and 120°C (—) °C, respectively.

4.3. Simplified Protocol Accelerating Aging. To gain more experimental evidences about the additives behavior in the plastic material, aged sterilized, and aged nonsterilized samples, thermally treated during FT-IR/ATR measurements, from 30°C to 120°C, were subsequently subjected to a SPAA process. Figure 5 shows the spectra collected at 30°C and 120°C for the samples before and after the SPAA process. Spectra collected at 30°C for aged samples (not SPAA process applied) present the heat stabilizers related bands that disappear at 120°C as previously described. The same samples, after an equivalent aging time of nine months, measured at 30°C (SPAA 30°C) present the band at 1540 cm^{-1} correlated to the presence of Zn carboxylates on the inner surface of the tubes. This behavior could be probably ascribed to a different distribution phenomenon of this additive from the bulk to the surface of the material as a consequence of the supplemental aging process. The fact that only the zinc carboxylates band appeared might confirm the exchange reaction between zinc chloride and calcium carboxylates that regenerates the active zinc carboxylates and, at the same time, consumes the calcium soap that probably reduces its concentration on the surface under the detection limit of the FT-IR/ATR technique. Consumption/exchange reactions and redistribution phenomena of the additives probably occur simultaneously but on a different time scale and, considering

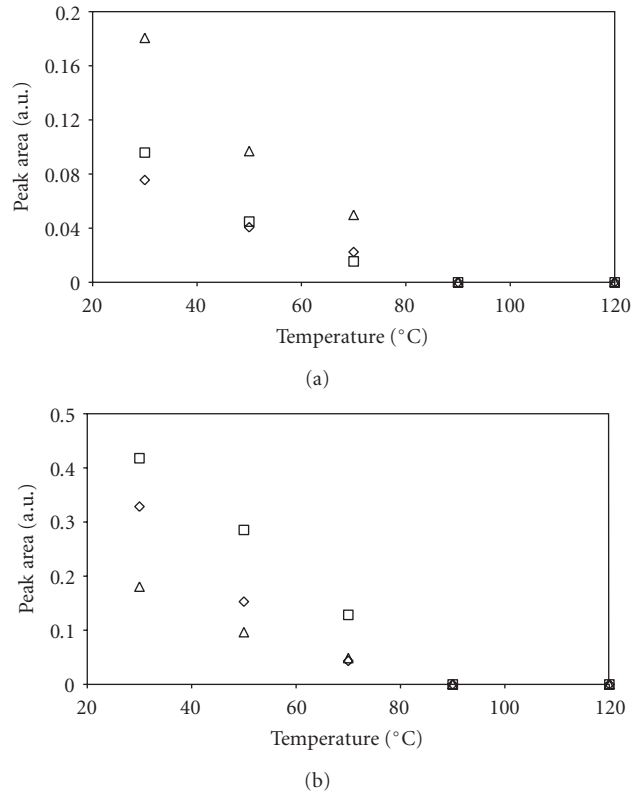


FIGURE 4: Plot of the calcium carboxylates (1576 cm^{-1}), (a), and zinc carboxylates (1540 cm^{-1}), (b), peak area at 30°C, 50°C, 70°C, 90°C, and 120°C, respectively, for the nonsterilized (◊), one year aged nonsterilized (□) and one year aged sterilized (△) samples.

the present experimental setup, it is troublesome to show whether the main phenomenon that occurs in the material is the additives reaction and/or their simple migration through the polymer framework.

4.4. Temperature versus Time Effects. Thermal stabilizers behavior was also studied at different temperatures with respect to time, by means of kinetics experiment at different, but constant, temperature. Spectra on sterilized and nonsterilized, aged one year, PVC tubing fragments were collected at different time by heating the samples at 30°C, 50°C, and 70°C. Three replicates were acquired for each sample with a time frequency of 10 minutes, and the mean signal of the replicates was considered. Figures 6 and 7 depict the trend of the peaks areas calculated for both the stabilizers IR bands, against the heating time for aged sterilized, Figure 6, and aged nonsterilized, Figure 7, samples, respectively. For the aged sterilized samples at 70°C, it was possible to follow the thermal stabilizers behavior only for a short time, since the peak area of the IR bands rapidly decrease and the absorption contribution disappears after 10 minutes. Nevertheless, it is possible to observe a decreasing trend, as a function of time, for both samples typologies. Moreover, the higher the temperature, the faster the decrease of the heat stabilizers

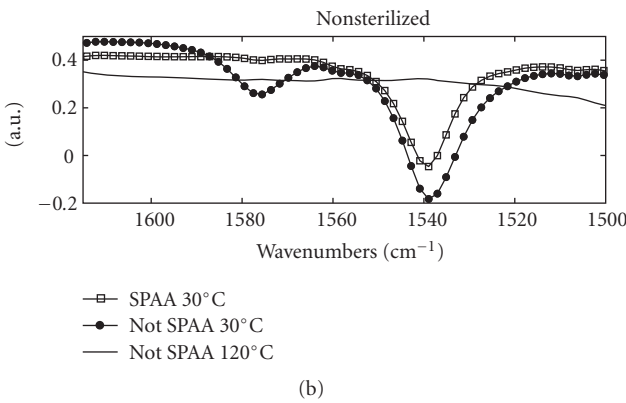
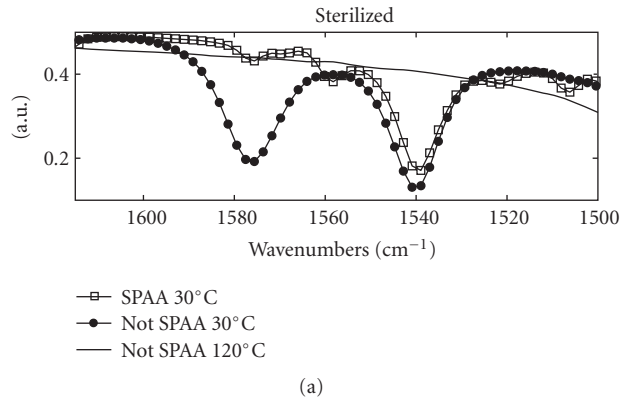


FIGURE 5: Extended view of the normalized FT-IR/ATR average spectra, wavelengths (cm^{-1}) versus arbitrary units (a.u.), of not SPAA and SPAA sterilized samples (a) and not SPAA and SPAA nonsterilized samples (b) at 30°C and 120°C.

bands is. Even in this case, temperature and time play an important role in the distribution phenomena of the calcium and zinc soaps in the plastic material even if PVC degradation processes are not excluded *a priori*; hence, a reaction between stabilizers degradation products are possible especially at high temperature.

5. Conclusions

Aim of this work was the description of the behavior of heat stabilizers in tubing components used for extracorporeal medical disposable devices. In particular, this work was focused on the study of calcium and zinc soaps distribution on the inner surface of extruded tubes as a function of temperature and sample state, namely, nonsterilized/sterilized and aged nonsterilized/sterilized.

In particular, nonsterilized and sterilized materials show a different IR fingerprint when considering the heat stabilizers distribution. The huge decrease of the thermal stabilizers related bands (1575 and 1540 cm^{-1}) for nonsterilized, aged nonsterilized, and aged sterilized samples from 30°C to 120°C seems to be correlated to a change in the distribution pattern of the additives from the surface to the bulk of the tube even if increasing the temperature above 70°C , a

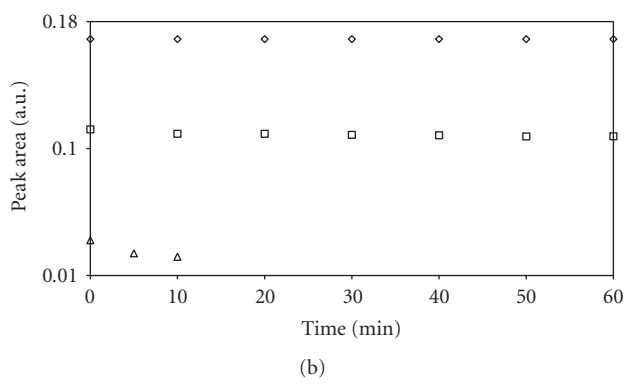
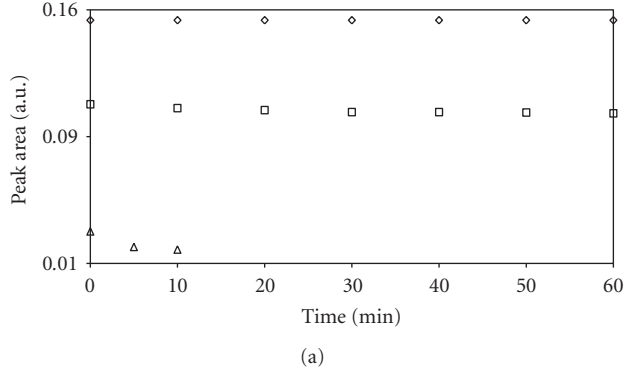


FIGURE 6: Plot of the calcium carboxylates (1576 cm^{-1}), (a), and zinc carboxylates (1540 cm^{-1}), (b), peak area versus heating time at constant temperature of 30°C (\diamond), 50°C (\square), and 70°C (\triangle) $^\circ\text{C}$ for one year aged sterilized samples.

thermal degradation of PVC-based product probably occurs. Moreover, after a simulated supplementary aging process of 9 months, only the zinc carboxylates band (1540 cm^{-1}) was monitored probably because of the exchange reaction between zinc chloride and calcium carboxylates that regenerates the active zinc carboxylates protecting the resin itself from thermal degradation. The behavior of PVC thermal stabilizers was also studied at different temperatures, 30°C , 50°C , and 70°C , with respect to time. It is possible to observe a decreasing trend of the intensities of calcium and zinc carboxylates bands as a function of time and temperature for both sterilized and nonsterilized aged samples. Results suggest that the behavior of thermal stabilizers is quite complex, and the investigated phenomena, migration, and/or consumption of the additives probably occur simultaneously in the material. In particular, at temperature below 50°C , it is reasonable to hypothesize that migration phenomena prevail upon reaction mechanisms, since at these temperatures, PVC degradation is quite unexpected. On the contrary, higher temperatures probably induce both consumption and redistribution of the heat stabilizers species within the PVC material. However, further investigations on the role and properties of calcium and zinc soaps in PVC-based formulations for biomedical applications are needed.

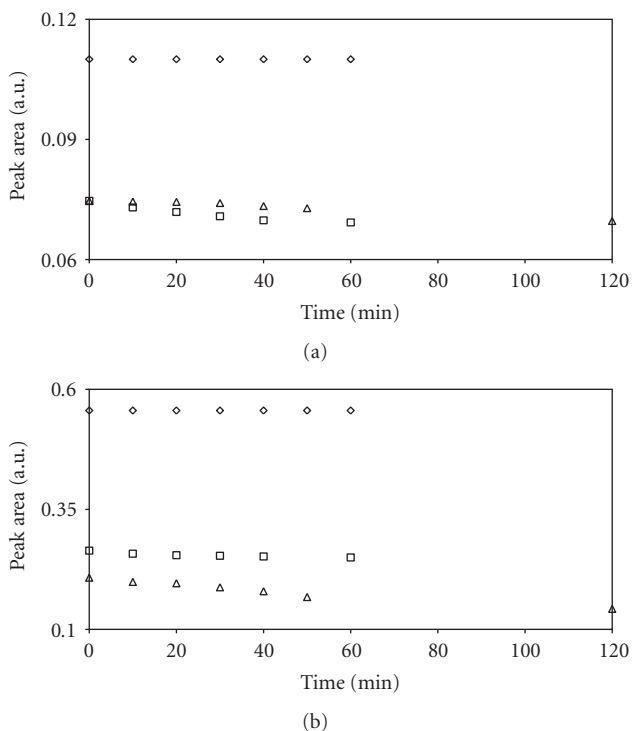


FIGURE 7: Plot of the calcium carboxylates (1576 cm^{-1}) (a), and zinc carboxylates (1540 cm^{-1}), (b), peak area versus heating time at constant temperature of 30 (◊), 50 (□) and 70 (△) $^{\circ}\text{C}$ for one year aged nonsterilized samples.

Acknowledgment

Gambro Dasco S.p.A is kindly acknowledged for the use of its facilities during the production and sampling stages and also for the fruitful collaboration with the University of Modena and Reggio Emilia, Department of Chemistry.

References

- [1] R. Bacalogulu, M. H. Fisch, J. Kaufhold, and H. J. Sander, "PVC Stabilizers," in *Plastics Additives Handbook*, H. Zweifel, Ed., chapter 3, Munich, Germany, 5th edition, 2001.
- [2] M. Hakkarainen, "New PVC materials for medical applications—the release profile of PVC/polycaprolactone-polycarbonate aged in aqueous environments," *Polymer Degradation and Stability*, vol. 80, no. 3, pp. 451–458, 2003.
- [3] R. Ito, F. Seshimo, Y. Haishima et al., "Reducing the migration of di-2-ethylhexyl phthalate from polyvinyl chloride medical devices," *International Journal of Pharmaceutics*, vol. 303, no. 1-2, pp. 104–112, 2005.
- [4] Y. R. Shashoua, "Effect of indoor climate on the rate and degradation mechanism of plasticized poly(vinyl chloride)," *Polymer Degradation and Stability*, vol. 81, no. 1, pp. 29–36, 2003.
- [5] Q. Wang and B. K. Storm, "Separation and analysis of low molecular weight plasticizers in poly(vinyl chloride) tubes," *Polymer Testing*, vol. 24, no. 3, pp. 290–300, 2005.
- [6] Y. B. Liu, W. Q. Liu, and M. H. Hou, "Metal dicarboxylates as thermal stabilizers for PVC," *Polymer Degradation and Stability*, vol. 92, no. 8, pp. 1565–1571, 2007.
- [7] Y. Haishima, R. Matsuda, Y. Hayashi, C. Hasegawa, T. Yagami, and T. Tsuchiya, "Risk assessment of di(2-ethylhexyl)phthalate released from PVC blood circuits during hemodialysis and pump-oxygenation therapy," *International Journal of Pharmaceutics*, vol. 274, no. 1-2, pp. 119–129, 2004.
- [8] K. Kambia, T. Dine, B. Gressier et al., "Evaluation of childhood exposure to di(2-ethylhexyl) phthalate from perfusion kits during long-term parenteral nutrition," *International Journal of Pharmaceutics*, vol. 262, no. 1-2, pp. 83–91, 2003.
- [9] N. M. K. Lamba, J. M. Courtney, J. D. S. Gaylor, and G. D. O. Lowe, "In vitro investigation of the blood response to medical grade PVC and the effect of heparin on the blood response," *Biomaterials*, vol. 21, no. 1, pp. 89–96, 2000.
- [10] X. Zhao and J. M. Courtney, "Influence on blood of plasticized polyvinyl chloride: significance of the plasticizer," *Artificial Organs*, vol. 23, no. 1, pp. 104–107, 1999.
- [11] M. Manfredini, A. Marchetti, D. Atzei et al., "Radiation-induced migration of additives in PVC-based biomedical disposable devices. Part 1. Surface morphology by AFM and SEM/XEDS," *Surface and Interface Analysis*, vol. 35, no. 4, pp. 395–402, 2003.
- [12] M. Manfredini, A. Marchetti, D. Atzei et al., "Radiation-induced migration of additives in PVC-based biomedical disposable devices part 2. Surface analysis by XPS," *Surface and Interface Analysis*, vol. 35, no. 8, pp. 673–681, 2003.
- [13] L.J. Gonzalez-Ortiz, M. Arellano, M.J. Sanchez-Pena, E. Mendizabal, and C.F. Jasso-Gastinel, "Effect of stearate preheating on the thermal stability of plasticized PVC compounds," *Polymer Degradation and Stability*, vol. 91, no. 11, pp. 2715–2722, 2006.
- [14] D. Briggs, *Surface Analysis of Polymer by XPS and Static SIMS*, Cambridge University Press, New York, NY, USA, 1998.
- [15] W. H. Starnes, "Structural and mechanistic aspects of the thermal degradation of poly(vinyl chloride)," *Progress in Polymer Science*, vol. 27, no. 10, pp. 2133–2170, 2002.
- [16] D. Atek and N. Belhaneche-Bensemra, "FTIR investigation of the specific migration of additives from rigid poly(vinyl chloride)," *European Polymer Journal*, vol. 41, no. 4, pp. 707–714, 2005.
- [17] M. Minegawa, "New developments in polymer stabilization," *Polymer Degradation and Stability*, vol. 25, no. 2–4, pp. 121–141, 1989.
- [18] "European pharmacopoeia IV," Section 3.1, 2002.
- [19] A. A. De Queiroz, É. R. Barrak, and S. C. De Castro, "Thermodynamic analysis of the surface of biomaterials," *Journal of Molecular Structure*, vol. 394, no. 2-3, pp. 271–279, 1997.
- [20] C. Anton-Prinet, G. Mur, M. Gay, L. J. Audouin, and J. Verdu, "Photoageing of rigid PVC—I. Films containing Ca/Zn thermal stabiliser," *Polymer Degradation and Stability*, vol. 60, no. 2-3, pp. 265–273, 1998.
- [21] R. Benavides, M. Edge, and N. S. Allen, "The mode of action of metal stearate stabilisers in poly(vinyl chloride): II. Influence of pre-heating on induction times and carbonyl formation," *Polymer Degradation and Stability*, vol. 49, no. 1, pp. 205–211, 1995.
- [22] R. Benavides, M. Edge, and N. S. Allen, "The mode of action of metal stearate stabilisers in poly(vinyl chloride). I. Influence of pre-heating on melt complexation," *Polymer Degradation and Stability*, vol. 44, no. 3, pp. 375–378, 1994.
- [23] I. Fras, P. Cassagnau, and A. Michel, "Lubrication and slip flow during extrusion of plasticized PVC compounds in the presence of lead stabilizer," *Polymer*, vol. 40, no. 5, pp. 1261–1269, 1999.

- [24] I. Fras, P. Cassagnau, and A. Michel, "Influence of processing conditions on the leaching of thermal stabilizers from plasticized polyvinyl chloride in the presence of water," *Journal of Applied Polymer Science*, vol. 70, no. 12, pp. 2391–2400, 1998.
- [25] L. M. Bodecchi, M. Cocchi, M. Malagoli, M. Manfredini, and A. Marchetti, "Application of infrared spectroscopy and multivariate quality-control methods in PVC manufacturing," *Analytica Chimica Acta*, vol. 554, no. 1-2, pp. 207–217, 2005.
- [26] M. Beltrán, J. C. García, and A. Marcilla, "Infrared spectral changes in PVC and plasticized PVC during gelation and fusion," *European Polymer Journal*, vol. 33, no. 4, pp. 453–462, 1997.
- [27] F. Garbassi, M. Morra, and E. Occhiello, *Polymer Surfaces. From physics to Technology*, chapter XII, Wiley, Chichester, UK, 1998.
- [28] B. D. Ratner, "Biomaterials science: an interdisciplinary endeavor," in *Materials in Medicine*, B. D. Ratner, A. S. Hoffman, F. J. Schoen, and J. Lemons, Eds., chapter I, Academic Press, San Diego, Calif, USA, 1996.
- [29] D. Coombs, "The use of diamond as an ATR material," *Vibrational Spectroscopy*, vol. 2, pp. 3–5, 1999.
- [30] B. Singh and N. Sharma, "Mechanistic implications of plastic degradation," *Polymer Degradation and Stability*, vol. 93, no. 3, pp. 561–584, 2008.
- [31] B. J. Lambert and F. W. Tang, "Rationale for practical medical device accelerated aging programs in AAMI TIR 17," *Radiation Physics and Chemistry*, vol. 57, no. 3–6, pp. 349–53, 2000.
- [32] AAMI, "Compatibility of materials subject to sterilization," Tech. Rep. AAMI TIR17, Association for the Advancement of Medical Instrumentation, Washington Boulevard, Calif, USA, 2008.
- [33] C. A. Andersson and R. Bro, "The N-way toolbox for MATLAB," *Chemometrics and Intelligent Laboratory Systems*, vol. 52, no. 1, pp. 1–4, 2000.
- [34] M. M. Hirschler, "Hydrogen chloride evolution from the heating of poly(vinyl chloride) compounds," *Fire and Materials*, vol. 29, no. 6, pp. 367–382, 2005.

Research Article

Effect of Artificial Saliva on the Apatite Structure of Eroded Enamel

Xiaojie Wang,^{1,2} Boriana Mihailova,¹ Arndt Klocke,^{3,4}
Stefanie Heidrich,¹ and Ulrich Bismayer¹

¹Department of Earth Sciences, University of Hamburg, Grindelallee 48, 20146 Hamburg, Germany

²Department of Preventive, Restorative and Pediatric Dentistry, School of Dental Medicine, University of Bern, Freiburgstrasse 7, CH—3010 Bern, Switzerland

³Division of Orthodontics, Department of Orofacial Sciences, The University of California San Francisco, 707 Parnassus Avenue, San Francisco, CA 94143-0438, USA

⁴Department of Orthodontics, University Medical Center Hamburg-Eppendorf, Martinistraße 52, 20246 Hamburg, Germany

Correspondence should be addressed to Boriana Mihailova, boriana.mihailova@uni-hamburg.de

Received 25 March 2011; Accepted 2 May 2011

Academic Editor: Sergio Armenta Estrela

Copyright © 2011 Xiaojie Wang et al. This is an open access article distributed under the Creative Commons Attribution License, which permits unrestricted use, distribution, and reproduction in any medium, provided the original work is properly cited.

Citric acid-induced changes in the structure of the mineral component of enamel stored in artificial saliva were studied by attenuated total reflectance infrared spectroscopy as well as complementary electron probe microanalysis and scanning electron microscopy. The results indicate that the application of artificial saliva for several hours (the minimum time period proved is 4 h) leads to slight, partial recovering of the local structure of eroded enamel apatite. However, artificial saliva surrounding cannot stop the process of loosening and breaking of P–O–Ca atomic linkages in enamel subjected to multiple citric acid treatments. Irreversible changes in the atomic bonding within 700 nm thick enamel surface layer are observed after three times exposure for 1 min to aqueous solution of citric acid having a pH value of 2.23, with a 24-hour interval between the individual treatments. The additional treatment with basic fluoride-containing solutions (1.0% NaF) did not demonstrate a protective effect on the enamel apatite structure per se.

1. Introduction

Acidic foods or beverages tend to cause tooth erosion, a chemical dissolution of surface hard tissues resulting from a tooth exposure to a variety of acids [1, 2]. Salivary flow plays an important role in minimizing enamel erosion by acid attack [2, 3]. To elucidate how saliva counteracts erosive demineralization, several characteristics of enamel, for example, hardness, surface morphology, mineral loss, and lesion depth, have been investigated [4–7]. It is speculated that saliva buffering capacity, content of calcium and phosphate groups, pellicle acquired on tooth surface and so forth, can act either solely or in combination to inhibit the tooth erosive procedures [8–10]. *In vitro* and *in vivo* studies proved that natural saliva and its synthetic substitutes reduce enamel mineral loss [4, 5], enhance enamel rehardening [7, 11], and decrease erosive lesion depth [4, 5]. Sodium fluoride solutions have been aimed at minimizing erosive processes.

Recently, it has been reported that the *in vitro* application of NaF solutions on enamel reduces the acidic-induced mineral loss [12, 13]. Hughes et al. [14] also found that fluoride application in acidic solutions or as a pretreatment reduced enamel erosion although the benefit observed was small and probably not clinically relevant. Hove et al. [15, 16] came to a similar conclusion when investigating enamel exposed to HCl (simulating a gastric reflux situation); while the *in vitro* study demonstrated a reduction of etching depth by 25% due to a protective effect of NaF, a followup *in situ* study could not confirm the protective effect. Hence, further investigations are required to better understand the effect of saliva and sodium fluoride on the interatomic bonding in the mineral component of eroded enamel.

Recently, attenuated total reflectance infrared (ATR IR) spectroscopy has been successfully applied to analyze the effect of tooth bleaching and acid challenge on enamel crystal structure [17, 18]. This technique probes the crystal structure

of outermost layers of the tooth tissue within micron and submicron thickness. It was demonstrated that the position of the most intense ATR IR peak, which arises from the antisymmetrical $\nu_3(\text{PO}_4)$ mode of apatite, indicates the occurrence of structural changes in superficial enamel apatite treated with acidic reagents [17, 18]. Combined chemical and spectroscopic analyses showed that acidic agents loosen and/or even break a part of the Ca–O bonds in apatite, which leads to stiffening of the adjacent P–O bonds and, subsequently, to a shift of the major ATR IR peak to higher wavenumbers [18]. Our previous *in vitro* study on the local structural alteration of enamel apatite induced by citric acid and NaF-containing solutions revealed that the application of fluoride alone does not suppress the local structural changes in apatite exposed to acidic agents [17].

Saliva is a very important biological parameter related to dental erosion development [19]. Several mechanisms might be involved into the protection of saliva against tooth erosion: (i) saliva directly acts on the erosive agent itself by diluting, clearing, neutralizing, and buffering acids; (ii) the organic components of saliva may form a thin protective film (pellicle) on the enamel surface, which acts as a diffusion barrier or a perm-selective membrane, preventing direct contact between the acids and tooth surface and thus affecting the dissolution rate of dental hard tissue; (iii) due to the content of calcium and phosphate ions, saliva serves as a natural reservoir for apatite regrowth and/or nucleation of new nanocrystals. To elucidate which of these three effects plays a major protective role, the three contributions should be analyzed independently.

The aim of this study is to shed light on the effect of saliva as a source of calcium and phosphate ions as well as to check if the additional application of a basic sodium fluoride solution would influence the effect of saliva. For this purpose, citric acid-induced changes in the atomic structure and bonding of enamel stored in distilled water and in an artificial saliva environment were compared, using ATR IR spectroscopy as well as complementary electron probe microanalysis (EPMA) and scanning electron microscopy (SEM). Additionally, the effect of topical application of sodium fluoride on the eroded enamel stored in artificial saliva was analyzed.

2. Materials and Methods

2.1. Experimental Procedure. The enamel specimens used in this study were prepared from noncarious human molars. Slabs parallel to the enamel-dentin junction function (see Figure 1) and of approximate size $3 \times 2 \times 2$ mm were cut from the middle one-third of the enamel surface using a diamond wire saw. The outer surface of the enamel slabs was polished and further analyzed. About $100\text{ }\mu\text{m}$ of the outermost enamel layer was removed during the process of grinding and polishing. A suspension of 100-nm-sized colloidal silica was used at the final stage of polishing. The achieved quality of surface smoothness was excellent for spectroscopic, EPMA, and SEM experiments. To avoid any uncertainties and misinterpretation of the experimental data due to tooth-to-tooth variability, adjacent cuts from the

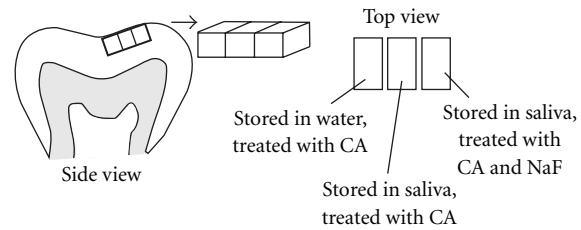


FIGURE 1: Sketch of enamel specimen design.

same tooth were subjected to different types of treatments (see Figure 1). When such an experimental design is used, the quantitative comparison of the effect of the treatment procedure is much more reliable, since ATR IR spectroscopy is sensitive to the specimen orientation as well as to the tooth-to-tooth variation in resistance to acidic challenge, which in turn is related to variations in tooth enamel texture, apatite crystal chemistry, organic-mineral component ratio, and so forth, [17, 18]. Spectra collected from specimens prepared from different teeth show slight statistical variations in the absolute peak positions and relative intensities, but the treatment-induced changes in the spectral features are independent of the specimen origin. We have verified this on more than 10 samples. Hence, for a better comparison, the experimental results presented in the paper are obtained on slabs cut from the same tooth, but the statistics over cuts from different teeth revealed the repeatability of the dependence of the spectral parameters on the sequence of chemical treatment.

In the first version of this paper we have already stated that spectra collected from specimens prepared from different teeth show slight statistical variations in the absolute peak positions and relative intensities, but the treatment-induced changes in the spectral features are independent of the specimen origin. We have verified this on more than 10 samples. However, we present the data collected only on one.

We applied three different treatment procedures to adjacent cuts of the same tooth.

(A) Enamel specimens were stored in distilled water at 37°C and manifold treated with a 0.1 mol/L citric acid solution having a pH value of 2.23; the time of a single acidic exposure was 1 min.

(B) Enamel specimens were firstly immersed into artificial saliva at 37°C for 7 days and then submitted to a demineralization cycle repeated three times. The demineralization treatment was performed also in a 0.1 mol/L citric acid solution for 1-minute. The short period of a 1 min exposure was chosen to mimic the conditions during beverage consumption, while the remineralization treatment was carried out in artificial saliva at 37°C for at least 4 h. After each treatment with citric acid solution, the samples were rinsed with distilled water, dried in air, and subjected to ATR spectroscopic measurements, while after each period of storage in artificial saliva, the samples were only dried in air and then subjected to ATR spectroscopic measurements. The artificial saliva was changed every 24 h.

(C) The same treatment as in procedure B, but the samples were additionally exposed to a 1.0% NaF solution

with a pH value of 10.05 for 5 min three times daily. This regimen was chosen to simulate a clinical situation using topical fluoride therapy recommended to prevent erosion.

Thus, the comparison between enamel subjected to procedure A and that subjected to procedures B and C can reveal the effect of artificial saliva on demineralization processes, while the comparison between enamel treated according to procedure B and procedure C demonstrates the cooperative effect of saliva and fluoride.

The artificial saliva was prepared according to Klimek et al. [20]: 0.002 g ascorbic acid, 0.030 g glucose, 0.580 g NaCl, 0.170 g CaCl₂, 0.160 g NH₄Cl, 1.270 g KCl, 0.160 g NaSCN, 0.330 g KH₂PO₄, 0.200 g urea, 0.340 g Na₂HPO₄, and 2.700 g mucin (Bacto-Mucin Bacteriological) in 1000 mL distilled water. The solution was further titrated with a phosphate buffer of 26.4 mL 0.06 M Na₂HPO₄·2H₂O and 7.36 mL 0.06 M KH₂PO₄, following the procedure described by Burgmaier et al. [21]. The achieved pH value of the artificial saliva solution was 8.0. This pH value is representative of saliva under conditions of stimulation [22] and is, thus, relevant for remineralization processes.

Aqueous solutions of 0.1 mol/L citric acid and 1.0% NaF were prepared by dissolving an appropriate amount of powder in distilled water.

2.2. Analytical Methods

2.2.1. ATR IR. ATR IR spectra were collected with a Bruker Equinox 55 FTIR spectrometer equipped with a Pike MIRacle ATR accessory, having a single-reflection sampling plate and a round contact surface between the ATR crystal and the sample with a diameter of 1.8 mm. The force applied to the sample to achieve a good contact with the ATR crystal was controlled by a micrometer pressure clamp, and for all samples, the magnitude of the force was the same as the maximal allowed by the device. The background spectrum was collected from an optically homogeneous polished plate-shaped KBr crystals (KBr window, Korth Kristalle GmbH). The use of a Ge ATR crystal assured a characteristic penetration depth of approximately 700 nm at 1000 cm⁻¹, which allowed the separation of the surface IR absorption from the bulk one by enhancing the signal coming from the submicron surface layer. The spectra were recorded with an instrumental resolution of 4 cm⁻¹ resolution, averaging over 512 scans. The spectra were measured in the spectral range 570–4000 cm⁻¹ and subsequently normalized to a constant penetration depth. Only slabs free of cracks observable under an optical microscope were investigated. The repeatability of the spectra was verified by collecting at least two spectra from the same specimen. No variations in the peak positions and relative intensities depending on the positioning of the sample in the ATR unit were detected. Since the contact surface area between the sample and ATR crystal is approximately 2.54 mm², lateral inhomogeneities of the sample on the micrometer- or submicrometer scale, cannot influence the overall IR signal.

2.2.2. SEM. To observe the surface morphology of dental enamel, samples coated with gold were studied by SEM

imaging. The micrographs were recorded with a Zeiss LEO 1455VP scanning electron microscope operating at 20 kV.

2.2.3. EPMA. The lateral chemical inhomogeneity of dental enamel was analyzed by conducting mapping of Ca, P, Na, and Cl, using an electron probe microanalyzer Cameca Microbeam SX100 equipped with a wavelength- and energy-dispersive system. The mapping was performed with a step size of 0.1 μm and a penetration depth of approximately 1.0 μm.

2.2.4. Background Results. Previous studies demonstrated that the spectral range of 900–1200 cm⁻¹, which is dominated by the stretching modes of PO₄ tetrahedra, is the range most pronouncedly impacted by acid challenge [17, 18]. ATR IR spectroscopy probes the atomic bonding of the outermost enamel apatite within a layer corresponding to the characteristic penetration depth, which in our experiment is 700 nm. A higher wavenumber of the peak related to the antisymmetric stretching mode of PO₄ tetrahedra is indicative of changes in the local structure of hydroxyapatite, namely, occurrence of loosened and/or broken Ca–O bonds and thus disturbing the typical atomic surroundings of PO₄ groups. Therefore, the degree of local atomic structural damage in surficial enamel apatite can be quantified by the change in the position of the strongest ATR IR peak near 1015 cm⁻¹ with respect to that of untreated enamel.

3. Results

Figure 2(a) shows the change in the major peak position of enamel stored in water as a function of the number of treatments with citric acid solution of pH = 2.23 for 1 min. The peak positions were determined by fitting the spectral profile in the range of 900–1200 cm⁻¹ using four Lorentz functions (see Figure 2(b)). The number of Lorentzians was consistent with the four internal stretching modes of PO₄ tetrahedra: one symmetric and three antisymmetric, which are nondegenerate in the case of irregular tetrahedron. According to group-theory analysis of apatite, the number of crystal phonon modes related to the internal stretching modes is larger than four, due to the multiplicity of the tetrahedral ions in the crystal. However, the experimental IR profile of untreated apatite shows four signals in the range of 900–1200 cm⁻¹, which indicates that the wavenumbers of the crystal phonon modes related to P–O stretching are grouped around the wavenumbers of the corresponding internal tetrahedral modes. Hence, the simplest model to fit the spectral range of 900–1200 cm⁻¹ of apatite involves four Lorentzians.

As can be seen in Figure 2(a), after three times of acid exposure, the degree of damage within a surface layer of ~700 nm, which is the characteristic penetration depth of our ATR IR experiments, reaches a saturation level. A similar trend was observed for enamel treated with milder acidic agents for longer time [17]. The statistics over a large number of samples show that when the structural damage of the surface layers reaches a saturation, the change in the position of the major peak is ~15 cm⁻¹ with a deviation of ±4 cm⁻¹.

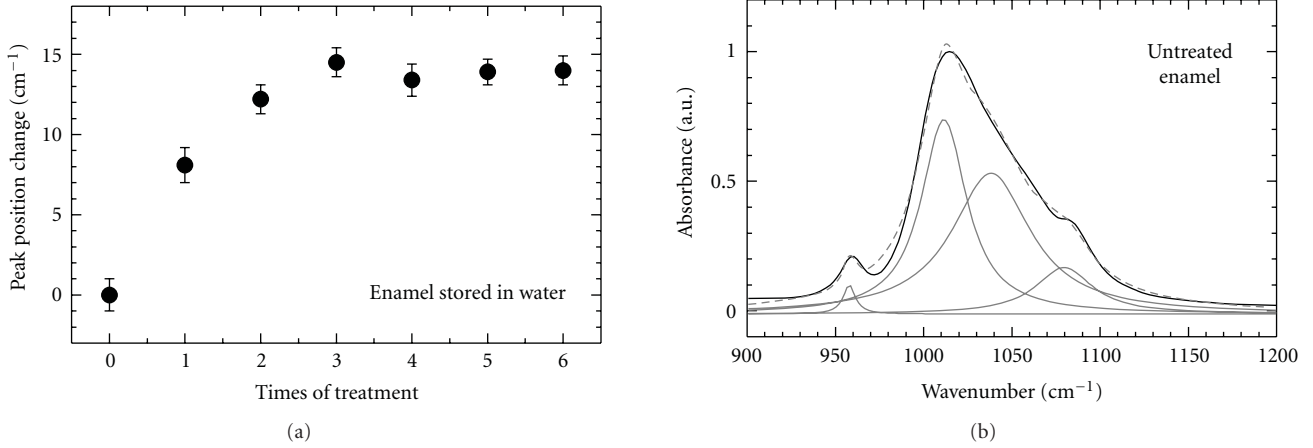


FIGURE 2: Shift of the major ATR IR peak near 1015 cm^{-1} for enamel stored in water versus number of 1-minute treatments with citric acid, pH = 2.23 (a); experimental spectrum of untreated enamel (bold black line) fitted with 4 Lorentzians (thin gray lines) and the resultant profile (dashed gray line) (b). The error bars in (a) correspond to uncertainties in peak positions resulting from spectrum profile fittings. The position of the second Lorentzian is 1012 cm^{-1} , which value was taken as initial wavenumber to calculate the peak position changes.

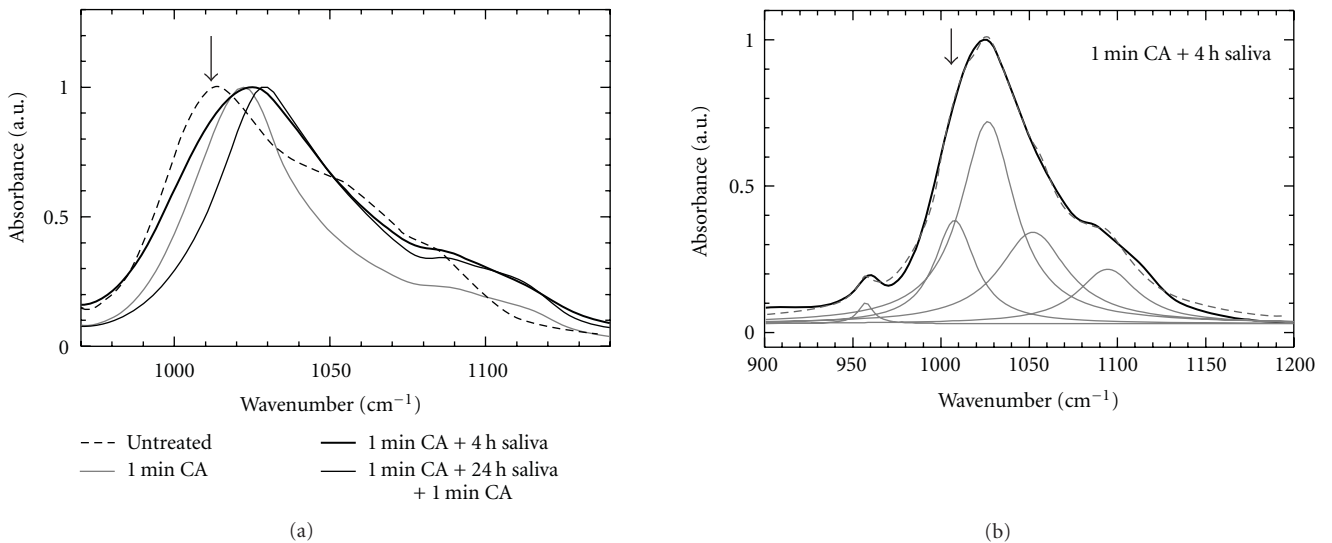


FIGURE 3: ATR IR spectra of untreated enamel (dashed line), treated with citric acid (CA) for 1 min (thin gray line), treated with CA for 1 min and then stored in saliva (S) for 4 h (bold black line), and treated with CA for 1 min, then stored in saliva for 24 h, and treated again with CA for 1 min (thin black line) (a); experimental spectrum of enamel treated with CA for 1 min and then stored in saliva for 4 h (bold black line) fitted with 5 Lorentzians (thin gray lines) and the resultant profile (dashed gray line) (b). The arrow in both plots points to the lower-wavenumber shoulder observed for enamel subsequently stored in saliva for 4 h, the position of which matches the position of the major ATR IR peak for untreated enamel.

Further, we compared the effect of citric acid on enamel stored in water and in artificial saliva. The preliminary soaking of enamel in saliva for 7 days did not affect the ATR IR spectrum, which confirms that the used chemical composition of artificial saliva is adequate to probe the acid-induced alteration of apatite atomic bonding in salivary surroundings. After a single treatment with citric acid with pH = 2.23 for 1 min, enamel prestored in saliva showed the same ATR IR spectrum as that of enamel kept in water, which

indicates that artificial saliva had no protective effect against such an acidic challenge under the experimental conditions. However, subsequent storage of enamel in saliva for 4 h led to detectable spectral changes. The main peak becomes broader and asymmetric in shape due to the appearance of a weak shoulder positioned lower wavenumbers (see Figure 3). Similar spectral changes were detected at the first step of acidic treatment of enamel subjected to a multistep acidic challenge and it indicates the development of an intermediate

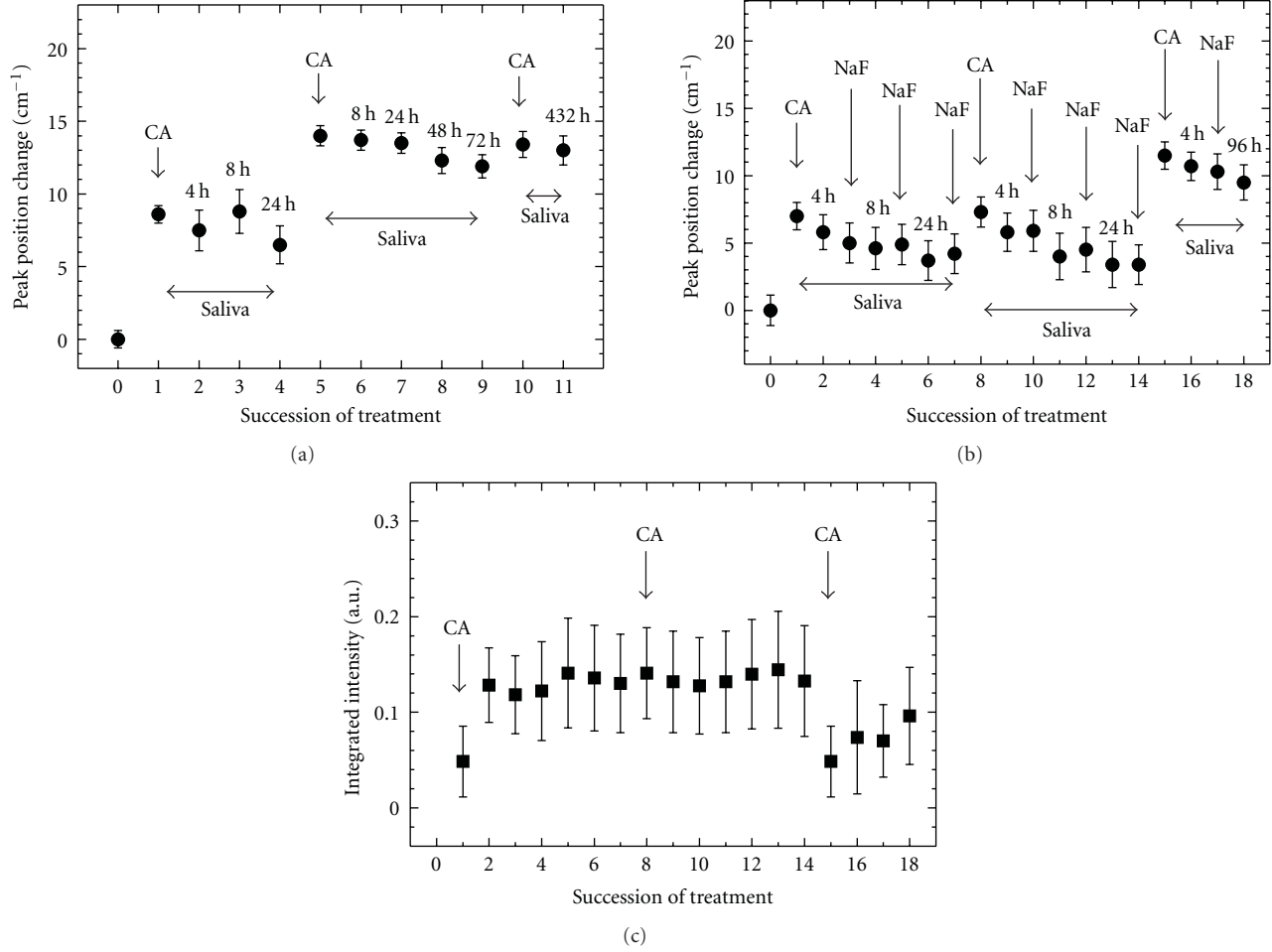


FIGURE 4: Shift of the major ATR IR peak near 1015 cm^{-1} for enamel stored in saliva (a) and for enamel stored in saliva and additionally exposed to NaF (b); each treatment with citric acid (CA) was performed for 1 min; the time of enamel storage in saliva is given with respect to the last treatment with citric acid; each treatment with NaF was performed for 5 min. The peak positions in (a) and (b) were obtained using a four-Lorentzian model to fit the spectrum profiles between 900 and 1200 cm^{-1} . (c) displays the integrated intensity of the lower-wavenumber side signal (see Figure 3) normalized to the total absorption intensity between 900 and 1200 cm^{-1} , when a five-Lorentzian model was applied to fit the spectrum profiles between 900 and 1200 cm^{-1} of samples stored in saliva and additionally exposed to NaF; for simplicity, only the points representing the citric-acid treatment are marked in (c); all other points exactly correspond to the points in (b).

structural stage consisting of spatial regions of heavily damaged apatite within a matrix of almost undamaged apatite [17]. Therefore, the results obtained on enamel stored in saliva after acidic exposure demonstrate a recovery effect of saliva on the local atomic structure of enamel apatite.

The signals arising from the affected and nonaffected/recovered regions are very close in wavenumber and overlap. Therefore, the two signals can be modelled as one Lorentzian, whose wavenumber would represent the weight coefficient of the two signals: a higher wavenumber indicates a larger contribution of the signal from the damaged regions, while a lower wavenumber indicates a larger contribution from the undamaged regions. Thus, when a four-Lorentzian model is used to fit the spectra of untreated and treated samples, the change in the peak position of the most intense IR band near 1015 cm^{-1} reflects the change in the fraction of damaged regions in enamel. Additionally, we have applied

a five-Lorentzian model to the spectra of samples stored in saliva. In this case, we have modelled the contribution from damaged and undamaged/recovered areas to the most intense IR band with two separate replicas. Thus, the trend in the intensity of the lower-wavenumber side band (see Figure 3) normalized to the total intensity in the range 900 – 1200 cm^{-1} represents the structural state of superficial enamel subjected to a deremineralization process: a lower intensity corresponds to a high degree of structural damage, while an increase in the intensity indicates recovering of the apatite structure. However, due to the strong overlapping of the peaks, the uncertainties in determining peak integrated intensities within a five-Lorentzian model are relatively large, which hampers the precise quantification of the degree of structural damage.

Figure 4 presents the trends of the spectral features of enamel stored in saliva. The change in the peak position as

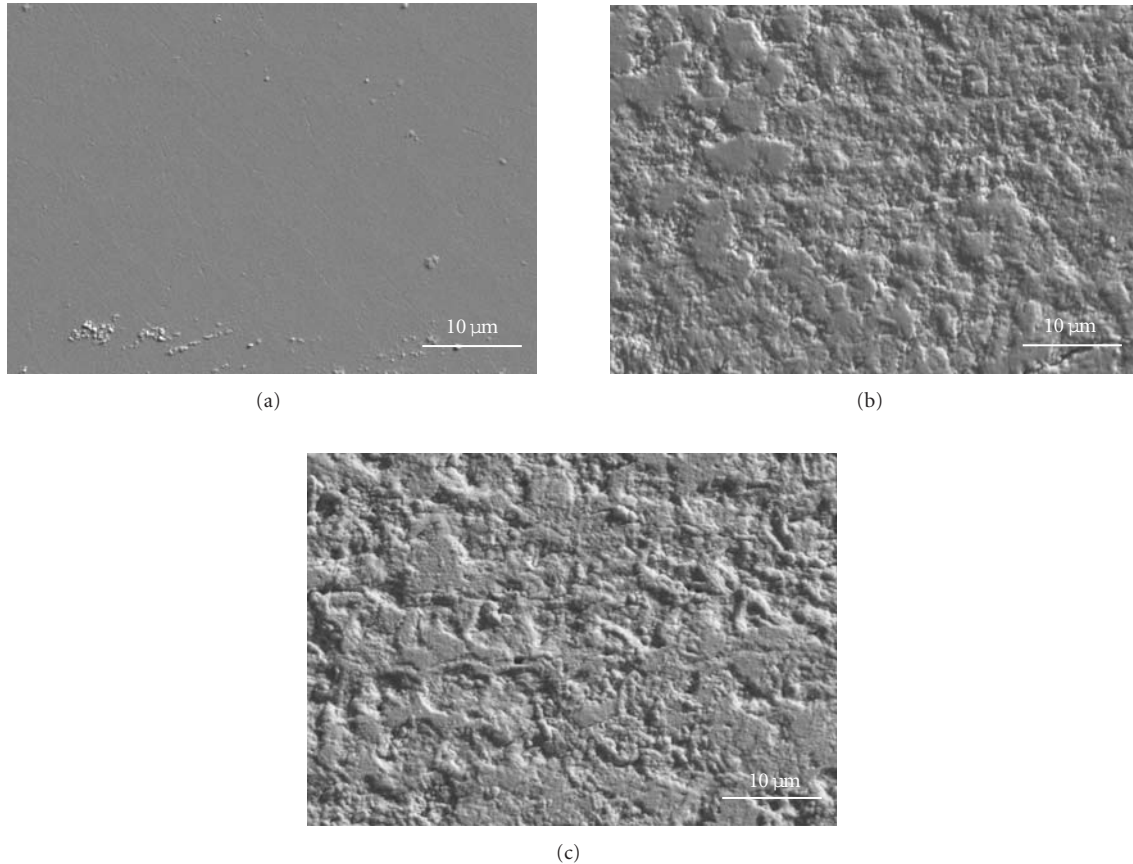


FIGURE 5: SEM micrographs of untreated enamel (a); enamel treated with citric acid and then remineralized in artificial saliva (b); enamel treated with citric acid and then remineralized in artificial saliva in combination with additional treated with NaF (c).

determined within a four-Lorentz model for enamel treated according to procedure B and C stored is shown in Figures 4(a) and 4(b), respectively. It is seen that artificial salivary environment leads to a partial recovery of the mineral component of enamel, but it cannot stop the overall violation of the atomic bonding in apatite upon multiple acidic attack.

The comparison between ATR IR data on enamel stored in saliva without and with additional NaF treatment (see Figures 4(a) and 4(b), resp.) reveals that topical application of NaF to artificial saliva does not inhibit the long-term structural alteration in eroded enamel. After a third acid exposure, the peak position change for enamel stored in saliva and additionally treated with NaF became the same as that of the peak position change for enamel stored in saliva, without being additionally treated with NaF. The use of the relative intensity of the lower-wavenumber side band (determined within the five-Lorentzian model) to estimate the structural state (see Figure 4(c)) confirms the results obtained within the four-Lorentzian model: the combination of saliva and a repetitive treatment with NaF opposes to the impact of citric acid after two times acidic exposure but have only a diminutive effect after a third treatment with citric acid.

SEM micrographs also show no detectable effect of NaF treatment in the experiment (Figure 5). The morphological changes observed for enamel subjected to a combination

of artificial saliva and NaF resemble those observed for enamel kept in artificial saliva, demonstrating in both cases apparent etching-like pattern. Moreover, the comparison between the Ca- and P-mapping images of enamel exposed to saliva and to saliva + NaF reveals a similar degree of lateral chemical inhomogeneity in the eroded surface (Figure 6). The mapping of Na and Cl (not shown) also revealed no difference between samples treated with artificial saliva alone and in combination with NaF.

4. Discussion

The position and the shape of the major ATR IR peak is a result of the existence of two overlapping components corresponding to noneroded and eroded enamel apatite. Figure 7 schematically represents the proposed mechanism of structure transformation processes in superficial enamel exposed first to citric acid and then to saliva. Initially, the treatment with citric acid leads to a formation of spatial areas with damaged apatite that exhibits local structural alteration, namely, broken and/or loosened P–O–Ca atomic linkages. After a prolonged treatment with citric acid, the entire surface layer probed by ATR IR spectroscopy (approximately 700 nm in thickness) is affected, and it consists of apatite with a high degree of local structural defects: PO_4 species

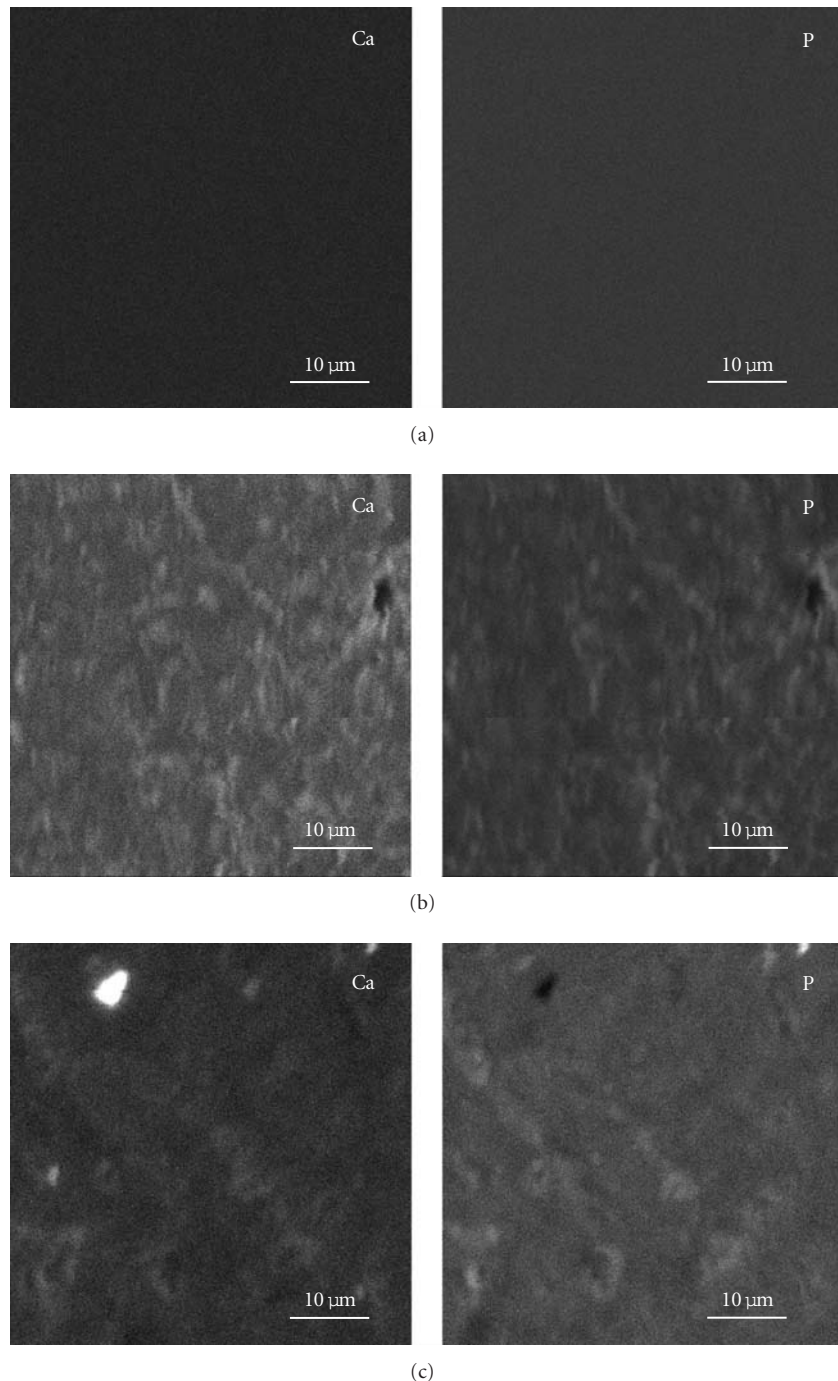


FIGURE 6: Electron-probe P- of Ca-mapping of untreated enamel (a); enamel treated with citric acid and then remineralized in artificial saliva (b); enamel treated with citric acid and then remineralized in artificial saliva in combination with additional treated with NaF (c).

with stiffer P–O bonds due to break and/or loosening of adjacent Ca–O bonds. Saliva stabilizes atomic linkages in apatite and favours the reappearance of spatial areas of defect-poor apatite. The resultant ATR IR peak shift with respect to position of the peak of untreated enamel actually reflects the different contribution of the two overlapping components: noneroded and eroded apatite. More abundant eroded enamel regions correspond to a larger peak shift.

Hence, the change in the major peak position is a reliable indicator of the degree of structural damage of apatite within a 700 nm surface layer. The spectroscopic results reveal subtle structural recovery of enamel eroded by citric acid with pH = 2.23 for 1 min after storage in artificial saliva for 4 hours. The effect of remineralization by saliva is more pronounced after 24 h; however, prolonged time of 3 days (see Figure 5(a)) does not lead to any further substantial changes. A repeated

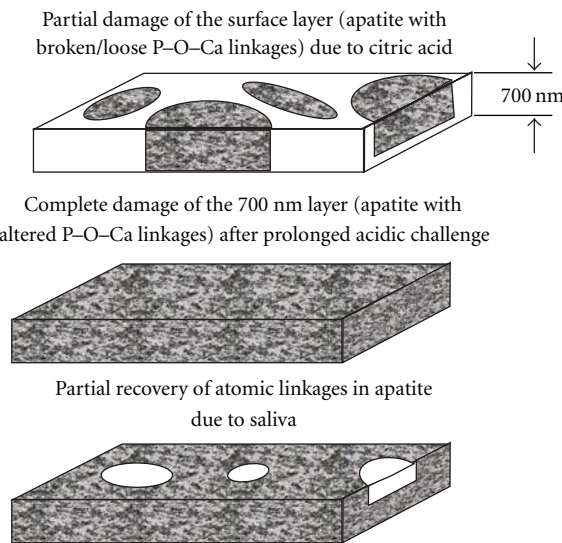


FIGURE 7: Sketch of deremineralization processes on enamel mineral surface layer of thickness ~ 700 nm; areas of undamaged apatite and damaged apatite (with broken or loose P–O–Ca atomic linkages) are represented by white and textured gray color, respectively.

application of deremineralization cycle leads to a more severe damage of enamel apatite, which cannot be recovered even after an exposure to artificial saliva for several days. These results, which are based on the change in atomic bonding and local arrangements, explain the detrimental effect of frequent intake of acidic foods and beverages, as resulting from the imbalance between acidic demineralization and salivary remineralization, which consequently leads to irreversible lesions of enamel apatite.

The results of the present study show that the topical application of NaF in the presence of artificial saliva does not suppress or reverse the loosening and break of atomic P–O–Ca linkages of enamel repeatedly exposed to acidic challenge. This indicates that saliva as a chemical reservoir is not the major reason for the enhancement of the long-term enamel resistance to an acidic challenge under a topical application of fluoride. Therefore, the mechanism of saliva + fluoride protective effect should be related to the pH value and/or the organic components of saliva. This is in agreement with previous findings based on *in vitro* study of enamel treated with various F-containing solutions [17], demonstrating that the potential of fluorine-containing agents to prevent enamel apatite from undesired acid-induced changes should be related mostly to the formation of a CaF₂ protective layer, which in turn depends on the pH value of the medium surrounding the enamel surface. Several studies on the hardness of enamel in a saliva environment also demonstrated that saliva is incapable of totally recovering the original surface structure of sound enamel [4, 23]. On the other hand, Eisenburger et al. [6] found that upon 24-hour remineralization in artificial saliva, eroded enamel returns to its normal level of resistance to ultrasonication. The controversial conclusions from different studies underline the complex effect of saliva and the necessity of well-designed experiments in order to

check the primary reason for the inhibition of the acid-induced damage in natural saliva environment.

The artificial saliva utilized in the present study was aimed at simulating saliva relevant for remineralization processes. Therefore, the pH value of the saliva was adjusted to levels natural saliva reaches under stimulation conditions and, thus, demonstrates improved salivary buffer capacity [22]. However, it should be emphasized that artificial saliva cannot model demineralization and remineralization processes in the intraoral environment related to various biological factors, such as salivary pellicle and biofilm, as well as to inherent F that favours the formation of protective CaF₂ layer. In general, natural saliva might offer a greater protection than artificial saliva due to the ability to form salivary pellicle that restricts the acid diffusion and transport of ions in and out of the enamel surface [24–27]. Therefore, under clinical conditions, the demineralization due to an erosive attack may be less pronounced compared to the conditions used in the current study.

In conclusion, partial recovery of the atomic bonding in the eroded enamel apatite occurs after several hours due to the favourable influence of the surrounding saliva. However, saliva as a chemical reservoir of calcium and phosphate ions cannot prevent irreversible local structural changes within a 700 nm layer of enamel apatite repeatedly exposed to acidic agents. Topical treatment with basic fluoride-containing agents seems to show a diminutive contribution to the ability of artificial saliva, supplying calcium and phosphate ions, to oppose to the acid-induced violation of the local atomic structure of enamel apatite.

Acknowledgments

The authors would like to thank Peter Stutz (University of Hamburg) for cutting and polishing dental samples and Yvonne Milker (University of Hamburg) for conducting SEM experiments. Financial support by the Deutsche Forschungsgemeinschaft (GRK-611) is gratefully acknowledged.

References

- [1] J. M. ten Cate and T. Imfeld, "Dental erosion, summary," *European Journal of Oral Sciences*, vol. 104, no. 2, pp. 240–244, 1996.
- [2] A. Lussi, T. Jaeggi, and D. Zero, "The role of diet in the aetiology of dental erosion," *Caries Research*, vol. 38, supplement 1, pp. 34–44, 2004.
- [3] G. A. Sánchez and M. V. Fernandez De Preliasco, "Salivary pH changes during soft drinks consumption in children," *International Journal of Paediatric Dentistry*, vol. 13, no. 4, pp. 251–257, 2003.
- [4] B. T. Amaechi and S. M. Higham, "In vitro remineralisation of eroded enamel lesions by saliva," *Journal of Dentistry*, vol. 29, no. 5, pp. 371–376, 2001.
- [5] B. T. Amaechi and S. M. Higham, "Eroded enamel lesion remineralization by saliva as a possible factor in the site-specificity of human dental erosion," *Archives of Oral Biology*, vol. 46, no. 8, pp. 697–703, 2001.
- [6] M. Eisenburger, J. Hughes, N. X. West, R. P. Shellis, and M. Addy, "The use of ultrasonication to study remineralisation of eroded enamel," *Caries Research*, vol. 35, no. 1, pp. 61–66, 2001.

- [7] D. Rios, H. M. Honório, A. C. Magalhães et al., "Effect of salivary stimulation on erosion of human and bovine enamel subjected or not to subsequent abrasion: an *in situ/ex vivo* study," *Caries Research*, vol. 40, no. 3, pp. 218–223, 2006.
- [8] A. F. Hall, C. A. Buchanan, D. T. Millett, S. L. Creanor, R. Strang, and R. H. Foye, "The effect of saliva on enamel and dentine erosion," *Journal of Dentistry*, vol. 27, no. 5, pp. 333–339, 1999.
- [9] T. Jaeggi and A. Lussi, "Toothbrush abrasion of erosively altered enamel after intraoral exposure to saliva: an *in situ* study," *Caries Research*, vol. 33, no. 6, pp. 455–461, 1999.
- [10] T. Attin, S. Knöfel, W. Buchalla, and R. Tütüncü, "In situ evaluation of different remineralization periods to decrease brushing abrasion of demineralized enamel," *Caries Research*, vol. 35, no. 3, pp. 216–222, 2001.
- [11] Y. Nekrashevych and L. Stösser, "Protective influence of experimentally formed salivary pellicle on enamel erosion: an *in vitro* study," *Caries Research*, vol. 37, no. 3, pp. 225–231, 2003.
- [12] N. Schlueter, C. Ganss, U. Mueller, and J. Klimek, "Effect of titanium tetrafluoride and sodium fluoride on erosion progression in enamel and dentine *in vitro*," *Caries Research*, vol. 41, no. 2, pp. 141–145, 2007.
- [13] C. Ganss, N. Schlueter, M. Hardt, P. Schattenberg, and J. Klimek, "Effect of fluoride compounds on enamel erosion *in vitro*: a comparison of amine, sodium and stannous fluoride," *Caries Research*, vol. 42, no. 1, pp. 2–7, 2008.
- [14] J. A. Hughes, N. X. West, and M. Addy, "The protective effect of fluoride treatments against enamel erosion *in vitro*," *Journal of Oral Rehabilitation*, vol. 31, no. 4, pp. 357–363, 2004.
- [15] L. Hove, B. Holme, A. Young, and A. B. Tveit, "The protective effect of TiF_4 , SnF_2 and NaF against erosion-like lesions *in situ*," *Caries Research*, vol. 42, no. 1, pp. 68–72, 2008.
- [16] L. Hove, B. Holme, B. Øgaard, T. Willumsen, and A. B. Tveit, "The protective effect of TiF_4 , SnF_2 and NaF on erosion of enamel by hydrochloric acid *in vitro* measured by white light interferometry," *Caries Research*, vol. 40, no. 5, pp. 440–443, 2006.
- [17] X. Wang, A. Klocke, B. Mihailova, L. Tosheva, and U. Bismayer, "New insights into structural alteration of enamel apatite induced by citric acid and sodium fluoride solutions," *Journal of Physical Chemistry B*, vol. 112, no. 29, pp. 8840–8848, 2008.
- [18] X. Wang, B. Mihailova, A. Klocke et al., "Side effects of a non-peroxide-based home bleaching agent on dental enamel," *Journal of Biomedical Materials Research A*, vol. 88, no. 1, pp. 195–204, 2009.
- [19] A. T. Hara, A. Lussi, and D. T. Zero, "Biological factors," in *Dental Erosion: From Diagnosis to Therapy (Monographs in Oral Science)*, A. Lussi, Ed., vol. 20, pp. 88–99, S. Karger AG, Basel, Switzerland, 2006.
- [20] J. Klimek, E. Hellwig, and G. Ahrens, "Fluoride taken up by plaque, by the underlying enamel and by clean enamel from three fluoride compounds *in vitro*," *Caries Research*, vol. 16, no. 2, pp. 156–161, 1982.
- [21] G. M. Burgmaier, I. M. Schulze, and T. Attin, "Fluoride uptake and development of artificial erosions in bleached and fluoridated enamel *in vitro*," *Journal of Oral Rehabilitation*, vol. 29, no. 9, pp. 799–804, 2002.
- [22] R. A. D. Williams and J. C. Elliott, *Basic and Applied Dental Biochemistry*, Churchill Livingstone, Edinburgh, Scotland, 1989.
- [23] H. Devlin, M. A. Bassiouny, and D. Boston, "Hardness of enamel exposed to Coca-Cola® and artificial saliva," *Journal of Oral Rehabilitation*, vol. 33, no. 1, pp. 26–30, 2006.
- [24] R. T. Zahradnik, D. Propas, and E. C. Moreno, "In vitro enamel demineralization by *Streptococcus mutans* in the presence of salivary pellicles," *Journal of Dental Research*, vol. 56, no. 9, pp. 1107–1110, 1977.
- [25] B. L. Slomiany, V. L. N. Murty, I. D. Mandel, S. Sengupta, and A. Slomiany, "Effect of lipids on the lactic acid retardation capacity of tooth enamel and cementum pellicles formed *in vitro* from saliva of caries-resistant and caries-susceptible human adults," *Archives of Oral Biology*, vol. 35, no. 3, pp. 175–180, 1990.
- [26] B. T. Amaechi, S. M. Higham, W. M. Edgar, and A. Milosevic, "Thickness of acquired salivary pellicle as a determinant of the sites of dental erosion," *Journal of Dental Research*, vol. 78, no. 12, pp. 1821–1828, 1999.
- [27] M. Hannig and M. Balz, "Influence of *in vivo* formed salivary pellicle on enamel erosion," *Caries Research*, vol. 33, no. 5, pp. 372–379, 1999.

Research Article

In Situ IR Characterization of CO Interacting with Rh Nanoparticles Obtained by Calcination and Reduction of Hydrotalcite-Type Precursors

F. Basile,¹ I. Bersani,¹ P. Del Gallo,² S. Fiorilli,^{3,4} G. Fornasari,¹ D. Gary,²
R. Mortera,^{3,4} B. Onida,^{3,4} and A. Vaccari¹

¹Dipartimento di Chimica Industriale e dei Materiali, Alma Mater Studiorum-Università di Bologna, V.le Risorgimento 4, 40136 Bologna, Italy

²Air Liquide, Centre de Recherche Claude Delorme1, Chemin de la Porte des Loges, BP 126, Les Loges-en-Josas, 78354 Jouy-en-Josas Cedex, France

³Dipartimento di Scienza dei Materiali e Ingegneria Chimica, Politecnico di Torino, Corso Duca degli Abruzzi 24, 10129 Torino, Italy

⁴CpR-INSTM for Materials with Controlled Porosity, Via Giusti 9, 50121 Firenze, Italy

Correspondence should be addressed to B. Onida, barbara.onida@polito.it

Received 3 May 2011; Accepted 21 June 2011

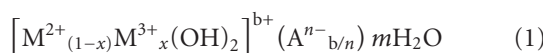
Academic Editor: Sergio Armenta Estrela

Copyright © 2011 F. Basile et al. This is an open access article distributed under the Creative Commons Attribution License, which permits unrestricted use, distribution, and reproduction in any medium, provided the original work is properly cited.

Supported Rh nanoparticles obtained by reduction in hydrogen of severely calcined Rh/Mg/Al hydrotalcite-type (HT) phases have been characterized by FT-IR spectroscopy of adsorbed CO [both at room temperature (r.t.) and nominal liquid nitrogen temperature] and Transmission Electron Microscopy (TEM). The effect of reducing temperature has been investigated, showing that Rh crystal size increases from 1.4 nm to 1.8 nm when the reduction temperature increases from 750°C to 950°C. The crystal growth favours the formation of bridged CO species and linear monocarbonyl species with respect to *gem*-dicarbonyl species; when CO adsorbs at r.t., CO disproportionation occurs on Rh and it accompanies the formation of Rh^I(CO)₂. The role of interlayer anions in the HT precursors to affect the properties of the final materials has been also investigated considering samples prepared from silicate-in instead of carbonate-containing precursors. In this case, formation of Rh^I(CO)₂ and CO disproportionation do not occur, and this evidence is discussed in terms of support effect.

1. Introduction

Hydrotalcites or layered double hydroxides (LDH's) belong to a large class of natural and synthetic anionic clays. Although they are less diffuse in nature than cationic clays, they can be easily synthesized [1]. Hydrotalcites-type (HT) compounds have the general formula:



The cations are present in a layer with brucite-type structure [Mg(OH)₂], in which part of Mg²⁺ is replaced by Al³⁺ and, as a consequence, the positive additional charge of the cations is balanced by the insertion of anions between layers. Usually

carbonates are used as anions, even if samples with silicates have shown higher thermal and textural stability [2].

The mixed oxides obtained after calcination of HT phases at temperature above 500°C are very useful for a wide range of applications like antiacids, anion exchanger, adsorbents, catalysts, and catalyst supports because of their undeniable advantages as high surface area and structural stability [3].

A further increase of the calcination temperature above 750°C gives rise to the segregation of the stoichiometric spinel phase and the formation of less defective MgO-type phase, giving rise to stable supports or catalysts for high temperature processes. In particular, the modification of the catalytic properties is possible by the substitution of part of Mg with other bivalent cation as Ni, Pt, Pd, Co, and/or

part of Al ions with Rh, Fe, Cr obtaining a high variety of formulation [3, 4].

The structure and surface properties of Mg-Al HT phases and of the resulting mixed oxides depend strongly on chemical composition and synthesis procedures [3].

Catalytic applications take advantage of their basic and/or redox properties, as the dispersion of the cations in the hydroxylated layers is retained after calcination, thus generating well-stabilized metallic particles. This property is particularly useful for catalysts active in H₂ production processes via reforming reactions. Considering that Rh is well known as one the most active metals for methane reforming, its insertion in the HT material leads to a very active catalyst with Rh particles highly dispersed on the surface of catalyst [5].

IR spectroscopy of adsorbed carbon monoxide has been widely used to characterize Rh-supported catalysts [6–11]. It is well known that three generalized types of chemisorbed CO are produced on dispersed Rh surfaces at room temperature, which are linear monocarbonyl species, Rh⁰(CO), bridging CO species, Rh₂⁰(CO), and *gem*-dicarbonyl complexes on oxidized Rh sites, Rh¹(CO)₂. The detection of the latter is considered significant for the existence of highly dispersed Rh, whereas linear and bridged carbonyl species are usually considered to form on extended Rh surface [6, 8, 10].

Besides giving information on dispersion of Rh, the study of interaction with CO allows to characterize the role of the support [7], which can strongly affect the catalytic activity [1]. Indeed, Rh in Rh/Mg/Al catalysts may be present in different phases. For instance, Rh/Mg/Al catalysts with high Rh content obtained by HT carbonate have been structurally characterised by sequential XRD and neutron diffraction Rietveld analysis, and Rh was shown to be present with a higher occupation factor inside the MgAl₂O₄ phase with respect to the MgO phase [12].

The aim of the work is twofold: on the one hand, the effect of the reducing treatment on Rh metal particles produced starting from Rh/Mg/Al HT precursors (1% by weight of rhodium) is investigated, analyzing two samples reduced at 750°C and at 950°C, respectively.

On the other hand, the effect of the support is investigated. To this purpose two materials with different M²⁺/M³⁺ ratio and different anions between layers were taken in exam: one sample was prepared with carbonate and the ratio M²⁺/M³⁺ was about 2, and the other one was prepared with silicate and the M²⁺/M³⁺ ratio was 4. In fact, different anions give rise to different phases in the calcined system: for instance, upon calcination silicates react with part of magnesium to give forsterite-type phase [2].

The characterization of supported Rh particles has been carried out by means of interaction with CO both at room temperature (r.t.) and at nominal liquid N₂ temperature, being the reactivity of CO depending on temperature [6]. The study of adsorbed CO₂ has been also carried out in order to characterize products of CO reaction at room temperature.

IR spectroscopy data are discussed on the basis of X-ray diffraction and TEM characterization.

2. Experimental

2.1. Materials Preparation. Carbonate and silicate-containing HT precursors were synthesized by coprecipitation method at constant pH and temperature following the method previously reported [4]. A solution of nitrate salts was added drop by drop to a basic solution containing carbonate or silicate anions. pH was kept constant at 10.5 by dropwise NaOH addition. The obtained suspension was aged by stirring for 1 hour at 56°C, then filtered and washed with distilled water. The precipitate was dried overnight at 60°C and calcined at 900°C for 12 h.

Samples obtained from the carbonate solution (nominal composition Rh_{0.43}Mg₆₈Al_{31.57}) were reduced at 750°C for 2 h or at 950°C for 4 h under a 50 mL/min flow of an H₂-Ar mixture (3:97 v/v) and from now on will be named Rh/HTCarb_750 and Rh/HTCarb_950, respectively. The material obtained from the silicate solution (nominal composition Rh_{0.5}Mg₈₀Al_{19.5}) was reduced under a 50 mL/min flow of an H₂-Ar mixture (3:97 v/v) and will be named as Rh/HTSil_750.

2.2. Samples Characterization. XRD powder analyses were carried out using a Philips PW1050/81 diffractometer equipped with a graphite monochromator in the diffracted beam and controlled by a PW1710 unit ($\lambda = 0.15418$ nm). A 2theta range from 5° to 80° was investigated at a scanning speed of 70°/h. In order to evaluate the particle size of phases, the silicon (plane (111)) was used to determine broadening of the X-ray reflections (FWHM). The calculation was performed with the X'Pert HighScore Program using the Scherrer's equation.

Transmission Electron Microscopy (TEM, JEOL 2010), combined with Energy Dispersive X-ray Spectrometry (EDS), was used to determine the size of the Rh particles in the samples reduced at different temperatures (according to that reported above) or obtained from carbonate- or silicate-containing HT precursors.

2.3. IR Study of Interaction with Probe Molecules. For IR, characterization powders were pressed into thin self-supporting pellets and then placed into a quartz IR cell. The activation treatment was carried out by connecting the cell to a vacuum-adsorption frame with a residual pressure below 10⁻³ mbar. In particular, prior to the adsorption measurements, all samples were activated by a treatment in H₂ (200 mbar) at 750°C (heating rate 2.5°C min⁻¹) for 1 h, outgassed under dynamic vacuum at 650°C for 2 h and then cooled to room temperature under Ar atmosphere.

FT-IR spectra were collected by using a Bruker Equinox 55 spectrometer, equipped with MCT cryodetector, at a spectral resolution of 2 cm⁻¹ and accumulation of 32 scans. CO and CO₂ (from Messer) were dosed in the pressure range from 0.1 to 35 mbar by connecting the IR cell to a vacuum frame. The interaction with CO was studied both at r.t. and at the nominal temperature of -196°C by using liquid nitrogen as coolant. The actual temperature of the sample is about -173°C, due to the heating effect of the IR beam. Adsorption of CO₂ was studied at r.t.

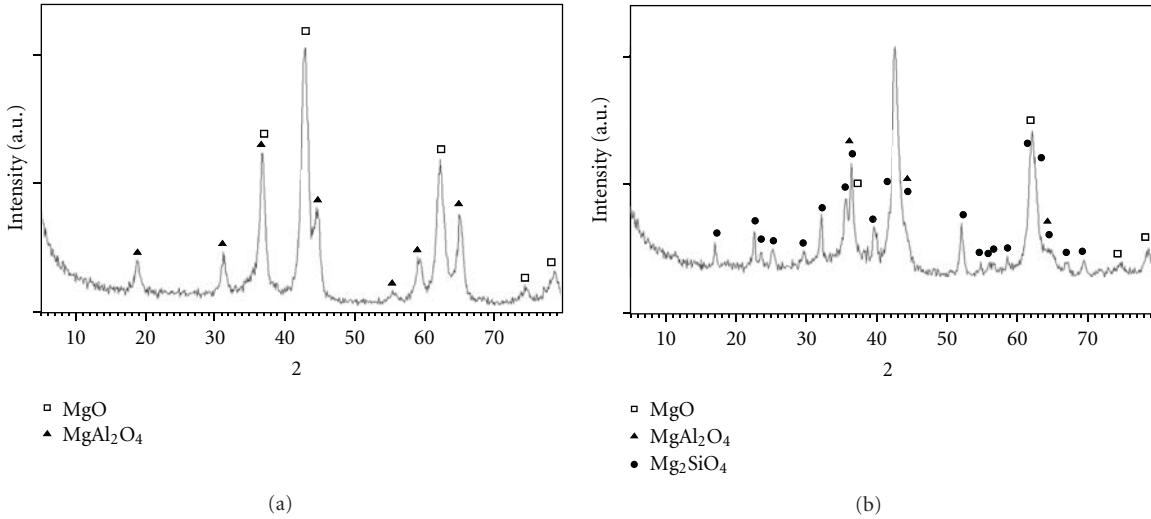


FIGURE 1: XRD patterns of Rh/HTCarb_750 (a) and Rh/HTSil_750 (b).

FT-IR spectra related to different samples were normalized dividing the registered intensities by the pellet weight (mg) and multiplying by the pellet area (mm^2). For this reason, absorbance is in arbitrary units (a.u.) and values are not reported in figures. All FT-IR spectra related to the dosage of CO and CO₂ are shown as difference spectra (the spectrum recorded before probe dosage was subtracted): positive bands indicate species which are formed during the *in situ* measurement, whereas negative bands, if present, are related to species which are consumed.

3. Results and Discussion

Rh/HTCarb_750 contains a spinel-type phase and a rock-salt-type phase, as revealed by the XRD pattern (Figure 1(a)).

The average particle sizes for MgO- and spinel-type phases, calculated by means of Sherrer's equation using the FWHM values of the most intense reflexions, are reported in Table 1. The average crystallite size of MgO-type phase in Rh/HT_Carb750 is close to 15 nm, while the spinel-type phase shows a slightly higher crystallite size (20 nm).

A complex pattern is observed for Rh/HTSil_750 (Figure 1(b)). Diffraction peaks assigned to a forsterite-like phase (Mg₂SiO₄) are indexed. Instead, no well-defined Al-containing phase (MgAl₂O₄) is detected [13]. In fact, only weak and broad reflections ascribable to a spinel-type phase are observed and the first two reflections at $2\theta = 19$ and 32°, ascribed to (111) and (220) planes, are not discernible in the pattern. This indicates that the silicates react with MgO to give the forsterite phase, affecting the formation of the spinel-type phase.

Since the MgO-type phase is the only phase observed in Rh/HTSil_750 also present in the Rh/HTCarb_750, the crystal size is estimated only for it and it appears larger than in the case of Rh/HTCarb 750.

For both Rh/HTCarb_750 and Rh/HTSil_750, no reflections due metallic Rh are observed, being its amount close to the instrumental detection limit.

TABLE 1: Crystal size of MgO- and MgAl₂O₄-type phases (nm) as obtained by XRD analysis.

| Phase (*) | Rh/HTCarb_750 | Rh/HTSil_750 |
|--|---------------|--------------|
| MgO (200) | 12 | 13 |
| MgO (220) | 15 | 17 |
| MgO | 13.5 | 15 |
| MgAl ₂ O ₄ (111) | 18 | / |
| MgAl ₂ O ₄ (220) | 34 | / |
| MgAl ₂ O ₄ (311) | 24 | / |
| MgAl ₂ O ₄ | 25 | / |

(*) Reflections used for crystal size evaluation are reported.

Figure 2 reports the spectra related to increasing amount of CO adsorbed at r.t. on Rh/HTCarb_750 in the range 2200–1300 cm⁻¹. At very low CO pressure (spectrum 1), a single band is observed at 2050 cm⁻¹, assigned to the stretching mode of linear monocarbonyl species on Rh metal particles, Rh⁰(CO) [14, 15]. At increasing CO pressure, two shoulders appear above and below the band at 2050 cm⁻¹, due to, respectively, the symmetric and antisymmetric stretching modes of dicarbonyl species on oxidized Rh species, that is, Rh¹(CO)₂ [16]. In same spectra, absorptions below 1800 cm⁻¹ increase, with maxima discernible at 1680 cm⁻¹ and 1313 cm⁻¹, due to bidentate carbonates, at 1394 cm⁻¹ and 1220 cm⁻¹, ascribed to hydrogenocarbonate-type and at 1380 cm⁻¹, assigned to formate-type species [17–19].

The spectrum recorded after removal of CO by out-gassing at r.t. is reported in Figure 3 (curve 1). The band due to Rh⁰(CO) species is clearly observed at 2050 cm⁻¹. The weak band discernible at 2096 cm⁻¹ is due to the symmetric stretching mode of Rh¹(CO)₂ species. The twin antisymmetric mode, expected at around 2030 cm⁻¹ [14–16], is most probably hidden in the tail of the main component at 2050 cm⁻¹, which indeed shows a low-frequency side asymmetry evidenced by the vertical broken line in the figure.

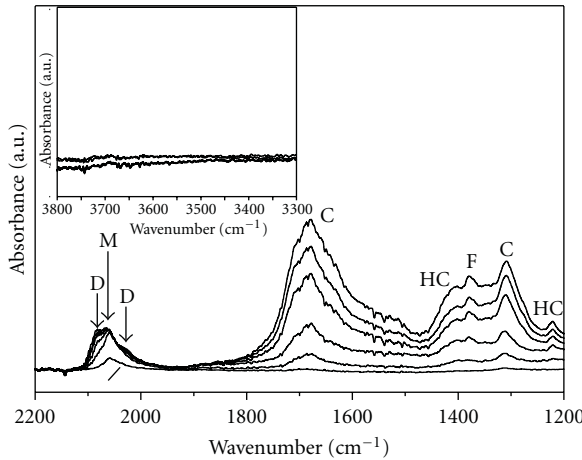


FIGURE 2: FT-IR spectra related to the adsorption of CO on Rh/HTCarb_750 at r.t. Section a: spectra recorded at increasing CO pressure. The inset shows the corresponding OH stretching region. Section b. Spectrum recorded after removal of CO from the IR cell at r.t. (D: *gem*-dicarbonyl, M: linear monocarbonyl, C: carbonate-, HC: hydrogenocarbonate-, and F: formate-type species).

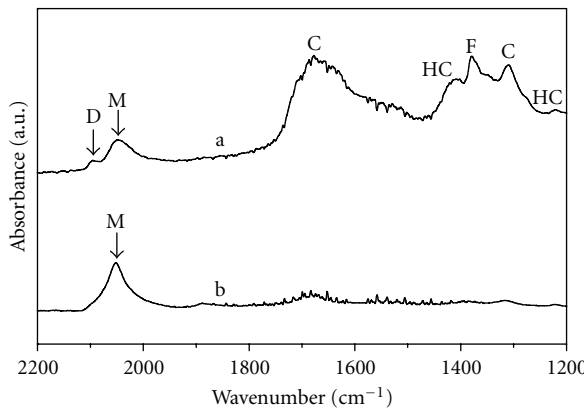


FIGURE 3: FT-IR spectra recorded after contact of CO with Rh/HTCarb_750 at r.t. (curve a) and at liquid N₂ temperature (curve b). (D: *gem*-dicarbonyl, M: linear monocarbonyl, C: carbonate-, HC: hydrogenocarbonate-, and F: formate-type species).

In the same spectra, bands due to carbonate-, hydrogenocarbonate-, and formate-type species are also observed.

As widely reported in the literature, species Rh^I are generally considered to form by reaction of CO on small Rh_x crystallites rather than present on the surface as such prior to contact with CO [10, 20, 21].

Indeed, the spectrum of CO adsorbed at low temperature (curve 2 in Figure 3) shows a single band at 2050 cm⁻¹ due to linear monocarbonyl species on Rh⁰. This suggests that species able to give *gem*-dicarbonyl species are not present on the surface, whereas they are formed by reaction with CO at room temperature.

The mechanism of formation of Rh^I(CO)₂ species upon reaction of CO is still under debate. It has been suggested that Rh-Rh bonds can be disrupted at r.t. and under CO pressure, due to the higher energy of the Rh-CO bond as compared

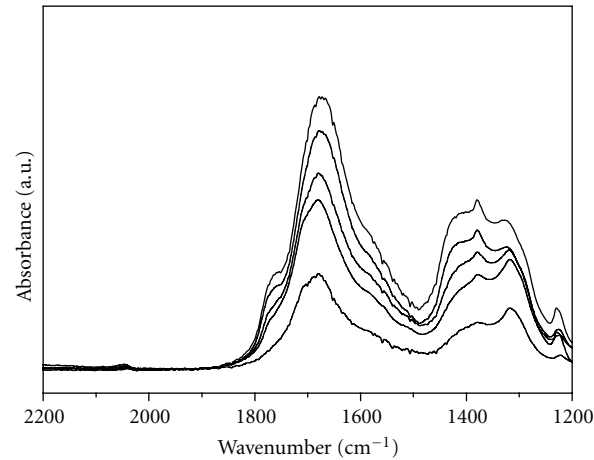
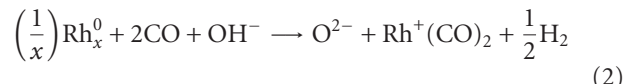


FIGURE 4: FT-IR spectra related to the adsorption of CO₂ on Rh/HTCarb_750 at r.t. (C: carbonate-, HC: hydrogenocarbonate-, and F: formate-type species).

to the Rh-Rh one [22], in small Rh_x particles. Some authors proposed that Rh^I(CO)₂ may form on two-dimensional Rh “islands” or Rh-isolated atoms [6, 23].

Primet [24] proposed that CO dissociation may occur even at -73°C on Rh, producing chemisorbed oxygen, leading to the formation of Rh⁺ sites which are able to adsorb two CO molecules.

Moreover, the involvement of support OH species has been also proposed in a few cases [10, 25] according to the mechanism:



In the present case, the role of surface OH species, if any, is negligible, as revealed by the investigation of spectra in the OH stretching region (inset in Figure 2), where no significant modifications during reaction with CO are observed.

Despite the debate concerning the formation mechanism of Rh^I(CO)₂ species, however, the detection of *gem*-dicarbonyls is generally considered a strong indication of the existence of highly dispersed Rh metal particles on the catalyst surface.

In the present case, the formation of Rh^I(CO)₂ species is accompanied by the formation of carbonate-, hydrogenocarbonate-, and formate-type species, revealing that disproportionation of CO to C and CO₂ occurs. Indeed adsorption of CO₂ on the catalyst gives rise to similar absorption in the IR spectrum (Figure 4).

The reaction of CO occurs on Rh, since no formation of carbonate-type species has been observed for reaction of CO with the Rh-free support (spectra not reported). Disproportionation of CO on Rh supported on several oxides (TiO₂, Al₂O₃, SiO₂, MgO) has been reported in the literature, though at temperature higher than 25°C [7].

It is worth noting that in the spectrum of CO adsorbed at low temperature no bands due to carbonate-type species are observed, suggesting that carbonates form when Rh^I(CO)₂ species form. Indeed, though at temperature higher than

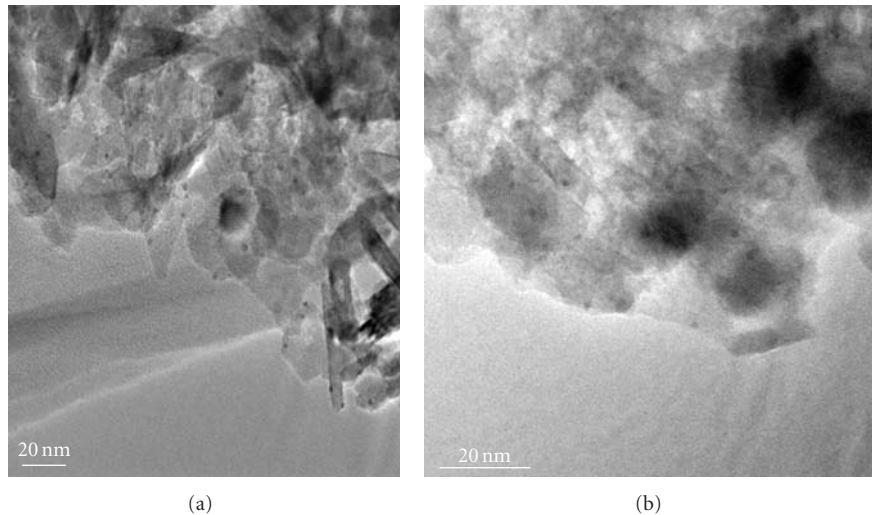


FIGURE 5: TEM micrographs of Rh/HTCarb_750 (upper part) and Rh/HTCarb_950 (lower part).

25°C, CO disproportionation on supported Rh was observed to occur with no evidence of presence of dicarbonyl species [7], some authors [26] suggested that the dissociation-disproportionation of CO should occur in the twin form in the case of Ru catalysts, which appears a reasonable mechanism, involving two CO molecules on the same metal site.

3.1. Effect of the Reducing Temperature. In order to investigate the effect of reducing temperature on the system, the sample reduced at 950°C (Rh/HTCarb_950) has been characterized following the same approach. The characterization has been completed by TEM analysis, and Figure 5 shows the TEM micrographs of Rh/HTCarb_750 and Rh/HTCarb_950. The Rh is in the form of well-dispersed nanoparticles in both cases. As expected, the average particle size appears smaller for the catalyst reduced at lower temperature (1.4 nm) than for that reduced at 950°C (1.8 nm).

Figure 6 shows the spectrum recorded after contact of Rh/HTcarb_950 with CO ($p = 30$ mbar) at r.t. and removal of the gas from the cell by outgassing. Spectra in presence of CO are similar and thus are not reported for sake of brevity.

The narrow band at 2060 cm^{-1} due to the $\text{Rh}^0(\text{CO})$ species dominates the spectrum, whereas the symmetric mode of *gem*-dicarbonyl complexes appears as a shoulder at 2093 cm^{-1} , accompanied by the twin peak as a tail hardly discernible at about 2030 cm^{-1} . The relative intensity of the monocarbonyl band with respect to the symmetric *gem*-dicarbonyl mode is higher than for Rh/HTCarb_750, suggesting a larger population of the former species in the present case.

Moreover, a broad absorption is observed at about 1910 cm^{-1} , due to bridged-bonded carbonyl species, $\text{Rh}_2^0(\text{CO})$ [25]. Both $\text{Rh}^0(\text{CO})$ and $\text{Rh}_2^0(\text{CO})$ arise from CO adsorbed on extended Rh faces. The lower amount of the former and the absence of the latter in Rh/HTCarb_750 are both in agreement with the existence of smaller Rh particles with respect to Rh/HTCarb_950, as revealed by

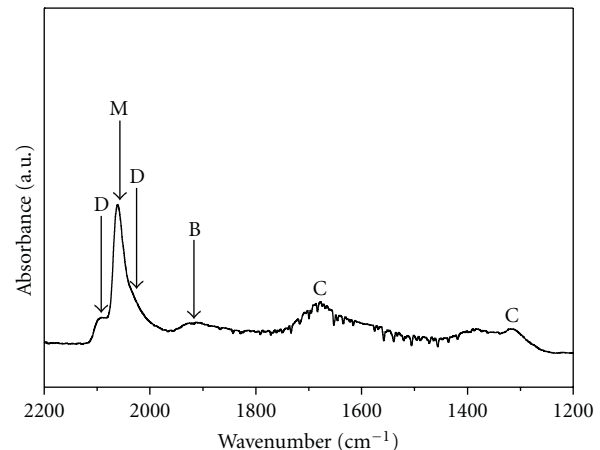


FIGURE 6: FT-IR spectrum recorded after contact of CO with Rh/HTCarb_950 at r.t. (D: *gem*-dicarbonyl, M: linear monocarbonyl, B: bridged-bonded CO, and C: carbonate-type species).

TEM analysis. In particular, it may seem that the limit of average crystal size above which bridged-bonded carbonyl species are formed falls in the range of 1.4–1.8 nm.

Though several authors reported the formation of bridged-bond $\text{Rh}_2(\text{CO})$ upon adsorption of CO on supported Rh, very rarely information on particle size from complementary techniques is provided. Finocchio et al. [10] observed the occurrence of bridged-bond $\text{Rh}_2(\text{CO})$ on particles with estimated size of 3.2 nm.

It is worth noting that in the case of Rh/HTcarb_950, only a very small amount of carbonate-like species are formed. The lower relative amount of $\text{Rh}^1(\text{CO})_2$ in the present case suggests that formation of carbonate-type species is related to formation of *gem*-dicarbonyls upon reaction with CO. As observed for Rh/HTCarb_750, only monocarbonyl species are formed upon adsorption of CO at low temperature (spectrum not reported).

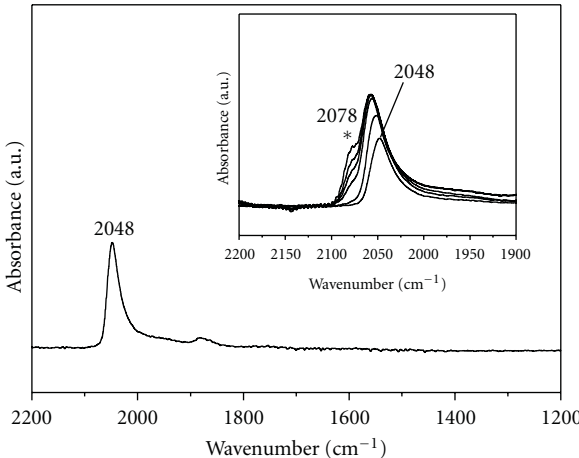


FIGURE 7: FT-IR spectrum recorded after contact of CO with Rh/HTSil₇₅₀ at r.t. Inset: spectra recorded at increasing CO pressure.

3.2. Role of the Support. The effect of the support has been investigated considering the reactivity of Rh/HTCarb_{.750} and Rh/HTSil_{.750} towards CO at r.t. Figure 7 reports the IR spectrum recorded after contact of Rh/HTSil_{.750} with CO ($p = 30$ mbar) at r.t. and removal of the gas from the IR cell by outgassing.

A single band is visible at 2048 cm^{-1} , due to monocarbonyl species on Rh surfaces. No bands due to *gem*-dicarbonyls are present, neither absorptions due to carbonate-type species. The results show that in Rh/HTSil_{.750} Rh is definitely less reactive towards CO with respect to Rh/HTCarb_{.750}.

The lower reactivity cannot be ascribed to larger Rh particle size, that from TEM analysis (image not reported) shows a size of 1.1 nm, that is smaller than those observed on Rh/HTCarb_{.750}.

An effect of the support may be instead envisaged, that may not favor the formation of Rh^I(CO)₂. The inset of Figure 7 reports the spectra recorded upon increasing CO pressure at r.t. Besides the shifting of the monocarbonyl band to higher frequency upon increasing coverage, due to dipole-dipole coupling among adsorbed CO molecules [10], a new component increases at 2078 cm^{-1} (labeled by an asterisk in figure). This absorption is depleted by outgassing at r.t., and in fact it is not visible in the spectrum reported in the main body of Figure 7, revealing that the related species is labile and adsorbed reversibly. We tentatively assign this band to monocarbonyl species on oxidized Rh, that is, Rh^I(CO) species [15]. A similar species was proposed to account for a band observed at 2087 cm^{-1} on Rh/TiO₂ catalyst during decarbonylation [27]. These authors suggested that this species is an intermediate in the conversion of Rh^I(CO)₂ to Rh⁰(CO) and proposed that the corresponding band is frequently overlapped with the band above 2090 cm^{-1} due to *gem*-dicarbonyl species, so being indiscernible in most cases. The same band had been previously observed during initial adsorption of CO at low temperature on Rh/Al₂O₃ and it was assigned to Rh^I monocarbonyl species [28].

Assuming that the mechanism of decarbonylation is the reverse of the conversion of Rh⁰(CO) to Rh^I(CO)₂,

we propose that the labile Rh^I(CO) species forms at increasing CO coverage and it is a precursor of the *gem*-dicarbonyl species. It most probably forms also in the case of Rh/HTCarb_{.750} (Figure 2), being the band at 2078 cm^{-1} overlapped with the symmetric mode of the Rh^I(CO)₂, as previously suggested [19]. Indeed, upon CO removal (Figure 3) the high frequency shoulder of the monocarbonyl band at 2050 cm^{-1} is largely depleted, suggesting that species contributing to this adsorption are reversibly adsorbed.

Unlike the case of Rh/HTCarb_{.750}, where *gem*-dicarbonyl forms, in the Rh/HTSil_{.750} the Rh^I(CO) species do not evolve into Rh^I(CO)₂ complexes. A possible explanation is that Rh^I(CO)₂ species are not stabilized by the support. The role of the support in stabilizing Rh^I(CO)₂ species was previously suggested [29]; for instance, it was reported that dicarbonyls are strongly favoured on Rh/Al₂O₃ compared to Rh/SiO₂ [8, 21].

Moreover, Rh^I(CO)₂ were observed to be dominant species on Rh/TiO₂ and Rh/Al₂O₃ reduced at 400°C , whereas this was not the case for Rh/SiO₂ and Rh/MgO reduced at the same temperature, mostly at low CO pressure [8].

Indeed, evidence of silicate forsterite-like phase (Mg₂SiO₄) is provided by XRD analysis, whereas no well-defined phase containing Al (MgAl₂O₄) is revealed, unlike Rh/HTCarb_{.750}. Moreover, MgO crystals are more extended in Rh/HTSil_{.750} than in Rh/HTCarb_{.750}.

It is worth noting that no carbonate-type species form on Rh/HTSil_{.750} upon interaction with CO, strongly suggesting, together with previous data, that Rh^I(CO)₂ are involved in CO disproportionation in these systems.

The lower reactivity in CO disproportionation of Rh/HTSil_{.750}, containing the silicate forsterite-like phase (Mg₂SiO₄) instead of MgAl₂O₄, is in agreement with the observation that the extent of CO disproportionation on Rh catalyst follows the order Rh/Al₂O₃ > Rh/SiO₂ > Rh/MgO [8].

In conclusion, we propose that in Rh/HTCarb_{.750} Rh nanoparticles are affected by the Al-containing support, that is, the MgAl₂O₄ type phase in which the Rh has been reported to have larger solubility than for the MgO, when both phases are present [12]. Instead, in Rh/HTSil_{.750} the metal is affected mainly by MgO, acting as support.

Table 2 summarizes IR data related to CO adsorption, together with Rh particle size obtained by TEM data analysis.

4. Conclusions

Rh metal particles obtained by reduction in diluted H₂ of Rh/Mg/Al calcined HT precursors have been characterized by FT-IR analysis of adsorbed CO and TEM. The particle size increases from 1.4 nm to 1.8 nm when reduction temperature increases from 750°C to 950°C . The crystal growth causes, upon interaction with CO at r.t., the formation of bridged CO species and the increase of population of linear monocarbonyl in comparison to *gem*-dicarbonyl species.

Disproportionation of CO occurs on Rh at r.t., giving rise to carbonate-, hydrogenocarbonate- and formate-type species, and it accompanies the formation of Rh^I(CO)₂,

TABLE 2: FT-IR data of CO interaction at r.t. and Rh particle size evaluated by TEM analysis.

| Sample | $\nu\text{Rh}^0\text{CO}$ (cm ⁻¹) | $\nu\text{Rh}^1(\text{CO})_2$ (cm ⁻¹) | $\nu(\text{Rh}_2)\text{CO}$ (cm ⁻¹) | CO disprop. ^c | d _{particles} (nm) |
|---------------|--|--|--|-----------------------------|--------------------------------|
| Rh/HTCarb_750 | 2050 | 2096 ^a | — | YES | 1.8 |
| Rh/HTCarb_950 | 2060 | 2093, 2032 ^b | 1915 | small extent | 1.4 |
| Rh/HTSil_750 | 2048 | — | — | NO | 1.1 |

^aThe asymmetric mode is overlapped with the monocarbonyl stretch.

^bLower relative amount with respect to Rh/HTCarb_750.

^cCO disproportionation as revealed by the formation of carbonate-like species.

whereas no *gem*-dicarbonyl species and CO disproportionation are observed for reaction with CO at nominal liquid N₂ temperature.

The formation of Rh¹(CO)₂ and disproportionation of CO at r.t. do not occur for the sample obtained from the silicate-containing HT precursor. A band at 2078 cm⁻¹ is ascribed to a labile Rh¹(CO) species, which does not evolve into *gem*-dicarbonyl species. This is attributed to an effect of the support, which, at variance with the system prepared from carbonate solution, does not contain a well-defined spinel phase. Instead, it contains a silicate forsterite-like phase, besides the MgO phase which acts as support.

Acknowledgments

Thanks are due to INSTM Consortium and Air Liquide for the financial support. Special thanks are due to Professors T. Chartier and F. Rossignol (SPCTS, Limoges F) for the TEM images.

References

- [1] S. Casenave, H. Martinez, C. Guimon et al., "Acid-base properties of Mg-Ni-Al mixed oxides using LDH as precursors," *Thermochimica Acta*, vol. 379, no. 1-2, pp. 85–93, 2001.
- [2] S. Albertazzi, F. Basile, P. Benito et al., "Effect of silicates on the structure of Ni-containing catalysts obtained from hydrotalcite-type precursors," *Catalysis Today*, vol. 128, no. 3-4, pp. 258–263, 2007.
- [3] F. Cavani, F. Trifirò, and A. Vaccari, "Hydrotalcite-type anionic clays: preparation, properties and applications," *Catalysis Today*, vol. 11, no. 2, pp. 173–301, 1991.
- [4] F. Basile, P. Benito, G. Fornasari, and A. Vaccari, "Hydrotalcite-type precursors of active catalysts for hydrogen production," *Applied Clay Science*, vol. 48, no. 1-2, pp. 250–259, 2010.
- [5] F. Basile, G. Fornasari, M. Gazzano, A. Kiennemann, and A. Vaccari, "Preparation and characterisation of a stable Rh catalyst for the partial oxidation of methane," *Journal of Catalysis*, vol. 217, no. 2, pp. 245–252, 2003.
- [6] J. T. Yates Jr., T. M. Duncan, and R. W. Vaughan, "Infrared spectra of chemisorbed CO on Rh," *Journal of Chemical Physics*, vol. 71, 3908 pages, 1979.
- [7] A. Erdöhelyi and F. Solymosi, "Effects of the support on the adsorption and dissociation of CO and on the reactivity of surface carbon on Rh catalysts," *Journal of Catalysis*, vol. 84, no. 2, pp. 446–460, 1983.
- [8] S. Trautmann and M. Baerns, "Infrared Spectroscopic Studies of CO Adsorption on Rhodium Supported by SiO₂, Al₂O₃, and TiO₂," *Journal of Catalysis*, vol. 150, no. 2, pp. 335–344, 1994.
- [9] L. Kundakovic, D. R. Mullins, and S. H. Overbury, "Adsorption and reaction of H₂O and CO on oxidized and reduced Rh/CeO_x(111) surfaces," *Surface Science*, vol. 457, no. 1, pp. 51–62, 2000.
- [10] E. Finocchio, G. Buscà, P. Forzatti, G. Groppi, and A. Beretta, "State of supported rhodium nanoparticles for methane catalytic partial oxidation (CPO); FT-IR studies," *Langmuir*, vol. 23, no. 20, pp. 10419–10428, 2007.
- [11] K. Hadjiivanov, E. Ivanova, L. Dimitrov, and H. Knözinger, "FTIR spectroscopic study of CO adsorption on Rh-ZSM-5: detection of Rh + CO species," *Journal of Molecular Structure*, vol. 661–662, no. 1–3, pp. 459–463, 2003.
- [12] F. Basile, G. Fornasari, M. Gazzano, and A. Vaccari, "Rh, Ru and Ir catalysts obtained by HT precursors: effect of the thermal evolution and composition on the material structure and use," *Journal of Materials Chemistry*, vol. 12, no. 11, pp. 3296–3303, 2002.
- [13] F. Basile, P. Benito, G. Fornasari et al., "Ni-catalysts obtained from silicate intercalated HTIcs active in the catalytic partial oxidation of methane: influence of the silicate content," *Catalysis Today*, vol. 142, no. 1-2, pp. 78–84, 2009.
- [14] T. Chafik, D. I. Kondarides, and X. E. Verykios, "Catalytic reduction of NO by CO over rhodium catalysts: 1. Adsorption and displacement characteristics Investigated by in situ FTIR and transient-MS techniques," *Journal of Catalysis*, vol. 190, no. 2, pp. 446–459, 2000.
- [15] D. I. Kondarides, T. Chafik, and X. E. Verykios, "Catalytic reduction of NO by CO over Rhodium catalysts: 2. Effect of oxygen on the nature, population, and reactivity of surface species formed under reaction conditions," *Journal of Catalysis*, vol. 191, no. 1, pp. 147–164, 2000.
- [16] H. Miessner, D. Gutschick, H. Ewald, and H. Müller, "The influence of support on the geminal dicarbonyl species Rhi(CO)₂ on supported rhodium catalysts: an IR spectroscopic study," *Journal of Molecular Catalysis*, vol. 36, no. 3, pp. 359–373, 1986.
- [17] A. M. Turek, I. E. Wachs, and E. DeCanio, "Acidic properties of alumina-supported metal oxide catalysts: an infrared spectroscopy study," *Journal of Physical Chemistry*, vol. 96, no. 12, pp. 5000–5007, 1992.
- [18] A. A. Davydov, M. L. Shepot'ko, and A. A. Budneva, "Study of the state of transition-metal cations on the catalyst surface by IR spectroscopy using adsorbed probe-molecules (CO, NO): X. Identification of the state of copper on the surface of Cu/SiO₂," *Kinetics and Catalysis*, vol. 35, p. 272, 1994.
- [19] J. C. Lavalle, "Infrared spectrometric studies of the surface basicity of metal oxides and zeolites using adsorbed probe molecules," *Catalysis Today*, vol. 27, no. 3-4, pp. 377–401, 1996.
- [20] G. Bergeret, P. Gallezot, P. Gelin et al., "CO-induced disintegration of rhodium aggregates supported in zeolites: in situ

- synthesis of rhodium carbonyl clusters,” *Journal of Catalysis*, vol. 104, no. 2, pp. 279–287, 1987.
- [21] F. Solymosi, M. Pásztor, and G. Rákhely, “Infrared studies of the effects of promoters on CO-induced structural changes in Rh,” *Journal of Catalysis*, vol. 110, no. 2, pp. 413–415, 1988.
- [22] H. F. J. Van’t Blik, J. B. A. D. Van Zon, T. Hulzinga, J. C. Vis, D. C. Koningsberger, and R. Prins, “An extended X-ray absorption fine structure spectroscopy study of a highly dispersed Rh/Al₂O₃ catalyst: the influence of CO chemisorption on the topology of rhodium,” *Journal of Physical Chemistry*, vol. 87, no. 13, pp. 2264–2267, 1983.
- [23] J. Raskó and J. Bontovics, “FTIR study of the rearrangement of adsorbed CO species on Al₂O₃-supported rhodium catalysts,” *Catalysis Letters*, vol. 58, no. 1, pp. 27–32, 1999.
- [24] M. Primet, “Infrared study of CO chemisorption on zeolite and alumina supported rhodium,” *Journal of the Chemical Society, Faraday Transactions 1*, vol. 74, pp. 2570–2580, 1978.
- [25] P. Basu, D. Panayotov, and J. T. Yates, “Rhodium-carbon monoxide surface chemistry: the involvement of surface hydroxyl groups on Al₂O₃ and SiO₂ supports,” *Journal of the American Chemical Society*, vol. 110, no. 7, pp. 2074–2081, 1988.
- [26] A. Bossi, G. Carnisio, F. Garmassi, G. Giunchi, G. Petrini, and L. Zanderighi, “Isotopic equilibration of carbon monoxide catalyzed by supported ruthenium,” *Journal of Catalysis*, vol. 65, p. 16, 1980.
- [27] K. L. Zhang, A. Kladi, and X. E. Verykios, “Structural alterations of highly dispersed Rh/TiO₂ catalyst upon CO adsorption and desorption investigated by infrared spectroscopy,” *Journal of Molecular Catalysis*, vol. 89, no. 1-2, pp. 229–246, 1994.
- [28] C. A. Rice, S. D. Worley, C. W. Curtis, J. A. Guin, and A. R. Tarrer, “The oxidation state of dispersed Rh on Al₂O₃,” *The Journal of Chemical Physics*, vol. 74, no. 11, pp. 6487–6497, 1981.
- [29] G. Lafaye, C. Mihut, C. Espezel, P. Marécot, and M. D. Amiridis, “FTIR studies of CO adsorption on Rh-Ge/Al₂O₃ catalysts prepared by surface redox reactions,” *Langmuir*, vol. 20, no. 24, pp. 10612–10616, 2004.

Research Article

Improving SERS Detection of *Bacillus thuringiensis* Using Silver Nanoparticles Reduced with Hydroxylamine and with Citrate Capped Borohydride

Hilsamar Félix-Rivera,¹ Roxannie González,¹ Gabriela Del Mar Rodríguez,¹
Oliva M. Primera-Pedrozo,¹ Carlos Ríos-Velázquez,² and Samuel P. Hernández-Rivera¹

¹Department of Chemistry, ALERT-DHS Center of Excellence, Center for Chemical Sensors Development, University of Puerto Rico-Mayagüez, P.O. Box 9000, Mayagüez, PR 00681-9000, Puerto Rico

²Microbial Biotechnology and Bioprospecting Laboratory, Department of Biology, University of Puerto Rico-Mayagüez, P.O. Box 9000, Mayagüez, PR 00681-9000, Puerto Rico

Correspondence should be addressed to Oliva M. Primera-Pedrozo, olivaprimera@yahoo.es

Received 1 May 2011; Accepted 14 June 2011

Academic Editor: Ahmed Aamouche

Copyright © 2011 Hilsamar Félix-Rivera et al. This is an open access article distributed under the Creative Commons Attribution License, which permits unrestricted use, distribution, and reproduction in any medium, provided the original work is properly cited.

The development of techniques that could be useful in fields other than biological warfare agents countermeasures such as medical diagnostics, industrial microbiology, and environmental applications have become a very important subject of research. Raman spectroscopy can be used in near field or at long distances from the sample to obtain fingerprinting information of chemical composition of microorganisms. In this research, biochemical components of the cell wall and endospores of *Bacillus thuringiensis* (*Bt*) were identified by surface-enhanced Raman scattering (SERS) spectroscopy using silver (Ag) nanoparticles (NPs) reduced by hydroxylamine and borohydride capped with sodium citrate. Activation of “hot spots”, aggregation and surface charge modification of the NPs, was studied and optimized to obtain signal enhancements from *Bt* by SERS. Slight aggregation of the NPs as well as surface charge modification to a more acidic ambient was induced using small-size borohydride-reduced NPs in the form of metallic suspensions aimed at increasing the Ag NP-*Bt* interactions. Hydroxylamine-reduced NPs required slight aggregation and no pH modifications in order to obtain high spectral quality results in bringing out SERS signatures of *Bt*.

1. Introduction

Bioterrorism's high potential for destruction has become a subject of great concern. Fast, efficient, and inexpensive detection techniques for microorganisms have become a very important subject in areas of national defense and homeland security. Techniques such as conventional Raman spectroscopy (RS) and surface-enhanced Raman scattering (SERS) require a minimum amount of sample for a fast detection [1] so that they can be implemented in near field or at long distances from the sample by obtaining fingerprinting information of the chemical composition of microorganisms. The time required for identification of pathogens is a determinant factor of

infection related sickness. The development of these techniques could be useful in fields other than biological warfare agents countermeasures such as medical diagnostics [2], industrial microbiology [3], and environmental applications [4].

Bacillus thuringiensis (*Bt*), a Gram-positive bacterium, is widely renowned for its toxicity on insect larvae and is commercially used as insecticide. *Bt*, as a *bacillus* species, has a bacterial life cycle in which it grows as vegetative cell forming endospores as defense mechanism. The bacterial cell wall contains a peptidoglycan layer responsible for strengthening the wall. This rigid layer in a Gram-positive species cell wall is typically much thicker. The peptidoglycan layer contains alternating repeats of N-acetylglucosamine (NAG)

and N-acetylmuramic (NAM) acid. It encloses a group of molecules called teichoic and lipoteichoic acids, which are unique to Gram-positive bacteria cell wall. *Bt* produces a crystalline protein during sporulation called parasporal body that is converted to a toxin by proteolytic cleavage in the larval gut.

Endospores are able to tolerate extreme environments, thus making them suitable for transporting before or during a biological attack. The bacterial endospores contain several well-known layers, from internal to external location. Among these are the cortex, the core wall, the spore coat, and the exosporium. Biochemical components of these layers include sugar chains, short peptides of peptidoglycan, polypeptides, fatty acids (lipids), carbohydrates, and proteins. In the core, thick layer of proteins, dipicolinic acid, and calcium ions normally exist in the form of a calcium-dipicolinate complex that stabilize and protect the genetic material of the endospore [5–7]. Biological samples as virus [8], pollen [9], essential components of bacterial cell wall, and bacterial endospores have been studied by SERS effect using Ag or Au metallic colloids to optimize procedures for detection, identification, and classification.

Citrate-reduced nanoparticles (NPs) have been widely used to classify and discriminate spores of different species by principal component analysis (PCA) of SERS spectra [10]. On the other hand, borohydride-reduced NPs have allowed *Bacillus subtilis* discrimination using SERS [11]. To increase the electrostatic interaction between the surfaces of the NPs with the bacterial cell-wall modifications to the surface charge of the NPs can be made, depending on the reducing agent of the metallic ions solutions [12]. Ag-borohydride NPs were modified by changing the pH of the colloid to obtain a more intimate interaction with the bacterial cell wall in which at low and high pH values (3.25 and 9.74) did not result in improved detection of *Escherichia coli* [13, 14]. Improved SERS signals at pH of 5 and higher were obtained for *Bacillus* Gram-positive species with citrate reduced nanoparticles [15] and for biological molecules with amine groups using hydroxylamine hydrochloride-reduced NPs [16]. The changes in NPs surfaces increase the formation of hot spots and consequently further augment of SERS effect that can be observed. To induce aggregation, pH changes as well as adding halide anions to the nanoparticles can also be used. The use of aggregation agents in SERS of bacterial samples was studied to allow the NPs-induced aggregation and to generate highly SERS-active interparticle spaces [17]. *Bacillus thuringiensis* detection has been studied by SERS using silver oxide films [18], Au NPs covered by SiO₂ [19], Ag colloids reduced by citrate [10] and by hydroxylamine hydrochloride [20]. However, *Bt* interaction with Ag-NPs capped with citrate and the optimization of the NPs to increase the SERS signals has not been reported in the literature.

The reproducibility and consistency of enhancement of vibrational signatures of microorganisms and their stability and dependence on morphology of SERS active substrates has also been studied in depth [19]. It is well known that the electromagnetic and chemical mechanisms of SERS produced by NPs upon interaction with analytes is in

general determined by the intimacy of the interaction of the molecules to the surface plasmon field and the charge transfer at the “hot spots” sites. The optimization procedure for achieving maximum signals played an important role in the attainment of high Raman enhancements for *Bt*. Since no specific studies addressing these important issues of *Bt* using these sensing platforms were found, it was decided to study them.

2. Experimental Section

2.1. Materials. Silver nitrate (AgNO₃, 99+%), sodium borohydride (NaBH₄, 98%), hydroxylamine hydrochloride (NH₂OH · HCl), trisodium citrate dihydrate (Na₃C₆H₅O₇ · 2H₂O), sodium chloride (NaCl, 99.9+%) and sodium hydroxide (NaOH) were acquired from Sigma-Aldrich Chemical Co., (Milwaukee, WI). Nanopure deionized ultra high purity water (UHP; 18.2 MΩ-cm) was used for the preparation of aqueous metal ions solutions. Glassware was cleaned by soaking in *aqua regia* and finally washing with distilled and deionized water several times. *Bt* strain (ATCC no. 35646) was provided by the Microbial Biotechnology and Bio-prospecting Lab, Biology Department, UPRM. It was grown using Miller modified Luria-Bertani (LB) agar and broth (Fisher Scientific International; Thermo Fisher Scientific, Waltham, Mass, USA).

2.2. Preparation of Ag-NPs. Borohydride reduced Ag-NPs were prepared using the method of Keir, Sadler and Smith [21] using 1 mL of 1% sodium citrate. The method was modified by using citrate as capping agent to avoid colloidal precipitation. A typical synthesis consisted of dissolving 3.4 mg of NaBH₄ in 75 mL of UHP water that had been previously degasified with N₂ and cooled at 4°C under vigorous stirring using rotating magnetic bar. Then, 1 mL of trisodium citrate was added to the flask. Finally, 9 mL of AgNO₃ 0.0022 M was added at a rate of 20.5 μL/s and stirred for 45 min. Hydroxylamine-reduced Ag colloids were prepared by the method of Leopold and Lendl [22] by dissolving 10.44 mg of hydroxylamine in UHP water (1.67×10^{-3} M) and 11.98 mg of NaOH 3.33×10^{-3} M in UHP water and 90 mL of pure degasified water for 15 min while stirring with a magnetic bar. Then, 10 mL of 1.0×10^{-2} M silver nitrate solution was added dropwise with constant nitrogen bubbling. Colloidal suspensions at different pH values were prepared using 0.1 and 0.01 M of both HCl and NaOH and the measurements were read using a pH meter.

2.3. Preparation of Bacterial Sample. Pure culture of *Bt* stored at -80°C in 20% glycerol was inoculated in LB agar plates and incubated at 32°C overnight. After transferring pure culture to 5.0 mL LB broth in a culture tube, it was placed in an orbital shaker at 32°C (~120 rpm) during 24 hr. An Erlenmeyer flask (250 mL) was prepared with nutrient media and microorganism culture to a final volume of 25 mL to obtain an initial optical density at 600 nm (OD₆₀₀) of 0.025. Samples were collected after bacteria were cultured for 15 hr then centrifuged for 12 min at 8228 rcf and the supernatant

was discarded. The pellet obtained was washed twice with 5 mL of 0.1 M NaCl and finally resuspended in 0.1 M NaCl. The bacterial concentration used was 10^7 cfu/mL, and the OD₆₀₀ (Biophotometer, Eppendorf) was measured before and after centrifugation. The bacterial samples were stored at 4°C until experiments were performed. Standard Biosafety Level 2 procedures were employed to handle, process, and discard the samples. Techniques such as Gram stain and Fulton-Schaeffer spore stain were used to characterize *Bt*.

2.4. Raman and SERS Sample Preparation. Bacterial samples were transferred to glass capillary tubes (1.5 × 90 mm) using sterile, disposable needles and syringes to obtain the Raman spectra. A small amount of the bacterial solution dissolved in 0.1 M NaCl was used for normal Raman experiments. For SERS experiments, 200 μ L of colloidal NPs suspensions (as prepared) were mixed with 25 μ L of bacterial suspension in a microcentrifuge tube and vigorously shaken in a minivortex. Small amounts of the mixtures were transferred to the capillary tubes and SERS spectra were obtained. To further increase Raman signals by stimulation of formation of hot spots on aggregation of NPs, clustering was promoted by addition of 1.0 M NaCl to colloidal suspensions [23]. To adjust the pH values of colloidal suspensions, small amounts of HCl and NaOH with concentration of 0.01 or 0.1 M were added until obtaining the desired pH (1 to 13). Then, the mixtures were prepared for SERS experiments using the same procedure as described.

3. Measurements and Analysis

3.1. Instrumentation. Ag-NPs were characterized by UV-VIS spectrophotometry and by transmission electron microscopy (TEM). Absorption spectra of the solutions were acquired using a Cary 5000 UV-VIS-NIR spectrophotometer (Varian, Palo Alto, Calif, USA). TEM images were recorded by in a model 1011 electron transmission microscope providing a resolution of 0.2 nm lattice with magnification of 50 to 10⁶ under the accelerating voltage of 40 to 100 kV (JEOL, Peabody, Mass, USA). Samples were prepared by placing 1.0 μ L of the Ag-NPs solution in ultrathin carbon film/holey carbon 400 mesh copper TEM grids (01824, Ted Pella, Inc., Redding, Calif, USA) and allowing the solvent to evaporate at room temperature. The grids were kept in desiccator to provide a dust-free environment. Raman experiments were done using a Raman Microspectrometer, model RM-2000, CCD camera, Leica LX microscope, 532 nm laser line, 10–50 s exposure time, 3 accumulations and a 10x objective lens in a spectra range of 100–3000 cm⁻¹ (Renishaw Inc., Hoffman Estates, Ill, USA). White light microscopy images of samples were acquired in order to determine the content of the sample. An Olympus America, Inc. (Center Valley, Pa, USA) model BH2-UMA high resolution optical microscope designed for mineralogy studies and equipped with 10–250x magnification and a 6.0 MB PAX-Cam image capturing CCD camera controlled by PAX-it! Software (Midwest Information Systems, Inc., Villa Park, Ill, USA) was used to capture the white light micrographs. Most of the images

captured were taken with 10x and 100x ultra long working distance objectives. Z-potential and hydrodynamic radius measurements were obtained using a Zetasizer Nano Series (Malvern Instruments Ltd., manufacturer, Worcestershire, UK).

3.2. Data Analysis. All the normal Raman and SERS spectra obtained were analyzed using OPUS software (Bruker Optics, Billerica, Mass, USA) by applying baseline correction to allow a proper tentative assignment of vibrational bands. Spectra were normalized for intensity, laser power and acquisition time (counts·mW⁻¹·s⁻¹).

4. Results and Discussion

4.1. Characterization of Ag-NPs. Borohydride reduced-citrate capped Ag NPs suspensions had a yellowish color when present in an atomic silver concentration of $\sim 10^{-4}$ M. The freshly prepared suspensions were slightly alkaline with a pH of 8.9 and an absorption maximum at 397 nm. The average diameter obtained from many TEM measurements was 19 ± 3 nm. Ag-NPs reduced with hydroxylamine were obtained after a few seconds and had a grayish-brown color with an atomic Ag final concentration of $\sim 10^{-3}$ M. The freshly synthesized NPs colloidal suspensions obtained by hydroxylamine reduction were acid with pH of 5.7 and an absorption maximum at 437 nm. Average particle diameter was 28 ± 10 nm. Figures 1(a) and 1(b) show the UV-Vis spectra, the color of freshly prepared sols and the corresponding TEM images of the borohydride and hydroxylamine nanoparticles, respectively.

4.2. Characterization of Biological Samples. *Bt* was characterized by Gram and Fulton-Schaeffer spore staining techniques. The Gram-staining technique confirmed the presence of Gram-positive *bacillus* strain (Figure 2). Endospores staining was performed to establish the presence of vegetative cells and endospores in the sample. Figures 2(a) and 2(b) show vegetative cells or/and endospores content of *Bt* strain used in the experiments under the white light microscope. Previous experiments were used to determine the samples which contained vegetative cells, endospores, and mixtures by a bacterial growth curve (data not shown). The samples used in the Raman/SERS experiments were obtained from the growth stage at 15 hr in which vegetative cells and endospores coexist as mixtures.

4.3. Raman and SERS Experiments. Silver nanoparticles have a plasmon resonance in the visible (VIS) region (400–700 nm) of the electromagnetic spectrum with excellent match with laser lines located at 514.5 and 488 nm and solid-state diode laser at 532 nm. [24] However, by using the excitation lines located at 633 and 785 nm will be far away from the transverse plasmon band of the silver nano-particles prepared in this research. This fact will have a small contribution to the electromagnetic SERS effect. Biological samples presents a highly fluorescence effect that should be quenched before obtain the SERS

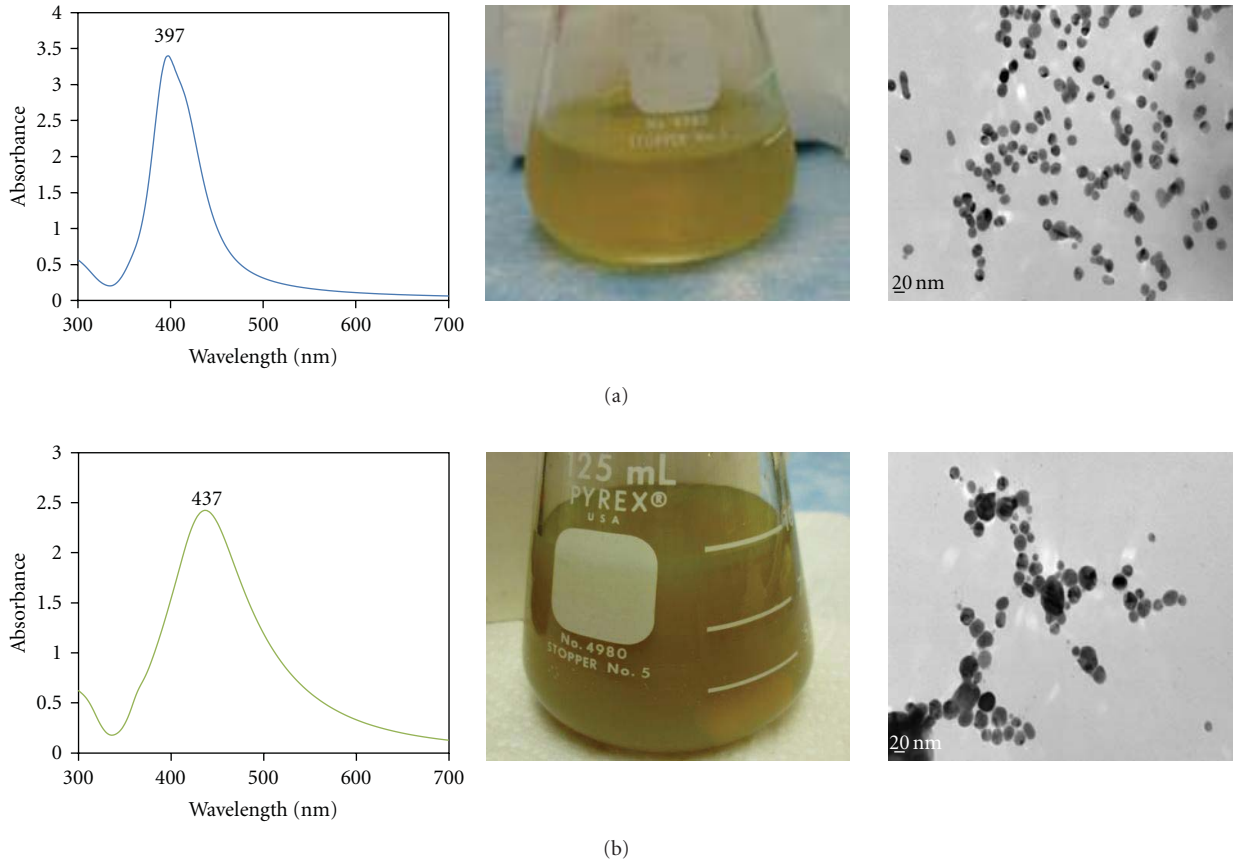


FIGURE 1: UV-Vis spectra (left), final color of freshly prepared sols (center) and TEM images (right) of: (a) borohydride reduced-citrate capped Ag NPs and (b) hydroxylamine reduced Ag-NPs used in the experiments described.

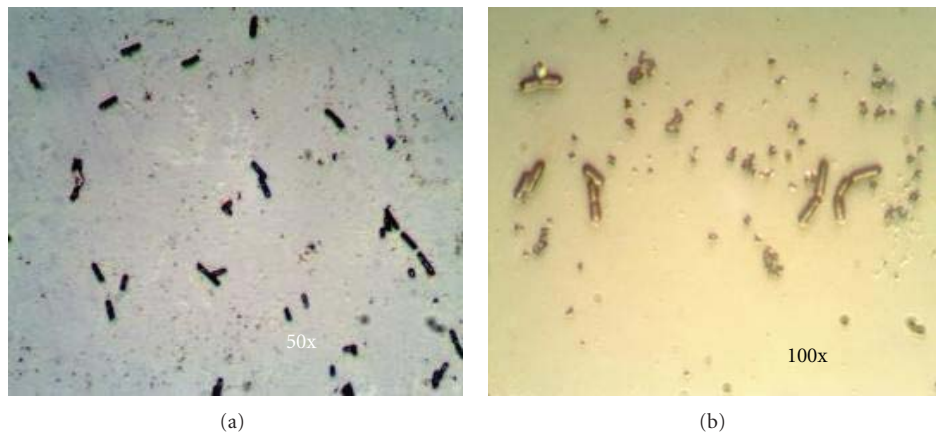


FIGURE 2: White light micrographs of *Bt* characterization at 15 hr of bacterial growth (a) 50x Gram staining (purple: Gram +); (b) 100x endospores staining with high magnification image of stained endospores.

spectra to obtain good SERS results. As mentioned in previous literature, the fluorescence of bacteria is “especially strong with 532-nm excitation, but some photobleaching is required even for near-infrared (NIR) excitation.” [25] In this study, 10 to 50 s of exposure time were used to minimize the fluorescence problems of the biological samples.

The Raman spectrum of *Bt* at 15 hr of bacterial growth was contaminated with fluorescence from the presence of fluorophores commonly found in many biological compounds. However, important signals could be tentatively assigned from spectra acquired of a highly concentrated bacterial suspension (Figure 3) even though many of them appeared as low-intensity bands in a highly congested background.

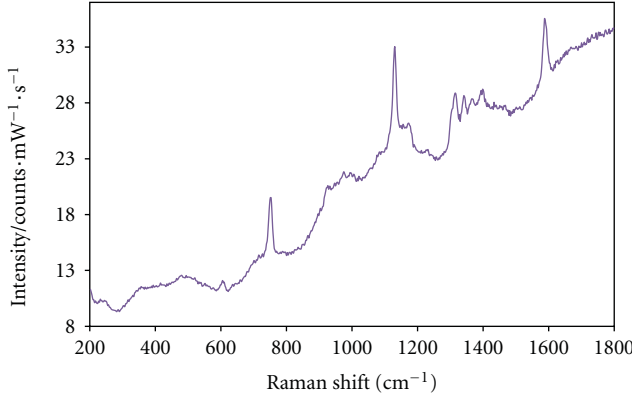


FIGURE 3: Raman spectrum of concentrated sample of *Bt* suspended in 0.1 M NaCl at 15 hr of bacterial growth.

Several of the bands observed were from glycosidic ring of NAG and NAM at 753 cm^{-1} , C–N and C–C stretching at 1130 cm^{-1} , signals from lipid content, =C–C= at 1144 cm^{-1} and C=C at 1588 cm^{-1} . Most of the signals observed are related to calcium dipicolinate (CaDPA), which is the main component of the protective layers of the central core cell, the endospores [26]. To enhance the signal identification of the biological content and decrease the fluorescence of the bacterial content several aspects of the biomolecular system under study had to be taken into account. To begin with, SERS spectra in these systems result from the interaction of the metal NPs surface with the outer coating content of the cells. Due to poor signal definition and limited chemical information in the Raman spectrum of *Bt*, the volume and concentration of the NPs colloidal suspensions used, the sample amount and concentration of the biological system under study analyzed, the charge of the layer of NPs and the aggregation induction effects of the colloidal NPs had to be optimized. The affinity of the biomolecular sample (*Bt*) to Ag-NPs was improved resulting in enhancement of the signal to noise of the SERS spectra obtained. Also, a significant decrease in fluorescence present in the Raman spectra of this *bacillus* was observed. Details of these effects are clearly discussed in the next sections with dealing with Ag-NPs reduced by borohydride and hydroxylamine.

4.3.1. Borohydride-Reduced Ag-NPs. The SERS spectra shown in Figure 4 clearly demonstrate the high signal enhancement of the vibrational modes of *Bt* when using borohydride reduced metallic suspension of NPs as SERS substrates. These small Ag-NPs have been used to successfully detect bacterial samples [13, 15, 17]. The biochemical composition of this *bacillus* sample could be identified mostly by the calcium dipicolinate (CaDPA) peaks that dominate the spore content among other bacterial wall content. The SERS spectrum of *Bt* (Figure 4(a)) has characteristic peaks that can be tentatively assigned based on literature values as shown in Table 1 [10, 27, 28]. The affinity of these nanoparticles to *Bt* can be increased by a slight aggregation of NPs [17] and by surface charge modification of the NPs when a biosample that does not induce any aggregation is used [16]. The

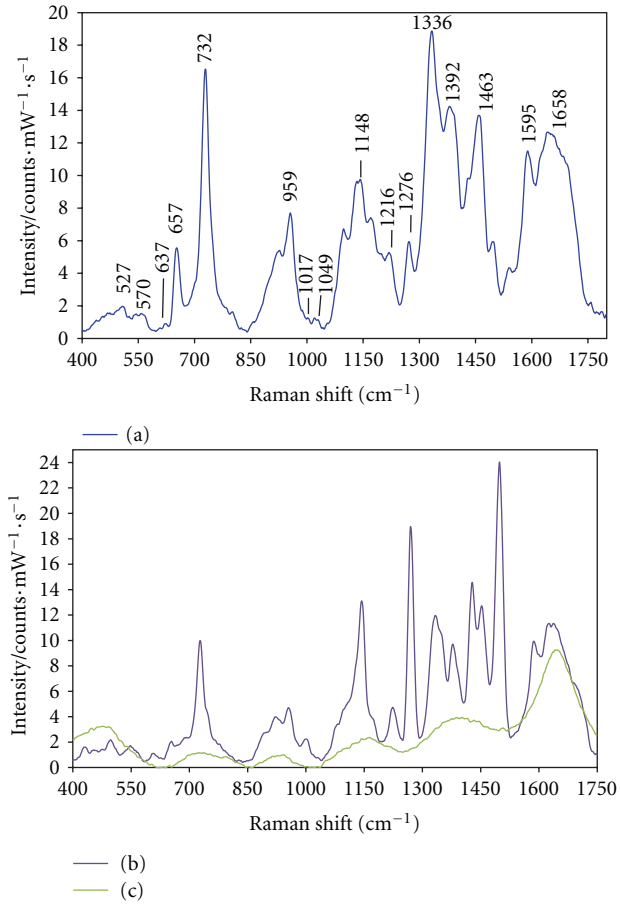


FIGURE 4: Enhanced Raman spectra of *Bt* and Ag-NPs: (a) Spectrum of *Bt* suspended in 0.1 M NaCl at 15 hr of bacterial growth in contact with citrate capped borohydride reduced Ag-NPs; (b) Spectrum of *Bt* using chloride anion (1.0 M, NaCl) as aggregation agent for Ag-NPs; (c) Spectrum of borohydride reduced Ag-NPs aggregated by chloride anion (1.0 M, NaCl) without microorganisms.

use of aggregation agents at low concentrations, such as chloride, with borohydride-reduced NPs and biomolecular compounds [29] has been used to distribute the nanoparticles on the cell wall obtaining the activation of “hot spots” on the NPs surface [17]. Because the concentration used for aggregation purposes is a critical parameter, high concentrations of the aggregation agent of 1.0 M results in a decrease of the plasmon band of the nanoparticles as shown in Figure 5 and the gray color in Figure 6(c), evidencing the oxidation of the NPs. The agglomeration does not occur uniformly as Ag NPs bind to only certain specific groups on the bacterial cell wall [30] causing a decrease of the close contact of the small NPs to the analyte and as a result a decrease of the SERS signal. The SERS spectrum of *Bt* using nanoparticles aggregated by chloride ions and the Raman spectrum of NPs aggregated by chloride anions (without *Bt*) can be observed in Figures 4(b) and 4(c), respectively.

However, the lower concentration of NaCl in which *Bt* was already suspended (0.1 M) can have an influence on the activation of “hot spots” on NPs, inducing a closer, more

TABLE 1: Tentative assignment of vibrational bands for (a) normal Raman spectrum of *Bt* and SERS spectra of *Bt* using (b) citrate capped borohydride reduced Ag-NPs and (c) hydroxylamine reduced Ag-NPs.

| Vibration mode | a | b | c |
|---|------|------------------------------|------|
| | | Raman shift/cm ⁻¹ | |
| S–S stretching of cysteine in spore coat | | 527 | 526 |
| C–C skeletal of carbohydrates | | 570 | 587 |
| C–S stretching of cysteine in spore coat | | 1049 | 1065 |
| N–H deformation of amide II in CaDPA | | 637 | |
| glycosidic ring of NAG and NAM | 753 | 657 | 657 |
| C=C deformation of tyrosine | | 732 | 728 |
| C=C deformation of tyrosine | 959 | | 962 |
| C–N and C–C stretching | 1130 | | |
| C–H in plane bending of CaDPA | | 1017 | |
| =C–C= of lipids or C–N aromatic in proteins | 1144 | 1148 | 1134 |
| amide III | | 1216 | 1246 |
| | | 1276 | |
| C–NH ₂ stretching of amide II | | 1336 | 1326 |
| COO [–] stretching in CaDPA | | 1392 | 1377 |
| C–H deformation of lipids | | 1463 | 1465 |
| C=C ring stretching of lipids | 1588 | 1595 | 1590 |
| amide I | | 1658 | 1705 |

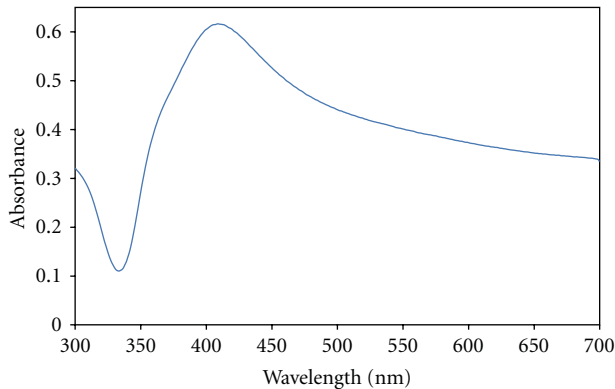


FIGURE 5: UV-Vis spectrum showing the decrease of the plasmon band when borohydride reduced Ag-NPs were aggregated with NaCl 1.0 M.

effective interaction with biological samples and consequently increasing SERS signals as shown in Figure 4(a). It is advantageous to use the already existing concentration of NaCl instead of using the bacterial sample suspended in water (washing away the salt) or adding a higher concentration of NaCl as aggregating agent to increase the SERS enhancement effect. This was confirmed with slightly change in the color when *Bt* is added to the Ag-NPs (Figures 6(a), and 6(b)).

The surface chemistry of Ag-NPs can be altered by adjusting the pH of the sols and thus promoting adsorption of *Bt* on the SERS active substrates [13–16]. At very low pH values of the colloidal suspension (pH < 2), the surface charge of the NPs began to be neutralized and at very high

pH values the Ag colloidal NPs were oxidized resulting in precipitation [12]. At this time, the absorbance of the NPs colloids decreased and the interaction with the bacterial wall became poor. In highly acidic and basic pH sols were very unstable. NPs decrease in size and precipitated after approximately 2–3 hr. Aggregation of NPs was confirmed by the values of hydrodynamic radii (nm): 17.60, 15.57, 14.64, and 14.50 at pH of 3, 5, 7, and 9, respectively.

As demonstrated in previous works [15], when the pH of borohydride reduced colloidal suspension are adjusted to more acidic pH values with respect of the initial value of pH ~ 9, the slightly negative charged induced by the citrate capping agent become slightly more positive with H⁺ ions added and the zeta potential values are more positive confirming the hypothesis. Biochemical content in the bacterial cell wall is dominated by negatively charged compounds such as phosphates in teichoic acids and carboxylate anions from the dipicolinate complex. Thus, strong electrostatic interactions dominate binding of NPs with the bacterial cell wall content [17]. The positive charge on the NPs surface is appropriate for promoting interaction with *Bt*, increasing the SERS effect in the biomolecular system. Figure 7 shows the SERS spectra of NPs upon interaction with bacterial suspension at pH 3, 5, 7, and 9. The number of peaks obtained for the target microorganism is significantly larger and the spectral clarity of SERS spectra of *Bt* interacting with borohydride reduced NPs with pH adjusted and surface charge modified is noticeably greater. For the SERS spectra obtained at pH 5 to 9, the bands observed are better defined than at higher values (pH 11: data not shown) or at lower values (pH = 3). Although it is expected to have more positive charges on the surface at pH 3 at this pH the NPs were aggregated to a larger extent and the SERS effect decreased.

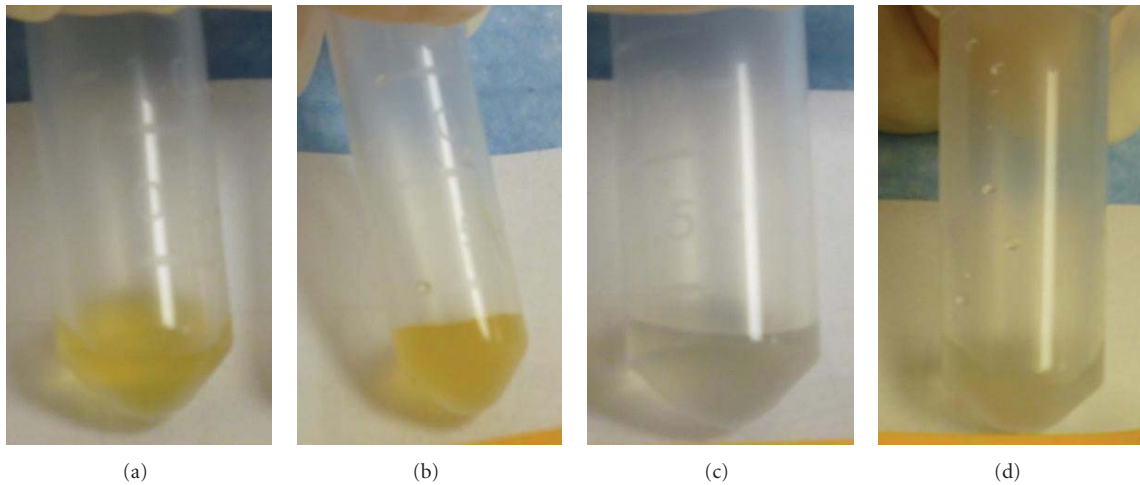


FIGURE 6: Changes in color of borohydride reduced Ag-NPs when mixed with bacterial samples and aggregated with NaCl 1.0 M. (a) Color of borohydride reduced NPs; (b) Slight change in color when *Bt* suspended in 0.1 M NaCl was added to sol; (c) Color of the borohydride reduced Ag-NPs aggregated with 1.0 M NaCl; (d) color of suspensions when *Bt* suspended in 0.1 M NaCl was added.

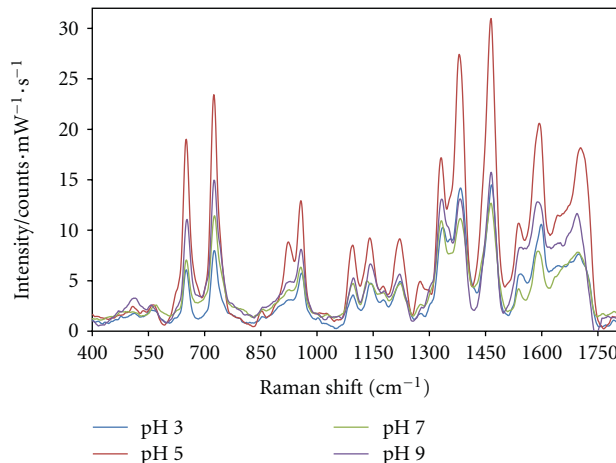


FIGURE 7: SERS spectra of *Bt* in contact with borohydride reduced Ag-NPs at pH 3, 5, 7, and 9 showing a higher SERS enhancement at pH 5.

4.3.2. Hydroxylamine Nanoparticles. Biochemical components of *Bt* cell wall were identified using NPs-reduced with hydroxylamine hydrochloride. A typical SERS spectrum of the bacterial suspension in contact with NPs (Figure 8(a)) allows the identification of S-S stretching (526 cm^{-1}) and C-S stretching (657 cm^{-1}) of cysteine in spore coat, glycosidic ring of NAG and NAM (728 cm^{-1}), C=C deformation of tyrosine (962 cm^{-1}), C-C skeletal (587 , 1065 cm^{-1}) of carbohydrates, =C=C= of lipids or C-N aromatic in proteins (1134 cm^{-1}), amide III (1246 cm^{-1}), C-NH₂ stretching of amide II (1326 cm^{-1}), COO⁻ stretching in CaDPA (1377 cm^{-1}), C-H deformation of lipids (1465 cm^{-1}), C=C ring stretching of lipids (1590 cm^{-1}) and amide I (1705 cm^{-1}) which could be tentative assigned based on literature values [10, 27, 28]. The Raman spectrum of the hydroxylamine-reduced NPs is free from anomalous

bands that can interfere with the identification of bacterial composition. Attempts of adding high concentrations of chloride ions as aggregator agent failed. The Raman spectrum of the NPs aggregated by chloride anions (Figure 8(c)) is too rich in spectroscopic information above 1160 cm^{-1} to use it as background Raman spectrum for microorganism studied. The vibrational bands of *Bt* in this region are masked by the vibrational modes of the nanoparticles aggregated by chloride ions, and thus, the bands cannot be properly assigned (Figure 8(b)). However, high and clear intensity vibrational bands before 1100 cm^{-1} can be properly assigned to bacterial components. Vibrational signals from hydroxylamine hydrochloride reduced NPs at acidic and alkaline pH values obtained in the SERS spectra interfere with the proper assignment of the vibrational modes of *Bt*. The high intensity anomalous bands founds on the addition of the aggregating agents and the pH-dependent ionizable functional groups that can undergo dissociation and protonation, depending on bulk solution pH values, for hydroxylamine-reduced silver colloids was previously explained by Yaffe and Blanch [31] and Kazanci et al. [16], respectively. As a result, no modification in the nanoparticles surface with pH changes to hydroxylamine reduced NPs were necessary for a successful detection of these *bacillus* gram-positive bacteria. NaCl contained in the suspension of bacterial sample was sufficient to activate “hot spots” of the hydroxylamine reduced NPs leading to strong SERS signals that could be used to characterize biochemical composition of *Bt*.

5. Conclusion

The results presented demonstrate that SERS spectra obtained with Ag-NPs reduced by hydroxylamine and borohydride capped by citrate and were successfully used to spectroscopically characterize *Bt*. The use of colloidal suspensions of metallic NPs is favorable to enhance the SERS detection

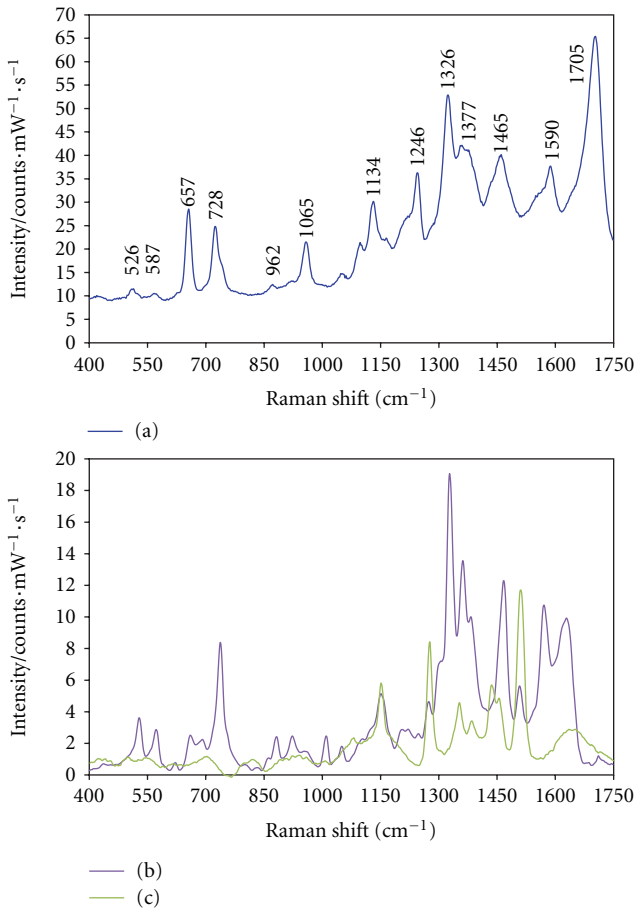


FIGURE 8: Enhanced Raman spectra of *Bt* and Ag-NPs reduced by hydroxylamine: (a) Spectrum of *Bt* suspended in 0.1 M NaCl at 15 hr of bacterial growth in contact with Ag-NPs; (b) Spectrum of *Bt* using chloride anion (1.0 M, NaCl) as aggregation agent for Ag-NPs; (c) Spectrum of hydroxylamine reduced Ag-NPs aggregated by chloride anion (1.0 M, NaCl) without microorganisms.

of large biological samples compared to the small size of the nanoparticles, because the electrostatic interactions that dominates the interaction of the NPs and bacterial content can occur around all the biological sample and not on one side as is the case of the Raman vibrational enhancement produced by solid metallic surfaces. The small borohydride nanoparticles used with a slightly activated “hot spots” and pH surface modifications of the NPs to more acidic pH values (7 to 3) than the pH of nanoparticles synthesis preparation (pH 9) resulted in good SERS substrates for *Bt* detection. High concentrations of NaCl, as 1.0 M, results in a nanoparticles oxidation and a decrease in the SERS signal. Bacterial samples suspended in low concentrations of NaCl (0.1 M) and modifications of the borohydride nanoparticles surface in a range of 5 to 9 pH values can improve SERS detection of *Bt*. As shown in this work, surface modifications of NPs with pH changes results in more reliable spectral information of *Bt* because neat Raman spectra with the modified NPs were obtained at all pH. Raman spectra obtained from NPs aggregated with NaCl presented several peaks that interfere

with the bacterial identification. Hydroxylamine NPs used as SERS substrates for *Bt* detection resulted in good SERS substrates with a slight activation of “hot spots” using low concentrations of NaCl in which the bacteria were suspended and no pH surface modifications of the NPs were required.

Results of SERS spectra of experiments with bacteria in contact with NPs at different pH values differ significantly from one another in some biomolecules and bacteria, depending on the conditions imposed to the interacting micro-organisms and NPs systems. An improved interaction, as judged from higher intensity SERS signals, was obtained for NPs with slightly positive charge surface was in contact with this Gram-positive bacteria (*Bt*) containing the negatively charged phosphate groups of the teichoic acids transverse in peptidoglycan layer and the carboxylic groups in the dipicolinic complex of the exosporium layer of endospores. The results suggest that high signal enhancements from the bacterial cell wall and endospores components of *Bt* can be obtained by tailoring the conditions of SERS experiments. However, SERS effect has to be proven with the *Bt* protoplast and individual endospore components in order to confirm the content of the biological sample and the assignment of bands obtained from SERS experiments.

Acknowledgments

Part of the work presented in this study was supported by the U.S. Department of Defense University Research Initiative Multidisciplinary University Research Initiative (URI)-MURI Program under grant no. DAAD19-02-1-0257. The authors also acknowledge contributions from Mr. Aaron LaPointe from the Night Vision and Electronic Sensors Directorate, Fort Belvoir, Va, Department of Defense, Dr. Jennifer Becker, MURI Program Manager, Army Research Office, DoD, and Dr. Stephen J. Lee, Chief Scientist, Science and Technology, Office of the Director, Army Research Office/Army Research Laboratory, DoD. Support from the U.S. Department of Homeland Security under Award no. 2008-ST-061-ED0001 is also acknowledged. However, the views and conclusions contained in this paper are those of the authors and should not be considered a representation of the official policies, either expressed or implied, of the U.S. Department of Homeland Security. Thanks are due to Kristina Soto-Feliciano for collaboration in the experiments. Dr. Rong Zhang from Jackson State University is acknowledged for facilitating the TEM images.

References

- [1] K. Maquelin, C. Kirschner, L. P. Choo-Smith et al., “Prospective study of the performance of vibrational spectroscopies for rapid identification of bacterial and fungal pathogens recovered from blood cultures,” *Journal of Clinical Microbiology*, vol. 41, no. 1, pp. 324–329, 2003.
- [2] J. Chan, S. Fore, S. Wachsmann-Hogiu, and T. Huser, “Raman spectroscopy and microscopy of individual cells and cellular components,” *Laser & Photonics Reviews*, vol. 2, no. 5, pp. 325–349, 2008.

- [3] R. Jarvis, S. Clarke, and R. Goodacre, "Rapid analysis of microbial systems using SERS," *Surface-Enhanced Raman Scattering*, vol. 103, pp. 397–408, 2006.
- [4] M. J. Ayora, L. Ballesteros, R. Pérez, A. Rupérez, and J. J. Laserna, "Detection of atmospheric contaminants in aerosols by surface-enhanced Raman spectrometry," *Analytica Chimica Acta*, vol. 355, no. 1, pp. 15–21, 1997.
- [5] D. White, *The Physiology and Biochemistry of Prokaryotes*, Oxford University Press, New York, NY, USA, 2007.
- [6] G. J. Tortora, B. R. Funke, and C. L. Case, *Microbiology: An Introduction*, Pearson Benjamin Cummings, San Francisco, Calif, USA, 2010.
- [7] M. T. Madigan and T. D. Brock, *Brock Biology of Microorganisms*, Pearson Benjamin Cummings, San Francisco, Calif, USA, 2009.
- [8] S. Shanmukh, L. Jones, J. Driskell, Y. Zhao, R. Dluhy, and R. A. Tripp, "Rapid and sensitive detection of respiratory virus molecular signatures using a silver nanorod array SERS substrate," *Nano Letters*, vol. 6, no. 11, pp. 2630–2636, 2006.
- [9] A. Sengupta, N. Brar, and E. J. Davis, "Bioaerosol detection and characterization by surface-enhanced Raman spectroscopy," *Journal of Colloid and Interface Science*, vol. 309, no. 1, pp. 36–43, 2007.
- [10] J. Guicheteau, L. Argue, D. Emge, A. Hyre, M. Jacobson, and S. Christesen, "Bacillus spore classification via surface-enhanced Raman spectroscopy and principal component analysis," *Applied Spectroscopy*, vol. 62, no. 3, pp. 267–272, 2008.
- [11] R. M. Jarvis, A. Brooker, and R. Goodacre, "Surface-enhanced Raman spectroscopy for bacterial discrimination utilizing a scanning electron microscope with a Raman spectroscopy interface," *Analytical Chemistry*, vol. 76, no. 17, pp. 5198–5202, 2004.
- [12] R. A. Alvarez-Puebla, E. Arceo, P. J. G. Goulet, J. J. Garrido, and R. F. Aroca, "Role of nanoparticle surface charge in surface-enhanced raman scattering," *Journal of Physical Chemistry B*, vol. 109, no. 9, pp. 3787–3792, 2005.
- [13] A. Sengupta, M. L. Laucks, and E. James Davis, "Surface-enhanced Raman spectroscopy of bacteria and pollen," *Applied Spectroscopy*, vol. 59, no. 8, pp. 1016–1023, 2005.
- [14] A. Sengupta, M. Mujacic, and E. J. Davis, "Detection of bacteria by surface-enhanced Raman spectroscopy," *Analytical and Bioanalytical Chemistry*, vol. 386, no. 5, pp. 1379–1386, 2006.
- [15] M. Kahraman, M. M. Yazici, F. Sahin, O. F. Bayrak, and M. Culha, "Reproducible surface-enhanced Raman scattering spectra of bacteria on aggregated silver nanoparticles," *Applied Spectroscopy*, vol. 61, no. 5, pp. 479–485, 2007.
- [16] M. Kazanci, J. P. Schulte, C. Douglas, P. Fratzl, D. Pink, and T. Smith-Palmer, "Tuning the surface-enhanced raman scattering effect to different molecular groups by switching the silver colloid solution pH," *Applied Spectroscopy*, vol. 63, no. 2, pp. 214–223, 2009.
- [17] M. Knauer, N. P. Ivleva, R. Niessner, and C. Haisch, "Optimized surface-enhanced Raman scattering (SERS) colloids for the characterization of microorganisms," *Analytical Sciences*, vol. 26, no. 7, pp. 761–766, 2010.
- [18] F. Yan, M. B. Wabuyele, G. D. Griffin, A. A. Vass, and T. Vo-Dinh, "Surface-enhanced Raman scattering, detection of chemical and biological agent simulants," *Institute of Electrical and Electronics Engineers Sensors Journal*, vol. 5, no. 4, pp. 665–670, 2005.
- [19] W. R. Premasiri, D. T. Moir, M. S. Klempner, N. Krieger, G. Jones, and L. D. Ziegler, "Characterization of the surface enhanced Raman scattering (SERS) of bacteria," *Journal of Physical Chemistry B*, vol. 109, no. 1, pp. 312–320, 2005.
- [20] F. Yan and T. Vo-Dinh, "Surface-enhanced Raman scattering detection of chemical and biological agents using a portable Raman integrated tunable sensor," *Sensors and Actuators B*, vol. 121, no. 1, pp. 61–66, 2007.
- [21] R. Keir, D. Sadler, and W. E. Smith, "Preparation of stable, reproducible silver colloids for use as surface-enhanced resonance Raman scattering substrates," *Applied Spectroscopy*, vol. 56, no. 5, pp. 551–559, 2002.
- [22] N. Leopold and B. Lendl, "A new method for fast preparation of highly surface-enhanced raman scattering (SERS) active silver colloids at room temperature by reduction of silver nitrate with hydroxylamine hydrochloride," *Journal of Physical Chemistry B*, vol. 107, no. 24, pp. 5723–5727, 2003.
- [23] G. P. GlasPELL, C. Zuo, and P. W. Jagodzinski, "Surface enhanced Raman spectroscopy using silver nanoparticles: the effects of particle size and halide ions on aggregation," *Journal of Cluster Science*, vol. 16, no. 1, pp. 39–51, 2005.
- [24] O. M. Primera-Pedrozo, J. I. Jerez-Rozo, E. De La Cruz-Montoya, T. Luna-Pineda, L. C. Pacheco-Londoño, and S. P. Hernández-Rivera, "Nanotechnology-based detection of explosives and biological agents simulants," *Institute of Electrical and Electronics Engineers Sensors Journal*, vol. 8, no. 5–6, Article ID 4529211, pp. 963–973, 2008.
- [25] J. Guicheteau, S. Christesen, D. Emge, and A. Tripathi, "Bacterial mixture identification using Raman and surface-enhanced Raman chemical imaging," *Journal of Raman Spectroscopy*, vol. 41, no. 12, pp. 1342–1347, 2010.
- [26] H. W. Cheng, W. Q. Luo, G. L. Wen, S. Y. Huan, G. L. Shen, and R. Q. Yu, "Surface-enhanced Raman scattering based detection of bacterial biomarker and potential surface reaction species," *Analyst*, vol. 135, no. 11, pp. 2993–3001, 2010.
- [27] J. De Gelder, P. Scheldeman, K. Leus et al., "Raman spectroscopic study of bacterial endospores," *Analytical and Bioanalytical Chemistry*, vol. 389, no. 7–8, pp. 2143–2151, 2007.
- [28] J. L. Chalmers and P. R. Griffiths, Eds., *Handbook of Vibrational Spectroscopy*, John Wiley & Sons, New York, NY, USA, 2002.
- [29] S. Sanchez-Cortes and J. V. Garcia-Ramos, "Anomalous Raman bands appearing in surface-enhanced Raman spectra," *Journal of Raman Spectroscopy*, vol. 29, no. 5, pp. 365–371, 1998.
- [30] L. Zeiri, B. V. Bronk, Y. Shabtai, J. Czégé, and S. Efrima, "Silver metal induced surface enhanced Raman of bacteria," *Colloids and Surfaces A*, vol. 208, no. 1–3, pp. 357–362, 2002.
- [31] N. R. Yaffe and E. W. Blanch, "Effects and anomalies that can occur in SERS spectra of biological molecules when using a wide range of aggregating agents for hydroxylamine-reduced and citrate-reduced silver colloids," *Vibrational Spectroscopy*, vol. 48, no. 2, pp. 196–201, 2008.

Research Article

Infrared and Raman Spectroscopic Study of Carbon-Cobalt Composites

André Tembre, Jacques Hénocque, and Martial Clin

Laboratoire de Physique de la Matière Condensée, Université de Picardie Jules Verne, 33 Rue Saint Leu, 80039 Amiens Cédex 1, France

Correspondence should be addressed to Martial Clin, martial.clin@u-picardie.fr

Received 20 May 2011; Revised 22 July 2011; Accepted 13 August 2011

Academic Editor: Ahmed Aamouche

Copyright © 2011 André Tembre et al. This is an open access article distributed under the Creative Commons Attribution License, which permits unrestricted use, distribution, and reproduction in any medium, provided the original work is properly cited.

Analysis of carbon-cobalt thin films using infrared spectroscopy has shown existence of carbon-cobalt stretching mode and great porosity. The Raman spectroscopy and high-resolution transmission electron microscopy have been used in order to investigate the microstructure of the films. These films exhibit complex Raman spectra suggesting the presence of amorphous and crystallized phases. The different fractions of phases and the correlation between the atomic bond structures and the Raman features depend on the cobalt content.

1. Introduction

In the last years, nanocrystalline magnetic materials made of metallic nanoclusters dispersed in an amorphous matrix have attracted considerable interest owing to their magnetic properties and promising applications as memory units for high-density storage and fundamental research [1, 2]. Hayashi et al. [3] have reported the fabrication and characterization of magnetic thin films of h.c.p cobalt nanocrystals of around 8 nm size encapsulated in graphite-like carbon cages. Due to their ferromagnetic nature, the cobalt grains have great potential for ultra-high-density magnetic recording media.

The incorporation in the carbon network of various metallic atoms, like Ti, Zr, Ta, Cr, Mo, W, Fe, Co, and Ni, is a good alternative to improve the tribological [4–7], electric [8–10], and magnetic [11–15] properties of carbon films for various applications as solid lubricant films, microelectrodes, or magnetic films. It has been reported that insertion of metallic atoms in amorphous carbon matrix changes the fraction of Csp^3 -coordinated carbon sites [16].

Various techniques have been used to fabricate metallic nanoclusters dispersed in an amorphous matrix; we can mention filtered cathodic vacuum arc [17, 18], pulsed laser deposition [19], cosputtering [10, 20], and dual beam evaporation system [5]. Among these different methods, cathodic

arc deposition is widely used [21, 22]; this technique is characterized by high degree of ionization and great ion kinetic energy and deposition rate. Cathodic arc processes produce unwanted macroparticles in the mm range which are removed from the plasma by a magnetic filter; on the contrary, anodic arc do not suffer from macroparticles contamination, which was the main motivation of using this deposition technique in the present study.

Recently, it has been reported that incorporation of iodine in amorphous carbon [23, 24] and boron in diamond [25] leads to a metal-insulator transition at low temperature. Cobalt-doped carbon thin films at 0.3% cobalt content, deposited by a pulsed anodic electric arc technique, have shown anomalous behaviour on electric and magnetic susceptibility measurements and evidence of metal-insulator transition around 60 K [26]. This work aims at obtaining more information about the correlation between microstructure and features of infrared and Raman spectra of these carbon-cobalt thin films.

2. Experimental Details

The carbon-cobalt films were deposited by pulsed anodic electric arc system, using graphite rod electrodes of 6 mm diameter. The anode was made of pure graphite rod stuffed with C/Co powder in a hole of 3 mm diameter in the center

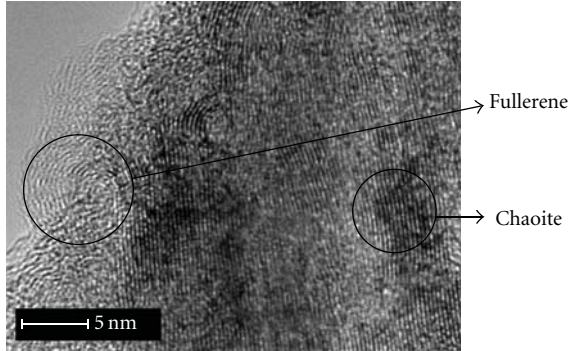


FIGURE 1: HRTEM image obtained for 0.3%-cobalt-doped carbon thin film. Regions with curved fringes of fullerene like graphitic layers and chaoite structure can be seen.

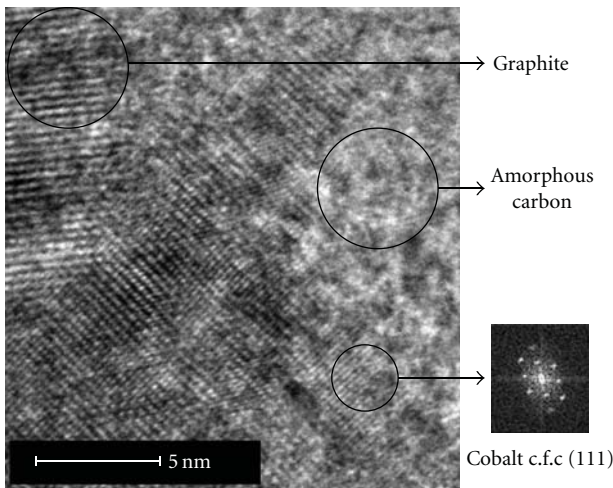


FIGURE 2: HRTEM image obtained for 0.3%-cobalt-doped carbon thin film. Regions with graphitic and amorphous carbon are shown. Crystallized cobalt aggregate of about 5 nm size can be seen.

of the rod. The cathode was made of pure graphite rod. Both purities of graphite and cobalt powder were 99.9%. The anodic arc is triggered when cathode and anode touch each other. The arc current was 70 A, and DC discharge voltage was 40 V with an arc duration of 1 s and pulse repetition rate of 5 Hz. A bias voltage of DC –400 V was applied to the substrate holder. The base pressure of the deposition chamber was 0.1 Pa. The content of cobalt in carbon films was determined by atomic absorption using a Perkin Elmer Analyst 300 apparatus. The cobalt content is monitored by the percentage cobalt in the C/Co powder used to make anode. The thickness of the films was about 400 nm.

The nanostructure of the films were observed by high resolution transmission electron microscopy (HRTEM) equipped with a microanalysis probe at accelerating voltage of 200 kV.

Fourier transform infrared measurements were performed using a Nicolet 510 spectrometer in the 400–4000 cm⁻¹ range. The Raman spectra were recorded by a Jobin Yvon T64000 triple monochromator Raman spectrometer. An argon ion laser with a wavelength of 514.5 nm served

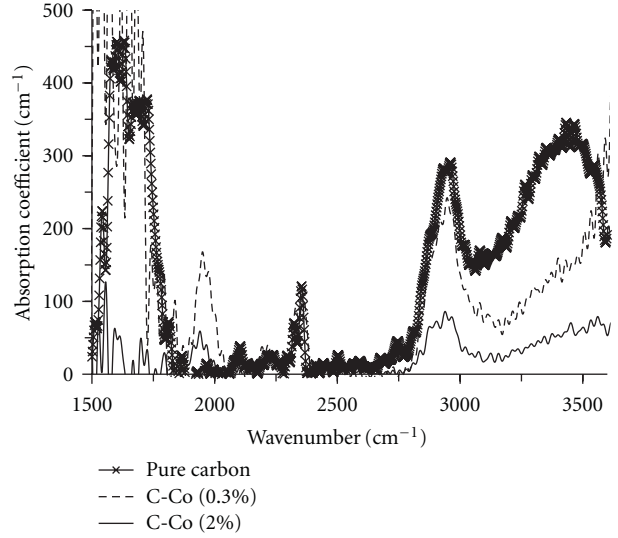


FIGURE 3: Infrared absorption spectra for different Co contents of C-Co films deposited by anodic arc plasma.

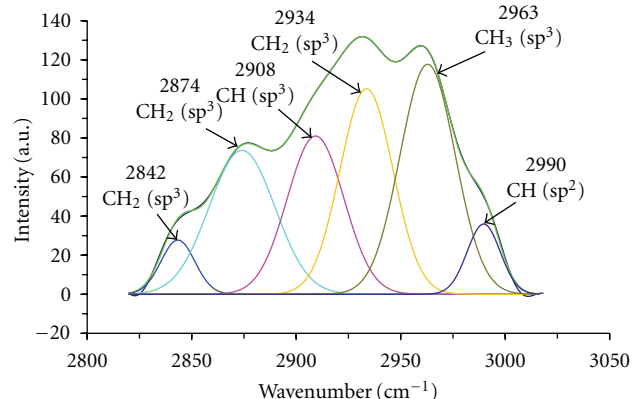


FIGURE 4: Deconvoluted infrared spectrum of pure carbon film in the region of the sp²- and sp³-hybridised bonds.

as the excitation source. The laser power was limited to 50 mW in order to prevent any material heating and damage. By using an Olympus BX40 microscope with a 50x objective lens, the explored area was limited to 3 μm².

3. Results and Discussion

The microstructure by HRTEM of doped and nondoped cobalt carbon films exhibits amorphous and crystallized zones which correspond to different phases of carbon. The presence of nanocrystallites of cobalt in doped cobalt samples is clearly evidenced by HRTEM and electron diffraction studies, and confirmed by microanalysis probe data. Figures 1 and 2 present a HRTEM images of sample for 0.3% cobalt content. These images show a mixture of amorphous and crystallized phases of carbon. Structures corresponding to graphite, chaoite, and fullerene were identified. The presence of cobalt was detected by microanalysis probe on regions well crystallized of an average size of approximately

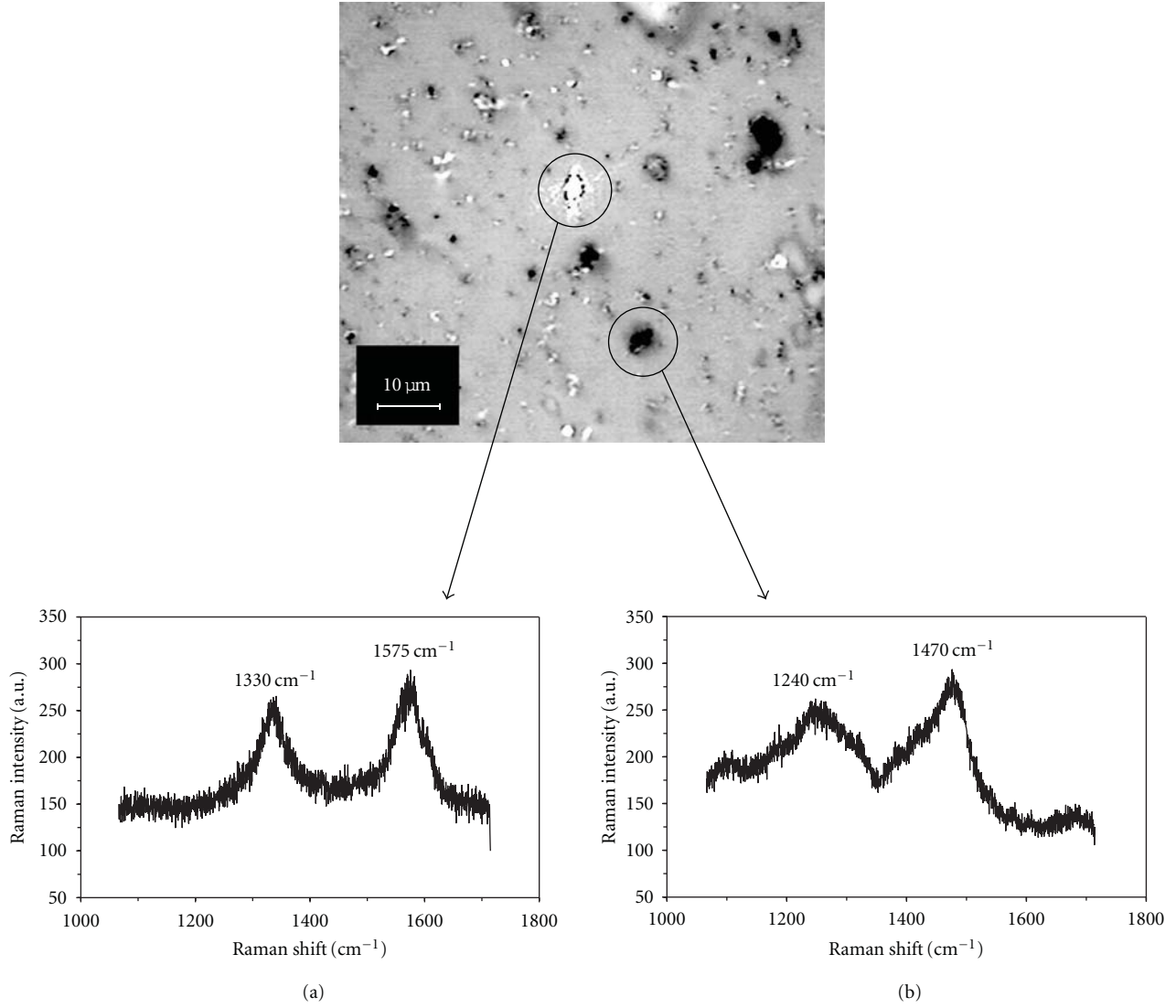


FIGURE 5: Raman spectra of pure carbon films showing the two types of D-G (sub) bands.

5 nm corresponding to a fringe spacing of 0.21 nm close to that of the interlayer separation in c.f.c Co (111).

Before starting the discussion on the Raman results, let us examine the features of the infrared spectra in the range 1500–3600 cm⁻¹ with a resolution of 2 cm⁻¹. We present on Figure 3 the infrared spectra for, respectively, 0%, 0.3%, and 2% cobalt contents. The strong fluctuation of the signal observed up to 1700 cm⁻¹ can be assigned to the electric conductivity of the films. The peak around 1950 cm⁻¹ which does not appear in pure carbon film is attributed to the linear mode of the CoC₃ configuration [27]. A quite surprising behavior is observed for 0.3% cobalt sample compared to that of 2% cobalt sample. Indeed, the intensity of the 1950 cm⁻¹ band is surprisingly lower for the 2% cobalt sample compared to 0.3% cobalt sample. This result suggests that cobalt in this material tends to segregate into clusters when the cobalt content increases. The band around 2350 cm⁻¹ can be attributed to the O–C–O antisymmetric stretching vibration of CO₂ in air. Above 2500 cm⁻¹, in the region

between 2800 and 3100 cm⁻¹, the wide broad band centered at approximately 2900 cm⁻¹ is due to the C–H vibrational mode and its different configurations [28]. We have performed a computed deconvolution of the experimental infrared spectra in order to assign the different C–H bondings which are reported in Figure 4. The fact that the intensity of this broad band decreases proportionally with increasing cobalt content suggests that the presence of cobalt in the carbon matrix inhibits the sp³-hybridized C–H bonds in accordance with the results previously reported for insertion of metallic atoms in an amorphous matrix [29]. The wide band observed at 3400 cm⁻¹ indicates a contamination of the samples by oxygen or water (which corresponds to the O–H bond-stretching mode).

Micro-Raman spectroscopy is one of the most informative methods for investigation of the microstructure of carbon. It is well known that natural diamond has a single Raman peak at 1332 cm⁻¹, whereas crystalline graphite has a Raman peak referred to as the G peak around 1580 cm⁻¹

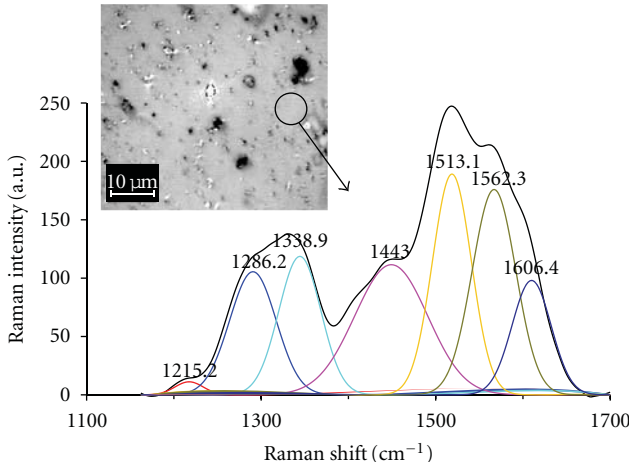


FIGURE 6: Deconvoluted Raman spectrum of C-Co (0.3%) film into three D-G pairs of Gaussian components plus one supplementary peak.

originated from E_{2g} symmetry of bond-stretching vibrations of sp^2 carbon sites. Nanocrystalline graphite and amorphous carbon have an additional peak referred to as the D peak at around 1355 cm^{-1} and originated from the A_{1g} breathing vibrations of the sixfold carbon rings. The D mode is forbidden in an ideal graphite structure, but appears when the disorder increases. It has been reported that the intensity of the D mode varies inversely with grain size of the graphite [30]. The width of the G and D peaks is due to the bond disorder of the sp^2 sites and the G peak is due to all sp^2 sites, while the D peak is only due to the sixfold carbon rings [31]. The position of the G peak moves to 1600 cm^{-1} when crystallized graphite change to nanocrystalline graphite and shift downwards to 1500 cm^{-1} for amorphous carbon when a loss of aromatic bonding appears [16]. A T peak due to sp^3 vibrations at around 1060 cm^{-1} is obtained for UV excitation [32]. In general, an amorphous carbon film has a mixture of sp^3 (diamond like) and sp^2 (graphite like) bonds.

The microstructure of our films was characterized by a micro-Raman spectrometer. The laser beam was focused onto the sample surface using an optical microscope with a magnification of 50x (laser spot area of about $3\text{ }\mu\text{m}^2$). On the surface of the films, some microparticles are visible under the optical microscope (Figure 5). The Raman spectra of the microparticles show two situations some spectra exhibit two bands at 1590 cm^{-1} and 1350 cm^{-1} which correspond, respectively, to the G band originated from the E_{2g} bond-stretching vibrations of sp^2 -bonded clusters and the D band from the A_{1g} breathing vibrations of the sixfold carbon rings (Figure 5(a)); the position of the G band is close to that of nanocrystalline graphite of nanometer-sized clusters [16]. For some spectra, the G band is shifted to lower wavenumbers (1470 cm^{-1}), suggesting that the sp^2 -bonded clusters are far from the sixfold carbon rings as it happens in fullerene or amorphous carbon [16] (Figure 5(b)). Let us discuss now the data obtained from the Raman investigation in regions of the surface without microparticles. Figure 6 shows Raman spectrum obtained for a 03%-cobalt-doped carbon thin film.

This spectrum exhibits several overlapping bands in the range 1200 – 1650 cm^{-1} . The broad band can be decomposed into subbands at 1215 , 1286 , 1339 , 1443 , 1513 , 1562 , and 1600 cm^{-1} (Figure 6). The peaks at 1562 and 1339 cm^{-1} are attributed to the D-G pair (D at 1339 cm^{-1} and G at 1562 cm^{-1}) belonging to nanocrystalline graphite clusters. The second D-G pair (D at 1286 cm^{-1} and G at 1513 cm^{-1}) can be assigned to clusters that have a bonding structure rather similar to that of amorphous carbon. The modes at 1215 and 1443 cm^{-1} can be attributed to Raman shift of C–C and C=C bonds observed in *trans*- and *cis*-polyacetylene chains [33]. Finally, the supplementary peak centered around 1600 cm^{-1} can be identified as a fullerene vibration mode [34, 35]. Similar features associated with mixed structures have also been reported previously for other type of metal doped carbon films ($\text{CN}_x\text{-Ni}$) [36]. The analyse of the Raman spectra with increasing cobalt concentration can be performed in the framework of the phenomenological three-stage model of Ferrari and Robertson [31]. In this model, an amorphization trajectory ranging from graphite to diamond is defined; the Raman spectra of all disordered carbons are classified within a three-stage model of increasing disorder as a function of the G peak position and the relative integrated intensity ratio I_D/I_G of the D and G peaks. In our samples, the relative integrated intensity ratio I_D/I_G for the D-G pair attributed to nano-crystalline graphite clusters goes from 0.47 for pure carbon sample to 1.47 for 2% cobalt sample, for the D-G pair attributed to amorphous carbon regions, the I_D/I_G ratio goes from 0.31 to 0.66 according to the increasing cobalt content. Moreover, the integrated intensities of modes assigned to fullerene and polyacetylene chains tend to increase with the cobalt content of the films. These results suggest that the presence of cobalt in the films modifies the arrangement of the different phases of carbon in the films, increases the disorder of the graphite layer by decreasing the aromatic bonds to the detriment of polyacetylene chains, and favors the growth of fullerene structure.

4. Conclusion

The correlation between the microstructure by using HRTEM and vibrational properties by using infrared and Raman spectroscopies, of cobalt-carbon thin films obtained by pulsed anodic electric arc system, has allowed us to identify the nature of various bondings which coexist in this material. These films show a complex microstructure composed of amorphous and crystallized zones and cobalt aggregates. We have attempted to determine the evolution of the arrangement of the different phases of carbon as function of the cobalt content in these films.

Acknowledgment

The authors are grateful to A. Cantaluppi for technical help.

References

- [1] P. Stamp, "Magnets get their act together," *Nature*, vol. 359, no. 6394, pp. 365–366, 1992.

- [2] B. Barbara, "Novel magnetic structures and nanostructures," *Journal of Magnetism and Magnetic Materials*, vol. 156, no. 1-3, pp. 123–127, 1996.
- [3] T. Hayashi, S. Hirono, M. Tomita, and S. Umemura, "Magnetic thin films of cobalt nanocrystals encapsulated in graphite-like carbon," *Nature*, vol. 381, no. 6585, pp. 772–774, 1996.
- [4] X. Han, F. Yan, A. Zhang et al., "Structure and tribological behavior of amorphous carbon films implanted with Cr⁺ ions," *Materials Science and Engineering A*, vol. 348, no. 1-2, pp. 319–326, 2003.
- [5] X. Nie, J. C. Jiang, L. D. Tung, L. Spinu, and E. I. Meletis, "Multifunctional Co-C nanocomposite thin films," *Thin Solid Films*, vol. 415, no. 1-2, pp. 211–218, 2002.
- [6] V. V. Uglava, V. M. Anishchik, Y. Pauleau et al., "Relations between deposition conditions, microstructure and mechanical properties of amorphous carbon-metal films," *Vacuum*, vol. 70, no. 2-3, pp. 181–185, 2003.
- [7] G. J. Kovacs, G. Safran, O. Geszti, T. Ujvari, I. Bertoti, and G. Radnoci, "Structure and mechanical properties of carbon–nickel and CNx–nickel nanocomposite films," *Surface and Coatings Technology*, vol. 180–181, pp. 331–334, 2004.
- [8] E. Liu, X. Shi, L. K. Cheah et al., "Electrical behaviour of metal/tetrahedral amorphous carbon/metal structure," *Solid-State Electronics*, vol. 43, no. 2, pp. 427–434, 1999.
- [9] J. C. Orlianges, C. Champeaux, A. Catherinot et al., "Electrical properties of pure and metal doped pulsed laser deposited carbon films," *Thin Solid Films*, vol. 453–454, pp. 291–295, 2004.
- [10] T. Takeno, Y. Hoshi, H. Miki, and T. Takagi, "Activation energy in metal-containing DLC films with various metals of various concentrations," *Diamond and Related Materials*, vol. 17, no. 7–10, pp. 1669–1673, 2008.
- [11] J. M. Bonard, S. Seraphin, J. E. Wegrowe, J. Jiao, and A. Chatain, "Varying the size and magnetic properties of carbon-encapsulated cobalt particles," *Chemical Physics Letters*, vol. 343, no. 3-4, pp. 251–257, 2001.
- [12] W. B. Mi, L. Guo, E. Y. Jiang, Z. Q. Li, P. Wu, and H. L. Bai, "Structure and magnetic properties of facing-target sputtered Co-C granular films," *Journal of Physics D*, vol. 36, no. 19, pp. 2393–2399, 2003.
- [13] V. Zhukova, J. M. Blanco, A. Zhukov, J. Gonzalez, A. Torcunov, and V. Larin, "Magnetostriction of glass-coated Co-rich amorphous microwires and its dependence on current annealing," *Journal of Magnetism and Magnetic Materials*, vol. 254–255, pp. 94–96, 2003.
- [14] H. Wang, M. F. Chiah, W. Y. Cheung, and S. P. Wong, "Structure, magnetic and electrical properties of soft magnetic Co—C amorphous thin films," *Physics Letters A*, vol. 316, no. 1-2, pp. 122–125, 2003.
- [15] N. Nishi, K. Kosugi, K. Hino, T. Yokoyama, and E. Okunishi, "Formation and magnetic characteristics of cobalt-carbon nanocluster magnets embedded in amorphous carbon matrices," *Chemical Physics Letters*, vol. 369, no. 1-2, pp. 198–203, 2003.
- [16] J. Robertson, "Diamond-like amorphous carbon," *Materials Science and Engineering R*, vol. 37, pp. 129–281, 2002.
- [17] D. H. C. Chua, W. I. Milne, B. K. Tay, P. Zhang, and X. Z. Ding, "Microstructural and surface properties of cobalt containing amorphous carbon thin film deposited by a filtered cathodic vacuum arc," *Journal of Vacuum Science and Technology A*, vol. 21, no. 2, pp. 353–358, 2003.
- [18] R. K. Y. Fu, Y. F. Mei, L. R. Shen et al., "Molybdenum-carbon film fabricated using metal cathodic arc and acetylene dual plasma deposition," *Surface and Coatings Technology*, vol. 186, no. 1-2, pp. 112–117, 2004.
- [19] N. Benchikh, F. Garrelie, K. Wolski et al., "Nanocomposite tantalum-carbon-based films deposited by femtosecond pulsed laser ablation," *Thin Solid Films*, vol. 494, no. 1-2, pp. 98–104, 2006.
- [20] P. Dubcek, N. Radic, and O. Milat, "Characterization of grains in tungsten-carbon films I," *Nuclear Instruments and Methods in Physics Research Section B*, vol. 200, pp. 329–332, 2003.
- [21] A. Anders, "Metal plasmas for the fabrication of nanostructures," *Journal of Physics D*, vol. 40, no. 8, Article ID 2272, 2007.
- [22] P. J. Martin and A. Bendavid, "Review of the filtered vacuum arc process and materials deposition," *Thin Solid Films*, vol. 394, no. 1-2, pp. 1–15, 2001.
- [23] L. Kumari, S. V. Subramanyam, S. Eto, K. Takai, and T. Enoki, "Metal-insulator transition in iodinated amorphous conducting carbon films," *Carbon*, vol. 42, no. 11, pp. 2133–2137, 2004.
- [24] L. Kumari and S. V. Subramanyam, "Tuning of the metal-insulator transition in iodine incorporated amorphous carbon," *Journal of Applied Physics*, vol. 99, no. 9, Article ID 096107, 2006.
- [25] E. Bustarret, P. Achatz, B. Sacépé et al., "Metal-to-insulator transition and superconductivity in boron-doped diamond," *Philosophical Transactions of the Royal Society A*, vol. 366, no. 1863, pp. 267–279, 2008.
- [26] A. Tembre, M. Clin, J.-C. Picot et al., "Magnetic and electric properties of C-Co thin films prepared by vacuum arc technique," *Journal of Alloys and Compounds*, vol. 509, no. 37, pp. 9123–9126, 2011.
- [27] S. A. Bates, J. A. Rhodes, C. M. L. Rittby, and W. R. M. Graham, "Fourier transform infrared observation of the $\nu_1(\sigma)$ mode of linear CoC₃ trapped in solid Ar," *Journal of Chemical Physics*, vol. 127, no. 6, Article ID 064506, 6 pages, 2007.
- [28] B. Dischler, A. Bubenzier, and P. Koidl, "Bonding in hydrogenated hard carbon studied by optical spectroscopy," *Solid State Communications*, vol. 48, no. 2, pp. 105–108, 1983.
- [29] G. M. Matenoglou, H. Zoubos, A. Lotsari et al., "Metal-containing amorphous carbon (a-C:Ag) and AlN (AlN:Ag) metallocodielectric nanocomposites," *Thin Solid Films*, vol. 518, no. 5, pp. 1508–1511, 2009.
- [30] F. Tuinstra and J. L. Koenig, "Raman spectrum of graphite," *Journal of Chemical Physics*, vol. 53, no. 3, pp. 1126–1130, 1970.
- [31] A. C. Ferrari and J. Robertson, "Interpretation of Raman spectra of disordered and amorphous carbon," *Physical Review B*, vol. 61, no. 20, pp. 14095–14107, 2000.
- [32] A. C. Ferrari and J. Robertson, "Resonant Raman spectroscopy of disordered, amorphous, and diamondlike carbon," *Physical Review B*, vol. 64, no. 7, Article ID 075414, 13 pages, 2001.
- [33] S. Shibahara, M. Yamane, K. Ishikawa, and H. Takezoe, "Direct synthesis of oriented trans-polyacetylene films," *Macromolecules*, vol. 31, no. 11, pp. 3756–3758, 1998.
- [34] V. Paillard, "On the origin of the 1100 cm⁻¹ Raman band in amorphous and nanocrystalline sp³ carbon," *Europhysics Letters*, vol. 54, no. 2, pp. 194–198, 2001.
- [35] V. Vincenzo, M. Pagliai, and G. Cardini, "The infrared and Raman spectra of fullerene C70. DFT calculations and

- correlation with C₆₀,” *Journal of Physical Chemistry A*, vol. 106, no. 9, pp. 1815–1823, 2002.
- [36] G. J. Kovacs, M. Veres, M. Koos, and G. Radnoci, “Raman spectroscopic study of magnetron sputtered carbon-nickel and carbon nitride-nickel composite films: the effect of nickel on the atomic structure of the C/CNx matrix,” *Thin Solid Films*, vol. 516, no. 21, pp. 7910–7915, 2008.